Industrial heat pumps for high temperature process applications.

A numerical study of the ammonia-water hybrid absorption-compression heat pump

Jensen, Jonas Kjær

Publication date:
2016

Document Version
Publisher's PDF, also known as Version of record

Industrial heat pumps for high temperature process applications

A numerical study of the ammonia-water hybrid absorption-compression heat pump

PhD Thesis

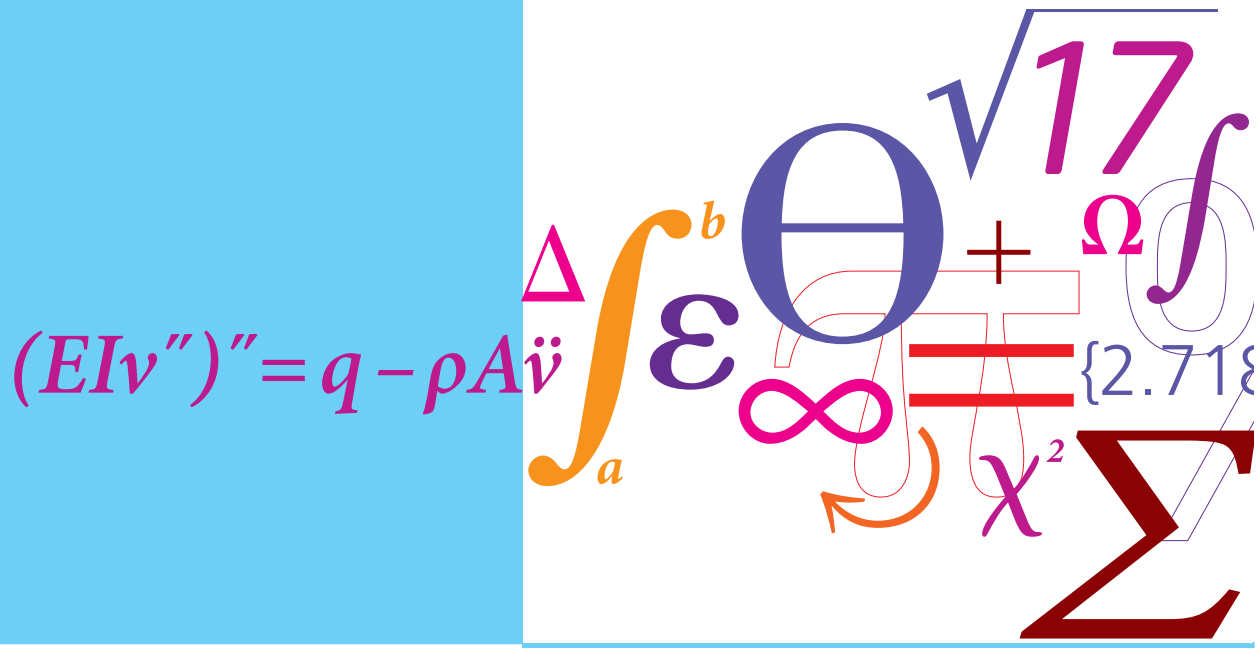

Jonas Kjær Jensen
DCAMM Special Report No. S207
December 2015

DTU Mechanical Engineering
Department of Mechanical Engineering

Industrial heat pumps for high temperature process applications

A numerical study of the ammonia-water hybrid absorption-compression heat pump

PhD Thesis

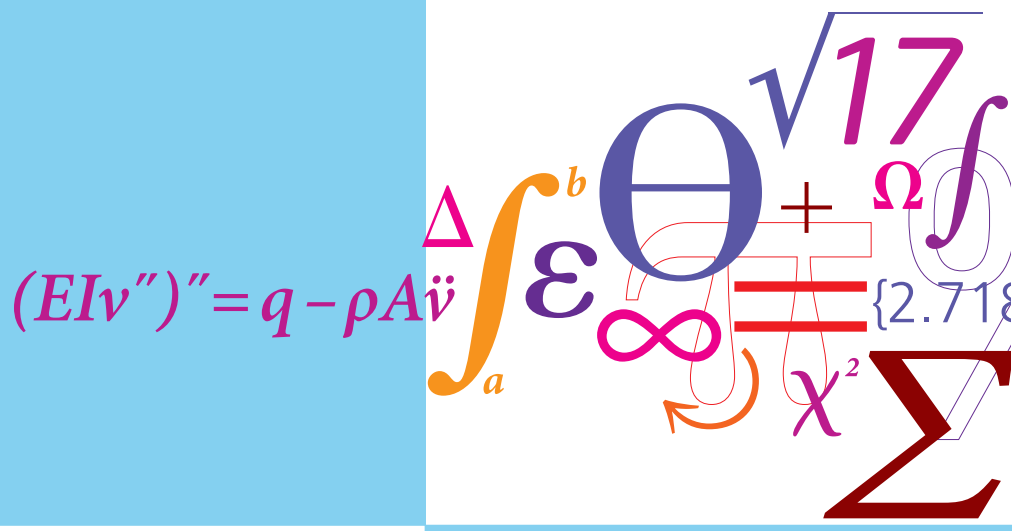

Jonas Kjær Jensen

December 2015

DTU Mechanical Engineering
Department of Mechanical Engineering

Industrial heat pumps for high temperature process applications

A numerical study of the ammonia-water hybrid absorption-compression heat pump

Jonas Kjær Jensen

Ph.D. Thesis

Kongens Lyngby 2015

Technical University of Denmark

Industrial heat pumps for high temperature process applications
A numerical study of the ammonia-water hybrid absorption-compression heat pump

Ph.D. Thesis

Supervisors:
Brian Elmegaard, DTU-MEK
Wiebke Brix Markussen, DTU-MEK
DTU Mechanical Engineering
Section of Thermal Energy
Technical University of Denmark

Nils Koppels Allé, Building 403
DK-2800 Kongens Lyngby
Denmark
Phone (+45) 45 88 41 31
Fax (+45) 45 88 43 25
www.mek.dtu.dk

ISBN: 978-87-7475-459-6
DCAMM Special Report no. S207

Preface

This thesis was submitted as partial fulfilment of the requirements for the Ph.D. degree at the Technical University of Denmark (DTU).

The thesis was completed at the Section of Thermal Energy, Department of Mechanical Engineering, Technical University of Denmark. The work was carried out in a three-year period which was initiated 1st of September 2012 and concluded December 31th 2015. The thesis work was conducted under the supervision of Associate Professor Brian Elmegaard and co-supervision of Assistant Professor Wiebke Brix Markussen.

An external research stay was undertaken from March 2014 to June 2014. The external stay was at The Technical Univeristy of Berlin, Institute of Energy Technology, section of Energy Conversion and Protection of the Environment. The purpose of the stay was collaboration with Professor Tatiana Morosuk and Professor George Tsatsaronis.

This research project was financially funded by EUDP (Energy Technology Development and Demonstration), project title: "Development of ultra-high temperature hybrid heat pump for process application", project number: 64011-0351

Jonas Kjær Jensen
Kgs. Lyngby, December 2015

Acknowledgements

I thankfully acknowledge the support of the Ph.D.-project by, EUDP (Energy Technology Development and Demonstration) and the collaboration with the Danish Technological Institute, Innoterm and Hybrid Energy who have contributed to the project by fruitful discussions and advise on the commercial aspects of the project.

I would like to extend my thanks and gratitude to my supervisors Brian Elmegaard and Wiebke Brix Markussen. Their support, advice, discussions and encouragement have helped shape the outcome of the thesis and have given me three exciting and inspiring years.

I would like to thank Tatiana Morosuk and George Tsatsaronis for allowing me to join their section in Berlin for my external research stay. Their guidance and advice on the advanced exergy-based analysis was a great help and inspiration for the project. Further, I would like to thank Oticon Fonden and IDA's og Berg-Nielsens Studie- og Støttefond for supporting the external stay in Berlin.

To my colleagues at the Section of Thermal Energy i would like to thank you all for an inspiring and pleasant work environment. You have all contributed to the project with our many fun and exciting discussions. A special thanks to Torben Ommen for his collaboration on the investigation of industrial heat pump working domains, this contribution has been very valuable for the project. I would also like to thank Martin Rhyl Kærn for the discussions and collaboration on the heat transfer and transport properties of ammonia-water mixtures as well as the modelling of maldistribution in plate heat exchangers. Further, i would like to thank Erasmus Damgaard Rothuizen for his collaboration on the cooling of hydrogen in refuelling stations.

Finally, I would like to thank my friends and family for supporting me

these last three years. The time spent with you have been a much needed break from academia. A special thanks to Christel for her patience and understanding especially in the stressful parts of the project.

Abstract

Industrial processes often consume large quantities of heat, while often dissipating large quantities of waste heat to the ambient. The main energy source for industrial heat supply is fossil fuels, either oil or natural gas. Thus, the heat consumption of industrial processes often entail large CO_2 emissions as well as emission of other harmful pollutants. As heat pumps can upgrade low temperature waste heat to a high temperature heat supply using only a fraction of primary energy, heat pumps may be applied to improve the energy efficiency of industrial processes. Further, Replacing oil or gas burners with heat pumps could lead to a reduction of the emissions, especially in a future energy system with a high penetration of renewable energy sources.

Many industrial heat pumps have been installed with a heat supply temperature ranging from 50 - 90 °C. The lack of installation in the temperature domain in excess of 90 °C is believed to be caused by the lack of cost efficient heat pumps, rather than a limited demand. Commercial components for industrial heat pumps are limited to a working pressure of 28 bar, although high pressure alternatives do exist for ammonia (50 bar) and CO_2 (140 bar). Most commercial compressors are not durable at compressor discharge temperature above 180 °C. Using these components, vapour compression heat pumps (VCHP) are limited to heat supply temperatures between 80 - 90 °C. Developing heat pumps that are capable of delivering temperatures above 90 °C may therefore allow heat pump implementation in more industrial processes than is currently possible.

The ammonia-water hybrid absorption-compression heat pump (HACHP) is of specific interest for development of high temperature heat pumps due to two properties inherent to the zeotropic working fluid: 1. Increased efficiency due to the reduction of thermal irreversibilities in the heat transfer processes between the working fluid and the external streams. 2. The reduction of vapour pressure compared to the vapour pressure of pure ammonia. The HACHP can therefore deliver higher

temperatures at higher efficiencies than conventional VCHP.

To investigate the possibility of developing high temperature HACHP, numerical models are developed for the one-stage cycle and several identified two-stage compression configurations. The design of the HACHP is governed by two extra degrees of freedom compared to the VCHP. These can be set by many criterion but is in this study set by the choice of the rich ammonia mass fraction and the circulation ratio. The influence of these parameters on the performance and size of the system is investigated. The performance and size of the identified two-stage compression configurations are compared to the one-stage cycle. One two-stage compression cycle performs better than the remaining, both in terms of increased efficiency, reduction of discharge temperature and needed compressor volume.

For the one-stage and the best two-stage cycle the constraints of commercial components are imposed on the choice of rich ammonia mass fraction and the circulation ratio at a number of supply temperatures. This showed that the 28 bar one-stage HACHP allow temperatures up to 111 °C, 50 bar up to 129 °C, and 140 bar up to 147 °C. For the two-stage HACHP, 28 bar components allow temperatures up to 126 °C, 50 bar up to 145 °C, and 140 bar up to 160 °C.

To determine the sources of thermodynamic irreversibilities as well as the formation of cost and environmental impact an advanced exergy-based analysis is applied to the HACHP. An exergy-based analysis consists of three steps: an exergy analysis is conducted to identify the exergy streams in the system and the thermodynamic irreversibilities (exergy destruction). Subsequently, an economic analysis is conducted and combined with the exergy analysis such that cost is associated with each stream of exergy and consequently, the cost of exergy destruction is determined. This is know as an exergoeconomic analysis. Further, a life cycle assessment is performed and combined with the exergy analysis to associate environmental impact to all streams of exergy and thereby determine the environmental impact of exergy destruction. This is known as an exergoenvironmental analysis. The advanced exergy-based analysis differs from the conventional analysis by accounting for component interdependencies as well as reduction potential. The highest rate of avoidable exergy destruction was associated with the desorber while

the highest rate of avoidable cost was associated with the absorber. It is found that the cost of most components are evenly distributed between operational and capital investment cost. The highest rate of avoidable environmental impact stems from the compressor. It is shown that the environmental impact of construction, transportation and disposal was negligible compared to the environmental impact related to the operation of the HACHP.

The working domain of the HACHP is investigated by imposing all technical constraints of commercial components to a variation of the heat supply temperature and temperature lift. An economic analysis is applied to the same variation such that the net present value in all points is attained. For all combinations it is evaluated whether the solution complies with the technical and economic constraint (net present value > 0) and thus whether the heat pump implementation is feasible. A similar analysis is conducted for VCHP, which allows a comparison, not only on which temperature levels and lift are attainable by the two technologies but also which technology is the more viable solution in the domain where both compete. This showed that the HACHP can be used to heat supply temperatures of 150 °C and temperatures up to 60 K. This increases the working domain of industrial heat pump. For the temperature range where the HACHP competes with ammonia VCHP: the HACHP is the most viable solution at low temperature lifts while VCHP are more profitable at high lifts. For the range where the HACHP competes with iso-butane or CO_2 the HACHP is always the more viable solution.

Resume

Industrielle processer forbruger ofte store mængder varme, mens der ofte dissiperes store mængder spildvarme til omgivelserne. Industriel varmeforsyning er typisk drevet af fossilt brændsel, enten olie eller naturgas. Varmeforbruget i industrielle processer er derfor ofte skyld i store udledninger af CO_2 samt udledning af andre skadelige stoffer. Da varmepumper kan opgradere lavtemperatur spildvarme til en højtemperatur varmekilde med kun en brøkdel af primær energi, kan varmepumper anvendes til at øge energieffektiviteten i industrielle processer. Yderligere kan udskiftning af olie- eller gasbrændere med varmepumper medføre en reduktion af udledningerne, især i et fremtidigt energisystem med øget integration af vedvarende energikilder.

Mange industrielle varmepumper er blevet installeret med en temperatur på 50-90 ° C. Manglen på installationer med temperature over 90 °C skyldes primært manglen på rentable varmepumper i dette temperaturområde, snarere end det skyldes en begrænset efterspørgsel. Standard komponenter til industrielle varmepumper er begrænset til et arbejdstryk på 28 bar, der findes dog højttryks alternativer til ammoniak (50 bar) og CO_2 (140 bar). De fleste kommercielle varmepumpekompressorer er ikke holdbare ved trykrørstemperature over 180 ° C. Med disse komponenter kan konventioneller varmepumper levere temperature mellem 80-90 °C. Udviklingen af en højtemperaturvarmepumpe, som er i stand til at levere temperaturer over 90 °C, kan derfor give mulighed for at implementere varmepumper i flere industrielle processer end hvad der er muligt i dag.

Ammoniakvand hybrid absorption-kompressions varmepumpen er af særlig interesse for udviklingen af højtemperaturvarmepumper. Dette skyldes to egenskaber som er knyttet til brugen af den zeotrope blanding: 1. Øget virkningsgrad grundet reduktion af termisk irreversibilitet i varmeoverførselen mellem arbejdsmedie og de eksterne strømme. 2. Reduktionen af damptrykket i forhold til damptrykket af ren ammoniak. Således kan hybridvarmepumpen leverer højere temperaturer med en

øget effektivitet i forhold til de konventionelle varmepumper.

For at undersøge muligheden for at udvikle højtemperatur hybridvarmepumper er der udviklet numeriske modeller af både en et-trins proces, samt flere to-trins kompressions processer. Hybridvarmepumpen har to ekstra frihedsgrader i forhold til den konventionelle varmepumpe. Disse kan bestemmes ud fra mange kriterier, men bestemmes her ud fra valget af ammoniakkoncentration og cirkulationsforhold. Disse parametres indflydelse på virkningsgrad og systemets størrelse undersøges. Yderligere, er virkningsgrad samt kompressorvolumen af de undersøgte to-trins processer blevet sammenlignet med et-trins processen. Et af de undersøgte to-trins processer præsterer bedre end den resterende, både i forhold til effektivitet, reduktion af trykrørstemperatur samt det nødvendige kompressorvolumen.

For et-trins processen samt den bedste to-trins proces er de tekniske begrænsninger for kommercielle komponenter blevet pålagt valget af ammoniakkoncentration og cirkulationsforhold ved en række forsyningstemperaturer. Dette viste, at en 28 bar et-trins proces kan bruges ved temperaturer op til 111 °C, 50 bar op til 129 °C og 140 bar op til 147 °C. For to-trins processen kan 28 bar komponenter bruges op til 126 °C, 50 bar op til 145 °C og 140 bar op til 160 °C.

Der er anvendt en avanceret exergi-baseret analyse til at bestemme kilderne til termodynamiske irreversibilitet, omkostninger samt miljøpåvirkning. En exergi-baseret analyse består af tre trin: først udføres en exergianalyse for at bestemme exergi-strømmene i systemet, samt de termodynamiske irreversibiliteter (exergidestruktion). Efterfølgende udføres en økonomisk analyse som kombineres med exergianalysen således at omkostninger knyttes til hver exergistrøm samt for at bestemme omkostningerne forbundet med exergidestruktion. Dette er kendt som en exergoøkonomisk analyse. Yderligere udføres en livscyklusvurdering som også kombineres med exergianalysen for at knytte miljøpåvirkningen til alle exergistrømme og derved bestemme den miljømæssige konsekvens af exergidestruktionen. Dette er kendt som en exergoøkologisk analyse. En avanceret exergi-baseret analyse adskiller sig fra den konventionelle analyse ved at tage højde sig for komponenternes indbyrdes afhængighed samt potentiellet for at reducere exergidestruktion. Den højeste undgåelige exergi-destruktion er forbundet med desorberen

mens de højeste undgåelige omkostninger er forbundet med absorberen. Det ses, at prisen for de fleste komponenter er jævnt fordelt mellem de operationelle- og kapital- omkostninger. Den højeste sats for undgåelig miljøbelastning stammer fra kompressoren. Det ses, at de miljømæssige konsekvenser forbundet med konstruktion, transport og bortskaffelse er ubetydelig sammenlignet med den miljøbelastning der er i finder sted i forbindelse med driften.

Arbejdsområdet af hybridvarmepumpen er blevet undersøgt ved at sammenfatte de tekniske begrænsninger for kommerciel komponent til en variation af forsyningstemperaturen og temperatur løftet. En økonomisk analyse er blevet udført på den samme variation, således at kapitalværdien i alle punkter er kendt. For alle kombinationer kan det så vurderes, om løsningen er i overensstemmelse med den tekniske og økonomiske begrænsninger (kapitalværdi > 0), og dermed hvorvidt implementeringen af varmepumpen er mulig. En tilsvarende analyse er foretaget for konventionelle varmepumper, hvilket gør det muligt at sammenligne, ikke kun hvilke temperatur niveauer og løft der er opnåelige, men også hvilken teknologi der er den mest rentable løsning i de områder, hvor begge konkurrere. Dette viste, at hybridvarmepumpen kan bruges til temperaturer op til 150 °C og løft op til 60 K. Dette øger arbejdsområdet af industriel varmepumper. I arbejdsområdet hvor hybridvarmepumpen konkurrerer med ammoniakvarmepumper er hybridvarmepumpen den mest rentable løsning ved lave løft, mens ammoniakvarmepumpen er mere rentable ved høje løft. For det område, hvor hybridvarmepumpen konkurrerer med iso-butan eller CO_2 er hybridvarmepumpen altid den mest rentable løsning.

List of publications

Journal Papers:

[P1] Jensen, J. K., Rothuizen, E. D., Markussen, W. B., Exergoeconomic optimization of coaxial tube evaporators for cooling of high pressure gaseous hydrogen during vehicle fuelling, Energy Conversion and Management. 85, p. 740–749, doi:10.1016/j.enconman.2014.02.023.

[P2] Jensen, J. K., Markussen, W. B., Reinholdt, L., Elmegaard, B., Exergoeconomic optimization of an ammonia-water hybrid absorption–compression heat pump for heat supply in a spraydrying facility, International Journal of Energy and Environmental Engineering 2015; 6 2, 195-211, doi:10.1007/s40095-015-0166-0.

[P3] Jensen, J. K., Markussen, W. B., Reinholdt, L., Elmegaard, B., On the development of high temperature ammonia-water hybrid absorption compression heat pumps, International Journal of Refrigeration 2015, doi:10.1016/j.ijrefrig.2015.06.006

[P4] Ommen, T., Jensen, J.K., Markussen, W.B., Reinholdt, L., Elmegaard, B.. Technical and economic working domains of industrial heat pumps: Part 1 - single stage vapour compression heat pumps. International Journal of Refrigeration 2015; 55: 168–182. doi:10.1016/j.ijrefrig.2015.02.012.

[P5] Jensen, J.K., Ommen, T., Markussen, W.B., Reinholdt, L., Elmegaard, B.. Technical and economic working domains of industrial heat pumps: Part 2 - ammonia –water hybrid absorption-compression heat pumps. International Journal of Refrigeration 2015; 55: 183-200. doi:10.1016/j.ijrefrig.2015.02.011.

[P6] Ommen, T., Verda, V., Jensen, J.K., Markussen, W.B., Elmegaard, B.. Thermoeconomic comparison of centralised district heating heat pumps. Energy Conversion and Management 2015; [To be submitted].

[P7] Kærn, M. R., Modi, A., Jensen, J.K., Haglind, F., An Assessment of Transport Property Estimation Methods for Ammonia–Water Mixtures

and Their Influence on Heat Exchanger Size, International Journal of Thermophysics 2015; 36 6: 1468-1497, doi:10.1007/s10765-015-1857-8

[P8] Kærn, M. R., Modi, A., Jensen, J.K., Andreasen, J.G, Haglind, F., An assessment of in-tube flow boiling correlations for ammonia-water mixtures and their influence on heat exchanger size, Applied Thermal Engineering, 93: 623-638, doi:10.1016/j.applthermaleng.2015.09.106

[P9] Jensen, J. K., Markussen, W. B., Elmegaard, B., Advanced exergy analysis of an ammonia-water hybrid absorption compression heat pump. [note: to be submitted]

[P10] Jensen, J. K., Morosuk, T., Markussen, W. B., Elmegaard, B., Advanced exergoeconomic analysis of an ammonia-water hybrid absorption compression heat pump. [note: to be submitted]

Peer-reviewed conference papers:

[P11] Jensen J.K, Rothuizen E.D, Markussen W.B, Entropy generation minimization of one and two-stage tube in tube ammonia evaporators cooling high pressure gaseous hydrogen for vehicle refuelling. Proceedings of ECOS 2013 - The 26th International Conference on Efficiency, Cost, Optimization, Simulation and environmental Impact of Energy Systems, Chinese Society of Engineering Thermophysics.

[P12] Jensen, J. K., Reinholdt, L., Markussen, W. B., Elmegaard, B., Investigation of ammonia/water hybrid absorption/compression heat pumps for heat supply temperatures above 100 °C, Proceedings of ISHPC 2014 - International Sorption Heat Pump Conference, University of Maryland.

[P13] Jensen, J. K., Markussen, W. B., Reinholdt, L., Elmegaard, B., Exergoeconomic optimization of an ammonia-water hybrid heat pump for heat supply in a spray drying facility, Proceedings of ECOS 2014 - The 27th International Conference on Efficiency, Cost, Optimization, Simulation and environmental Impact of Energy Systems, Åbo Akademi.

[P14] Ommen, T., Jensen, J.K., Markussen, W.B., Reinholdt, L., Elmegaard, B., Technical and economic working domains of industrial heat pumps: Part 1 - vapour compression heat pumps. 11th IIR - Gustav Lorentzen

Conference on Natural Refrigerants - GL 2014. Chinese Association of Refrigeration.

[P15] Jensen, J.K., Ommen, T., Markussen, W.B., Reinholdt, L., Elmegaard, B.. Technical and economic working domains of industrial heat pumps: Part 2 - ammonia–water hybrid absorption–compression heat pumps. 11th IIR - Gustav Lorentzen Conference on Natural Refrigerants - GL 2014. Chinese Association of Refrigeration.

[P16] Jensen, J. K., Markussen, W. B., Reinholdt, L., Elmegaard, B., Conventional and advanced exergoenvironmental analysis of an ammonia-water hybrid absorption –compression heat pump , Proceedings of ECOS 2015 - The 28th International Conference on Efficiency, Cost, Optimization, Simulation and environmental Impact of Energy Systems, ENSGTI.

[P17] Ommen, T., Jensen, J.K., Markussen, W.B., Elmegaard, B., Enhanced technical and economic working domains of heat pumps operated on series, Proceedings of ICR 2015 - 24th IIR International Congress of Refrigeration, Japan Society of Refrigerating and Air Conditioning Engineers.

[P18] Jensen, J.K., Kærn, M.R, Ommen, T., Markussen, W.B., Reinholdt, L., Elme- gaard, B., Effect of liquid/vapour maldistribution on performance of plate heat exchanger evaporators, Proceedings of ICR 2015 - 24th IIR International Cong-ress of Refrigeration, Japan Society of Refrigerating and Air Conditioning Engineers.

Contents

Nomenclature

Abbreviations

CRF	Capital recovery factor
EES	Engineering Equation Solver
HACHP	Hybrid absorption-compression heat pump
HEX	Heat exchanger
IHEX	Internal heat exchanger
LVS	Liquid-vapour separator
MRP	Manufacturer suggested retail price
NDA	Non-disclosure agreement
LP R717	Low pressure R717 components
HP R717	High pressure R717 components
TBP	Trade business price
VCHP	Vapour compression heat pump
LMTD	Logarithmic mean temperature difference

Roman letters

A_{HT}	Heat transfer area	(m^2)
A_{IN}	Investment area	(m^2)
b	Unit environmental impact of exergy	(mpt kW^{-1})
b	Plate press depth	(mm)
$\dot{B}$	Exergetic environmental impact rate	(mpt s^{-1})
Bo	Boiling number	(-)
c	Unit cost of exergy	(€ kW^{-1})
$\dot{C}$	Exergetic cost rate	(€ s^{-1})
c_p	Specific heat capacity	(kJ kg^{-1} K^{-1})
COP	Coefficient of performance	(-)
D_h	Hydraulic diameter	(m)
e	Specific exergy	(kJ kg^{-1})
$\dot{E}$	Exergy rate	(kW)
f	Circulation ratio	(-)
f_b	Exergoeconomic factor	(-)
f_c	Exergoenvironmental factor	(-)
f_Q	Heat loss ratio	(-)
F	Two-phase enhancement factor	(-)
FC	Annual cost of fuel consumption	(€)
h	Specific enthalpy	(kJ kg^{-1})

h_{fg}	Specific heat of vaporization	(kJ kg^{-1})
G	Mass flux	(kg s^{-1} m^{-2})
H	Yearly operating time	(s)
i	Interest rate	(-)
i^{eff}	Effective interest rate	(-)
i_L	Inflation rate	(-)
L	Plate length	(m)
LT	Technical lifetime	(years)
m	Mass	(kg)
$\dot{m}$	Mass flow rate	(kg s^{-1})
M	Number of channels	(-)
N	Number of plates	(-)
Nu	Nusselt number	(-)
NPV	Net present value	(€)
OMC	Operation and maintenance cost	(€)
PBP	Payback period	(years)
PEC	Purchased equipment cost	(€)
p	Pressure	(bar)
Δp	Pressure loss	(bar)
Pr	Prandtl number	(-)
PR	Pressure ratio	(-)
PV	Present value	(€)
q	Vapour mass fraction	(-)
q''	Heat flux	(kW m^{-2})
$\dot{Q}$	Heat rate	(kW)
r	Relative difference	(%)
Re	Reynolds number	(-)
s	Specific entropy	(kJ kg^{-1} K^{-1})
T	Temperature	(°C)
ΔT	Temperature difference	(K)
t	Plate wall thickness	(-)
TCI	Total capital investment	(€)
U	Overall heat transfer coefficient	(kW m^{-2} K^{-1})
u_{SL}	Superficial liquid velocity	(m s^{-1})
u_{SV}	Superficial vapour velocity	(m s^{-1})
V	Volume	(m^3)
v	Specific volume	(m^3 kg^{-1})
$\dot{V}$	Volume flow rate	(m^3 s^{-1})
W	Plate width	(m)
w	Specific work	(kJ kg^{-1})
$\dot{W}$	Power	(kW)

X	Size or capacity of component	(-)
x	Ammonia mass fraction	(-)
X_{tt}	Lockhart–Martinelli parameter	(-)
$\dot{Y}$	Non-exergetic environmental impact rate	(mpt s^{-1})
y	Exergy destruction ratio	(-)
y^*	Exergy destruction ratio	(-)
Z	Silver, Bell & Ghaly correlation factor	(-)
$\dot{Z}$	Non-exergetic cost rate	(€ s^{-1})

Greek letters

α	Heat transfer coefficient	(kW m^{-2} K^{-1})
β	Plate corrugation angle	(°)
γ	Cost function exponent	(-)
ϵ	Effectiveness	(-)
ε	Exergy efficiency	(-)
η	Efficiency	(-)
λ	Thermal conductivity	(-)
Λ	Plate corrugation spacing	(m)
μ	Viscosity	(Pa s)
ϕ	Plate area enhancement factor	(-)
φ	Plate corrugation inclination angle	(°)
ξ	Pressure drop coefficient	(-)
Σ	Summed	

Subscripts

0	Dead state
AB	Absorber
c	Critical
CM	Compressor
D	Destruction
dis	Displacement
DS	Desorber
el	Electrical
F	Fuel
gas	gas cost
IH	Internal heat exchanger
HP	Heat pump (HACHP)
i	Index
is	Isentropic
j	Stream index
k	Component index
l	Lean

l	Liquid
lf	Liquid film
lo	Liquid only
LM	Logarithmic mean
max	Maximum
MI	Mixer
NG	Natural gas
P	Product
PM	Pump
pp	Pinch point
r	Component index
r	Rich
suc	Suction line
sys	System
tp	Two phase
TV	Throttling valve
v	Vapour
vo	Vapour only
vol	Volumetric
w	Wall
W	Equipment with known cost
Y	Equipment with calculated cost

Superscripts

$\bar{}$	Average
AV	Avoidable
CH	Chemical
EN	Endogenous
EX	Exogenous
MX	Mexogenous
UN	Unavoidable
OP	Operational costs
PH	Physical
rev	Reversible

CHAPTER 1

INTRODUCTION

Industrial scale heat pumps may be applied to improve the energy efficiency of industrial processes [99] or for utility production in urban areas with district heating networks [79]. Heat pumps can upgrade waste heat at low temperatures to an utilizable high temperature heat source using only a fraction of primary energy. Hence, the integration of heat pumps in industrial processes provides a measure for the reduction of primary energy consumption [30].

Many industrial scale heat pumps have been installed with a heat supply temperature in the range of 50 - 90 °C. Current vapour compression heat pumps (VCHP) are restricted to a maximum heat rejection temperature in proximity of 90 °C. The lack of installations above 90 °C is therefore most likely due to the lack of cost efficient solutions in this temperature range, rather than a limited demand for high temperature heat pump solutions [2] [21]. Fossil fuel, specifically natural gas, is the primary energy source for industrial processes in the temperature domain in excess of 90 °C. In order to comply with the transition from the current fossil fuel based energy system to a future fossil-free energy system, with high penetration of renewables, an alternative energy supply for thermal industrial processes must be found. For this application a high temperature heat pump is a relevant technology to investigate.

For the development of efficient high temperature heat pumps the ammonia-water hybrid absorption-compression heat pump (HACHP), also known as the vapour compression heat pump with solution circuit, is regarded as a feasible solution. The HACHP is based on the Osenbrück cycle [80]. In the Osenbrück cycle the processes of condensation and evaporation are exchanged with absorption and desorption processes. It thus uses zeotropic mixtures as the working fluid, typically ammonia-water.

The HACHP has recently experienced gained interest, as commercial solutions have entered the market. The HACHP has been implemented for waste heat recovery and heat supply in industrial facilities such as dairies, abattoirs, district heating and sewage treatment plants [16]. These installations have a heat load ranging from 150 kW to 1200 kW and a heat supply temperature up to 85 °C [16].

The first theoretical study of the HACHP was performed by Altenkirch [15] and describes the advantage of the HACHP with the non-isothermal process of absorption-desorption compared to the isothermal process of condensation-evaporation in a conventional VCHP. Thereby, the HACHP is a feasible measure of approaching the Lorenz cycle [60], which can result in an increased COP due to the reduction of entropy generation driven by heat transfer over a finite temperature difference. The efficiency advantage of the HACHP over the VCHP requires the temperature change (glide) in the heat sink and heat source to be greater than 10 K [38]. The advantage remains even if economic considerations are included in the comparison [37]. This makes the HACHP a relevant technology for industrial heat supply and waste heat recovery as these processes often require large sink-source temperature glides.

A further advantage of using a zeotropic mixture as working fluid is the reduction of vapour pressure compared to the vapour pressure of the pure volatile component. This implies that the HACHP can achieve higher supply temperatures than a VCHP at the same working pressure. The HACHP is thus, of specific interest for high temperature applications as the maximum heat supply temperature is often restricted by the pressure constraint of compressors and heat exchangers. Brunin et al. [23] showed that it is technically and economically feasible to use the HACHP up to a heat supply temperature of 140 °C, this however is based on a high pressure constraint of 20 bar corresponding to the limitations of standard refrigeration components at the time of the study but did not include a constraint on the compressor discharge temperature. In the meantime new compressor types such as high pressure NH_3 (50 bar) and transcritical CO_2 (140 bar) have become commercially available and standard refrigeration components now operate at 28 bar. To evaluate to which extent these increased pressure constraint can be translated into feasible high temperature heat pump solutions is

to be investigated.

The two advantages of the HACHP:

- 1: Reduction of irreversibilities by matching of the temperature profiles.
- 2: Reduction of vapour pressure by decreasing the volatile component concentration.

implies that the HACHP has not only the potential of delivering heat at higher temperatures than conventional VCHP it also has the potential to do so with a higher efficiency.

Conversely, these two advantages also pose the greatest drawbacks of the HACHP. The reduction of irreversibilities attained by the matching of the temperature profiles also reduce the mean temperature difference and thus entails the need for an increased heat transfer area. Further, the use of a zeotropic mixture, which is needed to match the temperature profiles, cause a reduction of the heat transfer coefficient due to mass diffusion resistance [26, 87] which also implies the need for an increased heat transfer area. Lastly, the reduction of vapour pressure causes an increased specific volume in the compressor suction line. Hence, a larger compressor displacement volume is needed to attain the same heat load. All in all these conditions infer that the HACHP investment should be expect to exceed that of the VCHP. Whether the increased efficiency of the HACHP is enough to justify the increased investment should therefore be investigated.

1.1 Background

1.1.1 Project

The research presented in this thesis was conducted as part of the research and development project entitled "Development of ultra-high temperature hybrid heat pump for process application". This project was funded by EUDP - Energy Technology Development and Demonstration (project number 64011-0351).

The project consortium consists of eight partners from both industry and academia. The industrial partners covers both hybrid heat pump manufacturers as well as end users and a private research institution.

The involved heat pump manufacturers were Hybrid Energy A/S from Norway and Innoterm A/S from Denmark. Hybrid Energy A/S was founded in 2004 and is a spin-out from the Norwegian national research center for energy research "Institute for Energy Technology - IFE". Hybrid Energy A/S was founded to commercialise the hybrid absorption-compression technology to a high temperature heat pump for industrial scale waste heat recovery systems. At the time of writing Hybrid Energy have installed 11 hybrid heat pumps and have an other two under construction. The applications range from industries such dairies and slaughterhouses to district heating and waste water treatment. The capacity of the installed systems range from 350 kW to 1200 kW and the hybrid heat pumps deliver heat supply temperatures upto 100 °C.

Innoterm A/S is a Danish contractor and consultant specialised in industrial scale refrigeration and heat pump facilities and they have the agency for the Hybrid Energy technology in Denmark. Innoterm A/S have been responsible for the construction of a hybrid heat pump in Arla's powder milk factory Arinco, seen in Fig. 1.1 and are currently constructing a second one for district heating facility in Løgumkloster.

The Danish Technological Institute is also a partner in the project. The Danish Technological institute is a private research institution who develop and apply research based knowledge for the Danish and international business sector. The Danish technological institute is among other things specialised in experimental research in large scale refrigeration and heat pump systems.

Figure 1.1: HACHP at Arla's powder milk factory Arinco in Videbæk, Denmark.

From academia the Department of Mechanical Engineering at the Technical University of Denmark and the Department of Energy and Process Engineering at the Norwegian University of Science and Technology have been involved. Of these the Technical University of Denmark have been responsible for the PhD work presented in this thesis.

Several end user have participated in the project consortium, these are Arla Foods A.M.B.A and SPX Anhydro. As mentioned Arla has already implemented a hybrid heat pump in the spray drying facility Arinco while SPX Anhydro is a producer of spray dryers and liquid concentrators.

The collective objective of the project consortium is to increase the operating limits of the hybrid heat pump technology using newly developed high pressure components. The aim is to demonstrate that efficient and reliable high temperature heat pumps can be constructed in the temperature range of 180 - 250 °C using the hybrid heat pump technology.

1.1.2 Theoretical

Carnot versus Lorenz cycle

To elaborate on the thermodynamic advantages of the HACHP the concepts of Carnot and Lorenz cycles are helpful. The Carnot cycle is often assumed to represent a reversible power to heat conversion machine. However, this is only true if certain criteria are met.

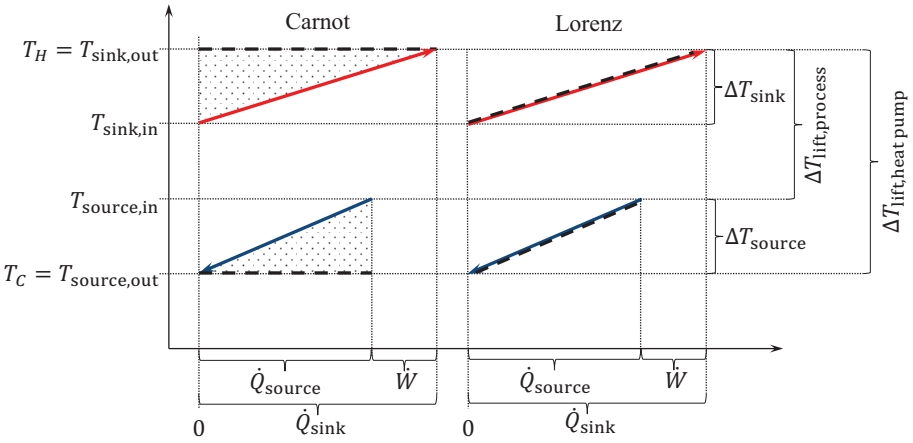

Figure 1.2: Carnot and Lorenz cycle operated between two finite reservoirs

Assuming the Carnot cycle to operate between two reservoirs, a low temperature reservoir of temperature T_C and a high temperature reservoir of temperature T_H: the coefficient of performance (COP) of the Carnot cycle can be calculated as seen in Eq. (1.1) (heat pump operation is assumed).

$$\text{COP}_{\text{Carnot}} = \frac{T_H}{T_H - T_C} = \frac{T_H}{\Delta T_{\text{lift,heatpump}}} \tag{1.1}$$

Defining the temperature lift of the heat pump as $\Delta T_{\text{lift,heatpump}} = T_H - T_C$ the COP of the Carnot cycle can be defined as the ratio of the temperature of the hot reservoir to the temperature lift. Hence, the higher $\Delta T_{\text{lift,heatpump}}$ the lower $\text{COP}_{\text{Carnot}}$ while the higher T_H, the higher $\text{COP}_{\text{Carnot}}$.

The Carnot cycle is comprised of four processes, an isentropic compression, an isothermal heat rejection at temperature T_H, an isentropic expansion and an isothermal heat absorption at temperature T_C. While the isentropic compression and expansion processes are reversible by definition, the heat rejection and heat absorption processes are only reversible if the temperature of the hot and cold reservoirs are constant, hence $\frac{dT_H}{d\dot{Q}_H} = 0$ and $\frac{dT_C}{d\dot{Q}_C} = 0$. This ensures that no temperature dif-

ference exists throughout both heat transfer processes and thus that the generation of entropy is 0.

Consequently, either the heat capacity or the mass of both reservoirs must be infinite in order to attain a fully reversible power to heat conversion with a Carnot cycle. The Carnot cycle COP is thus only the thermodynamic maximum for a heat pump working between two infinite reservoirs. For some applications, such as air to air air-conditioning systems, the amount of heat supplied and extracted from the reservoirs is often infinitesimally small compared to the capacity of the reservoir and thus the temperature change of the reservoir may be insignificant. For these cases the Carnot cycle may offer an appropriate estimation of the thermodynamic limitations.

Heat pumps for process applications often operate between finite reservoirs in which the temperature change of the reservoir, ΔT, is significant. A Carnot cycle operating between two such reservoirs may be seen in Fig. 1.2. The Carnot cycle in Fig. 1.2 heats a hot reservoir, termed the "sink", from a temperature of $T_{\text{sink,in}}$ to $T_{\text{sink,out}}$ while cooling a cold reservoir, termed the "source", from a temperature of $T_{\text{source,in}}$ to $T_{\text{source,out}}$. As seen, to ensure that the Carnot cycle abides the Second Law of thermodynamics the temperature of the isothermal heat rejection, T_H, cannot be below $T_{\text{sink,out}}$ while the temperature of the isothermal heat absorption, T_C, cannot be higher than $T_{\text{source,out}}$. This results in the large temperature differences depicted by the dotted areas in Fig. 1.2. Consequently, the Carnot cycle is far from reversible. It can be seen that the greater the temperature difference over the sink and source, ΔT_{sink} and ΔT_{source}, the greater this temperature difference will be and consequently the further the Carnot cycle will be from a reversible cycle.

Recognizing that the inefficiency of the single Carnot cycle stems from the fact that the temperature of $T_{\text{sink,out}}$ and $T_{\text{source,out}}$ set the limit of T_H and T_C, it can be concluded that the implementation of several Carnot cycles may offer an increased performance.

Three Carnot cycles working between two finite reservoirs may be seen in Fig. 1.3. Each of the three cycle heats an equal amount of the heat sink and cool an equal amount of the heat source. As seen, each of the three Carnot cycles operate with a lower $\Delta T_{\text{lift,heatpump}}$ that what

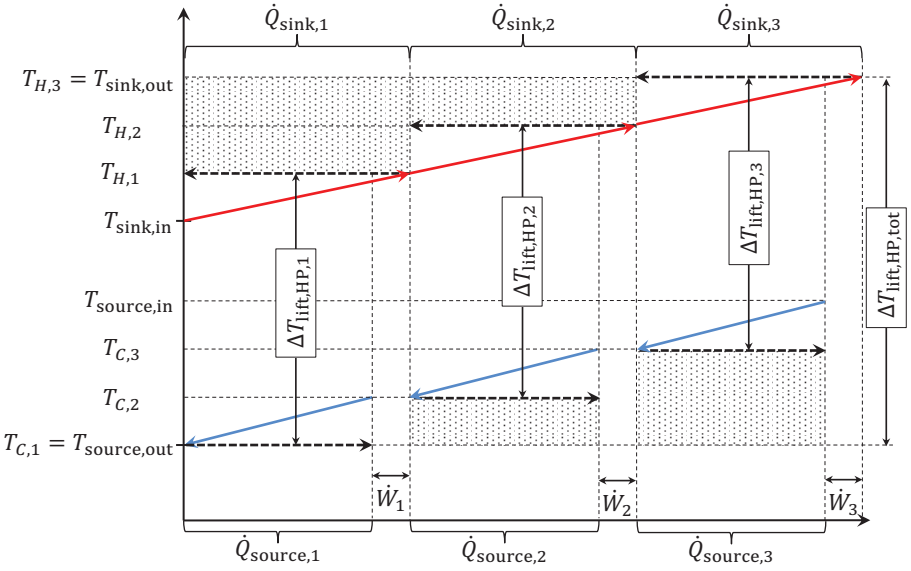

Figure 1.3: Three Carnot cycles supplying an equal amount of the total sink and source heat load.

the single Carnot cycle would and thus the total COP of using multiple Carnot cycles is greater than the single Carnot cycle.

Applying energy and entropy balances to the multiple Carnot cycle configuration an letting the number of cycles approach infinity results in the total COP seen in Eq. (1.2). This COP is the COP of the Lorenz cycle [60].

$$\text{COP}_{\text{Lorenz}} = \frac{\overline{T}_{\text{LM,sink}}}{\overline{T}_{\text{LM,sink}} - \overline{T}_{\text{LM,source}}} \tag{1.2}$$

Here $\overline{T}_{\text{LM}}$ is the logarithmic mean temperature of the sink and source, respectively, calculated as seen in Eq. (1.3).

$$\overline{T}_{\text{LM}} = \frac{T_{\text{in}} - T_{\text{out}}}{\ln\left(\frac{T_{\text{in}}}{T_{\text{out}}}\right)} \tag{1.3}$$

Recognising that $T_{\text{in}} - T_{\text{out}}$ can be written as ΔT, as also depicted in Fig.

1.2, $\overline{T}_{\mathrm{LM}}$ can be written as seen in Eq. (1.4).

$$\overline{T}_{\mathrm{LM}} = \frac{\Delta T}{\ln\left(\frac{T_{\mathrm{in}}}{T_{\mathrm{in}} - \Delta T}\right)} \tag{1.4}$$

From this is can be seen that $\overline{T}_{\mathrm{LM}} \rightarrow T_{\mathrm{in}}$ for $\Delta T \rightarrow 0$ and thus that $\mathrm{COP}_{\mathrm{Lorenz}} \rightarrow \mathrm{COP}_{\mathrm{Carnot}}$ for $\Delta T \rightarrow 0$

A Lorenz cycle operating between two finite reservoirs may be seen in Fig. 1.2. As seen, in the Lorenz cycle the isothermal heat rejection and heat absorption is replaced by non-isothermal processes with the same temperature variation as the sink and source. Both heat transfer processes in the Lorenz cycle are therefore reversible and assuming an isentropic compression and expansion means that the Lorenz cycle represents a fully reversible heat to power conversion between two finite reservoirs.

The ratio between the Lorenz and Carnot COP can be seen in Figs. 1.4 (a) and (b). Both are for a heat pump delivering $T_{\mathrm{sink,out}}$ = 100 °C and are presented as a function of the temperature lift at varying sink/source temperature difference ($\Delta T_{\mathrm{sink}} = \Delta T_{\mathrm{source}}$ is assumed).

Two different definitions of temperature lift are applied, a heat pump lift, $\Delta T_{\mathrm{heatpump}}$, and a process lift ,$\Delta T_{\mathrm{process}}$, both are presented graphically in Fig 1.2. The heat pump lift is defined as $\Delta T_{\mathrm{lift,heatpump}} = T_{\mathrm{sink,out}} - T_{\mathrm{source,out}}$ and thus describes the total temperature difference experienced by the heat pump. The process lift is defined as $\Delta T_{\mathrm{lift,process}} = T_{\mathrm{sink,out}} - T_{\mathrm{source,in}}$ as thus describes the difference between the required supply temperature and the temperature of the available heat source. For process integration of heat pumps the process lift definition may be more relevant as the source outlet temperature is typically not of significant importance.

As seen in Figs. 1.4 (a) and (b) both lift definitions produce the same trend: as the temperature lift increases the Lorentz cycle approaches the Carnot cycle. Further: the higher the sink/source temperature difference the better the Lorentz cycle performs compared to the Carnot cycle. It can also be seen that the greater the sink/source temperature difference the greater the difference is between the two lift definitions.

The highest increase in performance given by replacing a Carnot cycle

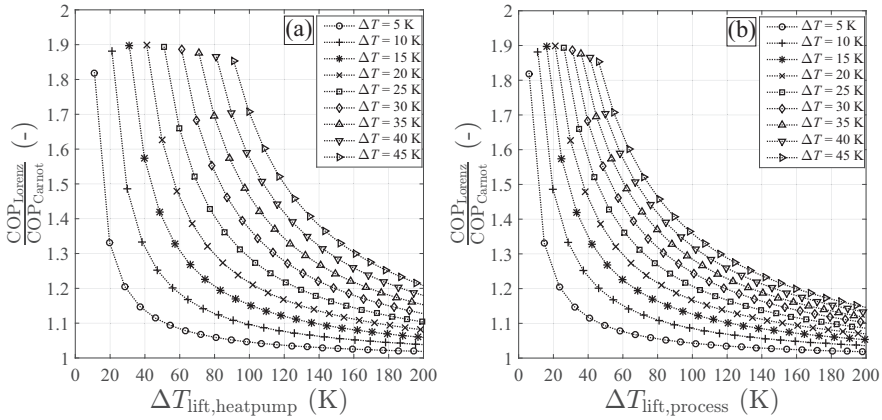

Figure 1.4: Ratio between $\mathrm{COP_{Lorenz}}$ and $\mathrm{COP_{Carnot}}$ as a function of the temperature lift and the temperature glide in the sink and source ($\Delta T_{\mathrm{sink}} = \Delta T_{\mathrm{source}}$ is assumed). (a) shows the variation with the heat pump temperature lift while (b) show the variation with the process temperature lift.

with a Lorenz cycle is attained at high sink/source temperature differences and low temperature lifts. However, this may lead to infeasible operating conditions being studied if special attention is not applied to the following criteria: heat pumps with $\Delta T_{\mathrm{sink}} > \Delta T_{\mathrm{lift,procees}}$ should not be considered as this implies that $T_{\mathrm{sink,in}} < T_{\mathrm{source,in}}$ and consequently that direct heat exchange is possible between the two streams.

For the remainder of this thesis the process lift definition will be applied as this makes is easier to evaluate the process integration potential and it makes it easier to determine whether the operating condition complies with the criteria stated above.

Ammonia-water as a zeotropic working fluid

In the following an introduction to the ammonia-water mixture as a zeotropic working fluid will be presented. A zeotropic mixture is defined as mixture which temperature changes during an isobaric phase change. Zeotropic mixtures thus differ from pure fluids and azeotropic mixtures by having a non-isothermal phase change. Hence, heat pumps

using zeotropic mixtures will ideally approach the Lorenz cycle rather than the Carnot cycle. Zeotropic mixtures are thus relevant for heat pumps working between finite reservoirs as is often seen in the process industry.

The properties of ammonia-water mixtures depends strongly on the composition of the mixture. In this thesis the concentration is defined by the ammonia mass fraction, x. Pressure - Enthalpy and Temperature - Enthalpy diagrams of ammonia-water mixtures at two ammonia mass fractions, $x = 0.25$ and $x = 0.75$, are shown in Figs. 1.5 & 1.6. Fig. 1.5 (a) and 1.6 (a) are for $x = 0.25$ while Fig. 1.5 (b) and 1.6 (b) are for $x = 0.75$. It should be noted the scale of the temperature and pressure axis are not the same for the two concentrations.

One difference that should be noted for the two ammonia mass fractions is the variation in the saturation temperature difference, ΔT_{sat}. Here the saturation temperature difference is defined as the difference between the temperature of saturation liquid and saturated vapour as the same pressure. As seen this is approximately 50 K for $x = 0.25$ while it is upto 90 K for $x = 0.75$. Further, it can be seen that the temperature profile of the isobaric phase change differs between the two ammonia mass fraction. It can be seen that the temperature to enthalpy relation for the $x = 0.25$ mixture exhibits a convex shape while the $x = 0.75$ mixture has a concave shape.

Examining the pressure of the saturated liquid mixtures in Fig. 1.5 it can be seen that the vapour pressure of the ammonia-water mixture also depends strongly on the ammonia mass fraction. E.g. it can be seen that the pressure of saturated liquid at 160 °C is 25.6 bar for $x = 0.25$ while it is approximately twice that for $x = 0.75$.

The differences in vapour pressure and ΔT_{sat} is highlighted in Figs. 1.7 and 1.8. As seen in Fig. 1.7 vapour pressure tends to decrease with ammonia mass fraction. This has an influence on the attainable temperatures using the pressure levels known for commercial components. In Fig. 1.7 pressures of 28 bar and 140 bar are highlighted as these are the pressure limits of standard refrigeration and transcritical CO_2 components, respectively. As seen, 28 bar components allow temperatures between 63 - 230 °C, while 140 bar allows temperatures between 163 - 337 °C. It can concluded from Fig. 1.7 that the temperature out-

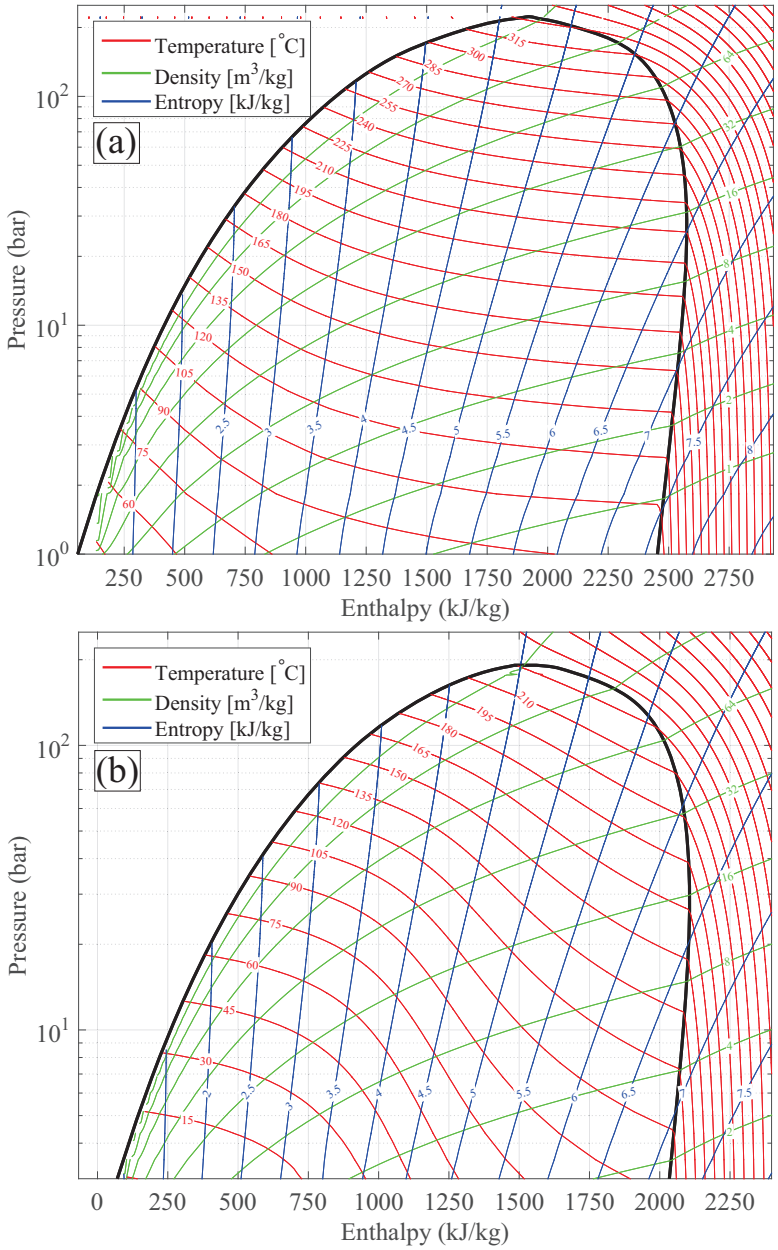

Figure 1.5: Log(p) - h diagram of ammonia water mixtures with an ammonia mass fraction of x = 0.25 (a) and x = 0.75 (b).

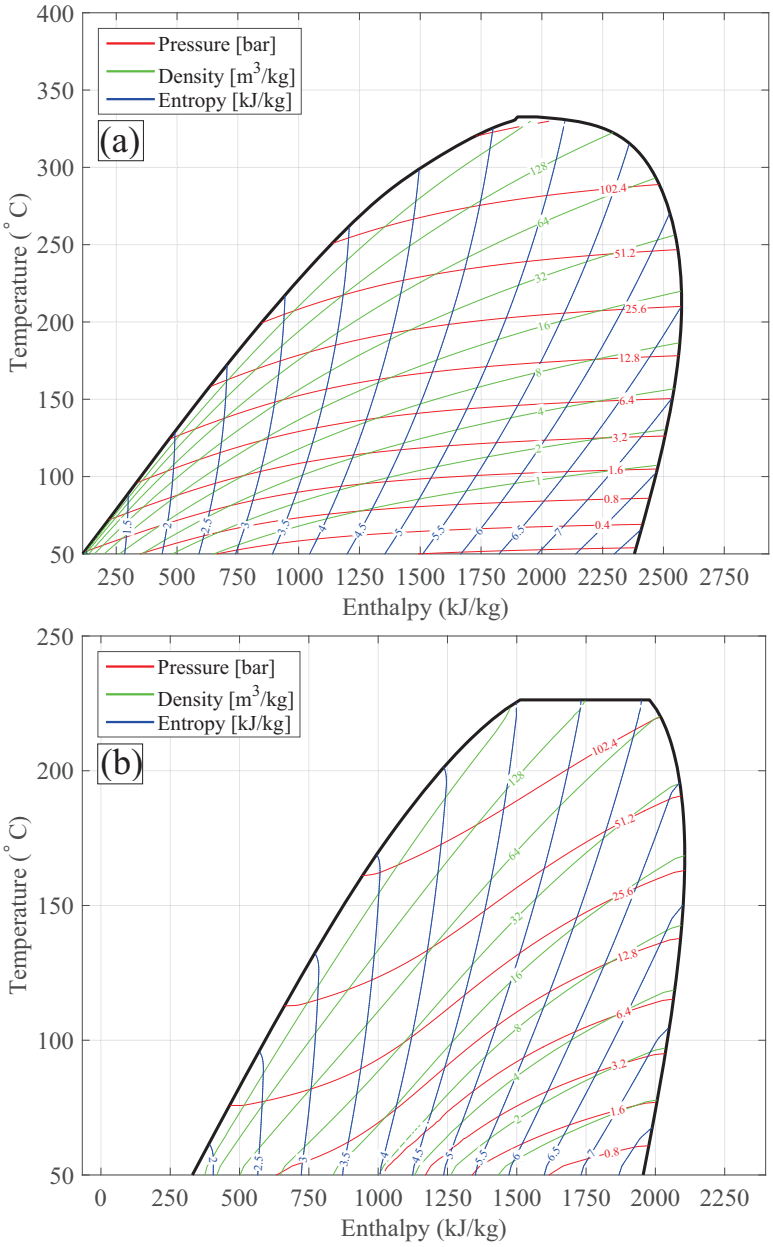

Figure 1.6: *T* - *h* diagram of ammonia water mixtures with an ammonia mass fraction of x = 0.25 (a) and x = 0.75 (b).

put of an ammonia-water heat pump can be increased by two measures: increasing pressure or decreasing ammonia mass fraction.

Fig. 1.8 show the variation of the ΔT_{sat} with the ammonia mass fraction and the temperature of the saturated liquid. As seen, ΔT_{sat} approaches 0 as the ammonia mass fraction approaches pure water (x = 0) and pure ammonia (x = 1) and as the temperature of the saturated liquid approaches the mixtures critical temperature. The highest ΔT_{sat} is attained at ammonia mass fractions between 0.5 and 0.8 and liquid saturation temperatures below 100 °C. Under these conditions the saturation temperature difference can be as high as 95 K. Further, it can be seen that for the low ammonia mass fractions ΔT_{sat} is mainly a function of the ammonia mass fraction while at high ammonia mass fractions ΔT_{sat} depends on both ammonia mass fractions and the liquid saturation temperature.

It is important to evaluate ΔT_{sat} when designing ammonia-water heat pumps working between finite reservoirs as the ΔT_{sat} should be close to the temperature difference of the sink and source to ensure a good performance.

Rankine versus Osenbrück cycle

Fig. 1.9 shows principle sketches of three different cycles. Fig. 1.9 (a) shows the conventional VCHP based on the Rankine cycle, this cycle can use both azeotropic or zeotropic working fluids. Fig. 1.10 shows the temperature heat load diagram of a VCHP with an azeotropic working fluid and a zeotropic working fluid.

As seen both processes start the heat transfer in the heat sink by de-superheating the vapour discharged from the compressor. The de-superheating process often has a larger temperature gradient than the heat sink and thus often leads a to significant temperature difference between the two streams. After the vapour is de-superheated the phase change starts, as seen this is an isothermal process for the azeotropic mixture while it occurs over a gliding temperature with the zeotropic mixture. As seen in the case ΔT_{sat} is close to ΔT_{sink} as thus the zeotropic mixture is expected to increase the performance compared to the azeotropic mixture. Equally, it is seen that the heat transfer process with the

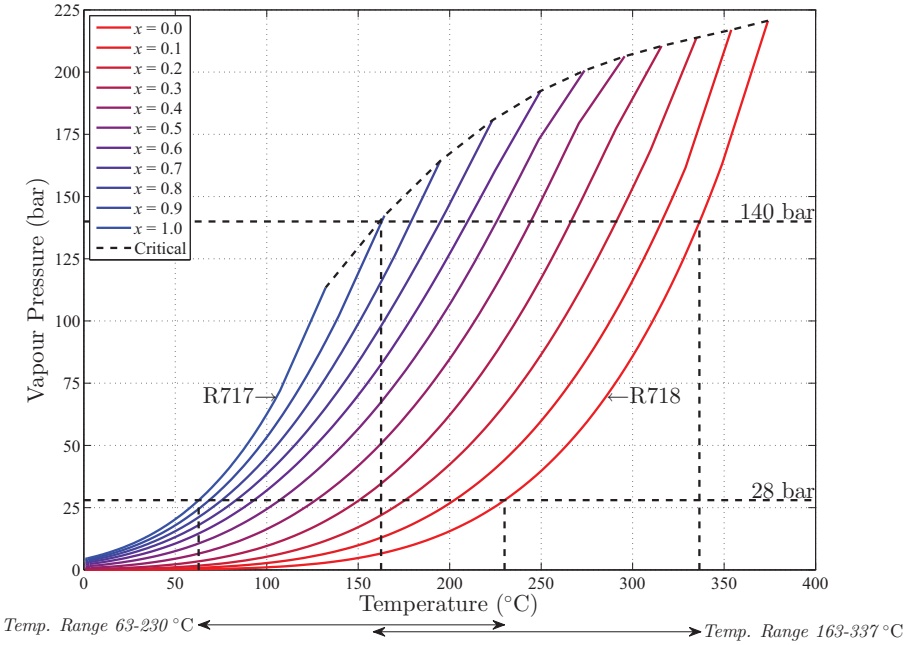

Figure 1.7: Vapour pressure as a function of temperature at varying ammonia mass fractions.

heat source also occurs over a smaller temperature difference with the zeotropic working fluid.

However, as shown in the previous section, ΔT_{sat} varies greatly with ammonia mass fraction and the liquid temperature. For a chosen temperature level and ammonia mass fraction ΔT_{sat} is thus given by the thermodynamic behaviour of the mixture and this value of ΔT_{sat} may not be a good match of temperature differences in the sink and source. Therefore, it may be beneficial to be able to control the temperature difference of the phase change. This can be done using the HACHP based on the Osenbrück cycle.

A principle sketch of the simplest Osenbrück cycle is seen in Fig. 1.9 (b). As seen, an internal liquid solution circuit is placed in parallel with the compressor, this allows the state before the compressor to be a liquid-vapour mixture. A liquid-vapour separator is applied to ensure that only vapour enters the compressor, while the rest is sent to the

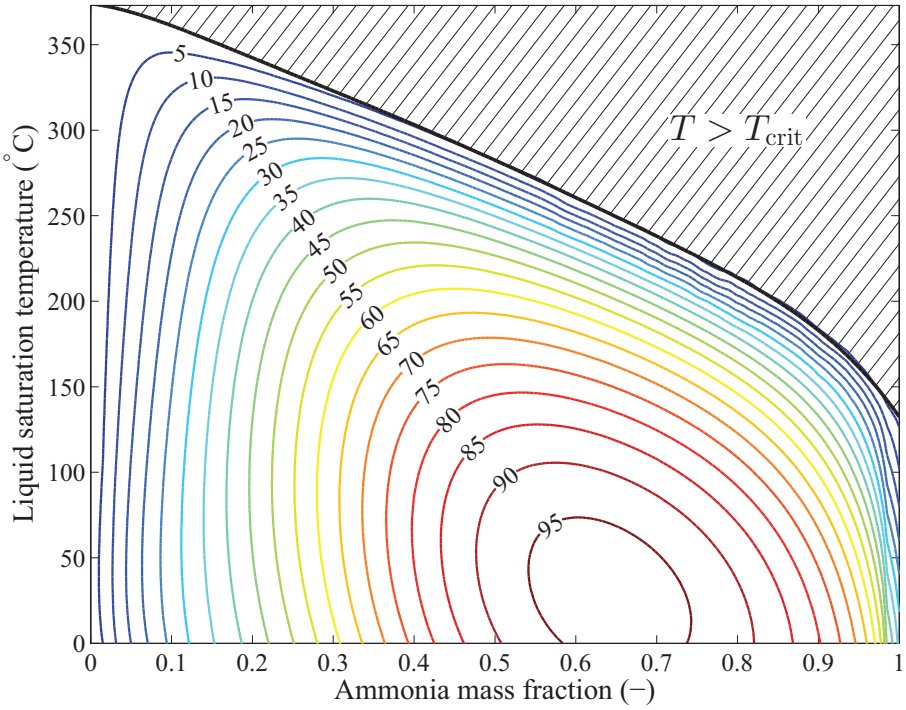

Figure 1.8: Temperature difference between saturated vapour and saturated liquid at the same pressure for varying ammonia mass fraction and liquid temperature.

pump. After the pump and compressor the liquid and vapour streams are mixed which typically results in a liquid-vapour mixture. Thus, for the entire heat transfer process with the heat source the ammonia-water mixture is in the two-phase region and subsequently entirely comprised of desorption of the ammonia from the mixture. Equally, for the entire heat transfer process with the sink the ammonia-water mixture will be in the two-phase region and is comprised only of absorption of the ammonia into the mixture.

The internal solution circuit gives an extra degree of freedom to the system: the vapour quality, q, entering the separator. The vapour quality can also be addressed as the liquid circulation ratio, f. The liquid circulation ratio is defined as the ratio between the mass flow rate of the liquid circulated by the pump and mass flow rate of the liquid-vapour

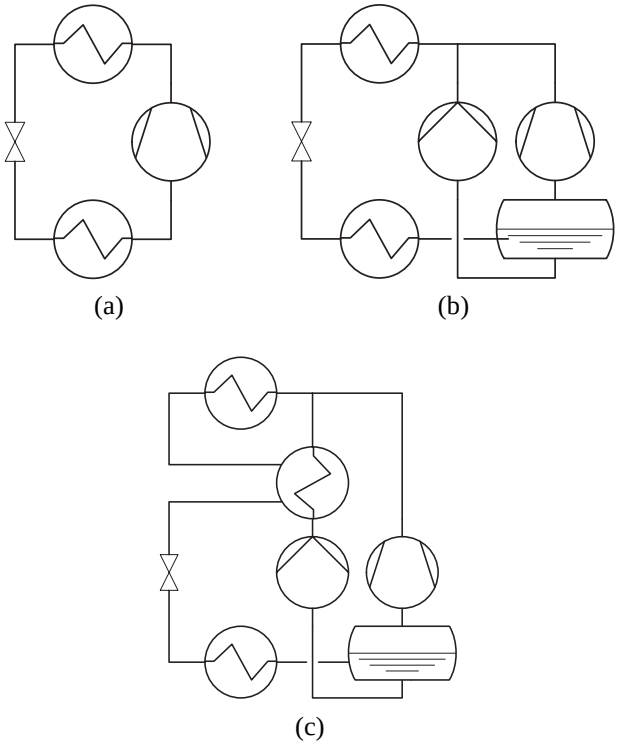

Figure 1.9: Principle sketches of: (a) conventional VCHP (Rankine Cycle), (b) HACHP (Osenbrück cycle) and (c) HACHP with internal heat exchange

mixture entering the separator. It can be noted that $f = q - 1$, thus the higher the vapour quality is at the inlet of the separator the lower the liquid circulation ratio will be.

The extra degree of freedom can be used to control the temperature difference of the absorption and desorption processes. This is exemplified in Fig. 1.11 where the HACHP process is shown with both a low and high liquid circulation ratio. As seen, for a given high and low pressure, a higher recirculation rate will reduce the temperature difference of the absorption and desorption processes, thus making it possible to provide a better match of the temperature difference of the sink and source.

However, increasing the circulation ratio may come at the cost of in-

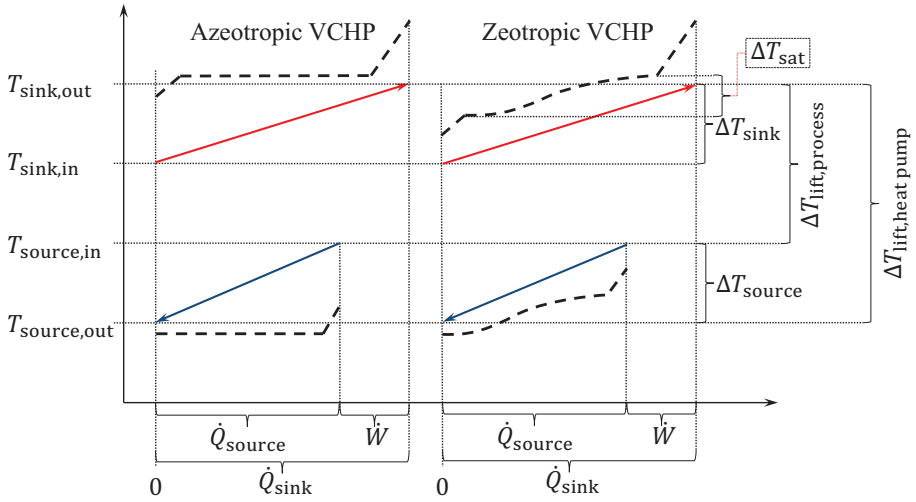

Figure 1.10: Temperature - heat load diagram of a VCHP using an azeotropic working fluid and a zeotropic working fluid.

creased irreversibilities causes by the mixing of the hot discharge gas from the compressor and the colder liquid from the pump. This irreversibility may be reduced by the implementation of the an internal heat exchanger as seen in Fig. 1.9 (c). This internal heat exchanger preheats the liquid before the mixing by sub-cooling the liquid after the absorption.

The difference between the HACHP and the VCHP with a zeotropic working fluid can be seen in Fig. 1.12. As seen, if designed correctly the HACHP may give give a good matching of the temperature profiles between the desorption and the source and between the absorption and the sink.

1.2 Thesis statement

The work of the present thesis aims to contribute to the development of high temperature HACHP by investigating the following:

- Which HACHP cycle configurations are relevant and how are their performance influence by the choice of design parameters

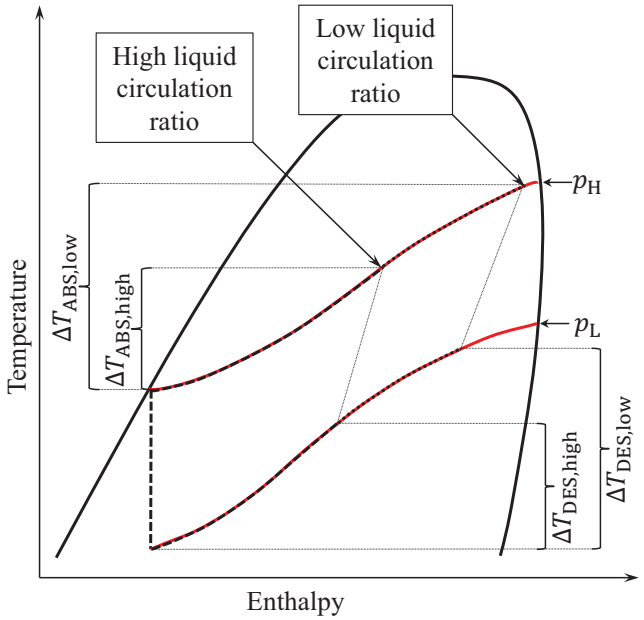

Figure 1.11: Temperature - Enthalpy diagram of a HACHP with a high and low liquid circulation ratio.

such as ammonia mass fraction and circulation ratio as well as operating conditions such as sink temperature glide, source temperature glide and temperature lift.

- What is the maximum heat supply temperature that can be attained by a HACHP within the range of commercial components currently available? Further, which of the component constraints limit the development of high temperature heat pumps?

- What are the main sources of irreversibilities as well as cost and environmental impact formation in a HACHP, to which extent are they interdependent and to which extent can they be avoided?

- How does the viability of a HACHP compare to the VCHP if a complete economic analysis is applied including both capital investment, maintenance and fuel cost over the lifetime of the system?

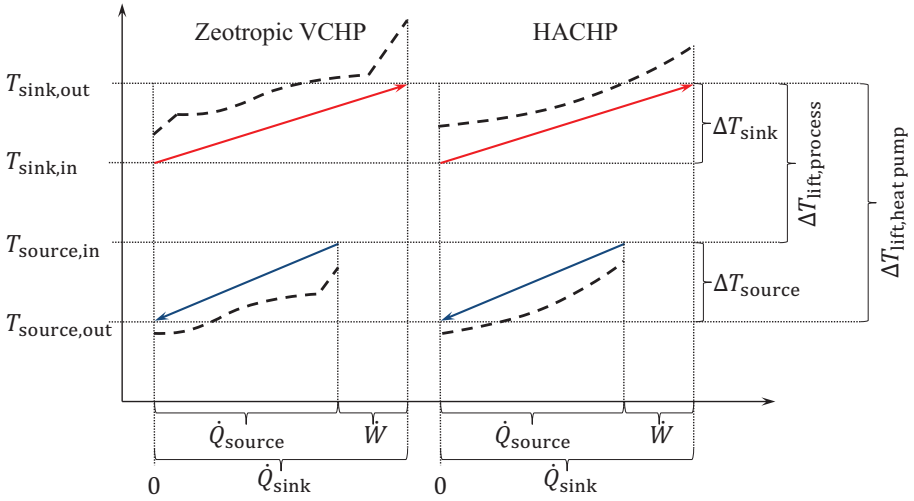

Figure 1.12: Temperature - heat load diagram of a VCHP with a zeotropic working fluid and a HACHP

1.3 Methodology

To answer the thesis statement a number of different methodologies were applied. In general the methods applied have focused on numerical modelling and analysis. The work was initiated with the development of steady state thermodynamic models of different cycle configuration. Based on the thermodynamic models Second Law considerations were accounted for by the means of exergy and advanced exergy analysis. Numerical models where development for the design of heat transfer components which, combined with aggregated economic data allowed an over all evaluation of the viability of a hybrid heat pump installation.

A detailed list of the methods and investigations applied can be seen below.

- To investigate the performance of both one-stage and two-stage HACHP, thermodynamic models of the identified configurations are constructed. Ammonia mass fraction and circulation ratio are identified as reasonable formulations of the extra degrees of freedom. Further, their influence of the performance is investigated through simulations of the constructed models. These simulations

are conducted for a range of sink glide, source glide and temperature lift combinations.

- To evaluate the maximum heat supply temperature, the constraints of a range of commercially available components have been aggregated. These are imposed on a parameter variation of the ammonia mass fraction and circulation ratio to find the set of feasible combinations for each type of components at a range of heat supply temperature.

- In order to conduct a complete economic analysis and a life cycle assessment, component cost and material inventory most be identified. Cost and material mass functions have been constructed based on aggregated data from Danish intermittent trade business and individual producers

- For the heat exchange equipment, estimating cost and material consumption requires the heat transfer area to be known. For the present study the application of plate heat exchangers are assumed. Applicable heat transfer and pressure loss correlation are identified along with estimations methods for the ammonia-water mixture transport properties. The influence of plate dimensions as well as ammonia mass fraction are investigated to give design guidelines for plate absorbers and desorbers.

- To gain a deeper insight to the thermodynamic irreversibilities as well as the formation of cost and environmental impact an advanced exergy-based analysis is applied. An exergy-based analysis consists of a exergy, exergoeconomic and exergoenvironmental analysis. In an advanced exergy-based analysis the interdependencies between component irreversibilities and dimensions is accounted for as well as the reduction potential. This increases the accuracy of the advanced analysis compared to the conventional exergy-based analysis.

- By combining the life time economic analysis of the HACHP with the identified technical constrains the working domain of the HACHP can be derived. The heat pump working domains

is defined as the combinations of heat supply temperature and temperature lift at which heat pump implementation result in a technically feasible and economically viable solution. This analysis is conducted for both HACHP and VCHP. Having conducted the economic analysis gives the net present value (NPV) in the entire working domain. Thus, the most viable solution can be identified for heat supply temperature and temperature lift combinations were several technologies compete.

1.4 Thesis outline

This thesis consists of 8 chapters and two appendices. Chapters 2 to 7 present the main body of work conducted in the thesis. These chapters all individually follow the IMRAD structure. Each chapter thus contains a separate introduction in which the study is motivated and the relevant literature is reviewed. The applied methodology is presented in each chapter, however as the chapters progress, methodology and conclusions from previous chapters will be applied. References to the relevant chapters are given. Every chapter is concluded with a discussion and conclusion. In Chapter 8 the conclusions of the chapters are summarized and future work is suggested.

Each chapter will be commenced with a small description of the dissemination of the presented results. Hence, in this paragraph the journal and conference papers in which the results have been published is described.

Chapter 1 This chapter broadly motivates the thesis and introduces the main scope and aim of the project. The thesis statement is given and the general methodology applied to resolve this statement is presented. An outline of the thesis structure is given.

Chapter 2 In this chapter the cycle layout of the simple one-stage HACHP is presented along with several identified two-stage compression configurations. The modelling approach and assumptions are presented and discussed. The influence of the ammonia mass fraction and circulation ratio is investigated for several sink glide,

source glide and temperature lift combinations. The optimum COP for these combinations is presented as a function of the ammonia mass fraction. The performance of the one-stage and two-stage cycles are compared.

Chapter 3 In this chapter, feasibility of high temperature development of the HACHP is investigated. This is done by imposing the constraints of relevant commercial components to a parameter variation of the ammonia mass fraction and circulation ratio at a range of heat supply temperatures. Thus, the set feasible combinations of ammonia mass fractions and circulation ratios are identified for each component type and at each temperature level.

Chapter 4 In this chapter the identified transport property estimation methods are presented and compared. The applied heat transfer and pressure drop correlations are described and the methodology for the dimensioning of plate heat exchanger absorbers and desorbers are presented. The influence of plate geometry as well as ammonia mass fraction on the needed heat transfer area and pressure drop is investigated.

Chapter 5 In this chapter the advanced exergy-based analysis is presented. This consists of and advanced exergy, exergoeconomic and exergoenvironmental analysis. To conduct exergoeconomics an economic analysis must be performed, the basis for this is presented here. To conduct an exergoenvironmental analysis a life cycle assessment most be performed, the basis for this is also presented here.

Chapter 6 This chapter presents the working domain of the HACHP. The working domain of the HACHP is compared to those of the VCHP to reveal to which extent the HACHP extends the applicability of industrial heat pumps. Further, the viability of the HACHP is compared to the viability of the VCHP in the range where both technologies are applicable.

Chapter 7 In this chapter a case study of implementing a high temperature HACHP in a spray drying facility as a waste heat recovery

and heat supply measure is presented. To find the best integration and design of the HACHP an exergoeconomic optimization is imposed. An approach to the exergoeconomic optimization based on partial derivatives of the exergetic and non-exergetic cost rates is proposed.

Chapter 8 This chapter concludes the thesis by identifying the main findings and presents the suggested future work.

Appendix A This appendix contains a collection of ammonia-water transport property estimation methods

Appendix B This appendix contains a collection of ammonia-water heat transfer and pressure drop correlations

CHAPTER 2

MODELLING AND PROCESS OPTIMIZATION

The work presented in this chapter serves as the foundation for the modelling and process optimization applied in the subsequent chapters. In this chapter the layout of the general one-stage HACHP is presented and the working principle is described. Further, several possible layouts of two-stage compression HACHP are identified and compared to the one-stage HACHP. The results presented here are not published but the methodology described has been applied in all publications.

2.1 Introduction

When designing and analysing the HACHP it is important to account for the two extra degrees of freedom possessed by the HACHP. These extra degrees of freedom can be attributed to the composition of the zeotropic mixture and the solution circuit design. The working fluid composition and the rate of solution circulation are thus values that can be chosen freely by the system designer. The choice of these values have been shown in literature to have a great influence on the size and performance of the system. Different approaches to satisfying and optimizing these extra degrees of freedom is suggested by several authors. Their conclusions and suggestions are presented below.

Stokar and Trepp [93] and Stokar [92] investigates the ammonia-water HACHP both experimentally and numerically. The hypothesis of this study is that, apart from the increased coefficient of performance (COP), the HACHP can ensure better capacity control than a VCHP. The improved capacity control is attributed to the adjustment of the ammonia mass fraction. Thus, by decreasing the ammonia mass fraction the vapour pressure of the working fluid is reduced and consequently

a fixed speed compressor will provide a lower mass flow rate subsequently reducing the heat load. The analysis was performed at a fixed operating condition in which the sink is heated from 40 °C to 70 °C while cooling the source from 40 °C to 15 °C. It is concluded that for each capacity (ammonia mass fraction) there exists one circulation rate that will optimize the COP. It is further seen that the optimum COP is attained at the point where the temperature difference ratio of the working fluid and sink is close to 1, however optimum ratios between 0.8 and 1.2 are observed.

Åhlby et al. [34] conducted a numerical optimization study of the ammonia-water HACHP. The optimization was performed at four operating conditions all with a heat supply temperature of 80 °C but with varying values of ΔT_{sink} and ΔT_{source}. Further, the HACHP is compared to a R12 VCHP. The objective of the optimization was to determine the optimum internal temperature difference in the absorber (temperature difference between inlet and outlet of the absorber) for a given value of maximum allowable pressure. This showed that for each maximum pressure there exists one value of internal temperature difference that will optimize the COP. The optimum internal temperature difference depends strongly on the external conditions. Åhlby et al. [34] state that the optimum internal temperature difference can differ significantly from the external temperature difference, especially if the external temperature difference is low. For low external temperature differences it is shown that the internal temperature difference should be considerably higher than the external to optimize the COP. Further, Åhlby et al. [34] conclude that the highest COP is attained at the highest pressure. For all the investigated operating conditions the HACHP yields a higher COP than the R12 VCHP.

Åhlby et al. continued their work in [35] by investigating the use of the ternary fluid NH_3-H_2O-LiBr. This showed to improve the COP up to 10 %, with the highest increase for the cases with large sink-source temperature differences.

Itard and Machielsen [40] discuss the issues that arise when modelling and comparing HACHP. It is shown that it is important to account for the non-linear relation of temperature and enthalpy during equilibrium absorption and desorption. Not accounting for the non-linearity may lead

to infeasible temperature profiles as cross overs may be encountered. The external conditions must therefore be included in the evaluation of the pressure needed to ensure feasible profiles. Itard and Machielsen [40] claim that these considerations were not applied in previous studies such as Åhlby et al. [34, 35] and thus it is unclear whether the conclusions from these studies rely on infeasible temperature profiles. Itard and Machielsen [40] state that temperature-enthalpy diagrams are useful to visualize the heat transfer process and ensure feasible profiles. Another consequence of the non-linearity, stated by Itard and Machielsen [40], is the inapplicability of the logarithmic mean temperature difference (LMTD). LMTD is based on an assumption of constant capacity rates. Thus, applying LMTD to absorption or desorption processes may lead to under or over estimation of the mean temperature difference. Further, Itard and Machielsen [40] compared the solution circuit design with the wet compression cycle and found that no clear conclusion can be drawn as to which cycle yields the best performance. Which cycle performs best depends on both the chosen mixture, concentration, temperature level and operating condition.

Brunin et al. [23] compared the working domain of the HACHP to several VCHP. The working domains are evaluated based on two technical constraints: a maximum high pressure and minimum low pressure as well as two economic indicators: minimum COP and minimum volumetric heat capacity (VHC). The HACHP is evaluated at three ammonia mass fractions 0.25, 0.35 and 0.45 and with a fixed concentration difference between the rich and lean stream of 0.10. The working domains are conducted for a fixed sink-source temperature difference of 10 K. Brunin et al. [23] conclude that the only solution for high temperature heat pumps is either the HACHP or a hydrocarbon VCHP. The study by Brunin et al. [23] was carried out without the considerations of non-linearity discussed by Itard and Machielsen [40], further it is unclear how the constant concentration difference of 0.10 relates to the optimum circulation rates discussed by Stokar [92] or optimum temperature difference shown in Åhlby et al. [34].

In the present study the HACHP is modelled such that the rich ammonia mass fraction and the circulation ratio are inputs to the model and thus these parameters are applied to satisfy the two extra degrees

of freedom. By choosing the ammonia mass fraction as one input all possible solutions can be accounted ranging from a pure water cycle x_r = 0.0 to a pure ammonia cycle x_r = 1.0. By choosing the circulation ratio as the second input all solutions ranging from the VCHP cycle f = 0 to a cycle with no phase change, f = 1 (not a physical solution) can be modelled. Thus, simultaneously varying x_r and f from 0 to 1 result in the evaluation of all possible solution for a given operating condition.

Several one and two-stage configurations will be modelled and compared. Parameter variations of the ammonia mass fraction and the circulation ratio is performed to compare the importance of glide matching in the absorber or desorber as well as the effect of choosing a fixed concentration difference.

The one and two-stage configurations are compared based on both COP and VHC and well as high pressure and compressor discharge temperature. The comparison is performed at 6 operating conditions combining low and high temperature lifts with small and large sink/source temperature glides. The investigated operating conditions are:

- ΔT_{sink} = 10 K, ΔT_{source} = 10 K, ΔT_{lift} = 30 K
- ΔT_{sink} = 10 K, ΔT_{source} = 10 K, ΔT_{lift} = 50 K
- ΔT_{sink} = 30 K, ΔT_{source} = 10 K, ΔT_{lift} = 30 K
- ΔT_{sink} = 30 K, ΔT_{source} = 10 K, ΔT_{lift} = 50 K
- ΔT_{sink} = 30 K, ΔT_{source} = 30 K, ΔT_{lift} = 30 K
- ΔT_{sink} = 30 K, ΔT_{source} = 30 K, ΔT_{lift} = 50 K

2.2 Methodology

2.2.1 One-stage hybrid absorption-compression heat pump

Working principle

The process diagram of the one-stage HACHP is seen in Fig. 2.1. The working principle of the HACHP is as follows. At the outlet of the des-

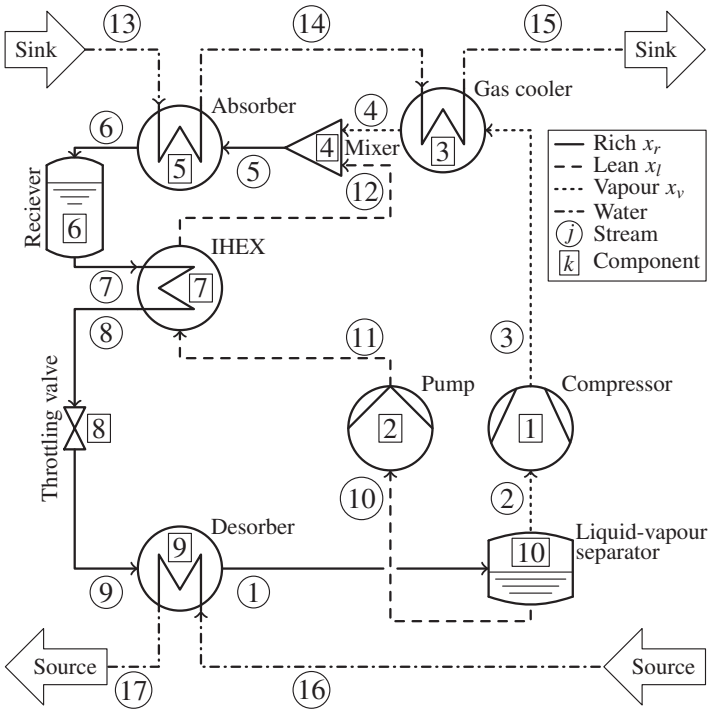

Figure 2.1: Principle sketch of the one-stage hybrid heat pump.

orber the working fluid is a liquid-vapour mixture. The liquid phase will have a lean concentration of ammonia, while the vapour phase consists primarily of ammonia (at low pressures the vapour water content can be substantial). The bulk ammonia concentration of the stream exiting the desorber is the rich ammonia mass fraction.

Before elevating the pressure the vapour and liquid phases must be separated such that liquid does not enter the compressor. This is done in the liquid-vapour separator (LVS) placed after the desorber. The vapour is drawn from the top of the tank to the compressor in which the pressure and temperature are increased. Next the vapour passes to the gas cooler in which the vapour temperature is reduced, while releasing heat to the sink. The lean liquid is drawn from the bottom of the LVS to the pump where the pressure is elevated to the high pressure. As the liquid is close to incompressible the temperature increase over the pump is small. The

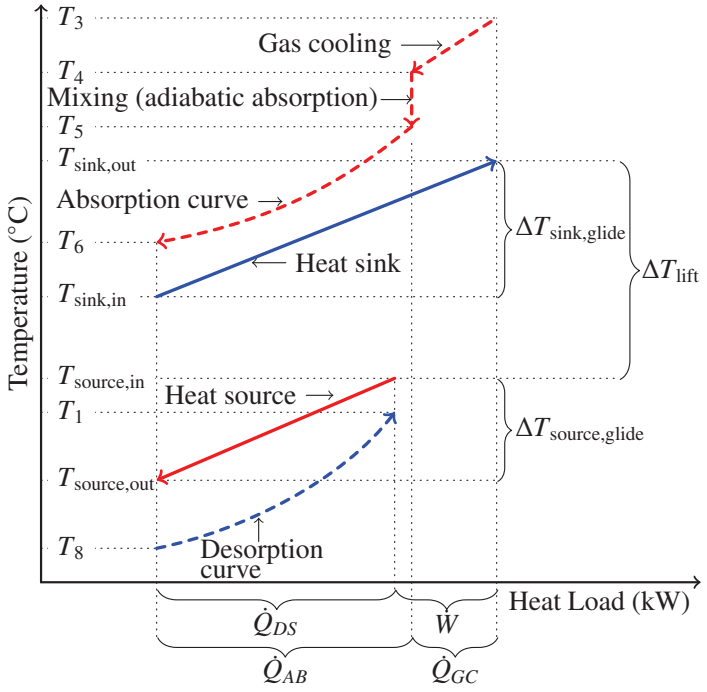

Figure 2.2: The one-stage hybrid heat pump process sketched in a $\dot{Q}-T$ diagram.

liquid is therefore heated in the internal heat exchanger (IHEX). This reduces the entropy generation when mixing the liquid and vapour at the high pressure.

Prior to the absorber the vapour and liquid phases are mixed in an adiabatic process which results in a vapour-liquid mixture in thermal, mechanical and chemical equilibrium. In a physical system this would not be a separate component, but the adiabatic absorption process would takes place in the first part of the absorber. In a thermodynamic model both treatments yield the same result. When thermodynamic equilibrium is reached the diabatic absorption process begins. Here the ammonia is absorbed in the lean liquid solution while releasing heat to the sink

At the absorber outlet a saturated liquid rich in ammonia is delivered. This is sub-cooled in the IHEX. The sub-cooled rich ammonia solution

is throttled to the low pressure resulting in a low temperature liquid-vapour mixture. This is fed to the desorber in which vapour is generated by supplying heat from the source.

The process described above is sketched in the temperature – heat load diagram shown in Fig. 2.2. Here the temperature lift, ΔT_{lift}, is defined as the difference between the sink outlet temperature (heat supply temperature) and the source inlet temperature. The temperature glide, ΔT_{glide}, is defined as the temperature difference between the inlet and outlet of the sink and source, respectively. Further, it is seen that the profiles of the absorption and desorption processes are non-linear. This has been described in detail by Itard and Machielsen [40]. In Fig. 2.2 these processes are depicted as convex curves. Depending on the ammonia mass fraction and circulation ratios these profiles could also exhibit a concave curve or have a convex and a concave part. This is well described in Zheng et al. [107]. Thus, when modelling the HACHP it is not sufficient to use a lumped parameter model of the component to ensure a positive temperature difference at the inlet and outlet of the absorber and desorber. To ensure a feasible profile it is necessary to use a distributed model and verify that there is a positive temperature difference over the entire heat transfer process.

Thermodynamic modelling

A numerical model of a HACHP has been developed in MATLAB 2015a [64]. The thermodynamic properties of the ammonia-water mixture were calculated using the Refprop [31] interface for MATLAB. The so called 'Ammonia (Lemmon)' formulation was applied. As discussed by Modi and Haglind [66] this formulation significantly increases the robustness of the property calculations compared to the default Tillner Roth and Friend [98] formulation, especially in the two-phase region. The robustness is achieved without significantly compromising the accuracy of the property calculations [66].

The MATLAB model was applied to derive the results presented in Chapter 2 and 3. The results presented in Chapters 3 - 7 are derived with a previous version of the model developed in EES [54]. The system of equations solved in the two models are the same. The main difference

Table 2.1: Component inputs to the thermodynamic model

Component	Input	Value	Unit
Compressor	η_{is}	0.75	(-)
Compressor	η_{vol}	0.90	(-)
Compressor	η_{e}	0.90	(-)
Compressor	f_Q	0.10	(-)
Pump	η_{is}	0.75	(-)
Pump	η_{e}	0.90	(-)
Pump	f_Q	0.10	(-)
Gas cooler	ε	0.85	(-)
Absorber	ΔT_{pp}	5.00	(K)
IHEX	ε	0.85	(-)
Desorber	ΔT_{pp}	5.00	(K)

between the implementation is that the EES model uses the Ibrahim and Klein equation of state [39] to determine the thermodynamic properties of the ammonia-water mixture. The output of the two-models were found to be comparable.

Each component was modelled based on steady state mass and energy balances. Further, the model ensured that the second law of thermodynamics is fulfilled in all components.

Heat and pressure losses in heat exchangers, vessels and pipping were neglected. The rich ammonia mass fraction, x_r, and circulation ratio, f, were inputs to the model. The rich ammonia mass fraction was present in state 5-9 and 1. The circulation ratio was defined as the ratio between the mass flow rate of the rich solution, $\dot{m}_r$, and the lean solution, $\dot{m}_l$, see Eq. (2.1). Hence, the circulation ratio was directly linked to the vapour quality in state 1 exiting the desorber, such that: $q_1 = 1 - f$. From this it can be concluded that if the circulation ratio is 0 then the HACHP is in principle a VCHP with a zeotropic working fluid.

$$f = \frac{\dot{m}_l}{\dot{m}_r} \tag{2.1}$$

As pressure and heat losses were neglected the temperature and pressure in the LVS were the same as that exiting the desorber. It was as-

sumed that the vapour and liquid exiting the desorber were saturated, q_2 = 1 and $q_1 0$ = 0. The vapour and lean ammonia mass fraction, x_v and x_l, were then determined.

The processes in the compressor and pump were modelled with given isentropic efficiencies, η_{is} and given heat loss ratios f_Q. The transferred heat in the IHEX and gas cooler were calculated based on given values of heat exchanger effectiveness, ϵ. The mixing or adiabatic absorption process found prior to the absorber was modelled only by a mass and energy balance. Thus, state 5 was the equilibrium state attained when mixing stream 4 and 12. The state exiting the absorber was assumed to be saturated, q_6 = 0. The expansion in the throttling valve was assumed to be isenthalpic, $h_8 = h_9$.

The high and low pressures, p_H and p_L, were determined to satisfy given values of pinch point temperature difference, ΔT_{pp}, in the absorber and desorber. As enthalpy and temperature are not proportional during absorption and desorption, the absorber and desorber were discretised in heat load, giving the specific enthalpy of both the sink-source and ammonia-water mixture at each step. Assuming constant pressure and constant bulk ammonia mass fraction the equilibrium temperatures and temperature differences were attained at each step. The pinch point temperature difference is defined as the minimum of these temperature differences. 40 steps were used in this model for both the absorber and desorber.

The COP of the HACHP was defined as given in Eq. (2.2). Here $\dot{W}_{\text{CM}}$ and $\dot{W}_{\text{PM}}$ were the work calculated based on the given isentropic efficiencies. The efficiency of the electric motors driving the pump and compressor was accounted for by the electric efficiency, η_e.

$$\text{COP} = \frac{\dot{Q}_{\text{AB}} + \dot{Q}_{\text{GC}}}{\dfrac{\dot{W}_{\text{CM}}}{\eta_{e,\text{CM}}} + \dfrac{\dot{W}_{\text{PM}}}{\eta_{e,\text{PM}}}} \tag{2.2}$$

The displacement volume of the compressor, $\dot{V}_{\text{dis}}$, was found by Eq. (2.3), here $\dot{V}_{\text{suc}}$ was the suction line volume flow rate, η_{vol} was the volumetric efficiency of the compressor and v_2 was the specific volume of

state 2.

$$\dot{V}_{\text{dis}} = \frac{\dot{V}_{\text{suc}}}{\eta_{\text{vol}}} = \frac{\dot{m}_2 v_2}{\eta_{\text{vol}}} \tag{2.3}$$

The VHC was calculated as the ratio between the heat output of the HACHP and the displacement volume of the compressor, see Eq. (2.4). VHC was thus a measure of the size of compressor needed to deliver a certain heat load.

$$\text{VHC} = \frac{\dot{Q}_{\text{AB}} + \dot{Q}_{\text{GC}}}{\dot{V}_{\text{dis}}} \tag{2.4}$$

The pinch point temperature difference of the absorber and desorber, the isentropic, volumetric and electrical efficiencies and the heat loss ratios of the compressor and pump and the effectiveness of the IHEX and gas cooler were fixed parameters. The applied values are listed in Table 2.1.

2.2.2 Two-stage hybrid absorption-compression heat pump

Development of a HACHP with a two-stage compression may be beneficial for the applicability of the technology, as a two-stage solution offers the possibility of increasing the COP while simultaneously reducing the compressor discharge temperature. Most commercial compressors are restricted to a certain compressor discharge temperature, reducing this may thus increase the temperatures attainable with current commercial components.

The principle of a two-stage compression heat pump is to reduce the needed compression work by splitting the compression process into a low and high pressure stage and installing an inter-cooler between them. For an ideal gas the optimal intermediate pressure is $p_{m,\text{opt}} = p_L \cdot \sqrt{\frac{p_H}{p_L}}$. Hence, the optimal intermediate pressure is that which ensures an equal pressure ratio over both compression stages. This may differ if real gas behaviour and the performance of the applied components are accounted for. In the present study the intermediate pressure will be found by optimization of the COP.

For the reduction of the compression work to entail an increase in the COP for a heat pump, it is essential that the heat removed in the inter-cooler is utilized, either internally in the cycle or to heat the sink directly. If this is not ensured an increase of the COP should not be expected.

Though the two-stage configurations are expected to increased COP, they are also expected to increase the investment, mainly due to the need for an extra compressor. By comparing the COP, VHC and compressor discharge temperature of the two-stage configurations it should be possible to quantify the pros and cons of the suggest two-stage configurations.

Several two-stage configurations have been identified and are presented below. The identified cycles are split into three categories: internal heat exchange, bubble through inter-cooler (BTI) and liquid injection. In the following the working principles of the suggested cycles are presented. They are all modelled based on the approach presented in Section 2.2.1.

Internal heat exchange

Two configuration have been suggested for the two-stage HACHP with internal heat exchange. These are depicted in Fig. 2.3 and Fig. 2.4. The basic principle of the two cycles are the same: to preheat the lean liquid using the heat removed from the vapour at the intermediate pressure.

The two suggested solutions differ only by the placement of the IHEX. Placement option 1 is shown in Fig. 2.3, as seen here the lean liquid is heated first by the rich liquid existing the absorber and subsequently heated by the intermediated pressure vapour.

Placement option 2, Fig. 2.4, first heats the liquid using the intermediate pressure vapour and then using the rich liquid exiting the absorber.

Bubble through inter-cooler

One configuration has been suggested for a two-stage HACHP using a bubble through inter-cooler. This is seen in Fig. 2.5. Here the vapour and liquid are mixed at the intermediate pressure. Thus, this configuration requires an extra pump compared to the configuration with internal

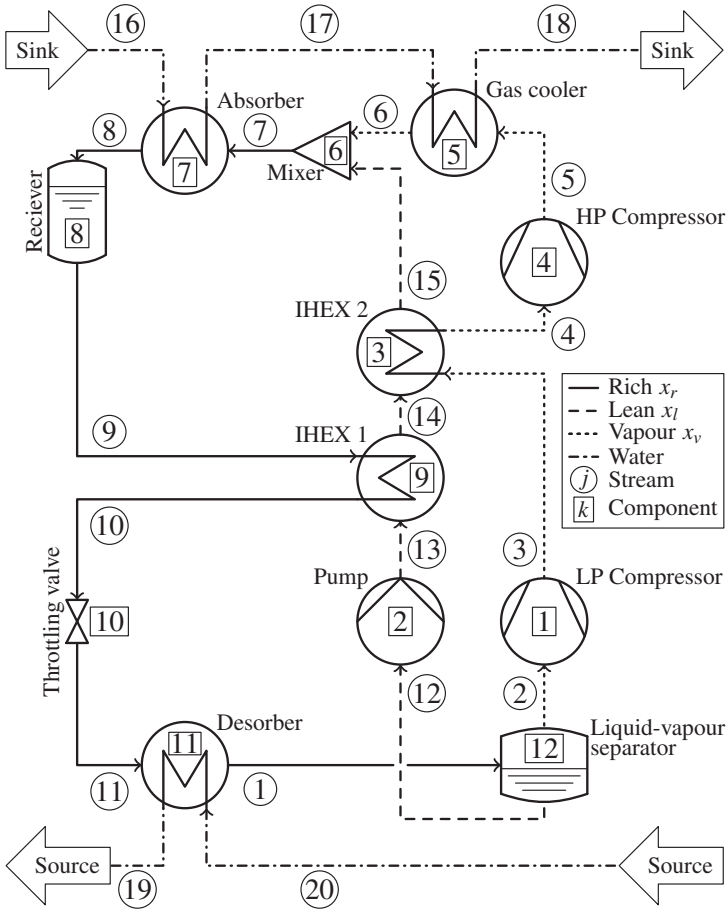

Figure 2.3: Principle sketch of a two-stage hybrid heat pump with internal heat exchanger (IHEX placement option 1)

heat exchange. Mixing the liquid and vapour in the inter-cooler results in a saturated liquid at a higher temperature and a saturated vapour at a lower temperature than the liquid and vapour entering the inter-cooler.

Mixing the two streams at the intermediate pressure also causes the composition of the vapour and liquid streams for the high pressure stage to differ from those of the low pressure stage. The circulation ratio for the high and low pressure stage will consequently differ.

The lean liquid exiting the high pressure pump is preheated using the

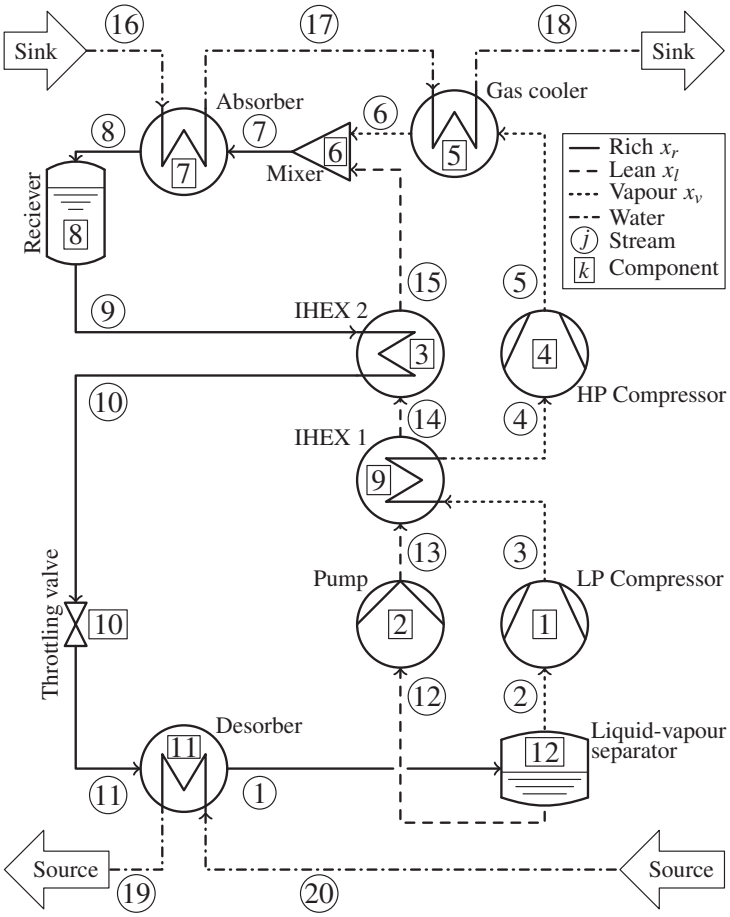

Figure 2.4: Principle sketch of a two-stage hybrid heat pump with internal heat exchanger (IHEX placement option 2)

rich liquid exiting the absorber before it is mixed with the vapour from exiting the gas cooler.

Liquid injection in suction line

The main principle for liquid injection is to cool the intermediate pressure vapour to the saturation point by mixing it with liquid extracted at some point prior to the throttling valve. Apart from reducing the temperature of the intermediate pressure vapour this also reduces the mass

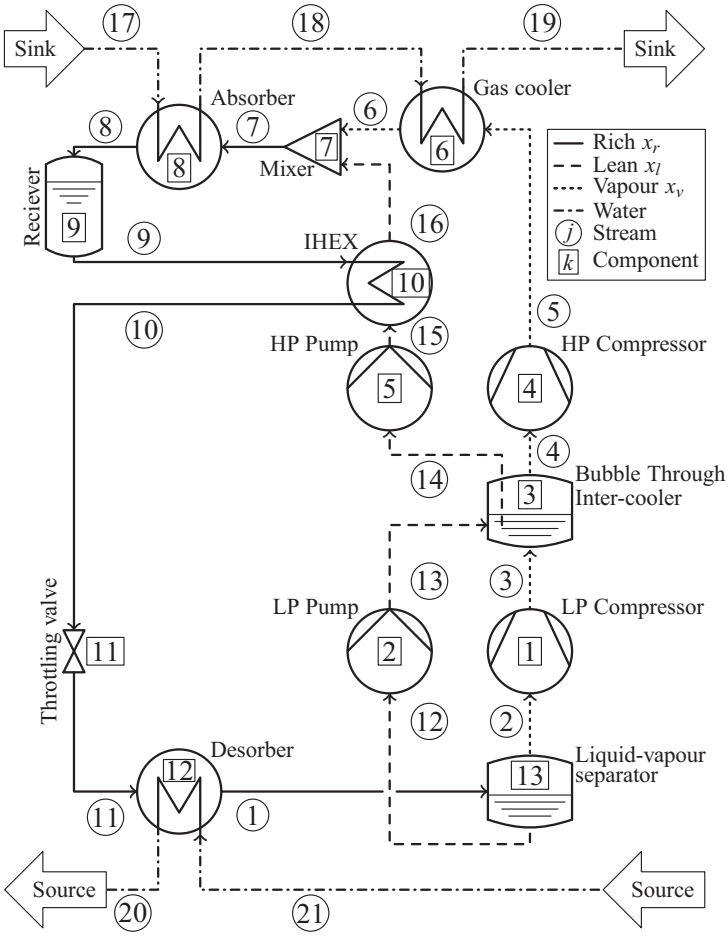

Figure 2.5: Principle sketch of a two-stage hybrid heat pump with BTI.

flow rate that is sent through the desorber and low pressure compressor. This method is often applied in VCHP.

In the HACHP one concern is that the injection of the rich liquid into the intermediate pressure vapour also decreases the bulk ammonia mass fraction of the vapour, which in turn increases the saturation temperature. Hence, it is expected that less liquid can be injected compared to a vapour compression cycle.

Two configurations have been suggested for the liquid injection two-stage HACHP. These are depicted in Fig. 2.6 and Fig. 2.7. As seen

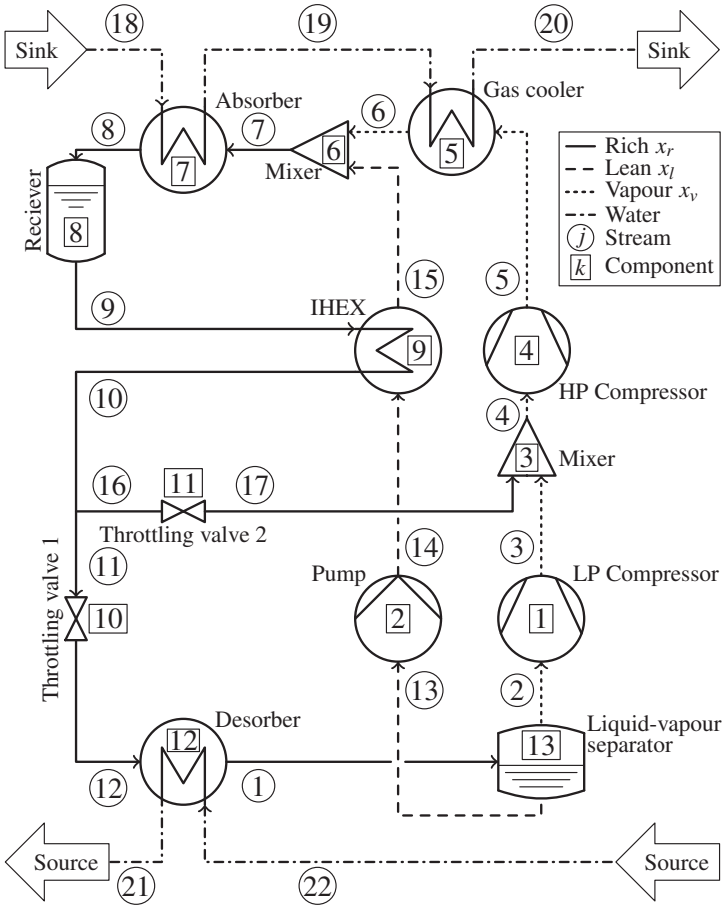

Figure 2.6: Principle sketch of a two-stage hybrid heat pump with liquid injection in suction line (liquid extraction option 1)

the two suggestions differ only by the point at which the rich liquid is extracted for injection. Liquid extraction option 1, Fig. 2.6, extracts the liquid after the rich solution is sub-cooled in the IHEX. Liquid extraction option 2 extracts the rich liquid prior to the IHEX.

As seen this solution does not require any additional heat exchangers or vessels, only an extra compressor and an additional throttling valve.

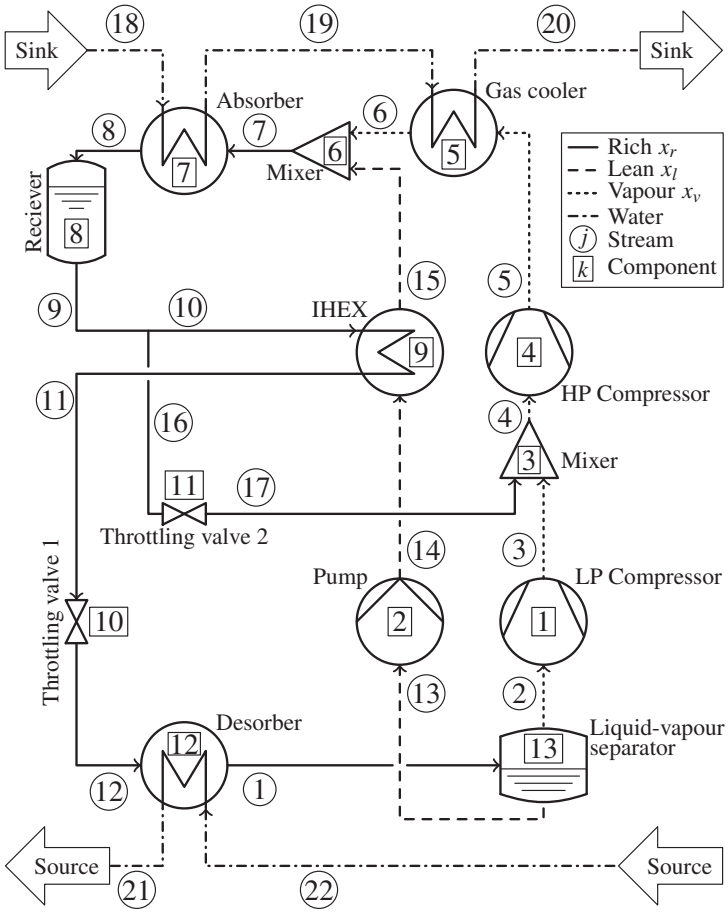

Figure 2.7: Principle sketch of a two-stage hybrid heat pump with liquid injection in suction line (liquid extraction option 2)

2.3 Results

2.3.1 One-stage HACHP

Influence of x_r and f on the performance of HACHP

Fig. 2.8 presents a parameter variation of the ammonia mass fraction and circulation ratio, both from 0.1 to 0.9. An operating condition of $\Delta T_{\text{sink}} = \Delta T_{\text{source}} = 10$ K, $\Delta T_{\text{lift}} = 30$ K and $T_{\text{sink,out}} = 100\,^{\circ}$C was applied.

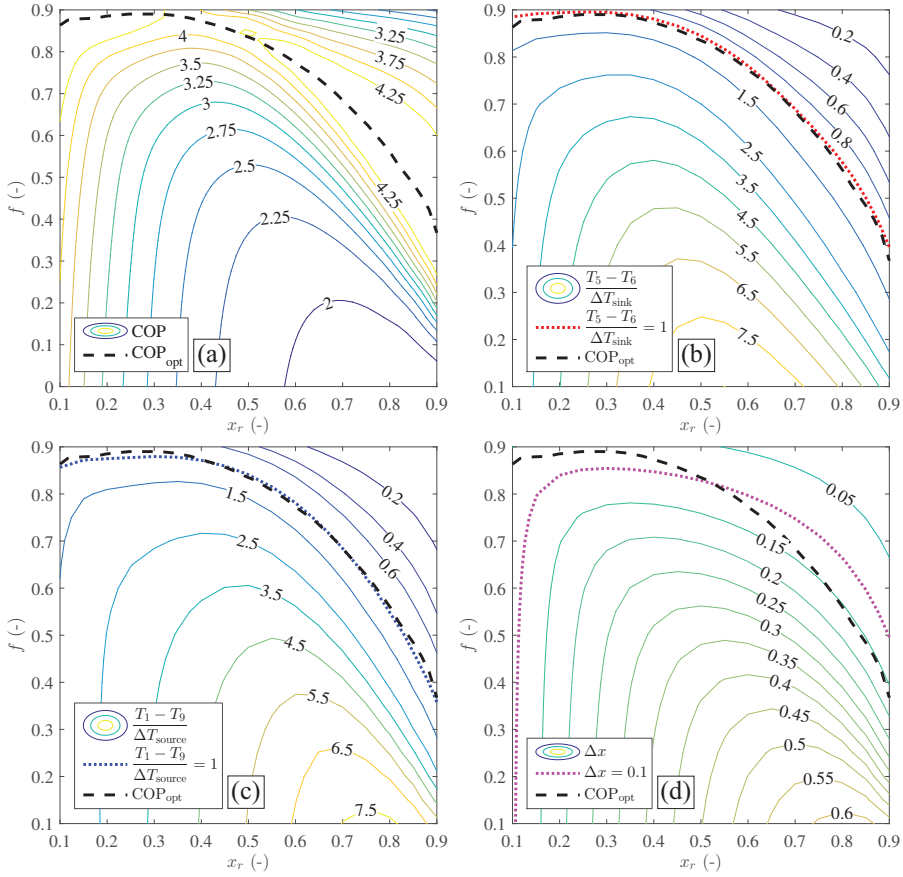

Figure 2.8: The variation of COP (a), sink temperature glide match (b), source temperature glide match (c) and concentration difference (d) for an operating condition of $\Delta T_{\mathrm{sink}} = \Delta T_{\mathrm{source}}$ = 10 K, ΔT_{lift} = 30 K and a heat supply temperature of $T_{\mathrm{sink,out}}$ = 100 °C

Fig. 2.8 (a) presents the contours of the COP as a function of the ammonia mass fraction and circulation ratio. Fig. 2.8 (b) shows the corresponding sink glide match ratio, $\frac{T_5 - T_6}{\Delta T_{\mathrm{sink}}}$, while the source glide match ratio, $\frac{T_1 - T_9}{\Delta T_{\mathrm{source}}}$, is presented in Fig. 2.8 (c). The glide match ratios are defined as the ratios of the average internal temperature gradient to the average external temperature gradient. Thus, when these ratios attain

a value of one the temperature profiles of the absorption or desorption processes match those of the sink or source. The non-linearity is not accounted for in these ratios and thus the overall minimization of the temperature difference may differ.

The contours of concentration difference, Δx, is seen in Fig. 2.8 (c), Δx is defined the difference between the lean and rich ammonia mass fractions.

As seen from Fig. 2.8 (a), the choice of ammonia mass fraction and circulation ratio have a large influence of the COP. For each choice of ammonia mass fraction one value of circulation ratio maximizes the COP. This is represented by the black dashed line. As seen the lower the ammonia mass fraction the higher the circulation ratio should be to optimize the COP.

Comparing the contours of the COP to the contours of the sink and source glide match ratios, it is clear that the maximum COP coincides with the matching of temperature profiles. If the circulation ratio is chosen below the optimum value, the glide match ratios are too high and vice versa. Hence, for a circulation ratio below optimum: the temperature difference over the absorption/desorption process is to large compared to the sink/source temperature difference. Choosing a circulation ratio above the optimum causes a temperature difference in the absorption/desorption process that is too low compared to the sink/source temperature difference.

Comparing the contours of the COP to those of the concentration difference, Fig. 2.8 (d), it can be seen that some discrepancy exists between the optimum COP and the constant concentration difference. However, it should be noted that the choice of $\Delta x = 0.1$ does keep the COP close to its optimal value.

Fig. 2.9 compares the optimum COP to a sink and source glide matching ratio of 1 and a constant concentration difference of $\Delta x = 0.1$. This is presented for the six investigated operating conditions. Fig. 2.9 (a) summarizes the results for the operating condition described in detail in Fig. 2.8. Fig. 2.9 (b) shows this for the same sink and source glide but with an increased temperature lift, $\Delta T_{\text{lift}} = 50$ K. As seen, with the increased temperature lift the matching of the sink glide differs slightly from the optimum COP. However, the optimum COP still coincides with

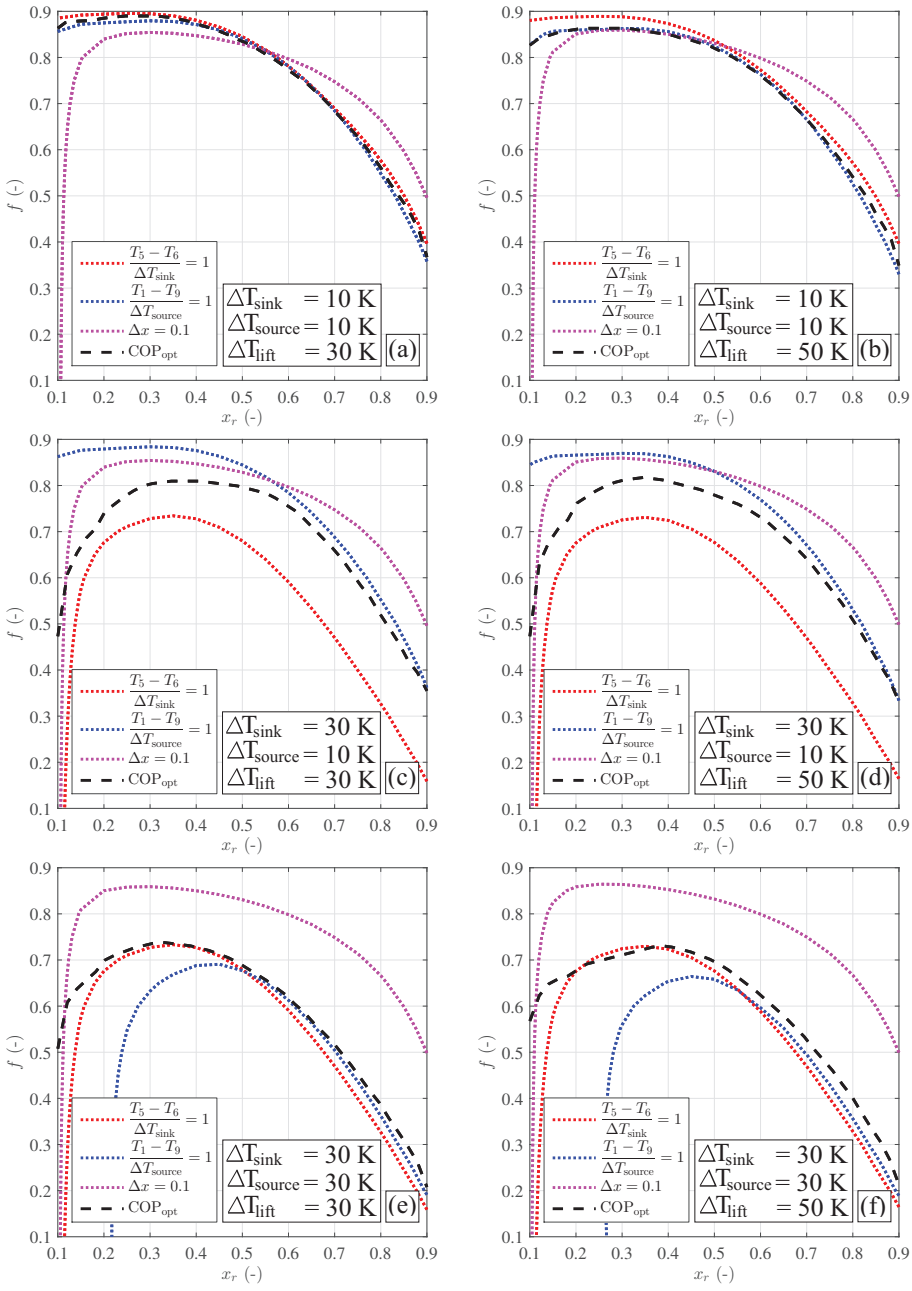

Figure 2.9: Comparison of the optimum COP, ΔT_{sink} glide match, ΔT_{sink} glide match and Δx for the six operating conditions.

the matching of the source glide, while also constant concentration difference differs slightly.

In Fig. 2.9 (c) and (d) the sink temperature glide is increased to ΔT_{sink} = 30 K while ΔT_{source} is kept at 10 K. For Fig. 2.9 (c) the temperature lift was 30 K, this is increased to 50 K in Fig. 2.9 (d). As seen, choosing to match the sink glide results in a circulation ratio well below the optimum COP, while choosing to match the source glides results in a circulation ratio slightly above the optimum COP. For ammonia mass fractions above 0.6, matching the source glide gives a reasonable approximation of the optimum COP at both lifts. Choosing a constant concentration difference of 0.1 results in a circulation ratio above the optimal. The difference between the optimum COP and Δx = 0.1 is larger than for the operating conditions shown on Fig. 2.9 (a) and (b).

In Fig. 2.9 (e) and (f) the sink and source temperature glides are set to $\Delta T_{sink} = \Delta T_{source}$ = 30 K. The temperature lift is ΔT_{lift} = 30 K in Fig. 2.9 (e) and ΔT_{lift} = 50 K in Fig. 2.9 (f). As seen for ammonia mass fractions above 0.5 matching the source glides gives the best approximation of the optimum COP. While matching of the sink glide gives the best approximation for ammonia mass fractions below 0.5. However, matching of the sink glide gives a close to optimum COP for all ammonia mass fractions at both ΔT_{lift} = 30 K and ΔT_{lift} = 50 K. Choosing a Δx of 0.1 when $\Delta T_{sink} = \Delta T_{source}$ = 30 K results in a circulation ratio well above the optimum COP and is not to be advised. However, a higher value of Δx may result in a good approximation of the optimal COP.

Whether the best performance of the HACHP is attained by matching of the sink or source glide is not easy to conclude at the recommendation differs based on the applied operating conditions. Only for low and equal values of sink and source glide will both approaches give the optimum COP. Constant Δx of 0.1 will only lead to a good approximation of optimum COP at sink and source glides of 10 K.

Influence of x_r on the optimum COP

Fig. 2.10 shows the COP at the optimum circulation ratio as a function of the rich ammonia mass fraction. The corresponding VHC is equally presented. The results are shown for the six investigated operating con-

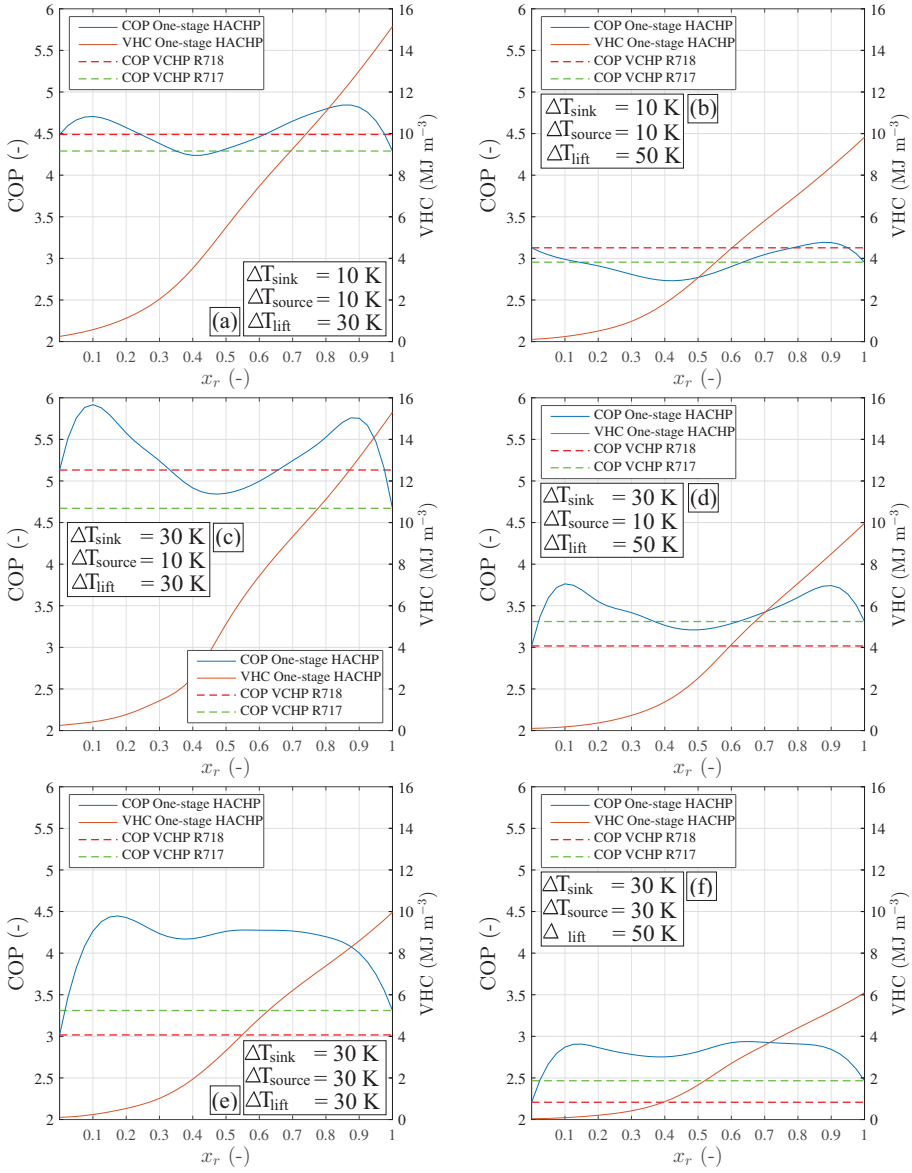

Figure 2.10: Optimum COP and the corresponding VHC as function of the rich ammonia mass fraction for the six operating conditions.

ditions. Fig. 2.11 shows the corresponding compressor discharge temperature, T_H, and high pressure, p_H.

Fig. 2.10 (a) represents the operating condition of $\Delta T_{\text{sink}} = \Delta T_{\text{source}}$ = 10 K and ΔT_{lift} = 30 K. It can be seen that two optima exists for the COP, one at an ammonia mass fraction of approximately 0.1 and one at approximately 0.9. The COP has a minimum at an ammonia mass fraction of 0.4, at this point the HACHP COP is inferior to both the pure water and pure ammonia VCHP. The highest COP is attained at $x_r \approx 0.9$, here the COP of the HACHP is approximately 0.4 higher than the COP of the best VCHP.

As seen, the VHC is strongly influenced by the ammonia mass fraction. Going from pure water to pure ammonia increases the VHC from 0.5 MJ m^{-3} to 15 MJ m^{-3}. Thus, the pure water VCHP would need 30 times the displacement volume to deliver the same heat load.

From Fig. 2.11 (a) it is seen that while the p_H increases with increasing ammonia mass fraction, the compressor discharge temperature decreases. Thus, when approaching pure water only around 1 bar of pressure is needed as opposed to 65 bar for pure ammonia. Up to 300 °C of compressor discharge temperature is seen for low ammonia mass fractions, which is reduced to around 140 ° C for the high ammonia mass fractions.

Fig. 2.10 (b) shows that when increasing the temperature lift to 50 K and keeping $\Delta T_{\text{sink}} = \Delta T_{\text{source}}$ = 10 K: only a small range of HACHP solutions perform better than the VCHP. These are all in the high ammonia mass fraction range. The increased performance in this range is minor and the benefits of the HACHP can be discussed.

Fig. 2.11 (b) shows that the temperature lift only has a minor influence on the high pressure while it significantly increases the compressor discharge temperature.

In Fig. 2.10 (c), $\Delta T_{\text{sink}} =$ is increased to 30 K while ΔT_{source} is kept at 10 K and ΔT_{lift} at 30 K. As seen, the same trend as in Fig. 2.11 (a) is observed. However, the difference between the COP of the HACHP and VCHP is increased. Thus, at these condition the HACHP is always better than the ammonia VCHP and apart from ammonia mass fractions between 0.35 and 0.65 the HACHP also performs better than the water VCHP. The same is observed in Fig. 2.10 (d), here the lift is increased

to 50 K, although the difference between the HACHP COP and VCHP COP diminishes.

In Fig. 2.10 (e) and (f) both ΔT_{sink} and ΔT_{source} are set at 30 K. Fig. 2.10 (e) has a lift of 30 K, while Fig. 2.10 (f) has a lift of 50 K. As seen in Fig. 2.10 (e) for these conditions the HACHP gives a significant increase of the COP compared to the VCHP for all choices of ammonia mass fraction between 0.1 and 0.9. The same is observed for the increased lift in Fig. 2.10 (f), although the increase in COP is smaller.

From Fig. 2.10 (a)-(f) it can be concluded that in order for the HACHP to ensure an increased COP compared to the VCHP the temperature glides of both the sink and source should be large, while the temperature lift should be low. This requirement may to some extent limit the applicability of the HACHP. Heat pump implementation where $\Delta T_{\text{sink}} > \Delta T_{\text{lift}}$ is not a sensible solution as direct heat exchange from the source to the sink is possible for some portion of the heat load, ideally until $\Delta T_{\text{sink}} = \Delta T_{\text{lift}}$. Hence, when increasing the temperature glides the benefits of the HACHP will increase. However, increasing the temperature glide inherently increases the minimum temperature lift, which in turn cause the benefits of the HACHP to be reduced. Thus, it is to be expected that the increased performance of the HACHP has an optimum at some temperature glide.

From Fig. 2.11 (a)-(f) it can be seen that the high pressure is only weakly influenced by the change in ΔT_{sink}, ΔT_{source} and ΔT_{lift} but highly influence by the choice of ammonia mass fractions. The higher the ammonia mass fraction the higher the pressure. The compressor discharge temperature is also highly influenced by the choice of ammonia mass fraction. The higher the ammonia mass fraction the lower the compressor discharge temperature. Balancing pressure and discharge temperature constraints are therefore an issue for the design HACHP, this is discussed further in Chapter 3.

2.3.2 Comparison of two-stage HACHP

Fig. 2.12 (a)-(f) shows the difference between the optimum COP of the one-stage HACHP and the suggested two-stage configurations. Fig. 2.13 (a)-(f) shows the difference in the corresponding VHC. The dif-

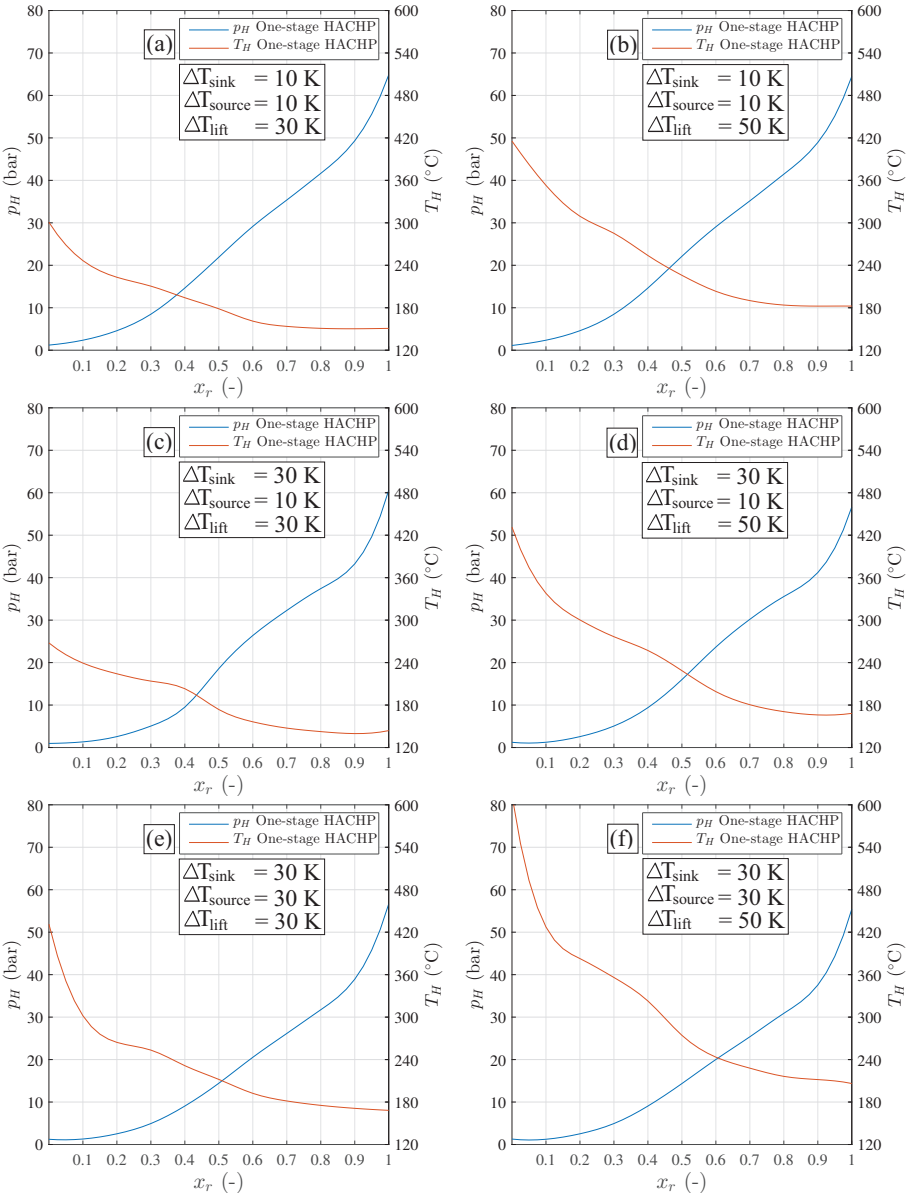

Figure 2.11: Compressor discharge temperature and high pressure at the optimum COP as function of the rich ammonia mass fraction for the six operating conditions.

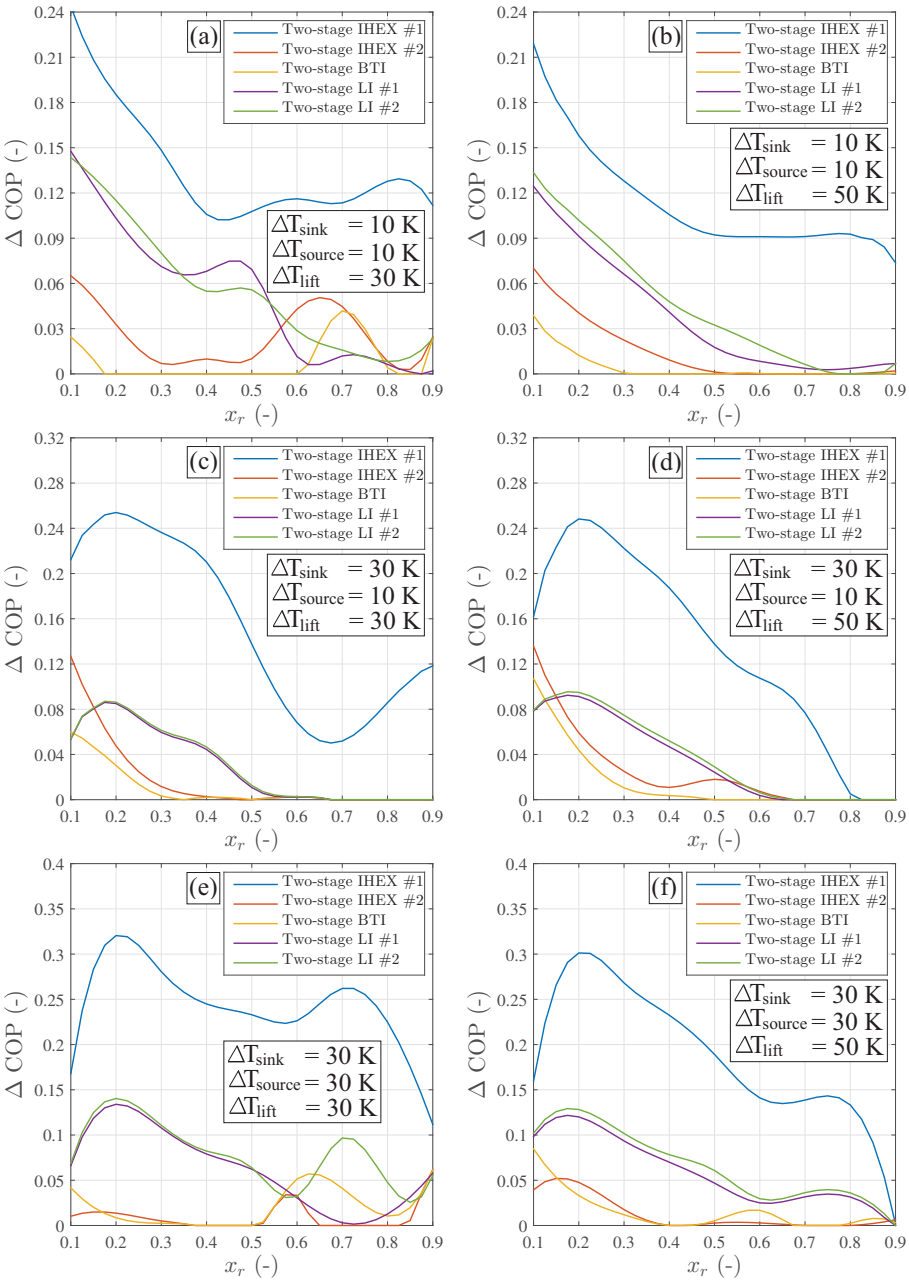

Figure 2.12: Difference between COP of the one and two-stage configurations as a function of the x_r for the six operating conditions.

ference in COP and VHC is show as a function of the ammonia mass fraction. For the two-stage configurations both circulation ratio and intermediate pressure are optimized in terms of COP for each ammonia mass fraction and operating condition. Again the analysis is presented for the six investigated operating conditions.

As seen in Fig. 2.12 (a)-(f) some general tendencies can be concluded. Generally the two-stage configuration with internal heat exchange, placement optional 1, always gives the highest increase in COP, regardless for the ammonia mass fraction and operating conditions. The benefit of the two-stage compression is generally higher for the low ammonia mass fraction than for the high ammonia mass fractions. The two liquid injection configuration are generally better than the configurations with internal heat exchange, placement option 2, and the BTI configuration. For the liquid injection configuration extraction option 2 seems to be the preferable solution. It may be seen that the higher the temperature glides the higher the benefit of the two-stage compression will be. However the advantage of the two-stage compression seems to be independent of the temperature lift.

The low performance of the both the internal heat change option 2 and the BTI configuration is found to be caused by an improper heat integration. Thus, heating the lean liquid with the intermediate pressure vapour prior to the IHEX results in a temperature too high to ensure a good subcooling of the rich liquid exiting the absorber.

The difference in VHC presented in Fig. 2.13 (a)-(f) can be viewed as an indication of the increased cost needed to attain the increased COP. Thus, it would preferable to have a ΔVHC as close to 0 as possible. As seen, the two-stage configuration with internal heat exchange placement option 1 gives the lowest reduction in VHC and thus is the best solution in terms of investment. This is regardless of the ammonia mass fraction and operating conditions. The second lowest reduction is found for the liquid injection configurations while the highest reduction is found for internal heat exchange option 2 and the BTI configuration.

It can thus be concluded that the configurations that attains the highest increase in COP also does this with the lowest reduction of the VHC.

The influence on the high pressure and compressor discharge temperature has also been investigated. This shows that the choice of two-stage

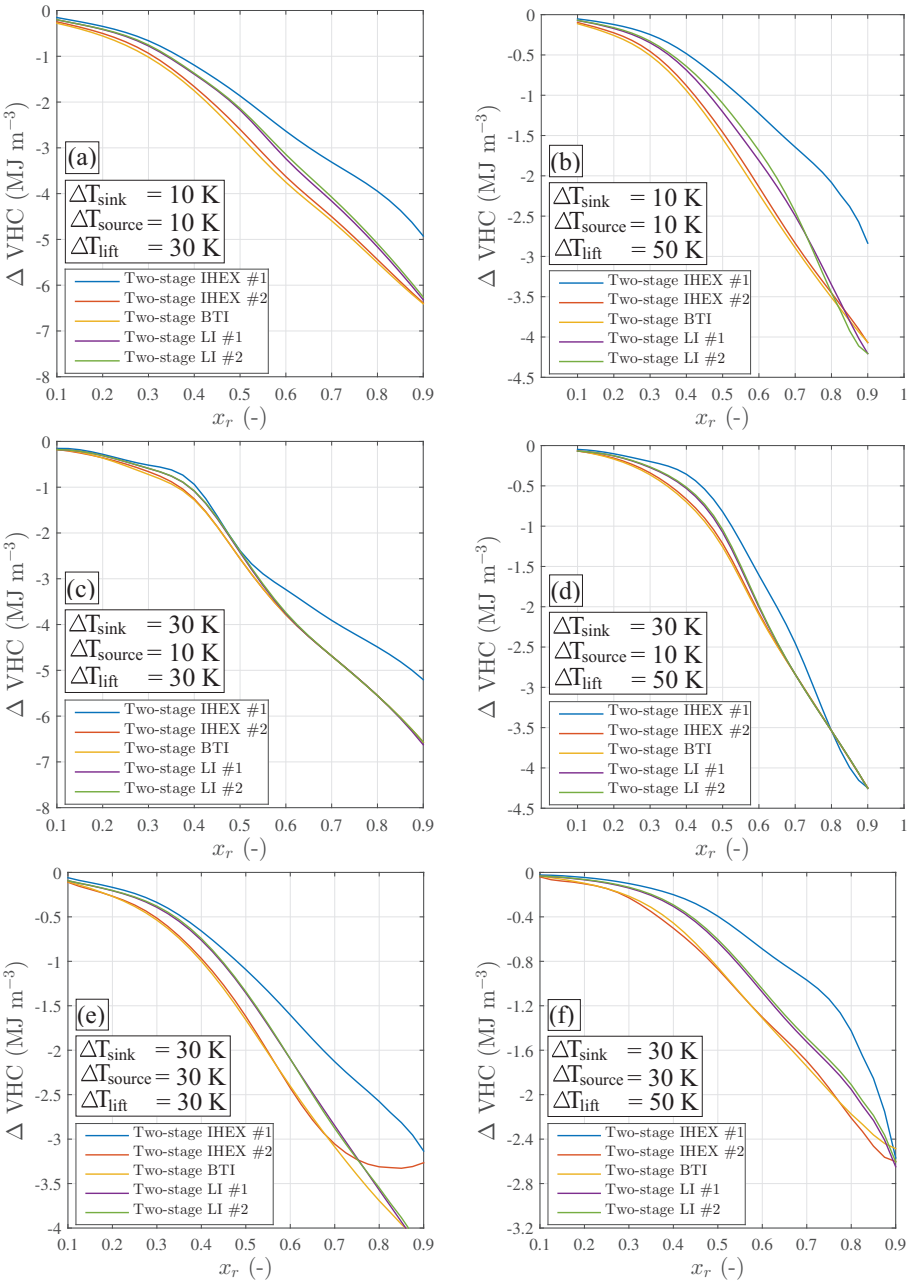

Figure 2.13: Difference between VHC of the one and two-stage configurations as a function of the x_r for the six operating conditions.

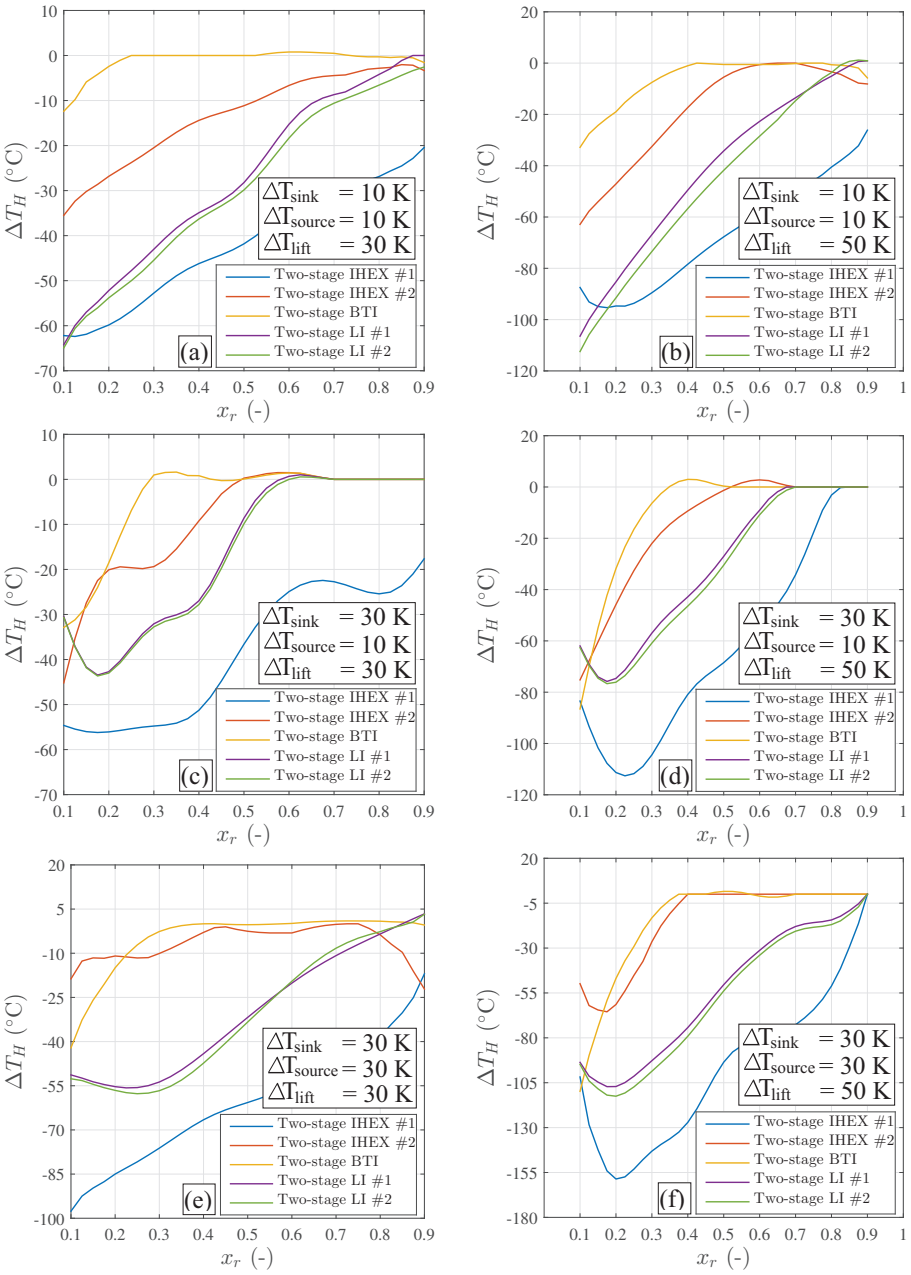

Figure 2.14: Difference between T_H of the one and two-stage configurations as a function of the $x_r$for the six operating conditions.

configuration has little influence on the high pressure, while the reduction of compressor discharge temperature differ significantly, see Fig. 2.14. Again the internal heat exchange configuration, placement option 1, is the preferable solution, as it ensures the largest reduction of the compressor discharge temperature. As seen the reduction can be up to 150 °C for low ammonia mass fractions, while typically being between 20 - 40 °C for the high ammonia mass fractions.

All in all it can be concluded that the internal heat exchange configuration, placement option 1, is superior to all other identified configurations, both in terms of increasing COP and reducing compressor discharge temperature. Further, the IHEX configuration does this with the smallest reduction of the VHC.

2.4 Discussion

As shown, for the operating conditions with low values of either ΔT_{sink} or ΔT_{source} or both, the highest COP is found close to the pure compositions, $x_r \approx 0.1$ and $x_r \approx 0.9$ while a minimum exists when the composition is around 0.5. These results coincide with the findings of Åhlby et al. [34]. However, the methodology applied by Åhlby et al. only led them to find the optimum at $x_r \approx 0.9$. Thus, leading to the conclusion that the highest COP is attained at the highest allowable pressure. As seen if the pressure is sufficiently reduced COP can found to increase with a decrease in pressure. For the operating condition with large values of both ΔT_{sink} and ΔT_{source} it is found that the COP is not as sensitive and to the choice of x_r and consequently the pressure.

As presented, the HACHP can attain a higher COP than the VCHP under all the investigated operating conditions, this in alignment with the conclusions of Åhlby et al. [34]. However, it is shown that for the low values of ΔT_{sink} or ΔT_{source} and especially for high temperature lifts, several choices of ammonia mass fraction result in a COP lower than that of the pure water and pure ammonia VCHP. For large values of ΔT_{sink} and ΔT_{source} the HACHP has a higher COP than the VCHP for all choices of ammonia mass fraction.

As shown, the two-stage liquid injection cycle does not perform as

good the two-stage cycle with IHEX option 1, although it does perform better than all the remaining two-stage configurations, especially at low ammonia mass fractions. However, the liquid injection cycle might result in a lower investment than the remaining two-stage configurations, as it does not need an additional heat exchanger but only an additional throttling valve. The liquid injection cycle might therefore be a competitive two-stage solution if a complete economic analysis is conducted.

Controlling the liquid injection mass flow rate to ensure both sufficient vapour cooling but also sufficient superheat to allow safe operation of the high stage compressor may be a troublesome task. Especially as the composition of the vapour changes with the injection of the liquid, making it hard to measure the vapour superheat. One measure of avoiding the issues of measuring superheat is to implement a vessel in which a floating device can be installed to control the throttling valve. Thereby saturated conditions are supply the high stage compressor. Installing an extra vessel might be as large an investment as an extra heat exchanger in which case the liquid injection cycle might again not be a favourable solution. All in all it is suggested to further investigate the application of the liquid injection cycle before it is finally discarded.

2.5 Conclusion

A procedure for thermodynamic modelling of HACHP was presented and several two-stage compression configurations were identified. The identified configurations included internal heat exchange solutions, a bubble through inter-cooler solution and liquid injection solutions. All identified configurations were modelled such that the performance of the cycle could be compared.

Six relevant operating conditions were investigated combining both high and low temperature glides with high and low lifts. Process optimization was applied to all six operating conditions.

Several approaches to estimate optimum COP were compared. Sink glide matching, source glide matching and constant concentration difference was compared to an optimization of the COP. It was found that if the temperature glide in the sink and source are low and equal to one

another both sink and source glide matching can be used to optimize the COP. As the temperature lift is increased, minor discrepancies can occur.

If the sink glide is larger than the source glide, matching of the sink glide does not lead to the optimum COP, while matching of the source glide gives only a good approximation.

If both the sink glide and source glides are large, sink and source glide matching can be used to optimize COP for high ammonia mass fractions, while only sink matching can be used at low ammonia mass fractions. All in all if the sink and source glides are larger than 10 K it is recommended to optimize COP rather than match the glides of the sink or source, as this will ensure a better performance of the HACHP. Constant concentration difference of 0.1 was found only to give a good approximation of the optimal COP at low sink and source glides.

Comparing the optimum COP of the HACHP to the COP of a pure ammonia and pure water VCHP showed that increased performance is only ensured when the sink and source temperature glides are high and the temperature lift is low. For low glides and high lifts HACHP with ammonia mass fractions around 0.5 do not attain a higher COP than the VCHP. Although increased performance can be attained at ammonia mass fractions around 0.1 and 0.9 for the same operating conditions.

All the identified two-stage configuration were compared with the one-stage HACHP in terms of both COP, VHC and compressor discharge temperature. This clearly showed that the two-stage configuration with internal heat exchange, placement option 1, always is the preferable two-stage configuration. This is regardless of the ammonia mass fraction and operating conditions. Thus, only this configurations will be included in the further analysis.

CHAPTER 3

FEASIBILITY OF HIGH TEMPERATURE DEVELOPMENT

The work presented in this chapter is based on results presented at the International Sorption Heat Pump Conference, University of Maryland, April 2014 [48]([P12]) and later published in the International Journal of Refrigeration [43] ([P3]).

The results presented in [48, 43] were based on a one-stage HACHP. However, as discussed in Chapter 2, two-stage HACHP may relax certain constrained parameters such as compressor discharge temperature and COP. Thus, the two-stage HACHP with IHEX (placement option 1) has been included for the present chapter.

3.1 Introduction

Brunin et al. [23] showed that it is technically and economically feasible to use the HACHP up to a heat supply temperature of 140 °C, this however is based on a high pressure constraint of 20 bar corresponding to the limitations of standard refrigeration components at the time of the study. In the meantime new compressor types such as high pressure NH_3 (50 bar) and transcritical CO_2 (140 bar) have become commercially available and further standard refrigeration components now operate at 28 bar. It is therefore of interest to evaluate how the application of these components changes the working domain of the HACHP.

One design constraint that is not discussed by Brunin et al. [23] is the compressor discharge temperature. However, most compressor manufacturers require this to be lower than 180 °C [73]. This is mainly due to the thermal stability of the lubricating oil and the thermal stress of the materials surrounding the compressor discharge line. This is mainly an issue for reciprocating compressors.

Changing the lubricant from a mineral oil to a synthetic oil could relax the constraint due to thermal stability. This however requires that a synthetic oil that meets the requirements of miscibility etc. is identified. Adjustments to the gasket materials and alike could also make the compressor durable at higher discharge temperatures. It is assumed to be a realistic estimate that compressor discharge temperatures up to 250 °C can be sustained with minor adjustments.

To evaluate the working domain of the HACHP using the recently developed high pressure equipment a set of design constraints are defined. A solution that satisfies this set of constraints will constitute an economically and technically feasible solution. The technical limitations are: the high pressure, governed by the choice of compressor technology, the low pressure, set to eliminate entrainment of air, and the compressor discharge temperature, as discussed above. Further, for the ammonia compressors a constraint is set on the vapour ammonia mass fraction. The economic constraints are: the Coefficient of Performance (COP) and the volumetric heat capacity (VHC), calculated as the ratio of the compressor displacement volume to the heat output of the HACHP [23].

As shown in Chapter 2 the rich ammonia mass fraction, x_r, and the circulation ratio, f, influence the design values of the constraining parameters significantly. The combination of these two govern the system pressure and thereby the VHC. Also the slope of the absorption-desorption curve and thereby the performance (COP) is influenced by these parameters.

3.2 Methodology

The present study investigates the set of feasible combination of x_r and f at heat supply temperatures of 100 °C, 125 °C, 150 °C and 175 °C. Working domains will be evaluated for all three mentioned types of refrigeration components.

The design constraints are listed in Table 3.1. The constraint on COP and VHC ensures the economic feasibility of the heat pump as a high COP ensures a low running cost and a high VHC indicates a low investment cost. The applied values for the COP, VHC and low pressure

Table 3.1: Design constraints for standard refrigeration, high pressure NH_3 and transcritical CO_2 components

	Unit	Standard ref.	HP NH_3	Transcrit. CO_2
$p_{H,\max}$	bar	28	50	140
$p_{L,\min}$	bar	1	1	1
$T_{H,\max}$	°C	170	170	250
$\text{COP}_{\min}$	-	4	4	4
$\text{VHC}_{\min}$	MJ m^{-3}	2	2	2
$x_{v,\min}$	-	0.95	0.95	0.00

constraint are set in agreement with those presented by Brunin et al. [23]. The high pressure constraints for the different compressor technologies are summarized by Ommen et al. [78].

For the two ammonia compressors a constraint was imposed on the vapour ammonia mass fraction, x_v. It was assumed that 5% water is acceptable in an ammonia compressor. For the modified transcritical CO_2 compressor no constraint was imposed on x_v as they may just as well be modified to handle the needed ammonia-water composition.

Nekså et al. [73] states that compressor discharge temperatures up to 180 °C should be possible without degeneration of lubricant, while Ommen et al. [78] state this could be as low as 160 °C. The value for the unmodified compressors was set to 170 °C in this study. For the modified transcritical CO_2 components, 250 °C was chosen as previously discussed.

Two HACHP cycles were investigated, the one-stage HACHP, Fig. 2.1 and the two-stage HACHP with IHEX (placement option 1), Fig. 2.3.

Both the one-stage and two-stage cycles were analysed at a fixed operating condition governed by the sink temperature difference, ΔT_{sink}, temperature lift ,ΔT_{lift} and the mass flow rates of the sink and source $\dot{m}_{\text{sink}}$ and $\dot{m}_{\text{source}}$. The applied values are stated in Table 3.2.

The component inputs were equally set as constant for both the one-stage and two-stage cycles. For the Two-stage cycle both compressors and both heat exchangers were assumed to operate with the same input. The applied values for the component inputs are stated in Table 3.3.

Table 3.2: Investigated operating condition

ΔT_{sink}	20	K
ΔT_{lift}	25	K
$\dot{m}_{\text{sink}}$	1	kg s^{-1}
$\dot{m}_{\text{source}}$	2	kg s^{-1}

Table 3.3: Component inputs to the thermodynamic model

Component	Input	Value	Unit
Compressor	η_{is}	0.75	(-)
Compressor	η_{vol}	0.90	(-)
Compressor	η_{e}	0.90	(-)
Pump	η_{is}	0.75	(-)
Pump	η_{e}	0.90	(-)
Gas cooler	ϵ	0.85	(-)
Absorber	ΔT_{pp}	5.00	(K)
IHEX	ϵ	0.85	(-)
Desorber	ΔT_{pp}	5.00	(K)

3.3 Results

3.3.1 Influence of x_r and f

Fig. 3.1 and 3.2 shows the contours of COP, VHC, compressor discharge temperature, T_H, high pressure, p_H, low pressure, p_L and vapour ammonia mass fraction, x_v for the one-stage and two-stage HACHP, respectively. The contours are shown as a function of the ammonia mass fraction and the circulation ratio. The component inputs, listed in Table 3.3, and the operating conditions, listed in Table 3.2, were held constant. For the two-stage HACHP the intermediate pressure was chosen to optimize COP. The optimum COP was determined for each combination of x_r and f. The heat supply temperature was, $T_{\text{sink,out}}$ = 100 °C. The calculations were carried out for x_r and f ranging from 0.1 to 0.9 in steps of 0.025. As the constrained parameters are independent of the heat load the presented results are valid for all HACHPs in which the

sink-source mass flow ratio is $\dot{m}_{\text{sink}}/\dot{m}_{\text{source}} = 0.5$.

As seen in Fig. 3.1 and 3.2 the general trend of all constrained variables with x_r and f are similar for both the one and two-stage HACHP. Although it can be noted that the COP is generally highest for the two-stage while the one-stage generally attains the highest VHC. Further, the compressor discharge temperature is lower for the two-stage HACHP compared to the one-stage. The trend of the compressor discharge temperature differs slightly, which is mainly due to the optimization of the intermediate pressure with regards to the COP. Both the variation and the values of the high pressure, low pressure and vapour ammonia mass fraction only differ slightly between the one and two-stage HACHP.

When comparing the contours of the high and low pressure it becomes evident that the circulation ratio has a greater influence on the low pressure than on the high pressure. The circulation ratio only influences the high pressure at high ammonia mass fractions and high circulation ratios. The low pressure is governed by both parameters such that an increase in ammonia mass fraction and an increase in circulation ratio will increase the low pressure. Thus, the lowest low pressure is found at $x_r = 0.1$, $f = 0.1$ and the highest low pressure is at $x_r = 0.9$, $f = 0.9$. From this it is apparent that a set of combinations induce a significant increase in the system pressure ratio (PR), see Figs. 3.3 (a) & (b). These are combinations with low circulation ratio and ammonia mass fractions around 0.5. This further induces a large increase in compressor discharge temperature varying from 150 °C for the low pressure ratio combinations to 450 °C in the high pressure ratio range.

The increased pressure ratio and compressor discharge temperature also have a significant influence on the COP. As seen, the COP contours resemble those of the pressure ratio and compressor discharge temperature. The COP is greatly reduced for the combinations with high pressure ratios as the increased compressor discharge temperature increases the entropy generation in the gas cooler and mixer due to the large temperature differences. It is seen that for all ammonia mass fractions one circulation ratio exists that optimizes the COP. This is indicated by the dashed line marked COP_{max}. For circulation ratios above this optimum line the COP drops although the pressure ratio is reduced. As seen, the higher the ammonia mass fraction, the lower the optimal circulation

ratio.

The VHC is directly influenced by the specific volume in the suction line and thus the low pressure governs this parameter. This is apparent when comparing the contours of the VHC and low pressure. Further, it is seen that also the vapour ammonia mass fraction is linked to the low pressure. As seen, the lower the pressure the lower the vapour ammonia mass fraction.

All important design parameters are greatly influenced by both ammonia mass fraction and circulation ratio and thus the behaviour of these cannot be attributed solely to one of the two. Thus, the main conclusion derived from Fig. 3.1 & 3.2 is that the correct combination of ammonia mass fraction and circulation ratio is needed in order to identify a feasible design.

3.3.2 Feasible design combination of x_r and f

In order to evaluate the applicability of the HACHP for high temperature operation ($T_{\text{sink,out}} > 100\ ^\circ\text{C}$) the feasible combinations of ammonia mass fraction and circulation ratios must be identified in this temperature range. The feasible design combinations are given by the design constraints listed in Table 3.1. As these are specific to the three technologies (standard, high pressure NH_3 and transcritical CO_2) three sets of feasible combinations are identified.

These sets of feasible combinations have been determined at four heat supply temperatures: $T_{\text{sink,out}} = 100\ ^\circ\text{C}$, 125 °C ,150 °C and 175 °C. Again the component inputs from Table 3.3 and the operating conditions from Table 3.2 were kept constant.

Figs. 3.4 & 3.5 shows the feasible combinations of the three compressor technologies at the four heat supply temperatures. Fig. 3.4 shows this for the one-stage, while Fig. 3.5 presents the results for the two-stage HACHP.

For the one-stage HACHP with $T_{\text{sink,out}} = 100\ ^\circ\text{C}$, Fig. 3.4 (a): a feasible set of combinations exist for all three compressor technologies. The set belonging to the standard refrigeration components is the smallest of the three and is constrained by the high pressure, p_H, and compressor discharge temperature, T_H. The set belonging to the high pressure

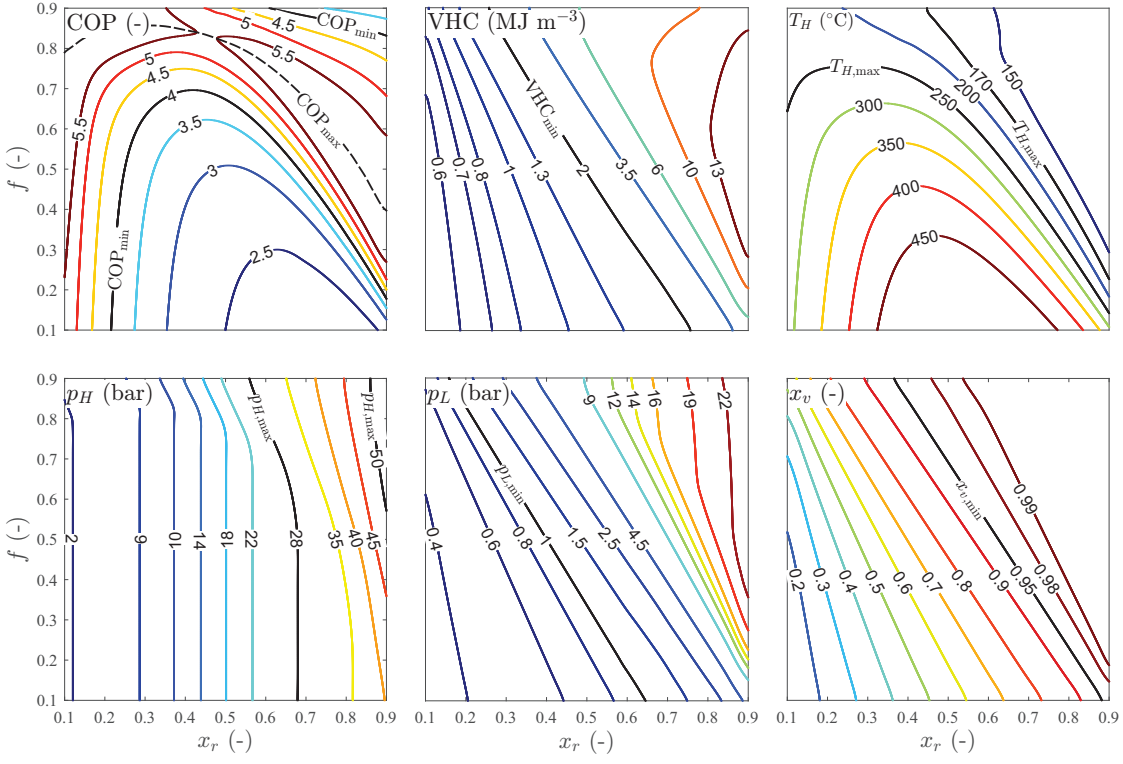

Figure 3.1: COP, VHC, compressor discharge temperature, T_H, high pressure, p_H, low pressure, p_L, and vapour ammonia mass fraction, x_v, as a function of the circulation ratio, f, and the ammonia mass fraction, x_r for the one-stage HACHP. Heat supply temperature $T_{\text{sink,out}}$ = 100 °C.

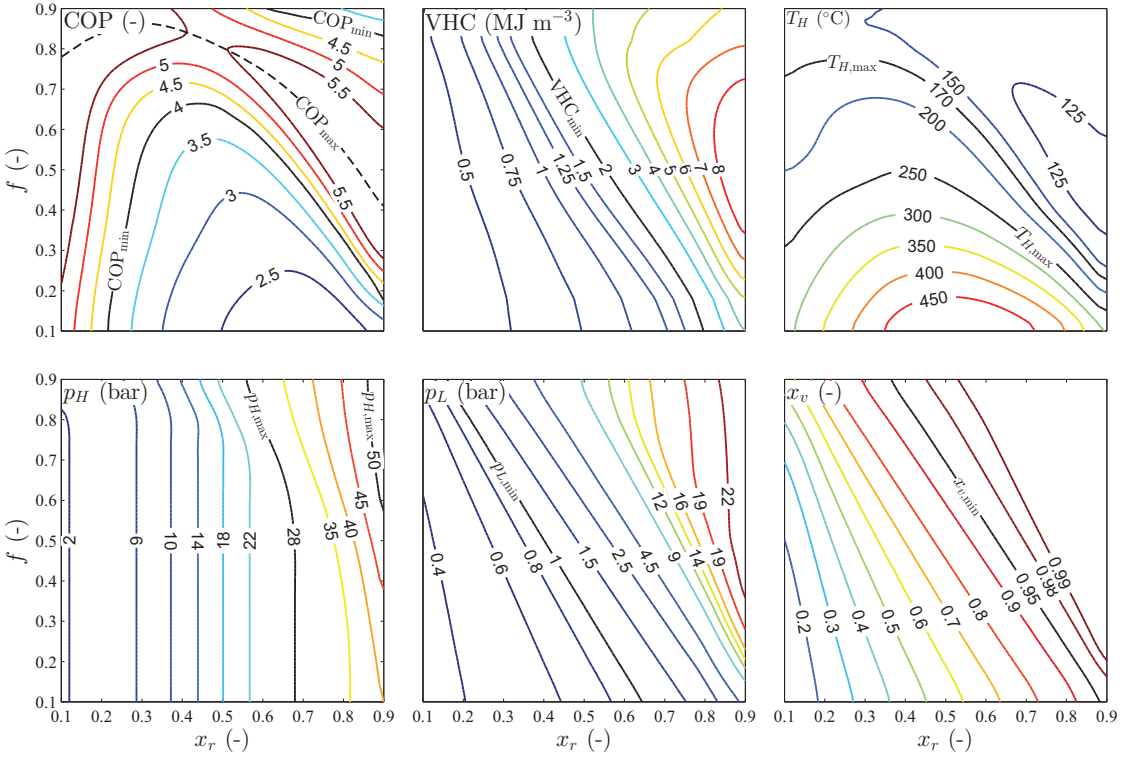

Figure 3.2: COP, VHC, compressor discharge temperature, T_H, high pressure, p_H, low pressure, p_L, and vapour ammonia mass fraction, x_v, as a function of the circulation ratio, f, and the ammonia mass fraction, x_r for the two-stage HACHP with IHEX (placement option 1). Heat supply temperature $T_{\text{sink,out}}$ = 100 °C.

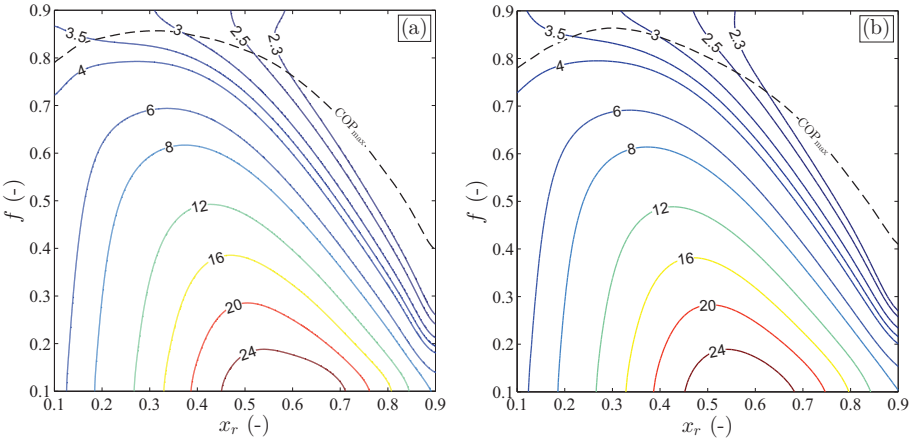

Figure 3.3: Pressure ratio (PR) as a function of the circulation ratio, f, and the ammonia mass fraction, x_r. Heat supply temperature $T_{\text{sink,out}}$ = 100 °C. (a) One-stage HACHP, (b) two-stage HACHP with IHEX (placement option 1)

NH_3 technology is significantly larger than that of the standard components. This set is constrained by p_H, T_H and COP. The largest set is that of the transcritical CO_2 components. This set is constrained by the VHC, T_H and COP. It can be noted that the x_v constraint is dominant over both the low pressure and VHC constraint in the entire range, thus these constraints are effectively extraneous.

For the two-stage HACHP, Fig. 3.5 (a), the set of feasible solutions for standard and high pressure NH_3 is increased compared to the one-stage HACHP, this is mainly due to the reduction of the compressor discharge temperature. Thereby, these sets are constrained by x_v instead of T_H. The set belonging to transcritical CO_2 components is reduced for the two-stage HACHP due to the increased VHC.

In Figs. 3.4 & 3.5 (b) the heat supply temperature is increased to 125 °C. As seen, for the one-stage HACHP, Fig. 3.4 (b), this has the consequence, that the high pressure constraint for the standard components moves beyond the compressor discharge temperature constraint, deeming the application of the standard refrigeration components infeasible. For the two-stage HACHP, Fig. 3.5 (b), a few solutions exist constrained only by T_H and p_H. A small set of feasible combinations

exist for the high pressure NH_3 components in the one-stage HACHP. This set is constrained by p_H and T_H.

For both the one and two-stage HACHP the set of feasible combinations for the transcritical CO_2 components is slightly increased as the VHC constraint is moved towards lower ammonia mass fractions. It should be noted that although the VHC and low pressure constraints have moved significantly towards lower x_r the vapour ammonia mass fraction constraint actually moved slightly towards higher x_r allowing fewer solutions to satisfy this constraint.

Figs. 3.4 & 3.5 (c) have a heat supply temperature of 150 °C. Here no combinations that satisfy the COP constraint also satisfy the constraint of $T_H < 170$ °C. This is the same for both the one and two-stage HACHP. Thus, neither standard refrigeration nor high pressure NH_3 components are applicable at a heat supply temperature of 150 °C.

For the one-stage HACHP the VHC constraint is no longer present due to the high temperature of the heat source and subsequently high desorber pressure. This again causes the set of feasible combinations for transcritical CO_2 components to expand. This set is only constrained by T_H and COP. For the two-stage HACHP the set of feasible solutions is still constrained by VHC, however, the reduced compressor discharge temperature increases the set for feasible solution for the two-stage HACHP compared to the one-stage HACHP

Figs. 3.4 & 3.5 (d) have a heat supply temperature of 175 °C. Again only the transcritical CO_2 components can be applied due to the high compressor discharge temperature. For the first time the high pressure constraint for transcritical CO_2, $p_H < 140$ bar, is present, while the VHC constraint is no longer present two-stage HACHP. For the one-stage HACHP, the set of the feasible combinations is reduced compared to a heat supply temperature of 150 °C due to the increased pressure. The set is constrained by T_H, COP and p_H.

It should be noted that the increased heat supply temperature attained by the use of the transcritical CO_2 components is only possible because of the increased tolerance on the compressor discharge temperature. As seen in Figs. 3.4 & 3.5 (c) & (d), a design that keeps the compressor discharge temperature below 170 °C is not possible. Hence, judging from Fig. 3.4, if the transcritical CO_2 compressor cannot be modified to

sustain these temperatures, these components cannot attain higher supply temperatures than the high pressure NH_3 components. Conversely it can be seen that if the standard refrigeration and high pressure NH_3 compressors are also modified to sustain 250 °C compressor discharge temperature and vapour ammonia mass fractions below 0.95, these can also attain heat supply temperatures up to 175 °C, although the set of feasible combinations of x_r and f is considerably smaller.

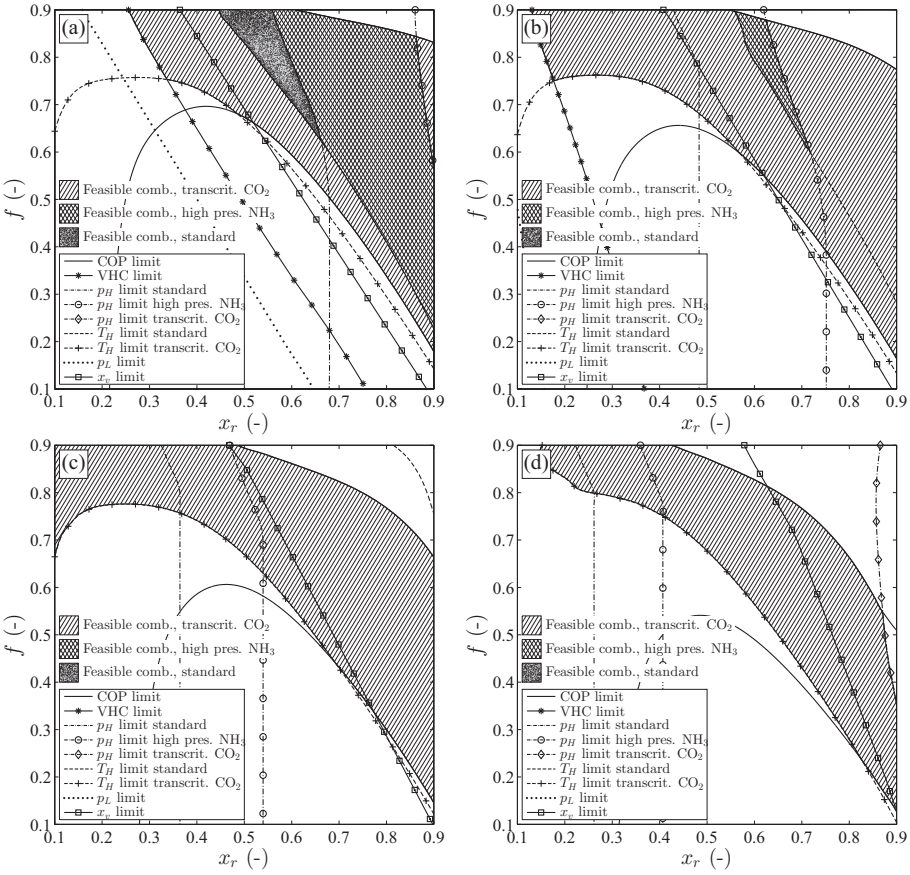

Figure 3.4: Feasible combinations of the circulation ratio, f, and the ammonia mass fraction, x_r, for standard, high pressure NH_3 and transcritical CO_2 components. Heat supply temperature (a): $T_{\text{sink,out}}$ = 100 °C, (b): $T_{\text{sink,out}}$ = 125 °C, (c):$T_{\text{sink,out}}$ = 150 °C, (d): $T_{\text{sink,out}}$ = 175 °C

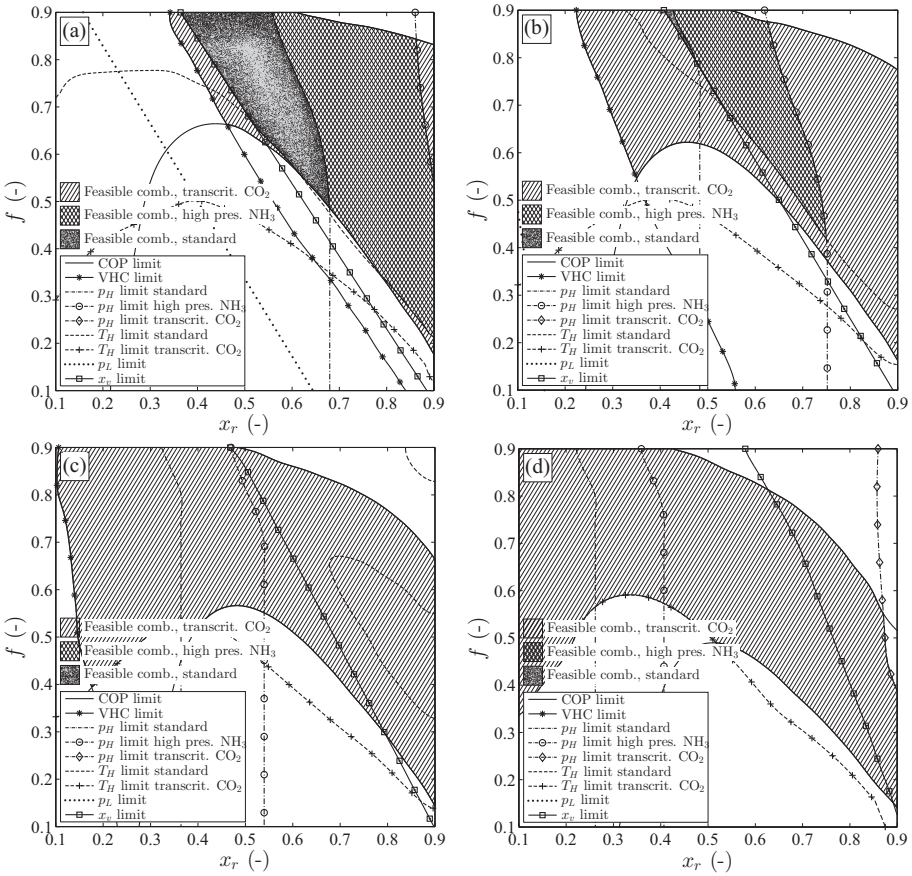

Figure 3.5: Feasible combinations of the circulation ratio, f, and the ammonia mass fraction, x_r, for standard, high pressure NH_3 and transcritical CO_2 components. Heat supply temperature (a): $T_{\text{sink,out}}$ = 100 °C, (b): $T_{\text{sink,out}}$ = 125 °C, (c):$T_{\text{sink,out}}$ = 150 °C, (d): $T_{\text{sink,out}}$ = 175 °C

3.3.3 Maximum heat supply temperature

To get a more detailed view of the temperature levels that can be achieved by the different components, the maximum heat supply temperature was derived. The maximum heat supply temperature was defined as the temperature level at which no combinations of x_r and f result in a feasible solution.

Fig. 3.6 shows the maximum heat supply temperature for the one-

stage HACHP (a) and two-stage HACHP (b). The maximum temperature is presented for all three component types with a compressor discharge temperature constraint of both $T_{H,\max}$ = 170 °C and $T_{H,\max}$ = 250 °C and with and without the vapour ammonia mass fraction constraint.

For the one-stage HACHP, with $T_{H,\max}$ = 170 °C and $x_{v,\min}$ = 0.95 a maximum heat supply temperature of 111 °C can be attained with 28 bar components, 129 °C with 50 bar components and 147 °C with 140 bar components. Using the two-stage HACHP this is increased to 126 °C 145 °C and 160 °C

Removing only the vapour ammonia mass fraction constraint does not lead to a further increase in attainable temperatures for the one-stage HACHP. For the two-stage HACHP the maximum temperature is increased by 8 °C for the standard components and 1 °C for the high pressure NH_3 components. No increase is observed for the transcritical CO_2 components.

Increasing $T_{H,\max}$ to 250 °C for the one-stage HACHP increases the maximum temperature by 16 °C for standard components, 20 °C for high pressure NH_3 and 40 °C for transcritical CO_2. For the two-stage HACHP, increasing $T_{H,\max}$ alone does not increase the maximum temperature for the standard refrigeration components. For the high pressure NH_3 components a slight increase of 4 °C is attained while the transcritical CO_2 components yield an increase of 27 °C.

As seen the largest increase in maximum heat supply temperature is attained when increasing $T_{H,\max}$ to 250 °C and simultaneously removing the vapour ammonia mass fraction constraint. This allows the one-stage HACHP to operate at heat supply temperature up to 182 °C, 193 °C and 223 °C for the respective pressure constraints. While, the two-stage HACHP allows 215 °C, 225 °C and 231 °C, respectively.

The use of high pressure NH_3 and transcritical CO_2 components with a compressor discharge temperature constraint of 170 °C could still be advantageous as the increased number of feasible solutions could lead to designs with higher efficiency or low investment cost or even both. To assess this, exergoeconomic analysis may be performed [19].

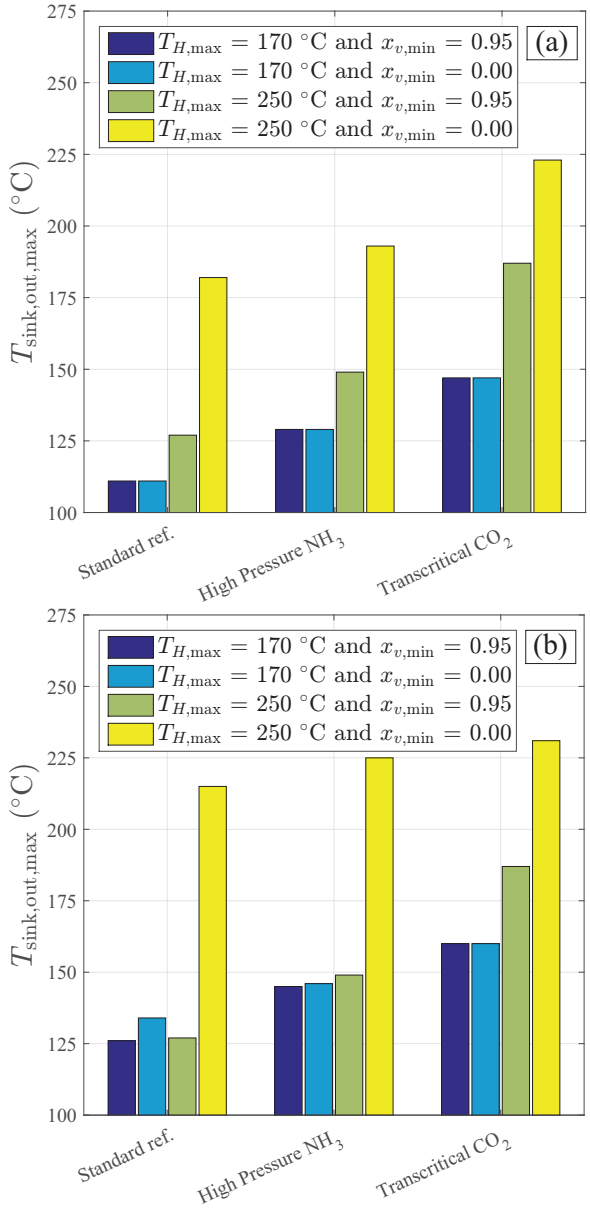

Figure 3.6: Maximum attainable heat supply temperature for the three investigated component types. Two maximum compressor discharge temperatures are imposed. Further, $T_{\mathrm{sink,out,max}}$ is presented with and without the vapour ammonia mass fraction constraint.

3.3.4 Sensitivity of the component performance parameters

The results presented above were all derived with constant component inputs to the thermodynamic model. The sensitivity of these assumed values on the constrained design parameters have been evaluated for the one-stage-HACHP at a heat supply temperature of $T_{\text{sink,out}}$ = 100 °C (Fig. 3.7) and $T_{\text{sink,out}}$ = 175 °C (Fig. 3.8), both with an ammonia mass fraction of x_r = 0.8 and a circulation ratio of f = 0.6. The sensitivity on the COP (a), VHC (b), high pressure, p_H, (c), low pressure (d), compressor discharge temperature, T_H, (e) and the vapour ammonia mass fraction, x_v, (f) is shown.

As seen the highest sensitivity on the COP is caused by the compressor electrical and isentropic efficiency. The assumed electrical efficiency of η_e = 0.9 should be attainable by most electrical motors, a reduction of 10% might happen over time thus leading to a reduction of COP of approximately 0.7. The isentropic efficiency, assumed at η_{is} = 0.75 would be significantly dependent on the applied compressor and its characteristics. A reduction of the isentropic efficiency up to 50% is not unlikely which leads to a significant reduction of COP by approximately 2. This should be avoided by choosing an appropriate compressor. The second highest influence is from the absorber and desorber pinch point temperature difference of which the absorber influence is slightly higher than that of the desorber for $T_{\text{sink,out}}$ = 175 °C while they are close to identical for $T_{\text{sink,out}}$ = 100 °C. The third highest influence is from the IHEX, it is seen that a reduction of the IHEX effectiveness of 50% results in a reduction of COP of approximately 1. The pump isentropic and electrical efficiency is seen to have a higher influence on the COP at $T_{\text{sink,out}}$ = 175 °C than at $T_{\text{sink,out}}$ = 100 °C. The gas cooler effectiveness is seen to have a minor influence on the COP at $T_{\text{sink,out}}$ = 175 °C while the influence at $T_{\text{sink,out}}$ = 100 °C is negligible.

The highest influence on the VHC is from the volumetric efficiency of the compressor, hence a reduction of the volumetric efficiency from the assumed η_{vol} = 0.90 causes a large decrease of the VHC. Reducing the compressor isentropic efficiency causes an increase in VHC, as a reduction of the isentropic efficiency causes less mass flow rate for the

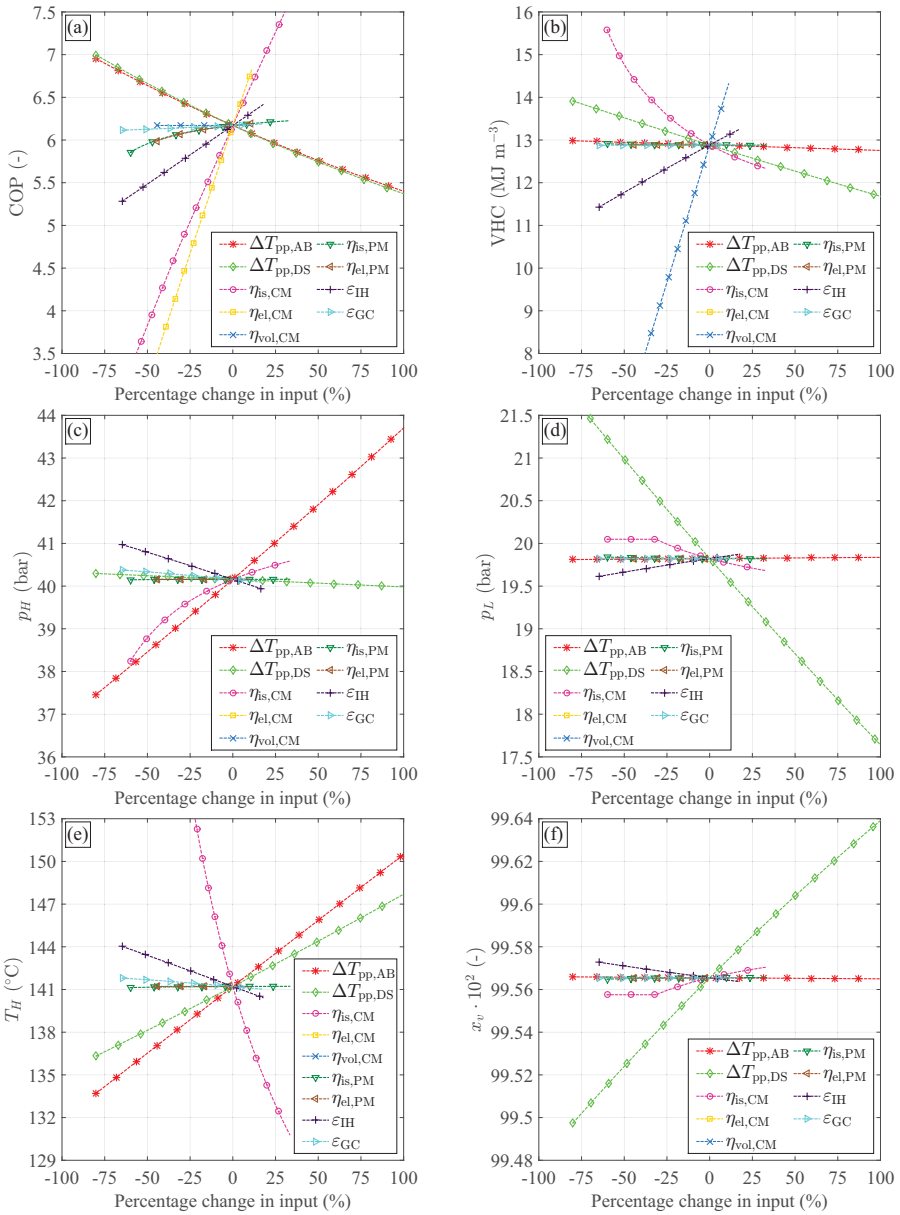

Figure 3.7: Sensitivity of the component inputs on the design constraints. (a): COP, (b): VHC, (c): p_H, (d): p_L, (e): T_H and (f): x_v. Heat supply temperature of: $T_{\text{sink,out}}$ = 100 °C, ammonia mass fraction of: x_r = 0.8 and circulation ratio of: f = 0.6

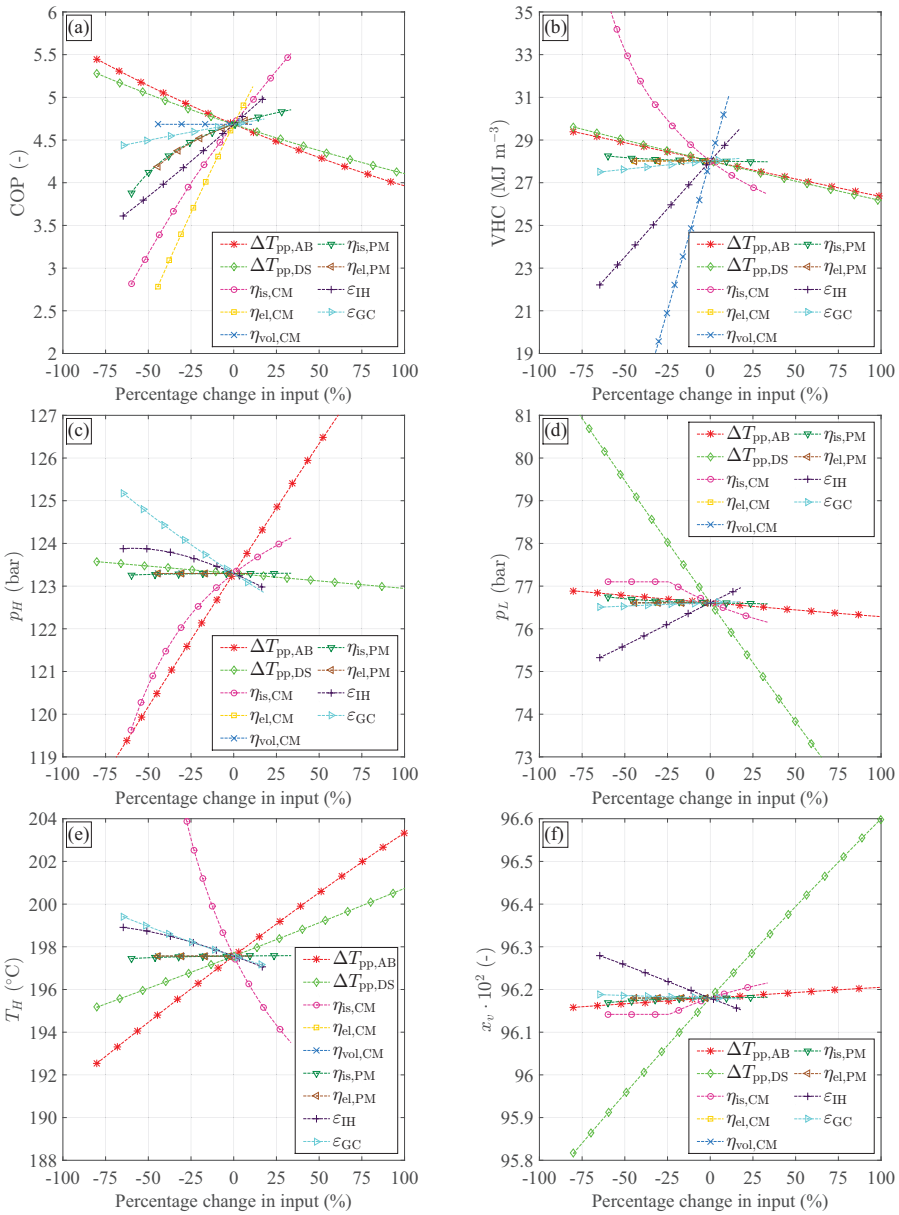

Figure 3.8: Sensitivity of the component inputs on the design constraints. (a): COP, (b): VHC, (c): p_H, (d): p_L, (e): T_H and (f): x_v. Heat supply temperature of: $T_{\text{sink,out}}$ = 175 °C, ammonia mass fraction of: x_r = 0.8 and circulation ratio of: f = 0.6

same heat output as the reduced isentropic efficiency increases the compressor discharge temperature. This, however causes a severe reduction of the COP. At $T_{\text{sink,out}}$ = 100 °C the VHC is positively influenced by a reduction of the desorber pinch point temperature difference, while it is almost insensitive to the absorber pinch point temperature difference at $T_{\text{sink,out}}$ = 175 °C. For $T_{\text{sink,out}}$ = 175 °C the VHC is almost equally influenced by the absorber and desorber pinch point temperature differences. A reduction of the IHEX effectiveness results in a decrease of the VHC, this influence is higher at $T_{\text{sink,out}}$ = 175 °C than at $T_{\text{sink,out}}$ = 100 °C. As for the COP the gas cooler effectiveness mainly influences the VHC at the high temperature. A reduction of ϵ_{GC} gives a reduction of the VHC. For both temperature levels the VHC is insensitive to a change in the pump isentropic and electrical efficiency.

The highest influence on the high pressure is from the absorber pinch point temperature difference while there is only a small influence from the desorber temperature difference. The second highest influence is from the compressor isentropic efficiency. A reduction of this leads to a reduction of the high pressure due to the increased compressor discharge temperature. This moves the pinch point further downstream in the heat exchanger resulting in the reduced pressure. A reduction of the IHEX effectiveness causes an increase in the needed high pressure for both $T_{\text{sink,out}}$ = 100 °C and $T_{\text{sink,out}}$ = 175 °C, while the gas cooler effectiveness mainly causes this behaviour for $T_{\text{sink,out}}$ = 175 °C.

As seen the main sensitivity on the low pressure stems from the desorber pinch point temperature difference. This is followed by the IHEX effectiveness which, especially for $T_{\text{sink,out}}$ = 175 °C has some effect on the low pressure. Further, the compressor isentropic efficiency has a minor influence on the low pressure. The low pressure is insensitive to the remaining inputs.

The compressor discharge temperature is mainly influenced by the isentropic efficiency. The second highest influence is from the absorber pinch point temperature difference followed by the desorber temperature difference. Both increase the compressor discharge temperature due the increased pressure ratio over the compressor. A reduction of the IHEX effectiveness causes an increased compressor discharge temperature for both $T_{\text{sink,out}}$ = 100 °C and $T_{\text{sink,out}}$ = 175 °C, while the gas

cooler effectiveness mainly causes this behaviour for $T_{sink,out}$ = 175 °C.

From Fig. 3.7 (f) and 3.8 (f) it is seen that the vapour ammonia mass fraction is generally insensitive to the variation of component inputs. The maximum variation of x_v is ±0.1% for $T_{sink,out}$ = 100 °C and ±0.4% for $T_{sink,out}$ = 175 °C. However, as seen from Fig. 3.1, x_v is close to constant for the point x_r = 0.8 and f = 0.6. Hence, the sensitivity may be larger for other combinations of x_r and f in which the x_v is less constant.

3.4 Discussion

Brunin et al.[23] evaluated the HACHP at rich ammonia mass fractions of 0.25, 0.35 and 0.45 and with a constant concentration difference of 0.10 between the rich and lean solution. This showed that heat supply temperatures up to 140 °C can be achieved with a high pressure constraint of 20 bar. This however does not include a constraint on the compressor discharge temperature. As shown in Chapter 2 the constant concentration difference may not always be the best choice to ensure the best performance. Ommen et al. [78] evaluated the HACHP at x_r of 0.7 and 0.9 and a constant source glide of 10 K. The high pressure constraint was 50 bar and the compressor discharge temperature constraint was 160 °C. Here the maximum supply temperature was found to be 125 °C. This is in good agreement with results of the present study.

From Figs. 3.4 & 3.5 it is seen that if the constraint on the compressor discharge temperature and vapour ammonia mass fraction are not considered, as done by Brunin et al. [23], supply temperatures of 182 °C are possible for standard equipment. This again proves the importance of evaluating all combinations x_r and f. It is shown that even when considering the compressor discharge temperature constraint the application of high pressure NH_3 and transcritical CO_2 components as well as an evaluation of all combinations of x_r and f, have expanded the HACHP working domains presented by Brunin et al. [23] and Ommen et al. [78] to cover heat supply temperatures up to 182 °C.

In general the compressor discharge temperature is shown to be the dominating constraint when assessing the HACHP applicability for high

temperature design. As shown implementing a two-stage compression does relax this constraint and increases the allowable heat supply temperature. Oil cooled compressors could be applied to reduce the compressor discharge temperature even further. Here it is important that the heat removed in the compressor cooler is utilized to heat either the lean solution or the heat sink, otherwise this will lead to a reduction of the COP despite of the reduced compressor work.

Nevertheless, the compressor discharge temperature will set the upper limit of the heat supply temperature. This can be concluded only from the second law as this dictates a positive temperature difference in the gas cooler and thus $T_H > T_{\text{sink,out}}$. Hence, if the constraint of 170 °C on the compressor discharge temperature cannot be increased then, the maximum heat supply temperature will never be higher than this.

The vapour ammonia mass fraction is also shown to influence the attainable temperatures, however to which extent the compression of a water-rich ammonia-water vapour poses a real issue for ammonia compressors is uncertain. From a thermodynamic perspective compression of such vapour is not an issue as long as a feasible COP and VHC are attained. Whether there exist material constraints that limit the allowable water content should be further investigated.

The vapour ammonia mass fraction could be increased by installing rectification in the suction line or by using a falling film desorber in which the desorbed vapour is in counter flow with the desorbing liquid, thereby reducing the vapour outlet temperature and consequently increasing the vapour ammonia mass fractions. However, both solutions will introduce irreversibilities to the system and will thus reduce the COP.

3.5 Conclusion

The presented results show that all constrained design parameters are highly influenced by the choice of rich ammonia mass fraction and circulation ratio. This emphasises the importance of finding a suitable combination. At circulation ratios below 0.5 and rich ammonia mass fractions between 0.2-0.8 a set of combinations induce a substantial in-

crease in pressure ratio. Consequently reducing the COP and increasing the compressor discharge temperature, designing the HACHP within this set of combinations is therefore not recommended.

Three sets of design constraints have been applied to the choice of rich ammonia mass fraction and circulation ratio. This shows that the one-stage HACHP using standard refrigeration components can attain heat supply temperatures of 111 °C with an unmodified compressor and 127 °C if the compressor is modified to sustain higher discharge temperatures. If the compressor is not constrained by the vapour ammonia mass fraction, temperatures of 182 °C can be attained. High pressure NH_3 components increase this to 129 °C, 149 °C and 193 °C. Heat supply temperatures of either 187 °C or 223 °C is possible using transcritical CO_2 components, depending on the allowable compressor discharge temperature. If the vapour ammonia mass fraction is constrained, as for the NH_3 compressors, the maximum heat supply temperature for the transcritical CO_2 components is reduced to 147 °C.

The two-stage HACHP using standard refrigeration components can attain heat supply temperatures of 126 °C with an unmodified compressor and 134 °C if the compressor is modified to sustain lower vapour ammonia mass fractions. If the compressor discharge temperature is simultaneously increased to 250 °C heat supply temperatures of 215 °C can be attained. High pressure NH_3 components increase this to 146 °C, 149 °C and 225 °C. Heat supply temperatures of either 187 °C or 231 °C is possible using transcritical CO_2 components, depending on the allowable compressor discharge temperature.

The dominating constraints when evaluating the maximum heat supply temperature are the high pressure, the compressor discharge temperature and the vapour ammonia mass fraction. If the attainable heat supply temperature of the HACHP is to be increased it is not sufficient to only increase allowable pressure, the allowable compressor discharge temperature and vapour ammonia mass fraction must also be increased.

The sensitivity analysis shows that the highest influence on the high pressure stems from the absorber pinch point temperature difference, while the highest influence on the compressor discharge temperature stems from the isentropic efficiency of the compressor. On the other hand vapour ammonia mass fraction is insensitive to the component

inputs.

CHAPTER 4

HEAT TRANSFER AND TRANSPORT PROPERTIES OF AMMONIA WATER MIXTURES

The work presented in this chapter regards the dimensioning of heat transfer equipment for ammonia-water systems. The work presented is related to that published in the International Journal of Thermophysics [57] ([P7]) and in Applied Thermal Engineering [56] ([P8]). Here, [57] provides an assessment of ammonia-water mixture transport property estimation methods and their influence on heat exchanger (HEX) size. While, [56] presents an estimation of in-tube flow boiling correlations and their influence on HEX size.

The focus of [57, 56] is the dimensioning of shell and tube type boilers for Kalina cycles, while the work presented here is related to the dimensioning of plate type absorbers and desorbers for the HACHP.

The plate HEX model presented in this chapter has been extended to evaluate the effect of liquid/vapour maldistribution. This was presented at the 24th IIR - International Congress of Refrigeration, August 16 - 22 2015, Yokohama, Japan [41] ([P18]). This study, so far, only includes pure fluids under evaporation but should be extended to include ammonia-water mixtures under both absorption and desorption in the future. A qualitative discussion on the effects under of liquid/vapour maldistribution on the performance ammonia-water plate absorbers and desorbers is included in the present chapter.

4.1 Introduction

The use of zeotropic mixture working fluids as a measure for increased energy efficiency of thermal energy conversion systems has been widely

investigated over the last decades. Systems such as the HACHP and the Kalina power cycle are among the systems that require zeotropic working fluids. In order to perform a dimensioning of such systems, the heat transfer and pressure drop characteristics of zeotropic mixtures must be evaluated. The evaluation of these processes are more complex than the single component processes as the transport properties change during the process due to the changing composition and due to the mass diffusion resistance of the volatile component in the region surrounding the liquid/vapour interface. Hence, to dimension heat transfer equipment for zeotropic mixture systems, correlations for mixture transport properties must be sought as well as heat transfer correlation that account for mass diffusion effects.

The focus in this chapter will be on evaluating correlations for the zeotropic mixture ammonia-water. Several transport property correlations will be compared and there application will be discussed. Further, heat transfer and pressure drop correlations for plate HEX with ammonia-water mixtures are presented.

A design parameter study of plate HEX desorbers and absorbers are presented, evaluating the influence of both the plate geometry and the ammonia-mass fraction.

4.1.1 Transport properties of ammonia-water mixtures

Transport properties such as viscosity and thermal conductivity are essential to the estimation of heat transfer coefficients and friction factors.

For pure fluids transport property correlations are readily available from sources such as Reid et al. [88], further many of these equations are already implemented in software such as EES [54] or RefProp [59].

Correlations for mixture transport properties are also presented by Reid et al. [88]. Of the presented correlations three methods have been evaluated for vapour viscosity. These are the Reichenberg, Wilke and Lucas correlations. Further, Fillipov's and Jamieson's correlations have been evaluated for the liquid thermal conductivity. For polar mixtures such as ammonia-water Reid et al. does not recommend any of the presented correlations for liquid viscosity and vapour thermal conductivity.

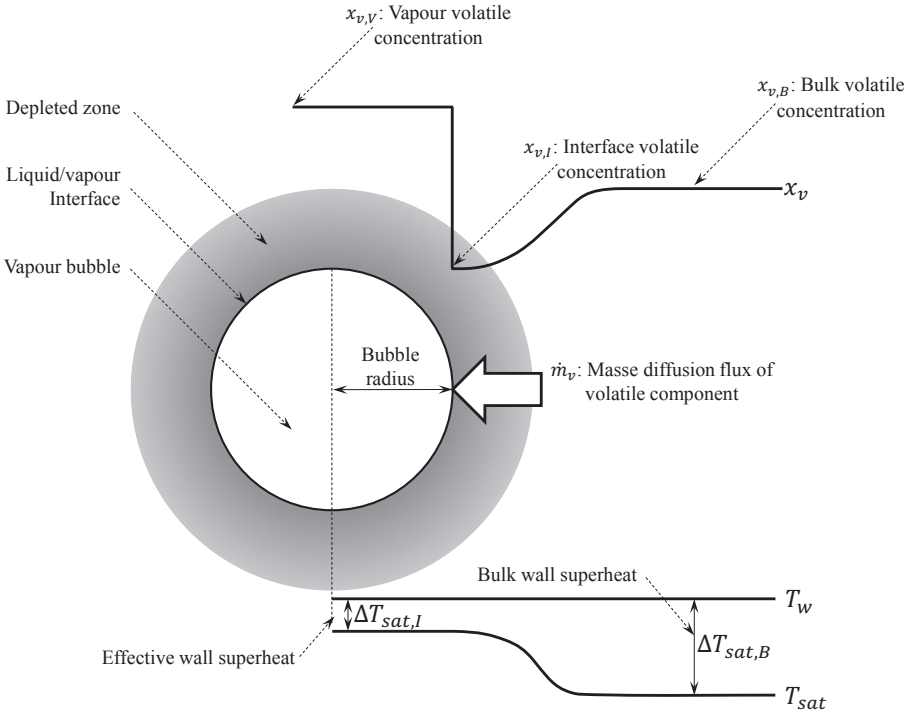

Figure 4.1: Bubble growth under evaporation of binary zeotropic mixture

Thorin [97] has conducted a review of existing methods for estimation of transport properties of ammonia-water mixtures. Here it is concluded that the correlation by El-Sayed [29] over all gives the best results for estimating heat transfer areas in power cycles. El-Sayed presents liquid and vapour correlations for both viscosity and thermal conductivity. M. Conde [3] has equally reviewed correlations for transport properties of ammonia-water and further presents new correlations for liquid viscosity and conductivity.

4.1.2 Nucleate boiling of zeotropic mixtures

Nucleate boiling phenomenon of zeotropic mixtures differs significantly from that of a single component fluid. The general consequence of the presence of a second component is the degradation of the heat transfer

coefficient. This is accounted to two properties related to the depletion of the volatile component in the region surrounding the liquid/vapour interface [87, 26].

This is depicted in Fig. 4.1. As the volatile component evaporates from the liquid/vapour interface the zone surrounding the bubble is depleted of the volatile component. Hence, the volatile component must diffuse from the bulk liquid through the depleted zone in order to evaporate. Depending on the mixture, mass diffusion resistance through the depleted zone can be profound and will inhibit the bubble growth rate and consequently heat transfer coefficients.

The reduced concentration of the volatile component in the depleted zone results in an increase of the local saturation temperature, see Fig. 4.1. Assuming a constant wall temperature, this reduces the effective wall superheat. Again leading to a reduction of the heat transfer coefficient.

4.1.3 Flow boiling in zeotropic mixtures

Forced convective flow boiling of zeotropic mixtures is described in detail by both Collier & Thome [26] and Radermacher & Hwang [87]. Again, it is evident from the presented studies that the heat transfer coefficient for mixtures suffers a degradation compared to the single component heat transfer coefficient.

For the low vapour qualities, nucleate boiling is dominant and the degradation can be accounted to the phenomenon described above. As the vapour quality is increased the contribution of evaporation from the liquid film becomes more dominant. When the liquid film thickness is sufficiently thin the nucleate boiling contribution is effectively suppressed. Due to the inhibited bubble growth rate in mixtures the suppression of nucleate boiling is found to occur at lower vapour qualities than for the corresponding pure components.

For the forced convective two-phase heat transfer, in which nucleate boiling is suppressed, there again exists simultaneous heat and mass transfer processes at the liquid/vapour interface. Here the interface is between the liquid film at the heated surface and the vapour core. Again the mass diffusion resistance causes a degradation of the heat transfer

coefficient.

According to several studies presented in Radermacher & Hwang [87] and Collier & Thome [26] the degradation of heat transfer coefficients due to mass diffusion resistance for some mixtures only accounted for 20% of the degradation while the remaining 80% was caused by an unfavourable change in transport properties.

4.2 Methodology

4.2.1 Transport properties of ammonia-water mixtures

As many of the correlations use mole fractions as opposed to mass fractions. Eq. (4.1) is used to convert between these. If x is the ammonia mass fraction then $y_{m,1}$ will be the corresponding ammonia mole fraction and $y_{m,2}$ the water mole fraction. $M_{w,1}$ and $M_{w,2}$ is the molar mass of ammonia and water, respectively.

$$y_{m,1} = \frac{x}{x + M_{w,1}\dfrac{1-x}{M_{w,2}}}, \quad y_{m,2} = \frac{1-x}{(1-x) + \dfrac{x \cdot M_{w,2}}{M_{w,1}}} \tag{4.1}$$

Some of the applied correlations uses reduced values of temperature, pressure etc. hence it is necessary to be able to evaluate the critical temperature and pressure of the mixture. This is done using Eqs. (4.2) and (4.3) [3].

$$T_{c,m} = 647.14 - 199.822371 \cdot y_{m,1} + 109.035522 \cdot y_{m,1}^2 - 239.626217 \cdot y_{m,1}^3 + 88.689691 \cdot y_{m,1}^4 \tag{4.2}$$

$$p_{c,m} = 220.64 - 37.923795 \cdot y_{m,1} + 36.424739 \cdot y_{m,1}^2 - 41.851897 \cdot y_{m,1}^3 - 63.805617 \cdot y_{m,1}^4 \tag{4.3}$$

Here $y_{m,1}$ is the ammonia mole fraction.

Four vapour viscosity correlations have been examined, these are those of Reichenberg, Wilke and Lucas, which are all presented in Reid et al. [88]. Further, a modified version of the Wilke correlation by El-Sayed [29] is included. The Reichenberg and Wilke correlations are both interpolative methods based on a simplification of the kinetic theory by Chapman & Enskog [88]. Both are applicable for low pressure vapour mixtures. The equations presented by Lucas are not interpolative and thus do not require the pure component viscosities to compute the viscosity of the mixture. These equations apply to both low and high pressure as they reduced directly to the low pressure equations when the pressure is reduced.

Three methods for determining liquid viscosities of ammonia-water mixtures have been investigated. These are those of El-Sayed [29], M. Conde [3] and one explicit correlation for ammonia-water published in Handbuch der Kältetechnik [85].

Four correlation have been identified for the estimation of liquid ammonia -water conductivity. These are El-Sayed [29], M. Conde [3], Jamieson [88] and Fillipov [88].

All the investigated transport property estimation methods are described in detail in Appendix A.

4.2.2 Heat transfer of ammonia-water mixtures

In the following section a method for calculating local two-phase heat transfer coefficients and friction factors for ammonia-water mixtures in plate HEX under both absorption and desorption is presented.

Table 4.1: Plate dimensions

L_p (mm)	L_{HT} (mm)	W (mm)	β (°)	Λ (mm)	b (mm)	t (mm)	λ_p (W/mK)
525	456	243	60	9.6	2.5	0.4	14.06

Most two-phase heat transfer correlations requires that the single phase coefficients are known. These are typically calculated as either the liquid only or vapour only heat transfer coefficients and are thus calculated assuming the HEX to be occupied entirely by the liquid or vapour

phase. Hence: to calculate the two-phase heat transfer coefficient in a plate HEX a single-phase plate HEX correlation must be applied.

Palm et al. [81] reviewed several single and two-phase heat transfer correlations for plate exchangers and suggested that Martin's [63] is used for single-phase heat transfer. Martin's correlation is a semi-empirical correlation based on a heat transfer to friction analogy. Martin's correlation is described in detail in Appendix B.1.

Desorption heat transfer of ammonia-water mixtures in plate HEX is investigated by Táboas et al. [96, 95, 94]. This work resulted in a correlation, which was applied in the present analysis. The correlation by Táboas et al. [96] uses a transition criterion to asses whether the desorption is dominated by apparent nucleate or convective flow boiling. The transition is based on an estimation of the superficial vapour and liquid velocities.

In the apparent nucleate boiling regime the correlation proposed by Táboas applies a modification of the saturated flow boiling correlation by Hseih and Lin [36].

For the convective flow boiling, Táboas et al. suggested the Margat et al. proposal [62], with a modified exponent for the Chisholm [24] two-phase multiplier. In the convective flow boiling regime Táboas et al. suggested to use the greater of the nucleate boiling heat transfer coefficient and convective flow boiling heat transfer coefficient.

A detailed description of the Táboas correlation is presented in Appendix B.2.

No correlation directly addresses the two-phase flow of ammonia-water in a plate HEX under absorption. Nordtvedt [74] suggested the use of the Silver/Bell-Ghaly method [90, 20]. This states that the effective two-phase heat transfer coefficient can be calculated as seen in Eq. (4.4).

$$\alpha_{\mathrm{TP,AB}} = \left(\frac{1}{\alpha_{\mathrm{lo}}} + \frac{Z}{\alpha_{\mathrm{vo}}} \right)^{-1} \tag{4.4}$$

Here α_{vo} is the vapour only heat transfer coefficient, in this case estimated by Martin's correlation [63]. α_{lo} is the heat transfer coefficient of the condensate layer corrected for two-phase flow effects. This is estimated using correlation proposed by Yan and Lin [106].

The factor Z in Eq. (4.4) is defined as seen in Eq. (4.5).

$$Z = qc_{p,\mathrm{v}}\frac{dT}{dh} \tag{4.5}$$

Here, q is the vapour mass fraction, $c_{p,\mathrm{v}}$ is the specific heat of the vapour phase and dT/dh is the gradient of the equilibrium absorption curve. The two-phase friction factor correlation by Yan and Lin [106] is applied to estimate the pressure drop.

A detailed description of the implementation of the Silver/Bell-Ghaly method for plate type absorbers is presented in Appendix B.3.

4.2.3 Working principal of plate heat exchangers

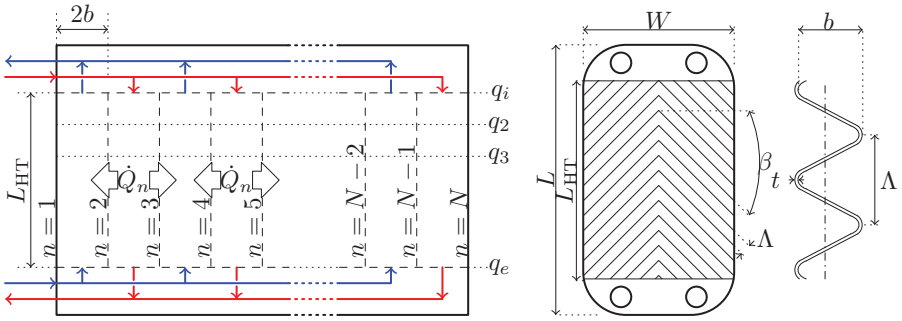

(a) Control volume sketch of plate heat exchanger model (b) Plate geometry

Figure 4.2: Principle of a plate heat exchanger

The working Principle of a plate HEX is depicted in Fig. 4.2. The channels in which the hot and cold fluid flows is created by the void that arises when pressing to corrugated plates against each other. The corrugation pattern may be seen in Fig. 4.2 (b). Every second plate is rotated 180°, thus creating a chequered pattern of channels. By alternating the gasket placement the flow of hot and cold fluid can be restricted to every second channel. A counter current arrangement is assumed.

The number of channels for the hot and cold fluid is thereby related to the number of plates the HEX is built up of: $N_{\mathrm{channel}} = N_{\mathrm{plates}} - 1$. If it is assumed that the first channel is a cold channel then the number of cold channels are: $N_{\mathrm{channel,cold}} = \mathrm{ceil}\left(\frac{1}{2}N_{\mathrm{channel}}\right)$ and the number of hot

are: $N_{\text{channel,hot}} = \text{floor}\left(\frac{1}{2}N_{\text{channel}}\right)$. Due to the end plates not all plates are active as heat transfer area between the two fluids, the number of heat transfer plates are: $N_{\text{HT}} = N_{\text{plates}} - 2$.

4.2.4 Dimensioning of plate heat exchangers

To calculate the actual heat transfer area of the corrugated plates the area enhancement factor ϕ is used, see Eq. (4.6) [63].

$$\phi = \frac{1}{6}\left(1 + \sqrt{1 + \frac{b\pi}{\Lambda^2}} + 4\sqrt{1 + \frac{b\pi}{2\Lambda^2}}\right) \tag{4.6}$$

As the plate size was given, the objective of the HEX dimensioning was to determine the number of plates, N, needed to attain a heat transfer area, A_{HT}, capable of transferring the required heat load, $\dot{Q}$. These parameters relate as seen in Eq. (4.7).

$$A_{\text{HT}} = N \cdot L_{\text{HT}} \cdot W \cdot \phi = \frac{U \cdot \Delta T_{\text{LM}}}{\dot{Q}} \tag{4.7}$$

Here U is the overall heat transfer coefficient of the HEX and ΔT_{LM} is the LMTD. L_{HT} is the length of the heat transfer section of the plate, W is the plate width and ϕ is the plate area enhancement factor calculated as suggested by [63] to account for the complex geometry of the channels.

The overall heat transfer coefficient was calculated as the inverse of the sum of the convective resistance of both streams and the conductive resistance through the plate, see Eq. (4.8).

$$U = \left(\frac{1}{\bar{\alpha}_1} + \frac{t}{\lambda} + \frac{1}{\bar{\alpha}_2}\right)^{-1} \tag{4.8}$$

Here, $\bar{\alpha}$ is the average heat transfer coefficient of the individual streams, t is the plate thickness and λ is the thermal conductivity of the plate.

The HEX pressure losses, Δp, were calculated as seen in Eq. (4.9).

$$\Delta p = \frac{2 \cdot \bar{\xi} \cdot G^2 \cdot v \cdot L_{\text{HT}}}{D_h} \tag{4.9}$$

Here G is the mass flux and D_h is the hydraulic channel diameter, set to $D_h = 2b\phi$ as suggested by [63]. Further, $\bar{\xi}$ is the average friction factor.

For the sink and source streams of the absorber and desorber and both streams in the internal HEX $\bar{\alpha}$ and $\bar{\xi}$ were evaluated at the mean temperature and pressure. This is a reasonable approach as the transport properties of the liquids only show a weak dependence on the pressure and temperature.

For the ammonia-water streams of the absorber and desorber this approach was not applicable as the ammonia mass fraction of the liquid and vapour phase changes through the HEX, which can lead to significant variations in the transport properties of the two phases. Further, α and ξ are strongly dependent on the vapour quality, q which also varies greatly during absorption and desorption. To account for these variations $\bar{\alpha}$ and $\bar{\xi}$ were determined based on a one-dimensional discretization in heat load and averaged as seen in Eqs. (4.10) and (4.11).

$$\bar{\alpha}_{\mathrm{tp}} = \left(\sum_{i=1}^{I} \alpha_{\mathrm{tp},i} \right) \cdot I^{-1} \tag{4.10}$$

$$\bar{\xi}_{\mathrm{tp}} = \left(\sum_{i=1}^{I} \xi_{\mathrm{tp},i} \right) \cdot I^{-1} \tag{4.11}$$

Here $\alpha_{\mathrm{tp},i}$ and $\xi_{\mathrm{tp},i}$ are the two-phase heat transfer coefficient and friction factor for the i^{th} cell, calculated based on the cell averages of: vapour quality, temperature, pressure and liquid and vapour ammonia mass fraction.

For the absorber and desorber the LMTD could not be directly applied as enthalpy and temperature are not proportional during absorption and desorption [40, 107]. To account for this an average LMTD was defined as seen in Eq (4.12).

$$\Delta\bar{T}_{\mathrm{LM}} = \dot{Q} \left(\sum_{i=1}^{I} \frac{\dot{Q}}{I} \cdot \frac{1}{\Delta T_{\mathrm{LM},i}} \right)^{-1} \tag{4.12}$$

Here $\Delta T_{\mathrm{LM},i}$ is the logarithmic mean temperature difference of the i^{th} cell calculated by the same discretization as applied in the heat transfer correlation.

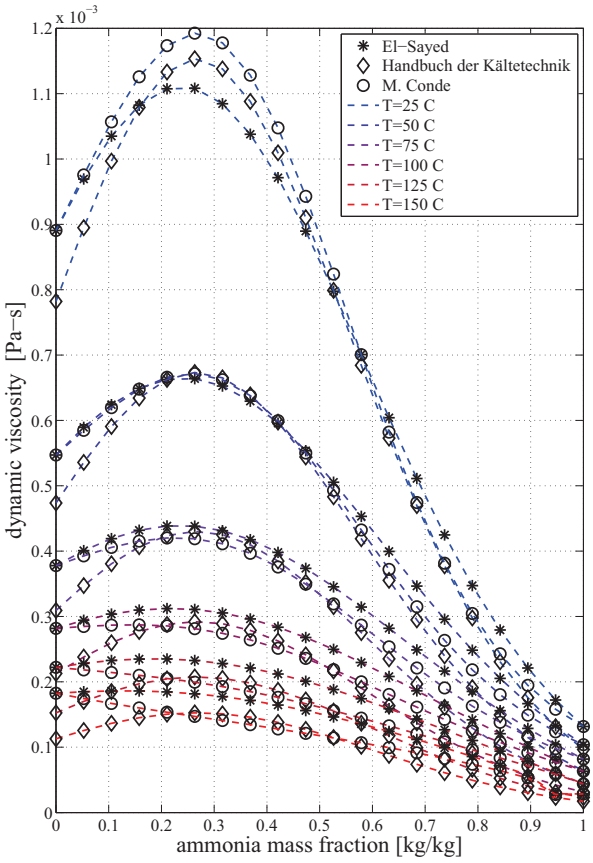

Figure 4.3: Comparison of dynamic viscosity of liquid ammonia water mixtures of varying temperatures with El-Sayed, Handbuch der Kältetechnik and M. Conde.

4.3 Results

4.3.1 Transport properties

Viscosity

Figs. 4.3 & 4.4 shows a comparison of the presented viscosity correlations for liquid (Fig. 4.3) and vapour (Fig. 4.4). The comparison is performed at varying pressure, temperature and ammonia mass fraction.

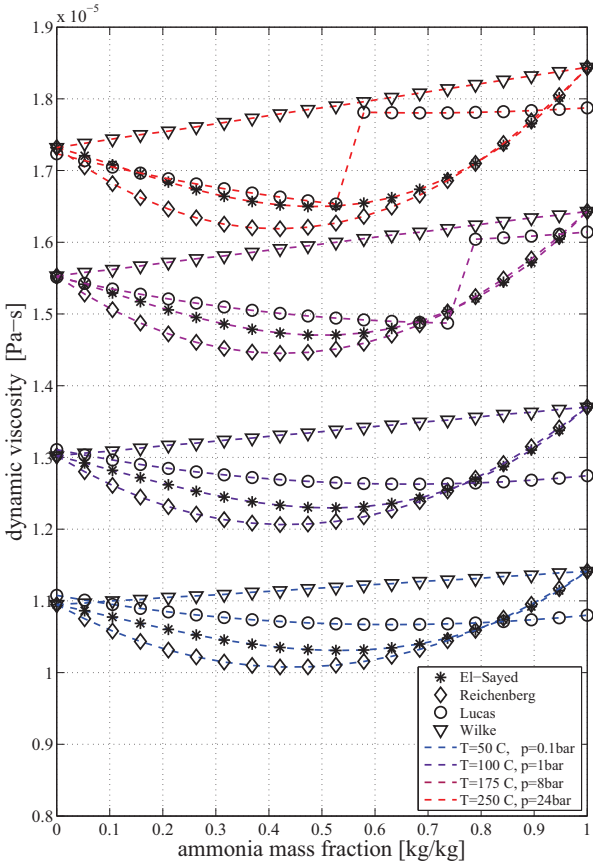

Figure 4.4: Comparison of dynamic viscosity of vapour ammonia water mixtures of varying temperatures and pressures with El-Sayed, Reichenberg and Lucas

From Fig. 4.3 it is seen that the viscosity decreases as the temperature is increased. Further, it is seen that the pure ammonia viscosity is always lower than the pure water viscosity. More importantly it can be seen that for the low temperatures, the viscosity of the mixture tends to be higher than the weighted average of the pure component viscosities with a maximum value around an ammonia mass fraction of $x = 0.25$. It is seen that the correlations by El-Sayed and Handbuch der Kältetechnik replicate this trend even at the high temperatures while the M. Conde correlation exhibits a close to linear relation with the ammonia mass

fraction at high temperatures. According to M. Conde this is in better agreement with experimental data than the trend exhibited by the two other correlations.

Fig. 4.4 shows that vapour viscosity increases with increasing pressure and temperature. It is seen that the deviation between the four correlations increase with increasing pressure and temperature. It is seen that the application of the Wilke correlation gives a close to linear interpolation of the pure component viscosities. This trend is not exhibited by El-Sayed, Reichenberg or Lucas. It is seen that El-Sayed and Reichenberg are in good agreement for the high ammonia mass fractions but tend to deviate at ammonia mass fraction below $x = 0.7$. The Lucas correlations is closest to the El-Sayed and Reichenberg correlations for the low ammonia mass fractions but as seen the Lucas correlation tends to under estimate the pure ammonia viscosity which leads to a larger deviation in the high ammonia mass fraction range. It is also seen that the Lucas correlation exhibits a discontinuity for the high pressure and temperature, this is caused by the change from the low pressure correlation to the high pressure correlation.

Conductivity

Figs. 4.5 & 4.6 shows the thermal conductivity of ammonia-water mixtures at varying composition, pressure and temperature. Fig. 4.5 is for the liquid phase while Fig. 4.6 is for the vapour phase.

From Fig. 4.6 is it seen that the method prosed by El-Sayed effectively gives a linear interpolation between the pure component viscosities.

From Fig. 4.5 it is clear that the pure ammonia conductivity is more sensitive to an increase in temperature. This yields the increased change in mixture conductivity at the higher temperatures. Further, it can be noted that the Jamieson and Fillipov correlations are in close agreement always yielding a value lower than the linear interpolation suggested by El-Sayed. The M. Conde correlation gives values lower than El-Sayed for the low ammonia mass fractions while giving a value higher than El-Sayed for the high ammonia mass fractions.

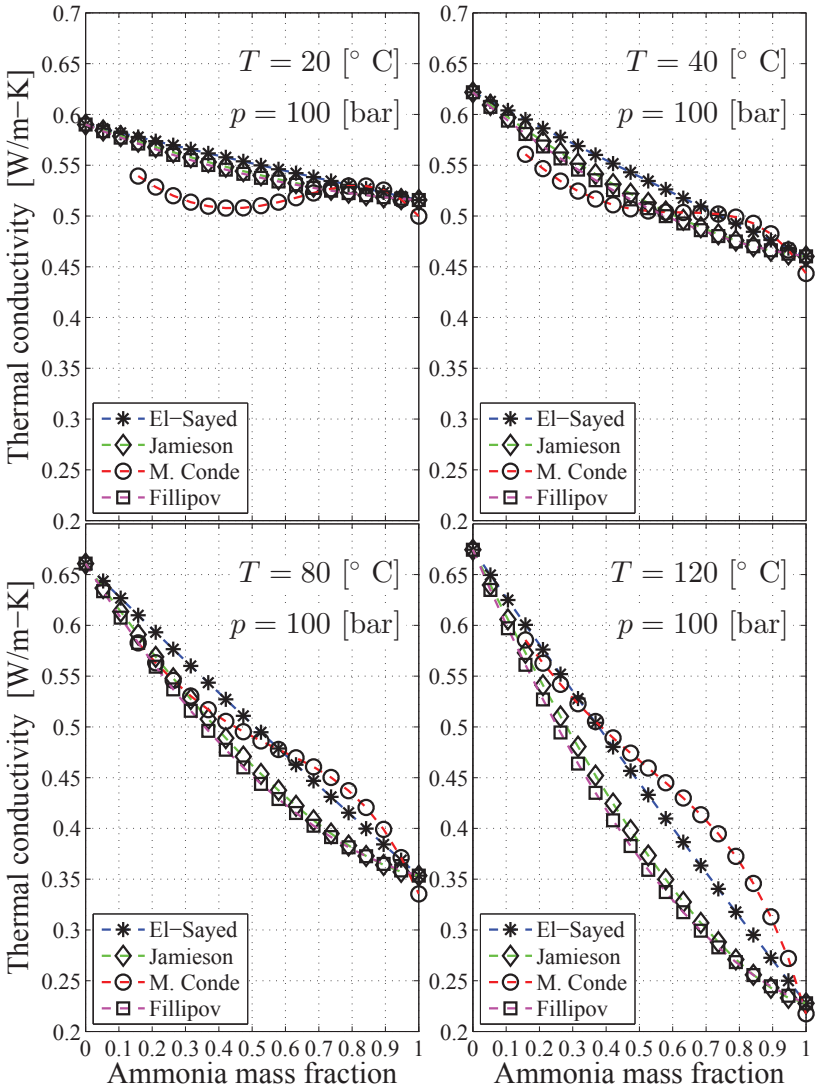

Figure 4.5: Conductivity of liquid ammonia water mixtures of varying temperatures with El-Sayed, Jamieson, M. Conde and Fillipov

4.3.2 Local heat transfer coefficients and friction factors

In the following local heat transfer coefficients and friction factors are calculated at varying quality, pressure and mass flux. For the liquid-

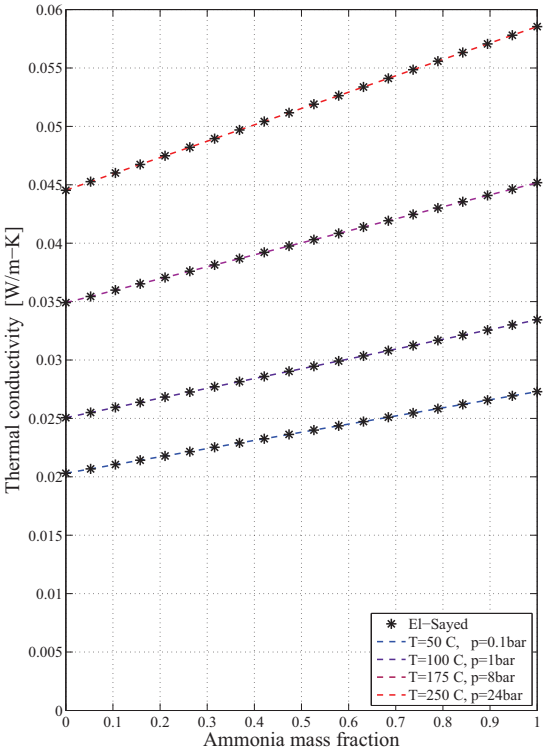

Figure 4.6: Conductivity of vapour ammonia water mixtures of varying temperatures and pressures with El-Sayed

phase transport properties: M. Conde is applied for viscosity and El-Sayed is applied for thermal conductivity. For the vapour-phase transport properties: Wilke is applied for viscosity while El-Sayed is applied for thermal conductivity. A plate with the dimensions listed in Table 4.1 is used for the following calculations.

Desorption

Fig. 4.7 shows the variation in the two-phase heat transfer coefficients and friction factor as a function of the local vapour quality. Fig. 4.7 (a) and 4.7 (b) show this for a pressure of 5 bar while Fig. 4.7 (c) and 4.7 (d) shows the same for a pressure of 25 bar. Ammonia mass fractions from 0.1 to 0.9 are depicted. The friction factor displayed here is the product

of the liquid only friction factor and the two-phase multiplier F and should thus be used in Eq. (B.6) with the density of liquid. Therefore, the friction factor presented here seems high in comparison with other friction factors. A constant mass and heat flux of $G = 100$ kg/m^2-s and $q'' = 20$ kW/m^2 are used.

For the pressure of 5 bar it is clear that the local heat transfer coefficient increases with vapour quality. Further it is seen that the local heat transfer coefficient decreases with increasing ammonia mass fraction upto $x = 0.8$. At $x = 0.9$ it is seen that the heat transfer coefficients at the low vapour qualities are higher than that of $x = 0.8$. From Fig. 4.7 (b) it is clear that the friction factor also increases with vapour quality while there is only little influence accounted to the ammonia mass fraction.

For a pressure of 25 bar, Fig. 4.7 (c), it is seen that the heat transfer coefficient peaks at a vapour quality between $q = 0.3$ and $q = 0.5$ dependent on the ammonia mass fraction. This is caused by the transition from nucleate boiling to forced convective boiling. As the pressure is increased the density is increased and the flow velocity becomes lower for the same mass flux. Hence: for the low vapour quality the heat transfer is dominated by apparent nucleate boiling. Again it is seen that the heat transfer coefficient decreases with increasing ammonia mass fraction upto $x = 0.8$. It is seen from Fig. 4.7 (d) that the friction factor again is not influenced by ammonia mass fraction.

Fig. 4.8 shows the influence of the mass flux on the heat transfer coefficient and the friction factor. Fig. 4.8 (a) and 4.8 (b) show this for a pressure of 5 bar while Fig. 4.8 (c) and 4.8 (d) is for a pressure of 25 bar. The heat flux and ammonia mass fraction are kept constant at $q'' = 20$ kW/m^2 and $x = 0.5$. The mass flux is varied from $G = 25$ kg/m^2-s to $G = 225$ kg/m^2-s in increments of 25 kg/m^2-s.

From Fig. 4.8 (a) and 4.8 (c) it is seen that heat transfer coefficient is greatly influenced by mass flux. Increasing mass flux increases heat transfer coefficients. Again it is seen that for the low mass fluxes a transition from nucleate to flow boiling occurs.

From Fig. 4.8 (b) and 4.8 (d) it is seen that the friction factor is also influenced by the variation in mass flux such that an increasing mass flux decreases the friction factor. By examining Eq. (B.6) it is seen that the mass flux it self influences the pressure drop an therefore: although

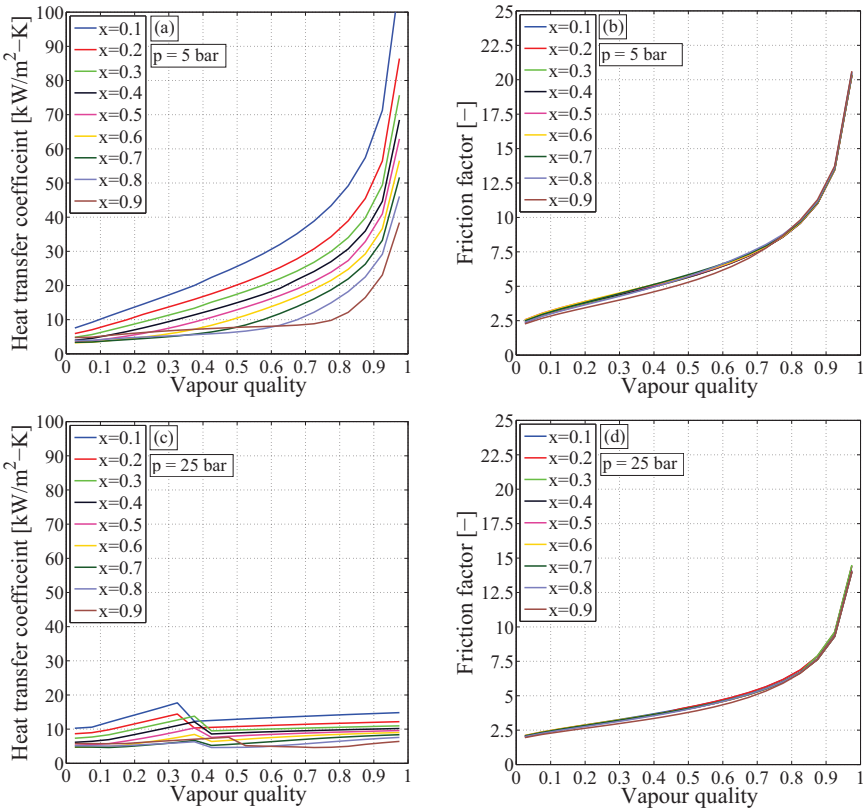

Figure 4.7: Desorption heat transfer and friction factors as a function of vapour quality at a range of ammonia mass fractions. (a) & (b) p = 5 bar (c) & (d) p = 25 bar. The mass and heat flux are kept constant at values of, G = 100 kg/m^2-s and q'' = 20 kW/m^2 are used.

the friction factor decreases with mass flux the pressure drop will still increases with mass flux.

Fig. 4.9 shows the influence of the heat flux on the heat transfer and pressure drop coefficient. Fig. 4.9 (a) and 4.9 (b) show this for a pressure of 5 bar while Fig. 4.9 (c) and 4.9 (d) is for a pressure of 25 bar. The mass flux and ammonia mass fraction are kept constant at G = 100 kg/m^2-s and x = 0.5. The heat flux is varied from q'' = 10 kW/m^2 to q'' = 90 kW/m^2 in increments of 10 kW/m^2.

From Fig. 4.9 (a) and 4.9 (c) it is seen that heat transfer coefficient

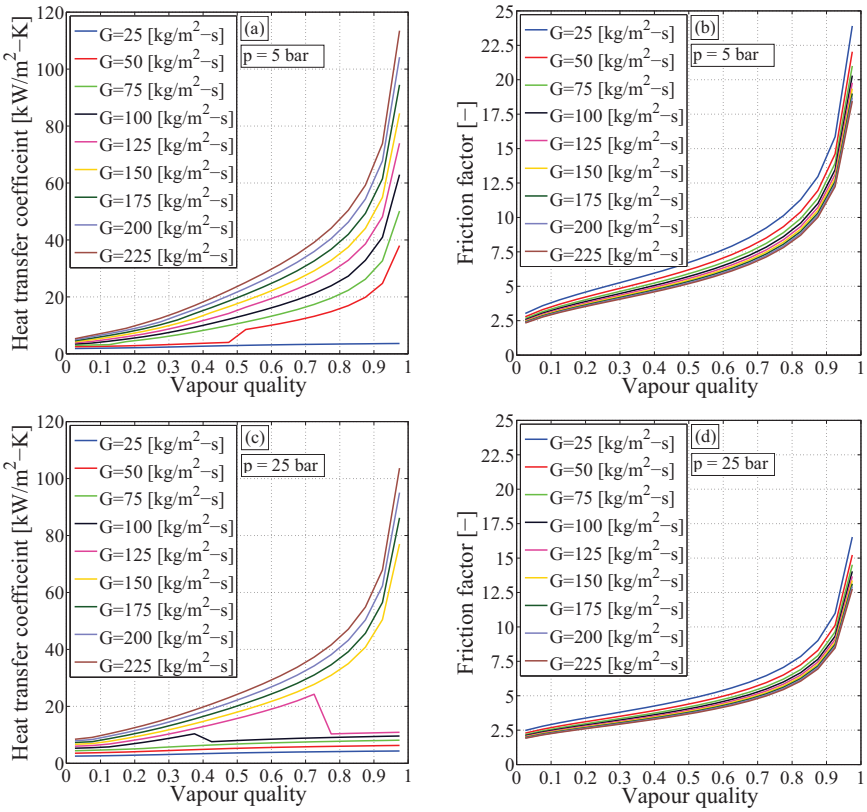

Figure 4.8: Desorption heat transfer and friction factors as a function of vapour quality at a range of mass fluxes. (a) & (b) p = 5 bar (c) & (d) p = 25 bar. The heat flux and ammonia mass fraction are kept constant at values of, q'' = 20 kW/m^2 and x = 0.5.

is only influenced by the heat flux at the high pressure. Again this is cause by the reduced flow velocity at the high pressure meaning the heat transfer is dominated by nucleate boiling.

From Fig. 4.9 (b) and 4.9 (d) it is seen that the friction factor is not influenced by the variation in heat flux while it exhibits the same trends as seen above: the friction factor increases with increasing vapour quality.

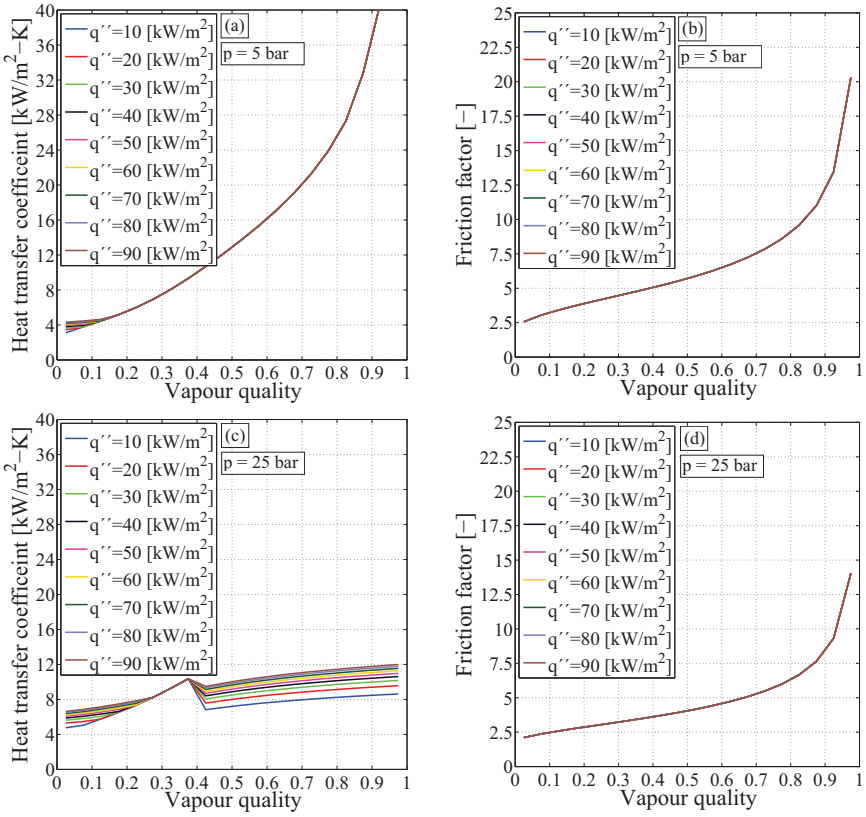

Figure 4.9: Desorption heat transfer and friction factors as a function of vapour quality at a range of heat fluxes. (a) & (b) p = 5 bar (c) & (d) p = 25 bar. The mass flux and ammonia mass fraction are kept constant at values of, G = 100 kg/m^2-s and x = 0.5.

Absorption

Fig. 4.10 shows the variation in the two-phase heat transfer coefficients and friction factor as a function of the local vapour quality. Fig. 4.10 (a) and 4.10 (b) show this for a pressure of 25 bar while Fig. 4.10 (c) and 4.10 (d) shows the same for a pressure of 75 bar. Ammonia mass fractions from 0.1 to 0.9 are depicted. A constant mass and heat flux of G = 100 kg/m^2-s and q'' = 20 kW/m^2 are assumed.

For the pressure of 25 bar it is seen that: for ammonia mass fractions

from $x = 0.1$ to $x = 0.7$ the heat transfer coefficient first decreases slightly with increasing vapour quality but subsequently increases with vapour quality. For the ammonia mass fractions above $x = 0.7$ the heat transfer coefficient first increases with vapour quality and then descends for the high vapour quality. It is seen that at high vapour quality the local heat transfer coefficient decreases with increasing ammonia mass fraction. At low vapour quality the local heat transfer coefficient has a minimum around an ammonia mass fraction of $x = 0.5$.

From Fig. 4.10 (b) it is clear that the friction factor increases with ammonia mass fraction. For the low ammonia mass faction the friction factor is only slightly influenced by vapour quality with a decreasing trend. For the high ammonia mass fraction the friction factor decreases with increasing vapour quality.

From Fig. 4.10 (a) and 4.10 (c), it is seen that the heat transfer coefficient exhibits the same trend for vapour quality and ammonia mass fraction for both the low and high pressure. It should be noted that the heat transfer coefficient is slightly lower for the high pressure.

Fig. 4.11 shows the influence of the mass flux on the heat transfer coefficient and friction factor. Fig. 4.11 (a) and 4.11 (b) show this for a pressure of 25 bar while Fig. 4.11 (c) and 4.11 (d) is for a pressure of 75 bar. The heat flux and ammonia mass fraction are kept constant at $q'' = 20$ kW/m^2 and $x = 0.5$. The mass flux is varied from $G = 25$ kg/m^2-s to $G = 225$ kg/m^2-s in increments of 25 kg/m^2-s.

From Fig. 4.11 (a) and 4.11 (c) it is seen that heat transfer coefficient is greatly influenced by mass flux. Increasing mass flux increases heat transfer coefficients.

From Fig. 4.11 (b) and 4.11 (d) it is seen that the friction factor is also influenced by the variation in mass flux such that an increasing mass flux decreases the friction factor.

Fig. 4.12 shows the influence of the heat flux on the heat transfer coefficient and friction factor. Fig. 4.12 (a) and 4.12 (b) show this for a pressure of 25 bar while Fig. 4.12 (c) and 4.12 (d) is for a pressure of 75 bar. The mass flux and ammonia mass fraction are kept constant at $G = 100$ kg/m^2-s and $x = 0.5$. The heat flux is varied from $q'' = 10$ kW/m^2 to $q'' = 90$ kW/m^2 in increments of 10 kW/m^2.

From Fig. 4.12 (a) and 4.12 (c) it is seen that heat transfer coefficient

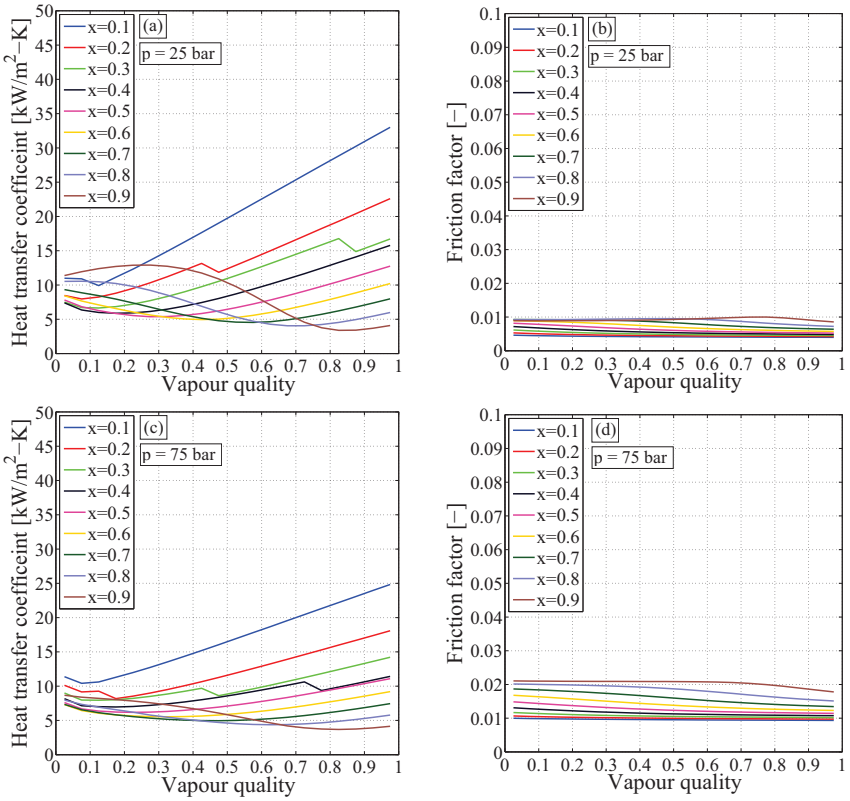

Figure 4.10: Absorption heat transfer and friction factors as a function of vapour quality at a range of ammonia mass fraction. (a) & (b) p = 25 bar (c) & (d) p = 75 bar. The mass and heat flux are kept constant at values of, G = 100 kg/m^2-s and q'' = 20 kW/m^{2}s.

is not influenced by the heat flux.

From Fig. 4.12 (b) and 4.12 (d) it seen that the friction factor is influenced by the variation in heat flux. This because the friction factor in Yan and Lin is correlated to the boiling number. Further it is seen that the friction factor exhibits the same trends as seen Fig. 4.10 and 4.11.

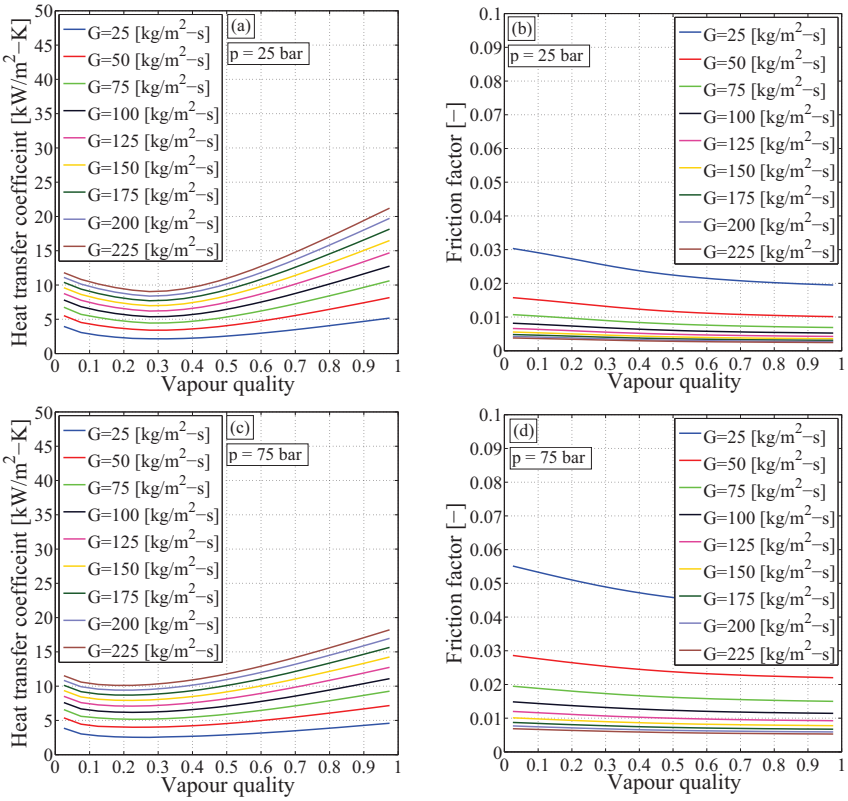

Figure 4.11: Absorption heat transfer and friction factors as a function of vapour quality at a range of mass fluxes. (a) & (b) p = 25 bar (c) & (d) p = 75 bar. The heat flux and ammonia mass fraction are kept constant at values of, q'' = 20 kW/m^2 and x = 0.5.

4.3.3 Heat exchanger dimensioning

In the following section the complete dimensioning process of a plate HEX absorber and desorber is presented using the described transport property, heat transfer coefficient and pressure drop correlations. The total heat transfer area is calculated for a heat load of $\dot{Q}$ = 1000 kW and ammonia mass fractions of x = 0.7, x = 0.8 and x = 0.9. The influence of the plate geometry is investigated. The secondary stream in both the absorber and desorber is assumed to water.

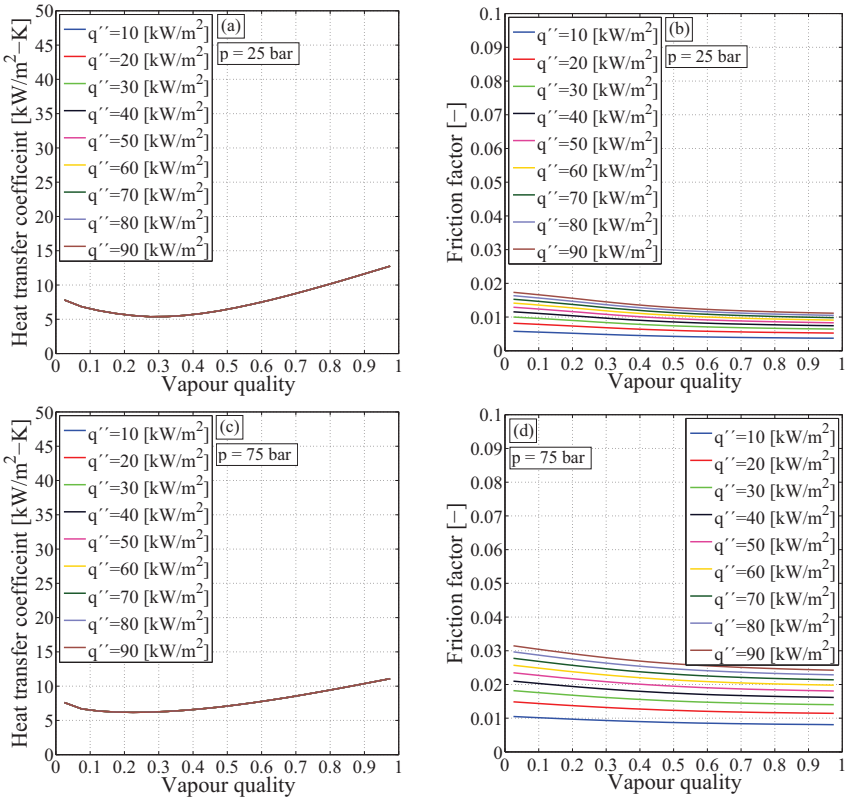

Figure 4.12: Absorption heat transfer and friction factors as a function of vapour quality at a range of mass fluxes. (a) & (b) p = 25 bar (c) & (d) p = 75 bar. The mass flux and ammonia mass fraction are kept constant at values of, G = 100 kg/m^2-s and x = 0.5.

Absorber

For the absorber an inlet vapour quality of q = 0.6 and an outlet vapour quality of q = 0.0 is assumed. The heated secondary stream of water is heated from T = 60 °C to T = 80 °C corresponding to a mass flow rate of $\dot{m}$ = 11.9 kg/s to match the desired heat load of $\dot{Q}$ = 1000 kW. The pressure of the ammonia-water stream is chosen to yield an average LMTD of $\Delta\overline{T}_{\mathrm{LM}}$ = 10 K.

The plate dimensions listed in Table 4.1 is the basis of the investigation, but in the following some of the parameters will be varied indi-

vidually to investigate the influence on the total heat transfer area and the pressure drop. These investigated parameters are: the plate press depth b, the plate corrugation angle β, the corrugation spacing Λ and the plate size. The influence of the plate size in performed by assuming a constant length to width ratio and then scaling the size of the plate accordingly.

Fig. 4.13 shows the results of these investigations. Fig. 4.13 (a) shows the influence of the plate size on the total heat transfer area and the pressure drop in the ammonia-water stream. As seen, the total heat transfer area needed increases with decreasing ammonia mass fraction. It is seen that the heat transfer area increases close to linearly as a function of the plate size factor and the slope increases with decreasing ammonia mass fraction. Conversely, the pressure drop decreases with increasing plate size, the pressure drop decreases rapidly from plate size factors of 0.5 to 1.1 hereafter it tends to converge towards a negligible pressure loss. It is seen that the pressure loss decreases with decreasing ammonia mass fraction.

Fig. 4.13 (b) shows the variation of the heat transfer area and pressure drop as a function of the plate press depth. For both the heat transfer area and pressure drop the same trend as for the plate size is seen. It is clear that the area is not as greatly influenced by the press depth as the plate size while the opposite is observed for the pressure drop

Fig. 4.13 (c) shows the variation of heat transfer area and pressure drop as a function of the plate corrugation angle. Here it is seen that the heat transfer area increases with increasing corrugation angle. The area increases rapidly for the high corrugations angles. The pressure drop decreases close to linearly as a function of the corrugation angle. Again it is seen that the lower the ammonia mass fraction the higher the heat transfer area and lower the pressure drop.

Fig. 4.13 (d) shows the variation of heat transfer area and pressure drop as a function of the plate corrugation spacing. Here it is seen that the heat transfer area increases with increasing spacing. At a spacing of $\Lambda = 10.5$ mm the area starts converging against a maximum. Again the trend for the pressure is the opposite and thus decreases with increased spacing.

Over all it is seen from Fig. 4.13 that the heat transfer area is mainly

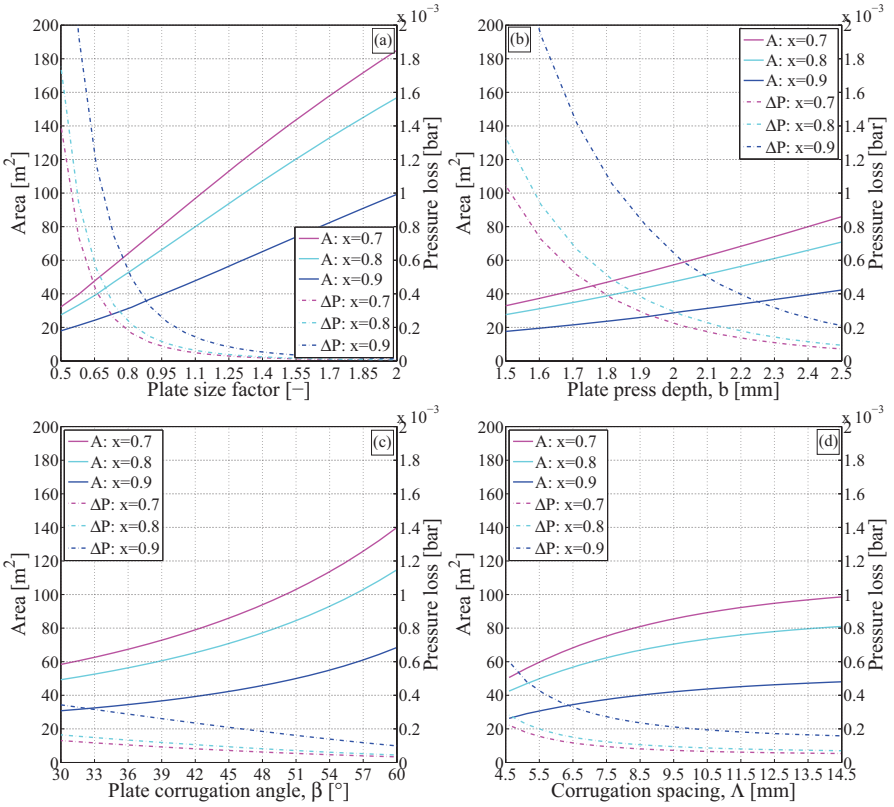

Figure 4.13: Total absorber heat transfer area and ammonia-water stream pressure drop as a function of plate size (a), plate press depth (b), plate corrugation angle (c) and plate corrugation spacing (d).

influenced by the plate size and plate corrugation angle, while the pressure drop is most influenced by plate size and press depth. A high ammonia mass fraction is always preferable in terms of heat transfer area but it should be noted the difference between $x = 0.9$ and $x = 0.8$ is greater than that between $x = 0.8$ and $x = 0.7$.

Desorber

For the desorber a constant inlet vapour quality of $q = 0.2$ is assumed while the outlet vapour quality is specific to the ammonia mass fraction, these are $q = 0.5$, $q = 0.6$ and $q = 0.7$ for $x = 0.7$, $x = 0.8$ and $x = 0.9$

respectively. This is needed in order to attain a constant average LMTD. The cooled secondary stream of water is cooled from T = 50 °C to T = 30 °C corresponding to a mass flow rate of $\dot{m}$ = 11.9 kg/s to match the desired heat load of $\dot{Q}$ = 1000 kW. The pressure of the ammonia water stream is chosen to yield an average LMTD $\Delta\overline{T}_{\mathrm{LM}}$ = 10 K. Again the plate dimensions in Table 4.1 is the bases of the investigation. The same parameters as for the absorber design is studied.

Fig. 4.14 shows the results of the parameter variations for the desorber design. Fig. 4.14 (a) shows the influence of the plate size on the total heat transfer area and the pressure drop in the ammonia-water stream. As seen the total heat transfer area needed increases with decreasing ammonia mass fraction. It is seen that the heat transfer area increases as a function of the plate size factor. The slope of the increase is uninfluenced by ammonia mass fraction. Conversely, the pressure drop decreases with increasing plate size, the pressure drop decreases rapidly from plate size factors of 0.5 to 1.1, hereafter it tends to converge towards a negligible pressure loss. It is seen that the pressure loss decreases with decreasing ammonia mass fraction.

Fig. 4.14 (b) shows the variation of heat transfer area and pressure drop as a function of the plate press depth. For both the heat transfer area and pressure drop the same trend as for the plate size is seen. Though it is clear that the area is not as greatly influenced by the press depth as the plate size while the opposite is seen for the pressure drop.

Fig. 4.14 (c) shows the variation in heat transfer area and pressure drop as a function of the plate corrugation angle. Here it is seen that the heat transfer area increases with increasing corrugation angle. The area increase is larger for the high corrugations angles. The pressure drop decreases as a function of the corrugation angle. Again it is seen that the lower the ammonia mass fraction the higher the heat transfer area and the lower the pressure drop.

Fig. 4.14 (d) shows the variation in heat transfer area and pressure drop as a function of the plate corrugation spacing. Here it is seen that the heat transfer area increases with increasing spacing. As for the absorber the area starts to converge against maximum at a spacing of Λ = 10.5 mm. Again the trend for the pressure is the opposite and thus decreases with increased spacing.

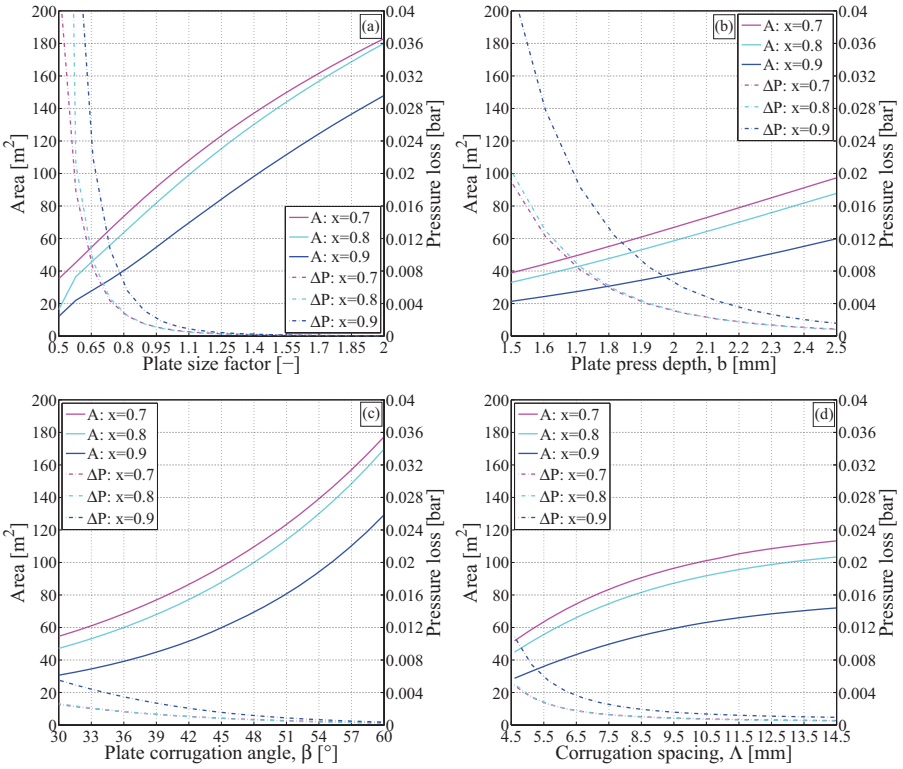

Figure 4.14: Total desorber heat transfer area and ammonia-water stream pressure drop as a function of plate size (a), plate press depth (b), plate corrugation angle (c) and plate corrugation spacing (d).

The over all conclusion from Fig. 4.14 is fairly similar to those of the absorber design. The heat transfer area is mainly influenced by the plate size and plate corrugation angle, while the pressure drop is most influenced by plate size and press depth. A high ammonia mass fraction is always preferable in terms of heat transfer area but as for the absorber the difference between $x = 0.9$ and $x = 0.8$ is greater than that between $x = 0.8$ and $x = 0.7$.

4.4 Discussion

As presented in Jensen et al. [41] the distribution of liquid and vapour in plate HEX evaporators has a significant influence on the performance of the such HEX. In the HACHP liquid/vapour distribution issues occur in both the desorber and absorber as the working fluid will be in two-phase state at the inlet of both components. In the VCHP, liquid/vapour distribution is only an issue in the evaporator as the working fluid is superheated at the inlet of the condenser.

Improper distribution of liquid and vapour entails a large difference in the mass flow rate distribution between the channels. Channels that receive larger ratios of vapour will exhibit a larger friction factor and thus the mass flow rate is reduced such the pressure losses over the channels are equated. These channels will hence have a low mass flow rate and high vapour quality. This results in the superheat to start significantly earlier in these channels, reducing the temperature difference and the heat transfer coefficients effectively resulting in parts of the HEX with a very low heat flux.

Maldistribution issues may be even more penalising in the HACHP as the non-ideal distribution of the liquid and vapour will cause the bulk ammonia mass fraction of each individual channel to differ from the overall composition. Thereby, the temperature gradient of each individual channel will be different which may limit the ability to attain a match of the temperature profiles.

The effect of maldistribution on the performance of plate HEX absorbers and desorbers should be investigated further, such that the distribution can be included in the design procedure.

4.5 Conclusion

This chapter has sought to investigate the correlations needed to determine heat transfer area and pressure drops in two-phase heat transfer equipment with zeotropic mixtures. The focus has mainly been on the zeotropic mixture ammonia-water in plate HEX.

Before being able to apply heat transfer and pressure drop correlations

the mixture transport properties such as viscosity and thermal conductivity must be determined. Correlations by Wilke, Lucas and Reichenberg were compared for vapour mixture viscosity. Of these Wilke was suggested to use in the heat transfer correlations. Correlations by El-Sayed, M. Conde and Handbuch der Kältetechnik were compared for liquid viscosity. Of these M. Conde was applied in the following analysis as it represents experimental data better over the entire temperature range. Only one correlation applicable for vapour thermal conductivity was identified, this was the El-Sayed correlation. For liquid thermal conductivity El-Sayed, M. Conde, Jamieson and Fillipov were compared, of these El-Sayed was applied to the heat transfer and pressure drop correlations.

The heat transfer and pressure drop characteristics of plate HEX was accounted for by the application of Martin's correlation. For the absorption process the two-phase effects were accounted for by the correlation of Yan and Lin, while mixture effects were accounted for by the application of the Silver-Bell-Ghaly method. For the desorption process the Taboas correlation was applied. This is developed explicitly for ammonia-water desorption in plate HEX. The influence of mass flux, heat flux, ammonia mass fraction and vapour quality on the local heat transfer coefficient and friction factor was investigated for both absorption and desorption. A general conclusion from this investigation is: that the heat transfer coefficient of low ammonia mass fraction mixtures tends to be higher than those of the high ammonia mass fraction mixtures. The heat transfer coefficient is smallest for the ammonia mass fractions around $x = 0.5$ to $x = 0.7$.

A complete design study of a 1000 kW plate absorber and desorber has been conducted for ammonia mass fractions of $x = 0.7$, $x = 0.8$ and $x = 0.9$. The influence of the plate geometry was also investigated. This showed that the heat transfer area is always smallest for $x = 0.9$ and highest for $x = 0.7$ the increased area need to go from $x = 0.8$ to $x = 0.7$ is though noticeably smaller than what is need to go from $x = 0.9$ to $x = 0.8$. The heat transfer area is most influenced by the plate size and plate corrugations angle, while the pressure drop is most influenced by the plate size and the plate press depth.

CHAPTER 5

ADVANCED EXERGY-BASED ANALYSIS

The results presented in the this chapter is disseminated in three papers. The conventional and advanced exergy analysis is presented in ([P9]), at the time of writing this paper is under review in Energy, the International Journal. The conventional and advanced exergoeconomic analysis is presented in ([P10]) which has yet to submitted. The conventional and advanced exergoenvironemental analysis is described in ([P16]) [45] and presented at the 28th International Conference on Efficiency, Cost, Optimization, Simulation and environmental Impact of Energy Systems (ECOS 2015) .

5.1 Introduction

An exergy-based analysis describes the combined application of an exergy, exergoeconomic and exergoenvironmental analysis. The advanced exergy-based analysis equally consists of an advanced exergy, advanced exergoeconomics and advanced exergoenvironmental analysis. The advanced version of the method differs from the conventional by accounting for the interdependency of component irreversibilities, cost and environmental impact as well as the reduction potentials of these.

The first step in an advanced exergy-based analysis is the application of a conventional exergy, exergoeconomic and exergoenvironmental analysis. Subsequently the conventional exergy analysis can be extended to an advanced exergy analysis that when combined with the results of the exergoeconomic and exergoenvironmental analysis can be used to conduct the advanced exergoeconomic and exergoenvironmental analysis.

The application of a conventional exergy analysis reveals information

on the location and magnitude of the thermodynamic irreversibilities in a system and is therefore a valuable method in the analysis and optimization of thermal energy systems [19, 55].

Advanced exergy analysis seeks to reveal the true source of thermodynamic irreversibilities and the potential for their reduction.

As components in a thermodynamic cycle are interdependent, the exergy destruction located in one component is not only caused by the inefficiencies of that component but also by the inefficiencies of the remaining components [102, 50, 51]. Further, the amount of exergy destruction that is possible to avoid by design improvements is bound by technological and economic constraints [105].

The advanced exergy analysis, as described in [102, 50, 51, 28, 105], is a generalized method capable of quantifying component interdependencies by splitting the exergy destruction in the k^{th} component into an *endogenous* (EN) part: associated solely with the inefficiency of the component itself and an *exogenous* (EX) part: associated with the inefficiencies of the remaining components. To quantify the reduction potential the exergy destruction in the k^{th} component is split into an *unavoidable* (UN) part: the component exergy destruction when implementing the "state of the art" technology and the *avoidable* (AV) part: the exergy destruction avoided by the application of the "state of the art" technology [28, 105].

Both the *endogenous* and *exogenous* destruction rates can be split into their *unavoidable* and *avoidable* parts [104].

By performing these splits of the k^{th} component exergy destruction, the information retrieved from the exergy analysis is improved and offers a level of insight not provided by the conventional exergy analysis [104].

Satapathy [89] presented a conventional exergy analysis of a HACHP for heating and cooling purposes with the working fluid mixture R22-E181. This concluded that the main contribution to the system exergy destruction is located in the compressor, followed by the absorber and IHEX. However, as concluded by Morosuk et. al [68, 72], where advanced exergy analysis is applied to different refrigeration machines, this does not necessarily imply that the compressor inefficiency is the main source of exergy destruction. In both [68] and [72], the conclusion

is that the highest rate of avoidable exergy destruction is inherent to the evaporator inefficiency.

Given the application of a zeotropic mixture working fluid and the solution circuit design the conclusions from [68, 72] may not be directly applicable to the HACHP, while the conclusion from [89] lack the level of detail attained by the advanced exergy analysis.

It is therefore relevant to apply the advanced exergy analysis to the HACHP to fully understand the sources and reduction potential of the exergy destruction in the system. This study will be conducted with the natural refrigerant mixture ammonia-water, which would be a more feasible option for future HACHP development as the working fluid R22, applied in [89], is being phased out due to its global warming potential.

Evaluation and optimization of the ammonia-water HACHP has been presented by several studies [34, 37, 38]. Berntsson et al. [37, 38] evaluated the feasibility of the design solely on the coefficient of performance (COP) while Åhlby et al. [34] evaluated both the COP and the VHC. In [37, 38] parameter variations are performed on the allocation of heat transfer area between the heat exchange components. Of these: the absorber and desorber are falling film shell and tube type while the IHEX is modelled as a black box with a given overall heat transfer coefficient (U-value). In Åhlby et al. [34] the heat exchangers are all modelled with constant U-value and a LMTD based on the inlet and outlet conditions, this approach however is troublesome due to the non-linearity of the absorption and desorption curves, discussed in detail in [40, 107].

The approaches applied in [34, 37, 38] give an indication of the order of importance at which a fixed heat transfer area should be allocated between the components to increase COP and thus reduce the running cost of the HACHP. However, information on the trade-off between investment cost and running cost is not supplied by these approaches. Hence, information indicating to which extent component investment cost should be increased to justify the reduction of the running costs seemingly lacks.

One method of attaining information on this trade-off is by the application of an exergoeconomic analysis [19, 55]. Exergoeconomic analysis combines analysis of the thermodynamic performance of a system or

component (exergy analysis [19, 55]) with economic principles to attain information on the cost-effectiveness of a thermal energy system [100].

An exergoeconomic analysis is thus a generalised method of evaluating the total annual cost of operating a component in a thermal energy system. The total annual cost is comprised of two contributions: the capital investment and operation and maintenance cost, measured by the cost rate $\dot{Z}_k$ (non-exergetic cost rate) and the cost of operating the component, measured by the cost rate related to the exergy destruction of the k^{th} component $\dot{C}_{D,k} = c_{F,k}\dot{E}_{D,k}$. By determining the total cost of the components in these two distinct measures it can be evaluated whether the total cost of a component is dominated by investment or by operating costs and thus whether the investment should be increased or decreased in order to ensure cost reduction.

In recent years advanced methods have been introduced to the field of exergoeconmic analysis [101]. These improve the accuracy of the analysis as they account for component interdependencies and reveal the potential for cost reduction [101, 104]. The component interdependencies are accounted for by splitting both the cost rate of exergy destruction, $\dot{C}_{D,k}$, and the non-exergetic cost rate, $\dot{Z}_k$, into an *endogenous* and an *exogenous* part [102, 50, 51]. Here, the endogenous part is the cost associated only with the design and operation of the component itself, while the exogenous part is the cost associated with the remaining components. To determine the reduction potential the cost rates $\dot{C}_{D,k}$ and $\dot{Z}_k$ are spilt into an *avoidable* and *unavoidable* part [28, 105]. Here, the unavoidable part of the cost rate $\dot{C}_{D,k}$ is the cost of exergy destruction when the k^{th} component exergy efficiency is increased to it's technical and economic limitations, while the unavoidable part of the cost rate $\dot{Z}_k$ is the non-exergetic cost rate when the exergy efficiency of the k^{th} component approaches 0.

The advanced exergoeconomic analysis has been applied to a range of thermal conversion systems such as power plants and combined heat and power plants [82, 83, 14, 61], a trigeneration system [13], a geothermal district heating system [49] and to vapour compression refrigeration machines [103, 69, 70].

By combining a LCA with the advanced exergy analysis an advanced exergoenvironmental analysis can be performed. This allows the en-

vironmental impact of both the operation of the HACHP and the construction, transportation and disposal of the HACHP to be allocated to the component that causes the environmental impact. Thus, it gives the system designer knowledge of which components have the highest environmental impact and thereby which components are of most interest for further improvement.

The exergoenvironmental analysis reveals whether the environmental impact of the component is dominated by operation or by the construction, transportation and disposal. Thereby, revealing whether the component is best improved by improving the exergy efficiency at the expense of an increased size or vice versa.

The total annual rate of environmental impact is comprised of two contributions: the non-exergetic environmental impact, associated with the construction, transportation and disposal, measured by $\dot{Y}_k$ and the environmental impact of operating the component, measured by the rate of environmental impact associated with the exergy destruction of the component, $\dot{B}_{D,k} = b_{F,k}\dot{E}_{D,k}$.

As for the exergoeconomic analysis, advanced methods have been introduced to the field of exergoenvironmental analysis [101] in recent years. These work analogous to the exergoeconomic analysis by splitting $\dot{B}_{D,k}$ and $\dot{Y}_k$ into an *endogenous* and an *exogenous* as well as *avoidable* and *unavoidable*.

5.2 Methodology

Fig. 5.1 shows the layout of the HACHP to which the advanced exergy-based analysis was applied. The used component and stream index numbers are stated. The operating conditions, to which the advanced exergy based analysis was applied, was based on a relevant industrial case with a given heat demand at defined sink temperatures and a heat source of given inlet conditions. It was thus defined by sink inlet and outlet temperature, $T_{\text{sink,in}}$ and $T_{\text{sink,out}}$, source inlet temperature, $T_{\text{source,in}}$, and the mass flow rate of the sink and source, $\dot{m}_{\text{sink}}$ and $\dot{m}_{\text{source}}$. The applied values are listed in Table 5.1 and were kept constant for all further analysis. The applied conditions result in a supplied heat load of

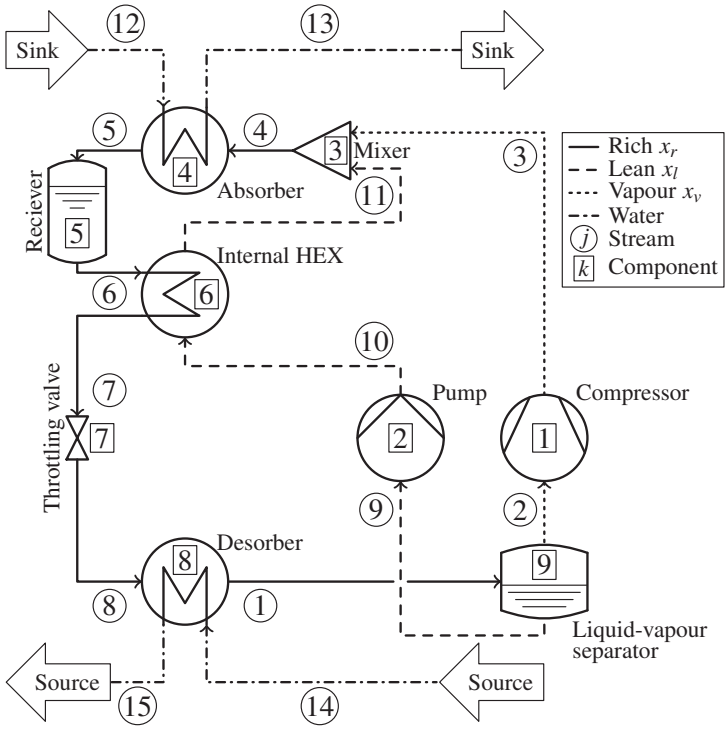

Figure 5.1: Principle sketch of the HACHP layout applied to the advanced exergy based analysis.

$\dot{Q}$ = 837 kW.

Table 5.1: Operating condition for the HACHP analysis

Variable	Value	Unit
$T_{\text{sink,out}}$	80	°C
$T_{\text{sink,in}}$	60	°C
$T_{\text{source,in}}$	55	°C
$\dot{m}_{\text{sink}}$	10	kg/s
$\dot{m}_{\text{source}}$	15	kg/s

5.2.1 Conventional exergy analysis

To derive the exergy destruction in all components the specific exergy of all streams were determined. The specific exergy is the sum of two contributions: a physical part e^{PH}, associated with reaching thermal and mechanical equilibrium with the dead state, and a chemical part e^{CH}, associated with reaching chemical equilibrium with the dead state [18]. The definition of physical exergy is given by Eq. (5.1).

$$e_j^{\mathrm{PH}} = h_j - h_{j,0} - T_0 \left(s_j - s_{j,0}\right) \tag{5.1}$$

Here, $h_{j,0}$ and $s_{j,0}$ are the specific enthalpy and entropy evaluated at the dead state: T_0, p_0. The dead state was chosen at: T_0 = 25 °C and p_0 = 1.0133 bar. The dead state enthalpy and entropy were evaluated at the ammonia concentration of the j^{th} stream, hence three dead state values were calculated for the mixture, one for x_r, x_l and x_v, respectively.

The specific chemical exergy of an ammonia-water mixture was calculated using Eq. (5.2) [19, 67].

$$e_j^{\mathrm{CH}} = x_j e_{\mathrm{NH_3}}^{\mathrm{CH}} + \left(1 - x_j\right) e_{\mathrm{H_2O}}^{\mathrm{CH}} + w_{X_j}^{\mathrm{rev}} \tag{5.2}$$

Here, $e_{\mathrm{NH_3}}^{\mathrm{CH}}$ and $e_{\mathrm{H_2O}}^{\mathrm{CH}}$ are the standard molar chemical exergy of ammonia and water, respectively. At a temperature of T_0 = 25 °C and a pressure of p_0 = 1.0133 bar, these attain values of $e_{\mathrm{NH_3}}^{\mathrm{CH}}$ = 336684 kJ/kmol and $e_{\mathrm{H_2O}}^{\mathrm{CH}}$ = 45 kJ/kmol [19]. The reversible specific work associated with the mixing of pure ammonia and pure water, $w_{X_j}^{\mathrm{rev}}$, was calculated using, Eq. (5.3) [67].

$$w_{X_j}^{\mathrm{rev}} = \left(h_{j,0} - x_j h_{\mathrm{NH_3},0} - \left(1 - x_j\right) h_{\mathrm{H_2O},0}\right) - T_0 \left(s_{j,0} - x_j s_{\mathrm{NH_3}} - \left(1 - x_j\right) s_{\mathrm{H_2O},0}\right) \tag{5.3}$$

The total exergy flow associated with each stream was calculated based on the found specific exergy values, using Eq. (5.4).

$$\dot{E}_j = \dot{E}_j^{\mathrm{PH}} + \dot{E}_j^{\mathrm{CH}} = \dot{m}_j \left(e_j^{\mathrm{PH}} + e_j^{\mathrm{CH}}\right) \tag{5.4}$$

Applying exergy balances to each component resulted in the exergy destruction rates given by Eqs. (5.5) - (5.11). Here, the exergy fuel, $\dot{E}_{F,k}$,

and exergy product, $\dot{E}_{P,k}$, of the components are indicated. All components were assumed adiabatic and thus all transferred exergy is related to the transfer of work (pump and compressor) and material streams.

(1) Compressor : $$\dot{E}_{D,\mathrm{CM}} = \underbrace{\dot{W}_{\mathrm{CM}}}_{fuel} - \underbrace{(\dot{E}_3 - \dot{E}_2)}_{product} \tag{5.5}$$

(2) Pump : $$\dot{E}_{D,\mathrm{PM}} = \underbrace{\dot{W}_{\mathrm{PM}}}_{fuel} - \underbrace{(\dot{E}_{10} - \dot{E}_9)}_{product} \tag{5.6}$$

(3) Mixer : $$\dot{E}_{D,\mathrm{MI}} = \dot{E}_4 - (\dot{E}_3 + \dot{E}_{11}) \tag{5.7}$$

(4) Absorber : $$\dot{E}_{D,\mathrm{AB}} = \underbrace{(\dot{E}_4 - \dot{E}_5)}_{fuel} - \underbrace{(\dot{E}_{13} - \dot{E}_{12})}_{product} \tag{5.8}$$

(6) IHEX : $$\dot{E}_{D,\mathrm{IH}} = \underbrace{(\dot{E}_6 - \dot{E}_7)}_{fuel} - \underbrace{(\dot{E}_{11} - \dot{E}_{10})}_{product} \tag{5.9}$$

(7) Throttling valve : $$\dot{E}_{D,\mathrm{TV}} = \dot{E}_7 - \dot{E}_6 \tag{5.10}$$

(8) Desorber : $$\dot{E}_{D,\mathrm{DS}} = \underbrace{(\dot{E}_{14} - \dot{E}_{15})}_{fuel} - \underbrace{(\dot{E}_1 - \dot{E}_8)}_{product} \tag{5.11}$$

Fuel and product are not indicated for the throttling valve and mixer as both components are dissipative, so meaningful definitions of component fuel and product cannot be determined [58].

The exergetic performance of the components were evaluated by the exergy efficiency, ε_k. This is defined in [19] as the ratio between the component product and fuel, see Eq. (5.12). This was applied for all non-dissipative components.

$$\varepsilon_k = \frac{\dot{E}_{P,k}}{\dot{E}_{F,k}} \tag{5.12}$$

Two exergy destruction ratios, y_k and y_k^*, were calculated as seen in, Eqs. (5.13) and (5.14) [19].

$$y_k = \frac{\dot{E}_{D,k}}{\dot{E}_{F,\mathrm{tot}}} \tag{5.13}$$

$$y_k^* = \frac{\dot{E}_{D,k}}{\dot{E}_{D,\text{tot}}} \tag{5.14}$$

Here, y_k is the exergy in the k^{th} component relative to the total exergy fuel supplied to the system. While y_k^* is the exergy destruction in the k^{th} component relative to the total exergy destruction in the system.

The exergy loss associated with the HACHP system is related to the exergy rate of stream 15 (the heat source exiting the desorber). Whether this loss should be allocated as exergy destruction caused the HACHP depends on the system boundaries. If it is assumed, that stream 15 is delivered to the ambient and thus, that the exergy content of stream 15 is dissipated, the exergy loss should be accounted as destruction. However, if the boundary is chosen at the outlet of the desorber the exergy of stream 15 is not destroyed and could be utilized as a fuel in other systems. In the present study the latter definition was applied and the exergy destruction of the HACHP was thus only related to the exergy destruction of the components.

5.2.2 Conventional exergoeconomic analysis

The basis of the conventional exergoeconomic analysis is the evaluation of the total cost of operating a component in a thermal energy conversion system. The total cost consists of two distinct measures, the levilized capital cost rate $\dot{Z}_k$ (non-exergetic cost) and the cost rate of exergy destruction $\dot{C}_{D,k}$ (exergetic cost).

Economic evaluation and cost levelization

To determine the non-exergetic cost rate, $\dot{Z}_k$, first the purchased equipment cost (PEC) of all major components were found. PEC functions were developed for all major components based on Danish intermediate trade business prices (TRB) and individual manufacturers suggested retail prices (MRP). The cost functions were constructed as proposed by [19], see Eq. (5.15).

$$\text{PEC}_Y = \text{PEC}_W \left(\frac{X_Y}{X_W} \right)^{\gamma} \tag{5.15}$$

Table 5.2: Used cost correlations coefficients for the component types divided by application limits

Equipment	PEC_W	X_W	γ	Source
Compressor:	(€)	($m^3\ h^{-1}$)		
LP R717	11914	178.4	0.66	TBP [1,2]
HP R717	NDA	NDA	NDA	MRP [4]
Electrical motor:	(€)	(kW)		
LP/HP R717	10710	250.0	0.65	TBP[1]
Receiver:	(€)	(m^3)		
LP R717	1444	0.089	0.63	TBP[1]
HP R717	1934	0.089	0.66	TBP[1]
Plate HEX:	(€)	(m^2)		
LP R717	15526	42.0	0.80	TBP[1,2,3]
HP R717	NDA	NDA	NDA	MRP[5]
Pump:	(€)	(kW)		
LP/HP R717	NDA	NDA	NDA	MRP[6]
LVS:	(€)	($m^3\ h^{-1}$)		
LP/HP R717	12702	525	0.39	TBP[1]

[1]H. Jessen Jürgensen [7], [2]F.K Teknik A/S [6]

[3]Ahlsell ApS [5], [4]Johnson Controls [8]

[5]SWEP International AB[10], [6]Grundfos DK A/S [9]

Here, PEC_Y is the PEC of the component at capacity X_Y, while PEC_W is the PEC at a chosen base capacity, X_W. The correlated capacities for the different components were as follows:

- PEC for a compressor was a function of the compressor displacement volume and the pressure limit.
- PEC for an electrical motor with a fixed efficiency was dependent

only on the shaft power.

- PEC for a heat exchanger was a function of the HEX area and the pressure limit.
- PEC for a pump was a function of the shaft power.
- PEC for a LVS was a function of the compressor suction line volume flow rate. The size was chosen to attain a vapour velocity of 0.4 m/s in the separator. This corresponds to an entrained liquid droplet size with a maximum diameter of 0.25 mm [91].
- PEC for a high pressure receiver was a function of the volume and pressure limit.

The values of PEC_W, X_W and γ attained are stated in Table 5.2 together with the source from which the cost information was supplied. Cost information for some components were supplied under a non-disclosure agreement (NDA) and thus the coefficients of the developed cost functions are not presented.

Once the PEC costs of all components were determined the total capital investment (TCI) of the components were found. As suggested by [19], it was assumed that the TCI was a factor of 4.16 higher than the PEC of the component, Eq. (5.16).

$$\text{TCI}_{\text{HP}} = \sum_{k=1}^{K} \text{PEC}_k \cdot 4.16 \tag{5.16}$$

The factor of 4.16 was applied to account for additional costs related to new investment at an existing facility. It was thus applied to account for additional direct costs such as: piping, instrumentation and control, electrical equipment, civil and structural work and service facilities as well as indirect costs such as: engineering and supervision costs and construction and contractor profit costs [19].

To determine the levelized capital cost rates of the k^{th} component the capital recover factor (CRF) Eq. (5.17) [19] was used.

$$\text{CRF} = \frac{i^{\text{eff}}(1+i^{\text{eff}})^L}{(1+i^{\text{eff}})^L - 1} \tag{5.17}$$

Here, i^{eff} is the effective interest rate over the the life time of the system, calculated as seen in Eq. (5.18), where i is the interest rate, assumed fixed at a value of 7 % and i_L is the inflation rate, assumed fixed at a value of 2 %.

$$i^{\text{eff}} = \frac{1+i}{1+i_L} - 1 \tag{5.18}$$

The technical life time, L, is assumed to be 15 years with 3000 operating hours per year, H. The levelized capital investment cost rate of the k^{th} component was then calculated as in Eq. (5.19).

$$\dot{Z}_k^{\text{CI}} = \frac{\text{TCI}_k \text{CRF}}{H} \tag{5.19}$$

The operation and maintenance cost rate of the k^{th} component was assumed to be 20 % of the levelized capital cost rates, $\dot{Z}_k^{\text{OM}} = 0.2 \cdot \dot{Z}_k^{\text{CI}}$. The total non-exergetic cost rate is the sum of the capital investment and the operation and maintenance cost rate, see Eq. 5.20.

$$\dot{Z}_k = \dot{Z}_k^{\text{CI}} + \dot{Z}_k^{\text{OM}} = 1.2 \cdot \dot{Z}_k^{\text{CI}} \tag{5.20}$$

The price of the electricity corresponds to an industrial process consumer in the Danish fiscal environment, for the year 2012 [1]. No cost is associated with the process stream utilized as the HACHP heat source.

Cost balances and exergoeconomic indicators

The basis of a conventional exergoeconomic analysis is the association of cost to all streams of exergy in the system. This cost is known as the unit cost of exergy: c_j. Hence, to determine c_j, an exergy analysis must be applied to the system such that the exergy flow rates, $\dot{E}_j$, of all streams are known. Based of the exergy flow rates the total exergy cost rate of each stream was calculated as: $\dot{C}_j = c_j \dot{E}_j$.

To determine the unit cost of exergy of each stream, cost balances were applied to all system components. For a non-dissipative component the cost balance can be formulated using fuel and product costs, see Eq. (5.21) [19].

$$\dot{C}_{P,k} = \dot{C}_{F,k} + \dot{Z}_k \tag{5.21}$$

Table 5.3: Component product and fuel definitions and auxiliary relations for the exergoeconomic analysis

k^{th}	comp.	Cost of fuel $\dot{C}_{F,k} =$	Cost of prod. $\dot{C}_{P,k} =$	Auxiliary relations
(1)	CM	$c_w\dot{W}_1$	$\dot{C}_3 - \dot{C}_2$	-
(2)	PM	$c_w\dot{W}_2$	$\dot{C}_{10} - \dot{C}_9$	-
(4)	AB	$\dot{C}_4 - \dot{C}_5$	$\dot{C}_{13} - \dot{C}_{12}$	$c_4 = c_5$, c_{12}=0
(6)	IH	$\dot{C}_6 - \dot{C}_7$	$\dot{C}_{11} - \dot{C}_{10}$	$c_6 = c_7$
(8)	DS	$\dot{C}_{14} - \dot{C}_{15}$	$\dot{C}_1 - \dot{C}_8$	$c_{14} = c_{15}$, c_{13}=0
Sys.		$\dot{C}_{F,1} + \dot{C}_{F,2} + \dot{C}_{F,8}$	$\dot{C}_{P,4}$	$c_2 = c_9$

The definition of the exergy fuel and product as well as fuel and product cost for the non-dissipative components and for the total HACHP system are stated in Table 5.3. To ensure that the set of equations are specified, a number of auxiliary relations are needed. The applied auxiliary relations are listed in Table 5.3 (the F-rule [19] was applied).

For the dissipative components (mixer and throttling valve) and for the liquid-vapour separator fuel and product cannot be defined in a meaningful way and the cost balance in Eq. (5.21) cannot be applied. By applying the general form [19] the cost balances for these three components can be derived, as may be seen in Eq. (5.22)-(5.25).

$$(3) \quad \text{Mixer}: \qquad \dot{C}_3 + \dot{C}_{11} + \dot{Z}_3 = \dot{C}_4 \tag{5.22}$$

$$(5) \quad \text{Reciever}: \qquad \dot{C}_5 + \dot{Z}_5 = \dot{C}_6 \tag{5.23}$$

$$(7) \quad \text{Throttling valve}: \qquad \dot{C}_7 + \dot{Z}_7 = \dot{C}_8 \tag{5.24}$$

$$(9) \quad \text{Liquid} - \text{vapour separator}: \qquad \dot{C}_1 + \dot{Z}_9 = \dot{C}_2 + \dot{C}_9 \tag{5.25}$$

Using the fuel and product definitions, the component specific fuel and product cost, $c_{F,k}$ and $c_{P,k}$, can be determined, as in Eqs. (5.26) and (5.27).

$$c_{F,k} = \frac{\dot{C}_{F,k}}{\dot{E}_{F,k}} \tag{5.26}$$

$$c_{P,k} = \frac{\dot{C}_{P,k}}{\dot{E}_{P,k}} \tag{5.27}$$

From these the conventional exergoeconomic indicators are determined, see Eqs. (5.28) and (5.29). These are the exergoeconomic factor, f_{ex}, indicating the impact of the non-exergetic cost on the total cost and the relative cost difference, r, indicating the relative increase in cost between the fuel and product of a component.

$$f_{c,k} = \frac{\dot{Z}_k}{\dot{Z}_k + c_{F,k}\dot{E}_{D,k}} \tag{5.28}$$

$$r_k = \frac{c_{P,k} - c_{F,k}}{c_{F,k}} \tag{5.29}$$

5.2.3 Convention exergoenvironmental analysis

The basis of the conventional exergoenvironmental analysis is the evaluation of the total environmental impact related to a component in a thermal energy conversion system. As for the exergoeconomic analysis, this consists of two distinct measures, the non-exergetic environmental impact, $\dot{Y}_k$, and the exergetic environmental impact, $\dot{B}_{D,k}$. The non-exergetic environmental impact is determined by the application of a LCA, after which the exergetic environmental impact can be determined by the application of environmental impact balances.

Life-cycle assessment

The LCA method is a generalized approach used to assess the environmental impact of all stages of a product from construction to disposal. The process of conducting a LCA has been standardised in [4]. To conduct a LCA it is necessary to first compile an inventory analysis of the needed materials, energy inputs and releases (pollutants). Subsequently, the environmental impact of all identified flows of materials, energy and pollutants are evaluated. From this the results can be interpreted, the main sources of environmental impact can be identified and measures to reduce them can be sought.

The mass of the main components were correlated based on the aggregated data for which cost functions were also constructed. The following assumptions were applied:

- The mass of a compressor was a function of the compressor displacement volume and the pressure limit [8].
- The mass of an electrical motor with a fixed efficiency was dependent only on the shaft power [7].
- The mass of a heat exchanger was a function of the HEX area and the pressure limit [11].
- The mass of a pump was a function of the shaft power [9].
- The mass of a LVS was a function of the compressor suction line volume flow rate. The size was chosen to attain a vapour velocity of 0.4 m/s in the separator [7]. This corresponds to an entrained liquid droplet size with a maximum diameter of 0.25 mm.
- The mass of a high pressure receiver was a function of the volume and pressure limit [7].

The material type used for the construction of the components were equally identified from these sources [8, 7, 11, 9]. The material inventory is stated in Table 5.4 along with the quantity of material needed to construct the HACHP with $\Delta T_{pp,4} = \Delta T_{pp,8}$ = 10 K, ϵ_6 = 0.7 $\eta_{is,1}$ = 0.75, $\eta_{el,1}$ = 0.95, $\eta_{is,2}$ = 0.85 and $\eta_{el,2}$ = 0.95. Table 5.4 states the relevant production method for each component type. The type "vessels" covers both the liquid/vapour-separator and the high pressure receiver.

In order to quantify the environmental impact of the material inventory data the Eco-indicator 99 [32] has been applied. Eco-indicator 99 uses average European data and has been applied in several exergoenvironmental studies [65, 22]. It is thus assumed to be a suitable indicator for the study at hand. The Eco-indicator 99 points for each material and production method investigated are stated in Table 5.4. The Total Environmental Impact (TEI) of all components is also presented.

The value of $\dot{Y}_k$ was found as the sum of: $\dot{Y}_k^{CO}$, the environmental impact related to construction, $\dot{Y}_k^{OM}$ the environmental impact related to maintenance and $\dot{Y}_k^{DI}$ the environmental impact related to disposal of the component. $\dot{Y}_k^{DI}$ is a negative value which accounts for the benefit of recycling the used materials at the end of the life cycle.

$\dot{Y}_k^{CO}$, $\dot{Y}_k^{OM}$ and $\dot{Y}_k^{DI}$ were calculated as seen in Eqs. (5.30) - (5.32). Here, H is the yearly operating time and L is the system lifetime. As seen $\dot{Y}_k^{OM}$ is assumed to be 20 % of $\dot{Y}_k^{CO}$ which is equivalent to the ratio applied in the exergoeconomic analysis.

$$\dot{Y}_k^{CO} = \frac{\mathrm{TEI}_k^{CO}}{H \cdot L} \tag{5.30}$$

$$\dot{Y}_k^{OM} = 0.2 \cdot \dot{Y}_k^{CO} \tag{5.31}$$

$$\dot{Y}_k^{DI} = \frac{\mathrm{TEI}_k^{DI}}{H \cdot L} \tag{5.32}$$

Environmental impact balance and exergoenvironmental indicators

The basis of a conventional exergoenvironmental analysis is the association of environmental impact to all streams of exergy in the system. The exergy specific environmental impact is known as : b_j. Hence, to determine b_j, an exergy analysis must be applied to the system such that the exergy flow rates, $\dot{E}_j$, of all streams are known. Based of the exergy flow rates the total environmental impact rate of each stream was calculated as: $\dot{B}_j = b_j \dot{E}_j$.

To determine b_j for each stream, environmental impact balances were applied to all system components. For a non-dissipative component the environmental impact balance can be formulated using fuel and product environmental impact, see Eq. (5.33).

$$\dot{B}_{P,k} = \dot{B}_{F,k} + \dot{Y}_k \tag{5.33}$$

The definition of the exergy fuel and product as well as fuel and product environmental impact for the non-dissipative components and for the total HACHP system are stated in Table 5.3. As for the exergoeconomic analysis auxiliary relations were applied to specify the set equation. Again the F-rule [19] was applied.

For the dissipative components (mixer and throttling valve) and passive components (liquid/vapour separator) exergy fuel and product could

Table 5.4: Estimation of needed materials for the real cycle and the ECO 99 indicator points for the materials, production, transportation and disposal of different types of components.

			ECO 99 (mpt/kg)	M^{real} (kg)	TEI^{real} (mpt)
Comp.	Materials				
		Cast Iron	240.0	937.6	$225 \cdot 10^3$
	Production				
		Milling	115.0	26.31	$302 \cdot 10^2$
Motor	Materials				
		88 % Cast iron	240.0	889.6	$213 \cdot 10^3$
		12 % Copper	1400	113.4	$159 \cdot 10^3$
Plate HEX	Materials				
		98 % High alloy steel	910.0	96.01	$873 \cdot 10^2$
		2.0 % Copper	1400	1.961	$274 \cdot 10^1$
	Production				
		Sheet production	30.00	96.01	$288 \cdot 10^1$
		Pressing	23.00	96.01	$221 \cdot 10^1$
Pump	Materials				
		69 % Cast iron	240.0	51.19	$123 \cdot 10^2$
		25 % Low alloy steel	110.0	18.55	$204 \cdot 10^1$
		6.0 % Copper	1400	4.451	$623 \cdot 10^1$
Vessels	Materials				
		High alloy steel	910.0	304.1	$276 \cdot 10^3$
	Production				
		Sheet production	30.00	304.1	$912 \cdot 10^1$
Fluid					
		Ammonia	160.0	11.90	$190 \cdot 10^1$
		Water	0.026	2.976	$773 \cdot 10^{-4}$
Transport					
		Truck 16t (1000 km)	34.00	2431	$827 \cdot 10^2$
Disposal					
		Recycling ferro metals	-70	2278	$-159 \cdot 10^3$

not be defined in a meaningful way. The environmental impact balances

Table 5.5: Component product and fuel definitions and auxiliary relations

k^{th}	Comp.	Fuel cost $\dot{B}_{F,k} =$	Prod. cost $\dot{B}_{P,k} =$	Auxiliary relations
(1)	CM	$b_w\dot{W}_1$	$\dot{B}_3 - \dot{B}_2$	-
(2)	PM	$b_w\dot{W}_2$	$\dot{B}_{10} - \dot{B}_9$	-
(4)	AB	$\dot{B}_4 - \dot{B}_5$	$\dot{B}_{13} - \dot{B}_{12}$	$b_4 = b_5$, b_{12}=0
(6)	IH	$\dot{B}_6 - \dot{B}_7$	$\dot{B}_{11} - \dot{B}_{10}$	$b_6 = b_7$
(8)	DS	$\dot{B}_{14} - \dot{B}_{15}$	$\dot{B}_1 - \dot{B}_8$	$b_{14} = b_{15}$, b_{14}=0
Sys.		$\dot{B}_{F,1} + \dot{B}_{F,2} + \dot{B}_{F,8}$	$\dot{B}_{P,4}$	$b_2 = b_9$

for these three components were derived as seen in Eq. (5.34)-(5.37).

$$(3)\quad \text{Mixer}: \qquad \dot{B}_3 + \dot{B}_{11} + \dot{Y}_3 = \dot{B}_4 \qquad (5.34)$$

$$(5)\quad \text{Reciever}: \qquad \dot{B}_5 + \dot{Z}_5 = \dot{B}_6 \qquad (5.35)$$

$$(7)\quad \text{Throttling valve}: \qquad \dot{B}_7 + \dot{Y}_7 = \dot{B}_8 \qquad (5.36)$$

$$(9)\quad \text{Liquid/vapour separator}: \qquad \dot{B}_1 + \dot{Y}_9 = \dot{B}_2 + \dot{B}_9 \qquad (5.37)$$

Using the fuel and product definitions, the specific fuel and product environmental impact of the components , $b_{F,k}$ and $b_{P,k}$, were determined, as seen in Eq. (5.38).

$$b_{F,k} = \frac{\dot{B}_{F,k}}{\dot{E}_{F,k}}, \quad b_{P,k} = \frac{\dot{B}_{P,k}}{\dot{E}_{P,k}} \qquad (5.38)$$

The value of b_w was set in accordance with the Eco-indicator 99 [32], to a value of 26 mpt/kWh corresponding to an average European value for low voltage electricity.

5.2.4 Advanced exergy-based analysis

Advanced exergy analysis

An approach based on thermodynamic cycles [51] was chosen to further analyse the exergy destruction in the HACHP, by splitting the exergy destruction of each component into different contributions. This

Table 5.6: Cycle inputs for the seven thermodynamic cycles used to split the exergy destruction into endogenous and exogenous parts.

k^{th}	CM	PM	AB		IH		TV	DS	
	η_{is} (-)	η_{is} (-)	ΔT_{pp} (K)	Δp (bar)	ϵ_{IH} (-)	Δp (bar)		ΔT_{pp} (K)	Δp (bar)
Real	0.75	0.85	10	0.05	0.8	0.05	$h_6 = h_7$	10	0.05
(1)	0.75	1	0	0	1	0	$s_6 = s_7$	0	0
(2)	1	0.85	0	0	1	0	$s_6 = s_7$	0	0
(4)	1	1	10	0.05	1	0	$s_6 = s_7$	0	0
(6)	1	1	0	0	0.8	0.05	$s_6 = s_7$	0	0
(7)	1	1	0	0	1	0	$h_6 = h_7$	0	0
(8)	1	1	0	0	1	0	$s_6 = s_7$	10	0.05

method was also applied by Morosuk et al. to split the exergy destruction in vapour compression cycles [68, 72] and absorption refrigeration machines [67].

Endogenous & exogenous By definition the sum of the k^{th} component endogenous, $\dot{E}^{\text{EN}}_{D,k}$, and exogenous, $\dot{E}^{\text{EX}}_{D,k}$, exergy destruction is the exergy destruction in the k^{th} component under the real operating conditions, $\dot{E}^{\text{Real}}_{D,k}$, see Eq. (5.39).

$$\dot{E}^{\text{Real}}_{D,k} = \dot{E}^{\text{EN}}_{D,k} + \dot{E}^{\text{EX}}_{D,k} \tag{5.39}$$

The endogenous exergy destruction is defined as the exergy destruction in the k^{th} component caused only by the irreversibilities of the component itself. With a thermodynamic model of the system the endogenous exergy destruction of the k^{th} component can be evaluated by simulating the cycle assuming all but the k^{th} component to operate with an exergy efficiency of one, while the k^{th} component maintains the initially assumed efficiency. For some components, such as unbalanced heat exchanger or throttling valves the assumption of ε_k = is not a physical solution and other approaches must be applied.

For throttling valves working above ambient temperature and pressure (dissipative component) no meaningful definition of exergy fuel

and product can be made as the valve dissipates both thermal and mechanical exergy. Thus, the exergy efficiency can be chosen as either $\varepsilon = 0$, as $\dot{E}_P = 0$, or as undefined. For the ideal operation of the throttling valve, it was assumed that it is replaced with an isentropic expander. Hence, the assumption: $h_6 = h_7$ was replaced by the assumption: $s_6 = s_7$. Thereby, for the ideal operation of the throttling valve: $\dot{E}_{D,\mathrm{TV}} = 0$ kW and $\varepsilon_{\mathrm{TV}} = 1$. This approach is equally applied in [67, 68, 72]

When evaluating the ideal operation of an unbalanced heat exchanger ($\dot{C}_1 \neq \dot{C}_2$) [19], the ideal operation cannot be meaningfully described by a component with $\varepsilon = 1$. For an unbalanced heat exchanger, $\varepsilon_k < 1$ if the component abides the Second Law. The difference in heat capacity will cause a temperature difference between the hot and cold fluid, thus leading to the destruction of thermal exergy. For the ideal operation of such a component a pinch point temperature difference of $\Delta T_{\mathrm{pp}} = 0$ K ($\epsilon = 1$) was assumed. Hence, an infinite heat transfer area is assumed. This approach is equally applied in [67, 68, 72].

For a component such as the mixer, where the exergy efficiency is not defined and an ideal replacement component is not applicable the best approach is to assume that all exergy destruction is caused by the remaining components and thus that the exergy destruction is exogenous. This off course implies that setting all other components in the system to their ideal operation would shed all exergy destruction related to the mixing of the lean liquid and the vapour. This however, is not the case. The correct allocation of this exergy destruction will be determined by a further splitting of the exogenous exergy destruction presented in Section 5.2.4.

The calculation procedure for determining the endogenous and exogenous parts using the thermodynamic cycle approach is first to solve the cycle with real efficiencies in all components. The inputs applied for the real cycle are seen in Table 5.6. The endogenous exergy destruction was then determined for each component apart from the mixer. This required one thermodynamic cycle for each component. These have the real component inputs for the k^{th} component and ideal performance for the remaining. The inputs for these cycles are listed in Table 5.6.

After simulating these cycles and thus attaining the endogenous exergy destruction for all components the exogenous part was calculated

Table 5.7: Inputs for the seven thermodynamic cycles used for the combined splitting of the exergy destruction into the avoidable/unavoidable and endogenous/exogenous parts

k^{th}	CM	PM	AB		IH		TV	DS	
	η_{is} (-)	η_{is} (-)	ΔT_{pp} (K)	Δp (bar)	ϵ_{IH} (-)	Δp (bar)		ΔT_{pp} (K)	Δp (bar)
UN.	0.95	0.95	1	0.001	0.98	0.001	$h_6 = h_7$	1	0.001
(1)	0.95	1	0	0	1	0	$s_6 = s_7$	0	0
(2)	1	0.95	0	0	1	0	$s_6 = s_7$	0	0
(4)	1	1	1	0.001	1	0	$s_6 = s_7$	0	0
(6)	1	1	0	0	0.98	0.001	$s_6 = s_7$	0	0
(7)	1	1	0	0	1	0	$h_6 = h_7$	0	0
(8)	1	1	0	0	1	0	$s_6 = s_7$	1	0.001

by applying Eq. (5.39).

Avoidable & unavoidable By definition the sum of the avoidable, $\dot{E}_{D,k}^{\text{AV}}$, and unavoidable, $\dot{E}_{D,k}^{\text{UN}}$, exergy destruction is equal to the component exergy destruction under real operating conditions, $\dot{E}_{D,k}^{\text{Real}}$.

$$\dot{E}_{D,k}^{\text{Real}} = \dot{E}_{D,k}^{\text{AV}} + \dot{E}_{D,k}^{\text{UN}} \tag{5.40}$$

The k^{th} component unavoidable exergy destruction was evaluated through the use a thermodynamic cycle in which the component inputs to the cycle were the values corresponding to the technological limits of the state of the art components [68]. For this analysis the following values were assumed: $\eta_{is}^{\text{UN}} = 0.95$, $\Delta T_{\text{pp}}^{\text{UN}} = 1$ K, $\epsilon^{\text{UN}} = 0.98$ and $\Delta p^{\text{UN}} = 1$ mbar. Simulating the thermodynamic cycle with unavoidable efficiencies in all components yields $\dot{E}_{D,k}^{\text{UN}}$. $\dot{E}_{D,k}^{\text{AV}}$ was then found by subtracting the unavoidable part from the exergy destruction under real operating conditions, Eq. (5.40).

Combining endogenous & exogenous with avoidable & unavoidable The exergy destruction in the k^{th} component can be further split when

realising that both the endogenous and exogenous destruction can be allocated as avoidable or unavoidable [104]. By definition the sum of the endogenous avoidable, $\dot{E}_{D,k}^{\mathrm{EN,AV}}$, and endogenous unavoidable, $\dot{E}_{D,k}^{\mathrm{EN,UN}}$, is the endogenous exergy destruction of the component, $\dot{E}_{D,k}^{\mathrm{EN}}$.

$$\dot{E}_{D,k}^{\mathrm{EN}} = \dot{E}_{D,k}^{\mathrm{EN,AV}} + \dot{E}_{D,k}^{\mathrm{EN,UN}} \tag{5.41}$$

Similarly the sum of the exogenous avoidable, $\dot{E}_{D,k}^{\mathrm{EX,AV}}$, and exogenous unavoidable, $\dot{E}_{D,k}^{\mathrm{EX,UN}}$, is the exogenous exergy destruction, $\dot{E}_{D,k}^{\mathrm{EN}}$.

$$\dot{E}_{D,k}^{\mathrm{EX}} = \dot{E}_{D,k}^{\mathrm{EX,AV}} + \dot{E}_{D,k}^{\mathrm{EX,UN}} \tag{5.42}$$

$\dot{E}_{D,k}^{\mathrm{EN,UN}}$ was evaluated using thermodynamic cycles in which the unavoidable efficiency was assigned to the k^{th} component, while the remaining components were ideal. The inputs for these cycles are listed in Table 5.7.

When $\dot{E}_{D,k}^{\mathrm{EN,UN}}$ was calculated $\dot{E}_{D,k}^{\mathrm{EN,AV}}$ was determined using Eq. (5.41) and $\dot{E}_{D,k}^{\mathrm{EX,UN}}$ using Eq. (5.44). $\dot{E}_{D,k}^{\mathrm{EX,AV}}$ was then found using Eq. (5.43).

$$\dot{E}_{D,k}^{\mathrm{AV}} = \dot{E}_{D,k}^{\mathrm{EN,AV}} + \dot{E}_{D,k}^{\mathrm{EX,AV}} \tag{5.43}$$

$$\dot{E}_{D,k}^{\mathrm{UN}} = \dot{E}_{D,k}^{\mathrm{EN,UN}} + \dot{E}_{D,k}^{\mathrm{EX,UN}} \tag{5.44}$$

The r^{th} component effect on the k^{th} The exogenous exergy destruction in the k^{th} component describes the lumped effect of the inefficiencies in the remaining $K-1$ components [50]. This can be split further to quantify the direct implication the inefficiency in the r^{th} component has on the exogenous exergy destruction in the k^{th} component [50]. This was again done by simulation of thermodynamic cycles. Here, the real efficiencies were placed in two components: the k^{th} and the r^{th}. Thereby the contribution from each of the R components to the exogenous exergy destruction of the k^{th} component was evaluated. This contribution was termed $\dot{E}_{D,k}^{\mathrm{EX},r}$

The total exogenous exergy destruction is found not to be equal to the sum of the contributions of the R components. Thereby there exists

an effect of multiple inefficiencies termed the mexogenous effect and consequently mexogenous exergy destruction $\dot{E}_{D,k}^{\mathrm{MX}}$, Eq. (5.45) [50].

$$\dot{E}_{D,k}^{\mathrm{MX}} = \dot{E}_{D,k}^{\mathrm{EX}} - \sum_{\substack{r=1 \\ r\neq k}}^{K-1} \dot{E}_{D,k}^{\mathrm{EX},r} \tag{5.45}$$

With regard to the mixer this further split accounts for the contribution from each of the R components to the exergy destruction caused by mixing. The exergy destruction not directly associated with any of the remaining components was then allocated as mexogenous exergy destruction, $\dot{E}_{D,k}^{\mathrm{MX}}$. The mexogenous exergy destruction in the mixer consequently includes both a part induced by multiple inefficiencies and a part induced only by the placement of the mixer in the system.

Using unavoidable inputs for the r^{th} and k^{th} components in the thermodynamic cycles, $\dot{E}_{D,k}^{\mathrm{MX}}$ and $\dot{E}_{D,k}^{\mathrm{EX,r}}$ were split in avoidable and unavoidable parts.

To evaluate the total rate of exergy destruction associated solely with the inefficiency of the k^{th} component, Eq. (5.46) [84] was used.

$$\dot{E}_{D,k}^{\Sigma} = \dot{E}_{D,k}^{\mathrm{EN}} + \sum_{\substack{k=1 \\ k\neq r}}^{n-1} \dot{E}_{D,r}^{\mathrm{EX},k} \tag{5.46}$$

Likewise, this was done using only the avoidable part, Eq. (5.47). As may be seen these are the endogenous parts of the k^{th} component exergy destruction, plus the sum of the exergy destruction induced in the remaining $K-1$ components.

$$\dot{E}_{D,k}^{\Sigma,\mathrm{AV}} = \dot{E}_{D,k}^{\mathrm{EN,AV}} + \sum_{\substack{k=1 \\ k\neq r}}^{n-1} \dot{E}_{D,r}^{\mathrm{EX,AV},k} \tag{5.47}$$

Based on this another destruction ratio was defined as given by Eq. (5.48).

$$y_k^{*\Sigma,\mathrm{AV}} = \frac{\dot{E}_{D,k}^{\Sigma,\mathrm{AV}}}{\dot{E}_{D,\mathrm{tot}}^{\mathrm{AV}}} \tag{5.48}$$

As seen this is the ratio between total avoidable exergy destruction induced by the k^{th} component and the total avoidable exergy destruction in the system. Thus, $y_k^{*\Sigma,\mathrm{AV}}$ is a measure of each components contribution to the total exergy destruction, similarly to y_k^*. However, $y_k^{*\Sigma,\mathrm{AV}}$ accounts for both component interdependencies and for the reduction potential and thus quantifies which components account for the highest actual rate of exergy destruction that technically can be removed.

Advanced exergoeconomic & exergoenvironmental

The advanced exergoeconomic and exergoenvironmental analysis builds upon the results of a conventional exergoeconomic and exergoenvironmental analysis and an advanced exergy analysis. Splitting the k^{th} component cost and environmental impact into endogenous and exogenous quantifies the extent of the cost and impact, the inefficiency in the k^{th} component is responsible for (endogenous). This consequently also quantifies the cost and impact associated with the inefficiencies in the remaining components (exogenous). This allows the system designer to focus on the components that actually cause the highest cost and impact, instead of the components in which the largest costs and impacts are located.

Splitting the component cost and impact into avoidable and unavoidable parts quantifies the extent of destruction cost and impact and non-exergetic cost and impact that can be avoided. This is related to technological and economic constraints specific to the component. A components unavoidable cost and impact of exergy destruction is the cost and impact when implementing the "state of the art" technology regardless of the high investment. While the unavoidable non-exergetic cost and impact is the cost and impact when implementing the cheapest components on the market regardless of the their low exergy efficiency and thus high cost and impact of exergy destruction. This split allows the system designer to focus on the components with large avoidable costs and impacts, thus the components where savings can actually be achieved in the current technological and economic environment.

As for the advanced exergy analysis, the concepts of endogenous and exogenous and avoidable and unavoidable can be combined, thereby

giving the avoidable and unavoidable parts of both the endogenous and exogenous costs and impact. The exogenous cost and impact of the k^{th} component can be split into the contribution specific to each of the remaining components. This allows the exogenous cost and impact of all components to be allocated to the component that is responsible for it.

Splitting cost and environmental impact of exergy destruction In order to split the cost and environmental impact of exergy destruction in the k^{th} component, it is necessary to know the k^{th} component specific fuel cost and specific fuel environmental impact under real operating conditions, $c_{F,k}^{\text{real}}$ and $b_{F,k}^{\text{real}}$. Further, the different contribution of the k^{th} component exergy destruction rate $\dot{E}_{D,k}$ is necessary. The specific cost of fuel and the specific fuel environmental impact for the k^{th} was determined from the conventional exergoeconomic and exergoenvironmental analysis.

Based on this the cost and impact of exergy destruction was split. The cost and impact of the k^{th} component endogenous exergy destruction was calculated as seen in Eq. (5.49).

$$\dot{C}_{D,k}^{\text{EN}} = c_{F,k}^{\text{real}} \dot{E}_{D,k}^{\text{EN}}, \quad \dot{B}_{D,k}^{\text{EN}} = b_{F,k}^{\text{real}} \dot{E}_{D,k}^{\text{EN}} \tag{5.49}$$

Hereafter, the exogenous cost and impact the k^{th} component was calculated as the difference between the real and the endogenous cost and impact, Eq. (5.50)

$$\dot{C}_{D,k}^{\text{EX}} = \dot{C}_{D,k}^{\text{real}} - \dot{C}_{D,k}^{\text{EN}}, \quad \dot{B}_{D,k}^{\text{EX}} = \dot{B}_{D,k}^{\text{real}} - \dot{B}_{D,k}^{\text{EN}} \tag{5.50}$$

Similarly, the unavoidable cost and impact of the k^{th} component was calculated as seen in Eq. (5.51)

$$\dot{C}_{D,k}^{\text{UN}} = c_{F,k}^{\text{real}} \dot{E}_{D,k}^{\text{UN}}, \quad \dot{B}_{D,k}^{\text{UN}} = b_{F,k}^{\text{real}} \dot{E}_{D,k}^{\text{UN}} \tag{5.51}$$

After which the avoidable cost and impact was calculated as in may be seen in Eq. (5.52).

$$\dot{C}_{D,k}^{\text{AV}} = \dot{C}_{D,k}^{\text{real}} - \dot{C}_{D,k}^{\text{UN}}, \quad \dot{B}_{D,k}^{\text{AV}} = \dot{B}_{D,k}^{\text{real}} - \dot{B}_{D,k}^{\text{UN}} \tag{5.52}$$

The endogenous unavoidable exergy destruction cost and impact of the k^{th} component, $\dot{C}_{D,k}^{\mathrm{EN,UN}}$ and $\dot{B}_{D,k}^{\mathrm{EN,UN}}$, was defined as may be seen in Eq. (5.53) .

$$\dot{C}_{D,k}^{\mathrm{EN,UN}} = c_{F,k}^{\mathrm{real}} \dot{E}_{D,k}^{\mathrm{EN,UN}}, \quad \dot{B}_{D,k}^{\mathrm{EN,UN}} = b_{F,k}^{\mathrm{real}} \dot{E}_{D,k}^{\mathrm{EN,UN}} \tag{5.53}$$

From $\dot{C}_{D,k}^{\mathrm{EN,UN}}$ and $\dot{B}_{D,k}^{\mathrm{EN,UN}}$ the endogenous avoidable and exogenous unavoidable cost and impact was calculated as may be seen in Eqs. (5.54) and (5.55)

$$\dot{C}_{D,k}^{\mathrm{EN,AV}} = \dot{C}_{D,k}^{\mathrm{EN}} - \dot{C}_{D,k}^{\mathrm{EN,UN}}, \quad \dot{B}_{D,k}^{\mathrm{EN,AV}} = \dot{B}_{D,k}^{\mathrm{EN}} - \dot{B}_{D,k}^{\mathrm{EN,UN}} \tag{5.54}$$

$$\dot{C}_{D,k}^{\mathrm{EX,UN}} = \dot{C}_{D,k}^{\mathrm{UN}} - \dot{C}_{D,k}^{\mathrm{EN,UN}}, \quad \dot{B}_{D,k}^{\mathrm{EX,UN}} = \dot{B}_{D,k}^{\mathrm{UN}} - \dot{B}_{D,k}^{\mathrm{EN,UN}} \tag{5.55}$$

The exogenous avoidable destruction cost and impact $\dot{C}_{D,k}^{\mathrm{EX,AV}}$ and $\dot{B}_{D,k}^{\mathrm{EX,AV}}$ was calculated as may be seen in Eq. (5.56).

$$\dot{C}_{D,k}^{\mathrm{EX,AV}} = \dot{C}_{D,k}^{\mathrm{EX}} - \dot{C}_{D,k}^{\mathrm{EN,UN}}, \dot{B}_{D,k}^{\mathrm{EX,AV}} = \dot{B}_{D,k}^{\mathrm{EX}} - \dot{B}_{D,k}^{\mathrm{EN,UN}} \tag{5.56}$$

The total cost and impact of exergy destruction caused by a component, $\dot{C}_{D,k}^{\Sigma}$ and $\dot{B}_{D,k}^{\Sigma}$, was determined as seen in Eq. (5.57). As seen, this is the endogenous exergy destruction cost or impact of the k^{th} component plus the cost or impact of exergy destruction the component induces in the remaining components. With a similar expression the avoidable total cost and impact, $\dot{C}_{D,k}^{\Sigma,\mathrm{AV}}$ $\dot{B}_{D,k}^{\Sigma,\mathrm{AV}}$, was determined.

$$\dot{C}_{D,k}^{\Sigma} = \dot{C}_{D,k}^{\mathrm{EN}} + \sum_{\substack{k=1 \\ k \neq r}}^{K-1} c_{F,r}^{\mathrm{real}} \dot{E}_{D,k}^{\mathrm{EX},r}, \quad \dot{B}_{D,k}^{\Sigma} = \dot{B}_{D,k}^{\mathrm{EN}} + \sum_{\substack{k=1 \\ k \neq r}}^{K-1} b_{F,r}^{\mathrm{real}} \dot{E}_{D,k}^{\mathrm{EX},r} \tag{5.57}$$

The cost and impact of the mexogenenous exergy destruction, $\dot{C}_{D,k}^{\mathrm{MX}}$ and $\dot{B}_{D,k}^{\mathrm{MX}}$, and avoidable mexogenous exergy destruction, $\dot{C}_{D,k}^{\mathrm{MX,AV}}$ and $\dot{B}_{D,k}^{\mathrm{MX,AV}}$, was calculated as seen in Eqs. (5.58) and (5.59).

$$\dot{C}_{D,k}^{\mathrm{MX}} = c_{F,r}^{\mathrm{real}} \dot{E}_{D,k}^{\mathrm{MX}}, \quad \dot{B}_{D,k}^{\mathrm{MX}} = b_{F,r}^{\mathrm{real}} \dot{E}_{D,k}^{\mathrm{MX}} \tag{5.58}$$

$$\dot{C}_{D,k}^{\mathrm{MX,AV}} = c_{F,r}^{\mathrm{real}} \dot{E}_{D,k}^{\mathrm{MX,AV}}, \quad \dot{B}_{D,k}^{\mathrm{MX,AV}} = b_{F,r}^{\mathrm{real}} \dot{E}_{D,k}^{\mathrm{MX,AV}} \tag{5.59}$$

Table 5.8: HACHP design variables to determine the real cost and environmental impact, unavoidable exergy destruction cost and environmental impact and unavoidable non-exergetic cost and environmental impact

k^{th}		Real			$\dot{C}_{D,k}^{UN}$ & $\dot{B}_{D,k}^{UN}$			$\dot{Z}_k^{UN}$ & $\dot{Y}_k^{UN}$		
(1)	CM	η_{is}	=	0.75	η_{is}^{UN}	=	0.95	PEC^{UN}	=	85 % of PEC^{real}
		η_{elec}	=	0.95	η_{elec}^{UN}	=	0.99			
(2)	PM	η_{is}	=	0.85	η_{is}^{UN}	=	0.95	PEC^{UN}	=	85 % of PEC^{real}
		η_{elec}	=	0.95	η_{elec}^{UN}	=	0.99			
(4)	AB	ΔT_{pp}	=	10 K	ΔT_{pp}^{UN}	=	1 K	ΔT_{pp}^{UN}	=	35 K
(6)	IH	ϵ	=	0.8	ϵ^{UN}	=	0.98	ϵ^{UN}	=	0.25
(8)	DS	ΔT_{pp}	=	10 K	ΔT_{pp}^{UN}	=	1 K	ΔT_{pp}^{UN}	=	35 K

Splitting the non-exergetic cost rate and environmental impact In order to split the non-exergetic cost an impact into an avoidable and unavoidable part it is necessary to know the unavoidable PEC, PEC_k^{UN} and unavoidable total environmental impact, TEI_k^{UN}.

For the heat exchange component PEC_k^{UN} and TEI_k^{UN} were determined by calculating the needed heat transfer area in a cycle with high temperature differences and thus high rates of exergy destruction. The inputs for the cycles are listed in Table 5.8.

For the compressor and pump PEC_k^{UN} and TEI_k^{UN} was assumed constant at 85 % of the real value.

Knowing PEC_k^{UN} and TEI_k^{UN}, $\dot{Z}_k^{UN}$ and $\dot{Y}_k^{UN}$ were calculated as seen in Eq. (5.60).

$$\dot{Z}_k^{UN} = \left(\frac{PEC_k^{UN}}{PEC_k^{real}}\right)\dot{Z}_k^{real}, \quad \dot{Y}_k^{UN} = \left(\frac{TEI_k^{UN}}{TEI_k^{real}}\right)\dot{Y}_k^{real} \tag{5.60}$$

Subsequently, the avoidable non-exergetic cost and impact were calculated as the difference between the real and the unavoidable cost and impact, Eq. (5.61).

$$\dot{Z}_k^{AV} = \dot{Z}_k^{real} - \dot{Z}_k^{UN}, \quad \dot{Y}_k^{AV} = \dot{Y}_k^{real} - \dot{Y}_k^{UN} \tag{5.61}$$

To determine the endogenous non-exergetic cost and impact of the k^{th}

component, $\dot{Z}_k^{\mathrm{EN}}$ and $\dot{Y}_k^{\mathrm{EN}}$, it was necessary to know the exergy product of the component under real operating conditions, $\dot{E}_{P,k}^{\mathrm{real}}$, and under endogenous operating condition, $\dot{E}_{P,k}^{\mathrm{EN}}$. The endogenous non-exergetic cost and impact was calculated as seen in Eq. (5.62).

$$\dot{Z}_k^{\mathrm{EN}} = \dot{E}_{P,k}^{\mathrm{EN}} \left(\frac{\dot{Z}_k}{\dot{E}_{p,k}} \right)^{\mathrm{real}}, \quad \dot{Y}_k^{\mathrm{EN}} = \dot{E}_{P,k}^{\mathrm{EN}} \left(\frac{\dot{Y}_k}{\dot{E}_{p,k}} \right)^{\mathrm{real}} \tag{5.62}$$

The exogenous non-exergetic cost and impact was calculated as the difference between the real cost and the calculated endogenous cost, Eq. (5.63).

$$\dot{Z}_k^{\mathrm{EX}} = \dot{Z}_k^{\mathrm{real}} - \dot{Z}_k^{\mathrm{EN}}, \quad \dot{Y}_k^{\mathrm{EX}} = \dot{Y}_k^{\mathrm{real}} - \dot{Y}_k^{\mathrm{EN}} \tag{5.63}$$

The endogenous unavoidable non-exergetic cost and impact, $\dot{Z}_k^{\mathrm{EN,UN}}$ and $\dot{Y}_k^{\mathrm{EN,UN}}$, were defined similarly to the endogenous cost and impact. Again, the exergy product of the component was needed, under both endogenous and unavoidable conditions. $\dot{Z}_k^{\mathrm{EN,UN}}$ and $\dot{Y}_k^{\mathrm{EN,UN}}$ were calculated as seen in Eq. (5.64).

$$\dot{Z}_k^{\mathrm{EN,UN}} = \dot{E}_{P,k}^{\mathrm{EN}} \left(\frac{\dot{Z}_k}{\dot{E}_{p,k}} \right)^{\mathrm{UN}}, \quad \dot{Y}_k^{\mathrm{EN,UN}} = \dot{E}_{P,k}^{\mathrm{EN}} \left(\frac{\dot{Y}_k}{\dot{E}_{p,k}} \right)^{\mathrm{UN}} \tag{5.64}$$

From $\dot{Z}_k^{\mathrm{EN,UN}}$ and $\dot{Y}_k^{\mathrm{EN,UN}}$ the endogenous avoidable and exogenous unavoidable was calculated as may be seen in Eqs. (5.65) and (5.66)

$$\dot{Z}_k^{\mathrm{EN,AV}} = \dot{Z}_k^{\mathrm{EN}} - \dot{Z}_k^{\mathrm{EN,UN}}, \quad \dot{Y}_k^{\mathrm{EN,AV}} = \dot{Y}_k^{\mathrm{EN}} - \dot{Y}_k^{\mathrm{EN,UN}} \tag{5.65}$$

$$\dot{Z}_k^{\mathrm{EX,UN}} = \dot{Z}_k^{\mathrm{UN}} - \dot{Z}_k^{\mathrm{EN,UN}}, \quad \dot{Y}_k^{\mathrm{EX,UN}} = \dot{Y}_k^{\mathrm{UN}} - \dot{Y}_k^{\mathrm{EN,UN}} \tag{5.66}$$

The exogenous avoidable cost and impact, $\dot{Z}_k^{\mathrm{EX,AV}}$ and $\dot{Y}_k^{\mathrm{EX,AV}}$, were calculated as may be seen in Eq. (5.67).

$$\dot{Z}_k^{\mathrm{EX,AV}} = \dot{Z}_k^{\mathrm{EX}} - \dot{Z}_k^{\mathrm{EX,UN}}, \quad \dot{Y}_k^{\mathrm{EX,AV}} = \dot{Y}_k^{\mathrm{EX}} - \dot{Y}_k^{\mathrm{EX,UN}} \tag{5.67}$$

To determine the contribution of the r^{th} component to the exogenous cost and impact of the k^{th} component, $\dot{Z}_k^{\mathrm{EX},r}$ and $\dot{Y}_k^{\mathrm{EX},r}$, it was necessary to know the exergy product of the k^{th} component under operation

with inefficiencies only in the k^{th} and r^{th} component: $\dot{E}_{P,k}^{\mathrm{EN},r}$. From this, $\dot{Z}_k^{\mathrm{EX},r}$ and $\dot{Y}_k^{\mathrm{EX},r}$ were calculated as the difference between the cost with inefficiencies in both components and the endogenous cost, Eqs. (5.68) & (5.69).

$$\dot{Z}_k^{\mathrm{EX},r} = \dot{E}_{P,k}^{\mathrm{EN},r} \left(\frac{\dot{Z}_k}{\dot{E}_{p,k}} \right)^{\mathrm{real}} - \dot{Z}_k^{\mathrm{EN}} \tag{5.68}$$

$$\dot{Y}_k^{\mathrm{EX},r} = \dot{E}_{P,k}^{\mathrm{EN},r} \left(\frac{\dot{Y}_k}{\dot{E}_{p,k}} \right)^{\mathrm{real}} - \dot{Y}_k^{\mathrm{EN}} \tag{5.69}$$

Similarly, the unavoidable part of the r^{th} components contribution to the exogenous cost and impact was calculates as seen in Eqs. (5.70) & (5.71)

$$\dot{Z}_k^{\mathrm{EX,UN},r} = \dot{E}_{P,k}^{\mathrm{EN},r} \left(\frac{\dot{Z}_k}{\dot{E}_{p,k}} \right)^{\mathrm{UN}} - \dot{Z}_k^{\mathrm{EN,UN}} \tag{5.70}$$

$$\dot{Y}_k^{\mathrm{EX,UN},r} = \dot{E}_{P,k}^{\mathrm{EN},r} \left(\frac{\dot{Y}_k}{\dot{E}_{p,k}} \right)^{\mathrm{UN}} - \dot{Y}_k^{\mathrm{EN,UN}} \tag{5.71}$$

Subsequently, the avoidable part was found as seen in Eq. (5.72).

$$\dot{Z}_k^{\mathrm{EX,AV},r} = \dot{Z}^{\mathrm{EX},r} - \dot{Z}^{\mathrm{EX,UN},r}, \quad \dot{Y}_k^{\mathrm{EX,AV},r} = \dot{Y}^{\mathrm{EX},r} - \dot{Y}^{\mathrm{EX,UN},r} \tag{5.72}$$

As for the cost and impact of exergy destruction, there exists a mexogenous non-exergetic cost and impact that accounts for the effect of multiple inefficiencies. The mexogenous non-exergetic cost and impact, $\dot{Z}_k^{\mathrm{MX}}$ and $\dot{Y}_k^{\mathrm{MX}}$, were calculated as seen in Eq. (5.73). A similar expression was applied to determine the avoidable mexogenous non-exergetic cost, $\dot{Z}_k^{\mathrm{MX,AV}}$.

$$\dot{Z}_k^{\mathrm{MX}} = \dot{Z}_k^{\mathrm{EX}} - \sum_{\substack{k=1 \\ k \neq r}}^{K-1} \dot{Z}_k^{\mathrm{EX},r}, \quad \dot{Y}_k^{\mathrm{MX}} = \dot{Y}_k^{\mathrm{EX}} - \sum_{\substack{k=1 \\ k \neq r}}^{K-1} \dot{Y}_k^{\mathrm{EX},r} \tag{5.73}$$

The total non-exergetic cost and impact of the k^{th} component, $\dot{Z}_k^{\Sigma}$ and $\dot{Y}_k^{\Sigma}$, were calculated as the sum of the components endogenous cost and

impact rate and the cost and impact the component induces in the remaining components, Eq. (5.74). Using the avoidable parts a similar expression was used to determine $\dot{Z}_k^{\Sigma,\mathrm{AV}}$.

$$\dot{Z}_k^{\Sigma} = \dot{Z}_k^{\mathrm{EN}} + \sum_{\substack{k=1 \\ k\neq r}}^{K-1} \dot{Z}_{D,k}^{\mathrm{EX},r}, \quad \dot{Y}_k^{\Sigma} = \dot{Y}_k^{\mathrm{EN}} + \sum_{\substack{k=1 \\ k\neq r}}^{K-1} \dot{Y}_{D,k}^{\mathrm{EX},r} \tag{5.74}$$

Based on the results from the advanced exergoeconomic and exergoenvironmental analysis two indicators were determined. The advanced exergoeconomic factor, $f_{c,k}^{\Sigma}$, Eq. (5.75) [83], indicating the impact of the total non-exergetic cost on the total cost. Thereby accounting for component interdependencies which the conventional exergoeconomic factor, $f_{c,k}$, does not. Equally the advanced exergoenvironmental factor, $f_{c,k}^{\Sigma}$, Eq. (5.75)

$$f_{c,k}^{\Sigma} = \frac{\dot{Z}_k^{\Sigma}}{\dot{Z}_k^{\Sigma} + \dot{C}_{D,k}^{\Sigma}}, \quad f_{b,k}^{\Sigma} = \frac{\dot{Y}_k^{\Sigma}}{\dot{Y}_k^{\Sigma} + \dot{B}_{D,k}^{\Sigma}}, \tag{5.75}$$

The advanced exergoeconomic and exergoenvironmental factor was equally calculated using only the avoidable part of the total cost and impact, Eq. (5.76) [83], thus accounting for both component interdependencies and for the technological and economic constraints of the components.

$$f_{c,k}^{\Sigma,\mathrm{AV}} = \frac{\dot{Z}_k^{\Sigma,\mathrm{AV}}}{\dot{Z}_k^{\Sigma,\mathrm{AV}} + \dot{C}_{D,k}^{\Sigma,\mathrm{AV}}}, \quad f_{b,k}^{\Sigma,\mathrm{AV}} = \frac{\dot{Y}_k^{\Sigma,\mathrm{AV}}}{\dot{Y}_k^{\Sigma,\mathrm{AV}} + \dot{B}_{D,k}^{\Sigma,\mathrm{AV}}} \tag{5.76}$$

5.3 Results

5.3.1 Exergy analysis

Thermodynamic analysis of the real cycle

The thermodynamic model has been solved for the operating conditions stated in Table 5.1 and the real cycle component design variables stated in Table 5.6. As a first approach the system design variables were chosen as a rich ammonia mass fraction of x_r = 0.75 and a circulation ratio

Table 5.9: Thermodynamic state points for the real cycle

j^{th}	media	$\dot{m}_j$ (kg/s)	x_j (kg/kg)	T_j (°C)	p_j (bar)	h_j (kJ/kg)	s_j (kJ/kgK)
(1)	NH_3-H_2O	1.64	0.750	44.99	8.384	527.3	2.165
(2)	NH_3-H_2O	0.655	0.997	44.99	8.384	1358	4.637
(3)	NH_3-H_2O	0.655	0.997	161.3	26.37	1607	4.783
(4)	NH_3-H_2O	1.64	0.750	92.40	26.37	692.6	2.444
(5)	NH_3-H_2O	1.64	0.750	73.54	26.32	181.6	1.008
(6)	NH_3-H_2O	1.64	0.750	73.54	26.32	181.6	1.008
(7)	NH_3-H_2O	1.64	0.750	63.76	26.27	117.6	0.822
(8)	NH_3-H_2O	1.64	0.750	31.57	8.434	117.6	0.850
(9)	NH_3-H_2O	0.985	0.585	44.99	8.384	-26.50	0.517
(10)	NH_3-H_2O	0.985	0.585	45.37	26.27	-23.76	0.518
(11)	NH_3-H_2O	0.985	0.585	68.00	26.32	81.26	0.837
(12)	Water	10.0	-	60.00	2.000	251.3	0.831
(13)	Water	10.0	-	80.00	1.950	335.0	1.075
(14)	Water	15.0	-	55.00	2.000	230.4	0.768
(15)	Water	15.0	-	44.30	1.950	186.6	0.629

of f = 0.6. The resulting state points are listed in Table 5.9. It is seen that the high pressure needed to attain the wanted absorber pinch point temperature difference is p_5 = 26.4 bar while the low pressure is p_1 = 8.4 bar, to attain the given desorber pinch point temperature difference. The ammonia mass fraction of the lean solution and the vapour are x_l = 0.59 and x_v = 0.99. The total heat load supplied by the HACHP is $\dot{Q}_{\mathrm{AB}}$ = 837 kW while the total power consumed is $\dot{W}_{\mathrm{tot}} = \dot{W}_{\mathrm{CM}} + \dot{W}_{\mathrm{PM}}$ = 166 kW. Thereby the Coefficient of Performance (COP) for HACHP is $\mathrm{COP} = \dot{Q}_{\mathrm{AB}}/\dot{W}_{\mathrm{tot}}$ = 5.04.

Conventional exergy analysis of the real cycle

Based on the results of the thermodynamic analysis the specific physical and chemical exergy and total exergy flows of all streams have been calculated. These are listed in Table 5.10.

The exergy destruction rates, exergetic efficiency and exergy destruc-

Table 5.10: Real cycle stream specific exergy and total exergy flow rate

j^{th}	media	e_j^{PH} (kJ/kg)	e_j^{CH} (kJ/kg)	e_j (kJ/kg)	$\dot{E}_j$ (kW)
(1)	NH_3-H_2O	150.7	14877	15027	24625
(2)	NH_3-H_2O	296.7	19818	20115	13185
(3)	NH_3-H_2O	502.2	19818	20321	13319
(4)	NH_3-H_2O	231.9	14877	15109	24758
(5)	NH_3-H_2O	149.0	14877	15026	24622
(6)	NH_3-H_2O	149.0	14877	15026	24622
(7)	NH_3-H_2O	141.3	14877	15018	24609
(8)	NH_3-H_2O	132.9	14877	15010	24595
(9)	NH_3-H_2O	52.56	11583	11636	11440
(10)	NH_3-H_2O	54.91	11583	11638	11442
(11)	NH_3-H_2O	64.98	11583	11648	11452
(12)	Water	8.071	-	8.071	80.710
(13)	Water	19.03	-	19.03	190.30
(14)	Water	6.017	-	6.017	90.250
(15)	Water	2.598	-	2.598	38.970

tion ratios for each of the components are listed in Table 5.11. As seen the highest rate of exergy destruction is located in the compressor, this rate corresponds to 26 % of the total exergy destruction and 13 % of the total fuel. The second highest exergy destruction rate is in the absorber while the third highest is located in the desorber. The exergy destruction in these components together account for 71 % of the total exergy destruction. The fourth and fifth largest contributions are from the mixer and the throttling valve. Together these two components account for 26 % of the total destruction rate. The overall system has an exergetic efficiency of 50 %.

Advanced exergy analysis

Avoidable & unavoidable exergy destruction The exergy destruction rates in each component has subsequently been split into its un-

Table 5.11: Results of the conventional and advanced exergy analysis

	Real Cycle										Splitting $\dot{E}_{D,k}$ (kW)						
	$\dot{E}_{F,k}$	$\dot{E}_{P,k}$	$\dot{E}_{D,k}$	ε_k	y_k	y_k^*	$\dot{E}_{D,k}^{UN}$	$\dot{E}_{D,k}^{AV}$	$\dot{E}_{D,k}^{EN}$	$\dot{E}_{D,k}^{EX}$	$\dot{E}_{D,k}^{UN}$ (kW)		$\dot{E}_{D,k}^{AV}$ (kW)		$\dot{E}_{D,k}^{\Sigma}$	$\dot{E}_{D,k}^{AV,\Sigma}$	$y_k^{*\Sigma,AV}$
k^{th}	(kW)	(kW)	(kW)	(%)	(%)	(%)	(kW)	(kW)	(kW)	(kW)	$\dot{E}_{D,k}^{EN,UN}$	$\dot{E}_{D,k}^{EX,UN}$	$\dot{E}_{D,k}^{EN,AV}$	$\dot{E}_{D,k}^{EX,AV}$	(kW)	(kW)	(%)
(1) CM	163	135	28.6	82.5	13.2	26.5	3.06 (11 %)	25.5 (89 %)	17.3 (60 %)	11.3 (40 %)	2.85 (10 %)	0.220 (1 %)	14.4 (50 %)	11.1 (39 %)	18.2	15.2	19.2
(2) PM	2.69	2.30	0.390	85.5	0.180	0.360	0.0700 (25 %)	0.320 (75 %)	0.210 (50 %)	0.180 (50 %)	0.0600 (15 %)	0.0100 (3 %)	0.160 (41 %)	0.160 (41 %)	0.200	0.150	0.180
(3) MI	-	-	13.9	-	6.41	12.9	5.10 (37 %)	8.83 (63 %)	0.000 (0 %)	13.9 (100 %)	0.000 (0 %)	5.10 (37 %)	0.000 (0 %)	8.83 (63 %)	0.000	0.000	0.000
(4) AB	136	110	26.2	80.7	12.1	24.3	8.44 (33 %)	17.8 (67 %)	26.2 (100 %)	0.000 (0 %)	8.45 (32 %)	0 .000 (0 %)	17.8 (68 %)	0.000 (0 %)	36.8	27.8	35.0
(6) IH	12.7	9.90	2.76	78.2	1.27	2.56	0.230 (9 %)	2.52 (91 %)	0.230 (9 %)	2.52 (91 %)	0.110 (4 %)	0.120 (5 %)	0.110 (4 %)	2.41 (87 %)	1.95	1.70	2.13
(7) TV	-	-	13.8	-	6.34	12.8	6.91 (50 %)	6.86 (50 %)	6.38 (46 %)	7.40 (54 %)	6.38 (46 %)	0.540 (4 %)	0.000 (0 %)	6.86 (50 %)	6.45	0.000	0.000
(8) DS	51.3	29.2	22.1	56.8	10.2	20.5	4.51 (21 %)	17.6 (79 %)	24.5 (109 %)	−2.35 (−9 %)	4.61 (20 %)	0.000 (0 %)	19.9 (89 %)	−2.24 (−9 %)	35.0	29.9	37.7
Mexo.	-	-	-	-	-	-	-	-	-	-	-	-	-	-	9.20 (9 %)	4.70 (4 %)	5.95
System	217	110	108	50.4	49.6	100	28.3 (27 %)	79.5 (73 %)	74.8 (69 %)	33.0 (31 %)	22.5 (25 %)	5.99 (2 %)	52.4 (48 %)	27.1 (25 %)	108	74.8	-

Table 5.12: The contribution from each of the R components to the exogenous exergy destruction of k^{th} component and the mexogenous contribution

Affected comp. k^{th}		Causing comp. r^{th} $\dot{E}^{\mathrm{EX}}_{D,k}$ (kW)	$\dot{E}^{\mathrm{EX},r}_{D,k}$ (1) CM (kW)	(2) PM (kW)	(4) AB (kW)	(6) IH (kW)	(7) TV (kW)	(8) DS (kW)	$\dot{E}^{\mathrm{MX}}_{D,k}$ (kW)
(1)	CM	11.3	-	0.00	5.10	0.45	0.10	5.85	-0.20
(2)	PM	0.18	0.00	-	0.10	0.00	0.00	0.10	0.00
(3)	MI	13.9	1.50	0.00	1.75	0.60	0.05	1.60	8.50
(4)	AB	0.00	-0.05	0.00	-	0.15	0.00	-0.05	-0.05
(6)	IH	2.52	-0.05	0.00	1.00	-	0.00	1.10	0.45
(7)	TV	7.40	-0.30	0.00	3.10	0.55	-	2.30	1.80
(8)	DS	-2.35	-0.15	0.00	-0.60	-0.10	-0.10	-	-1.20
$\sum_{\substack{k=1 \\ k\neq r}}^{n-1} \dot{E}^{\mathrm{EX},k}_{D,r}$		33.0	0.95	0.00	10.5	1.70	0.05	10.9	9.40

avoidable and avoidable parts. These are listed in Table 5.11. As seen 79.5 kW exergy destruction can be avoided, this corresponds to 73 % of the total exergy destruction. This is mainly achieved by a reduction of the exergy destruction in the compressor, absorber and desorber. A total of 60.9 kW can be avoided in these three components.

The highest percentage of avoidable exergy destruction is found in the IHEX, where 91 % of the exergy destruction can be avoided. Second highest is the compressor with 89 %. In the desorber and absorber 79 % and 67 %, respectively, can be avoided. The lower percentage of avoidable exergy destruction for the absorber and desorber is caused in part by the non-linearity of the equilibrium absorption and desorption curves and in part by a mismatch of the temperature glides between the sink/source and the absorption/desorption processes. Therefore, even when the pinch point temperature difference is reduced, significant temperature differences in other parts of the heat exchanger still exists.

The lowest percentage of avoidable exergy destruction is found in the mixer and throttling valve with 63 % and 50 %, respectively.

A total of 28.3 kW of exergy destruction cannot be avoided mainly due to the unavoidable exergy destruction in the absorber, throttling

valve and mixer.

Endogenous & exogenous exergy destruction. The exergy destruction was also split into the endogenous and exogenous parts. The results of this split is also presented in Table 5.11. It shows that for the total system 74.8 kW of exergy destruction is endogenous. Thereby, only 69 % of the total exergy destruction is caused by the component in which it is located. The remaining 31 % is related to component interdependencies and is thus exogenous.

It is seen that the absorber exergy destruction is purely endogenous meaning that all exergy destruction can be allocated to the absorber pinch point temperature difference. This result deviates from the results of [68, 72], in which the condenser exergy destruction is found to be around 25 % exogenous, this is mainly associated with the evaporator and compressor inefficiency. Both of these induce higher compressor discharge temperature and thus higher temperature difference in the condenser. In the HACHP, the desorber and compressor inefficiency also induce increased compressor discharge temperature but this causes increased exergy destruction in the mixer not the absorber. Thus, the mixer decouples the exergy destruction in the absorber from the remaining components.

It may be seen that the exogenous exergy destruction in the desorber is negative. This means that increasing the exergy efficiency of the remaining components increases the exergy destruction in the desorber. This can be explained by the temperature - heat load diagram seen in Fig. 5.2 (a). Here, the heat transfer processes of the real cycle and the desorber thermodynamic cycle are depicted. As may be seen the profiles of both the real and desorber cycle are close to identical but the increase of the exergy efficiency of the remaining components leads to an increase of the desorber load, because the specific enthalpy at the desorber inlet is reduced. Therefore, although the desorber exergy efficiency of the two cycles is approximately the same the increased load results in an increased absolute exergy destruction rate. This is a similar conclusion as the "effect of mass flow rate" discussed in [67, 72].

For the compressor only 60 % of the component exergy destruction is associated with the component itself while the remaining 40 % is

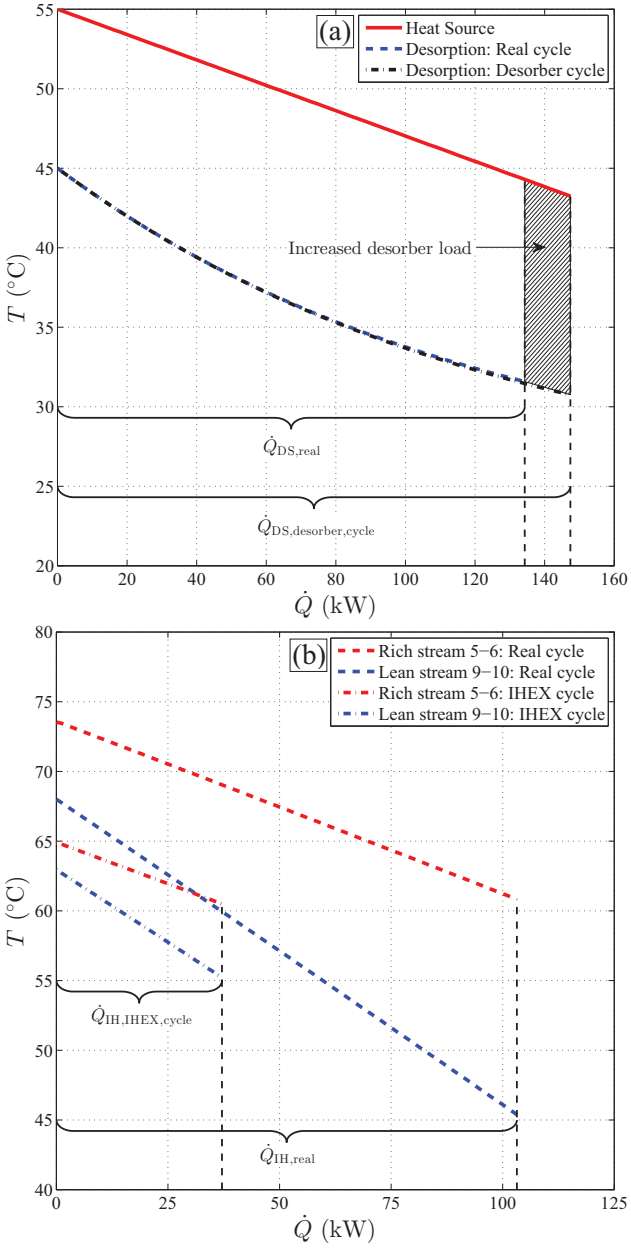

Figure 5.2: Temperature - heat load diagram of the real cycle and thermodynamic cycle for evaluation of endogenous exergy destruction (a) desorber (b) IHEX

induced by the remaining components. This can be rationalised as increasing the pinch point temperature differences in the absorber and desorber leads to a higher pressure ratio over the compressor and thus leads to a higher rate of exergy destruction.

For the IHEX it is seen that 91 % of the exergy destruction is exogenous meaning that the IHEX exergy destruction is almost only associated with the remaining components. A temperature - heat load diagram depicting the heat transfer of the real and IHEX thermodynamic cycle is seen in Fig. 5.2 (b). Here, it is seen that as the efficiency of the remaining components is increased, the temperature gap between the lean liquid and rich liquid is reduced. Therefore, for the same IHEX effectiveness the heat load is reduced and so is the temperature difference between the two streams. Thus, the IHEX exergy efficiency is increased and heat load is reduced by improving the remaining components. Both leading to a high percentage of exogenous exergy destruction.

For the throttling valve the endogenous and exogenous are close to equal with 46 % and 54 % respectively. Similar results for the splitting of throttling valve exergy destruction are presented in [67, 68, 72].

Combined split of avoidable & unavoidable and endogenous & exogenous The two splits have been combined to evaluate the avoidable and unavoidable parts of both the endogenous and exogenous exergy destruction. The results are listed in Table 5.11. By examining only the avoidable part of the endogenous and exogenous exergy destruction a better insight as to how the cycle is improved is found.

It is here apparent that the exergy destruction in the mixer and throttling valve can only be avoided by increasing the efficiency of other components. For the throttling it should be noted that the improved exergy efficiency of the system attained by replacing the valve with a turbine is assumed to be unavoidable as no commercial solution exists for such a component. If such a solution existed the result would be different.

The exergy destruction in the compressor can be reduced almost equally by improving the component itself or by improving other components. The exergy destruction in the absorber and desorber can only be reduced by increasing their own efficiencies. Further, it is seen that

the exogenous avoidable destruction in the desorber is negative. Thus, improving the exergy efficiency of the other components will cause an increase of the exergy destruction in the desorber.

The r^{th} component effect on the k^{th} As may be seen in Table 5.11 33 kW of the exergy destruction is exogenous. This corresponds to 31 % of the total exergy destruction and it is thus of interest to allocate this destruction rate to the inefficiency of the component that induces it. Therefore, the exogenous exergy destruction has been split into its contribution from the r^{th} component and a mexogenous contribution. These are listed in Table 5.12.

The highest exogenous exergy destruction rate is found in the mixer. Here, it is seen that this is induced mainly by the absorber, desorber and compressor and with a minor contribution from the IHEX. Further, it is seen that the highest contribution is the mexogenous destruction rate accounting for 60 %.

The second highest rate of exogenous exergy destruction is found in the compressor. From Table 5.12 it is apparent that this is mainly caused by the desorber and absorber inefficiency. This means that improving the desorber and absorber also improves the compressor.

The third highest exogenous exergy destruction is found in the throttling valve. This is mainly caused by the absorber and desorber and a mexogenous contribution.

By summing the contribution of the remaining $K-1$ components to the k^{th} component the main source of exogenous exergy destruction was found. As seen in Table 5.12, 21.3 kW of the exogenous exergy destruction is inherent to the absorber (10.5 kW) and desorber (10.9 kW) corresponding to 64 % of the total exogenous exergy destruction. Of the total exogenous exergy destruction, 28 % is allocated as mexogenous which is mainly the exergy destruction related to mixing.

The total exergy destruction related to each component $\dot{E}_{D,k}^{\Sigma}$ was found. These values are listed in Table 5.11. Here, it is seen that the absorber and desorber each account for approximately 33 % of the total exergy destruction while the compressor accounts for 17 %.

These values have also been found in avoidable terms to calculate the values of $\dot{E}_{D,k}^{\mathrm{AV},\Sigma}$ and $y_k^{*\Sigma,\mathrm{AV}}$, these are listed in Table 5.11. From this

it may be seen that the most important component for avoiding exergy destruction is the desorber with a total of 29.9 kW or 38 % of the total avoidable exergy destruction. The second highest is the absorber with 35 % and third is the compressor with 19.2 %.

In total 92 % of the avoidable exergy destruction can be attributed to the inefficiencies in these three components. This is a significantly different result than provided by the conventional exergy analysis in which these components together account for only 71 % of the total exergy destruction. Further, it is seen that the order of which the components should be improved, is not the same for the conventional and advanced exergy analysis. The conventional exergy analysis suggests the order of importance to be: compressor, absorber and desorber, while the conclusion from the advanced exergy analysis is: desorber, absorber and then compressor.

Design optimization using advanced exergy analysis

To evaluate the effect of the system design parameters, rich ammonia mass fraction, x_r, and circulation ratio, f, the advanced exergy analysis has been applied for a variation of the two parameters. The operating conditions were kept constant and equal to the values stated in Table 5.1.

Fig. 5.3 shows the HACHP: COP (Fig. 5.3 (a)), $\dot{E}_{D;\mathrm{tot}}$ (Fig. 5.3 (b)), $\dot{E}^{\mathrm{AV}}_{D;\mathrm{tot}}$ (Fig. 5.3 (c)) and $\dot{E}^{\mathrm{AV}}_{D;\mathrm{tot}}$ (Fig. 5.3 (d)). As may be seen, COP and the total exergy destruction rate is highly influenced by the choice of x_r and f. It is seen that for each value of x_r there exists one value of f that optimizes the COP, choosing a value above or below this value will lead to a reduction. Further, it may be seen that there is a direct link between the exergy destruction and the COP. The combinations of x_r and f that yield a high COP yield a low rate of exergy destruction. This behaviour was expected as the operating conditions and system exergy product were kept constant.

It should be noted that especially the area in which the circulation ratio is chosen below the optimal value, there is a severe increase in exergy destruction and consequently reduction of COP. By examining Figs. 5.3 (c) and 5.3 (d) it can be concluded that the increased exergy

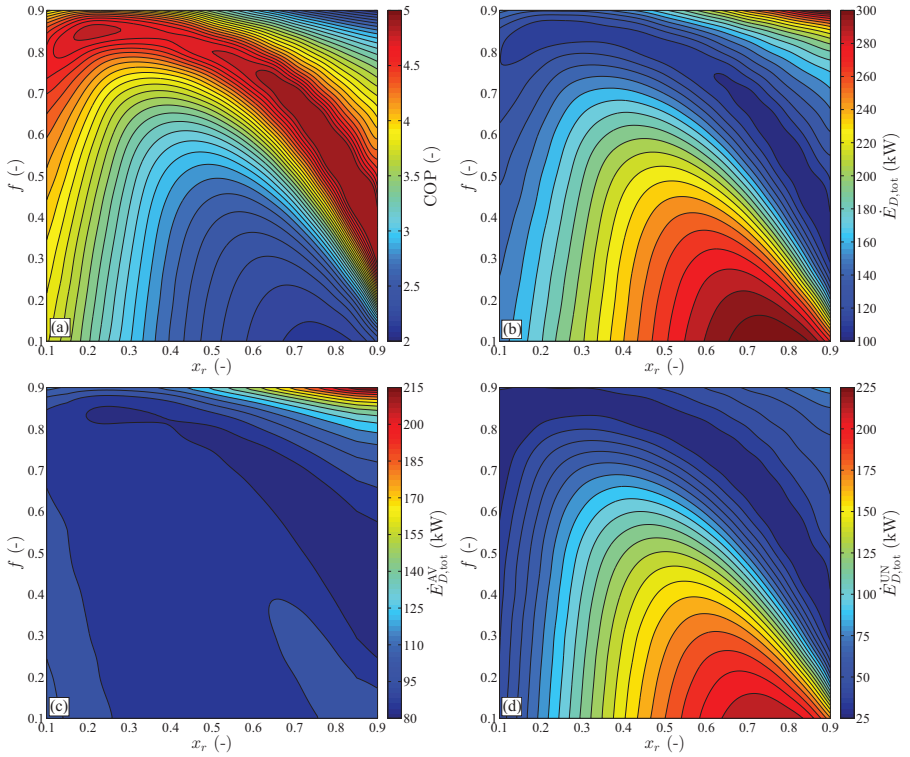

Figure 5.3: Influence of the ammonia mass fraction x_r and circulation ratio f on: (a) COP, (b) total exergy destruction, (c) total avoidable exergy destruction and (d) the total unavoidable exergy destruction.

destruction in this area is unavoidable. On the other hand the increased destruction that exists for values of circulation ratio above the optimum is mainly avoidable.

To attain a more complete understanding of which components are responsible for this increase the values of $\dot{E}^{\Sigma}_{D,k}$ are plotted for the compressor + pump, absorber, desorber and throttling valve. This is displayed in Fig. 5.4 along with the mexogenous exergy destruction. From Fig. 5.4 it may be seen that the increased exergy destruction in the area with circulation ratios below optimum is caused by an increase in all components except the IHEX. Further, it is seen that the increase is largest in the absorber and desorber, peaking at a value of approximately 115 kW.

Fig. 5.5 shows the total unavoidable exergy destruction $\dot{E}_{D,k}^{\Sigma,\mathrm{UN}}$, associated with the absorber (Fig 5.5 (a)) and desorber (Fig 5.5 (b)). The trend for the unavoidable exergy destruction is similar to the total exergy destruction seen in Fig. 5.4. It is seen that the unavoidable exergy destruction peaks at approximately 100 kW for the absorber and 90 kW for the desorber. Hence, at the peak, approximately 87 % of the absorber exergy destruction is unavoidable, this is 78 % for the desorber.

Based on this it can be concluded that in the area with circulation ratios below optimum the increase in unavoidable exergy destruction can mainly be attributed to the absorber and desorber.

Figs. 5.6 & 5.7 depicts the temperature - heat load diagram for two HACHP processes with x_r = 0.5, one with the optimum circulation ratio f = 0.8 (Fig. 5.6) and one with a circulation ratio below optimum f = 0.3 (Fig. 5.7). Examining these two diagrams it is evident why this unavoidable exergy destruction occurs in the absorber and desorber. In Fig. 5.7 it is seen that the curvature of the equilibrium absorption and desorption curves are far from matching those of the sink and source thus increasing the thermal exergy destruction. The majority of this temperature difference is unavoidable as reducing the pinch point temperature difference does not lead to any significant change in the curvature of the absorber and desorption process. Further, it is seen that only a small amount of the unavoidable temperature difference is due to the technological limitations.

By examining Fig. 5.6 it is seen that the curvature of both the absorption and desorption processes match the glides of the sink and source better than for the system seen in Fig. 5.6. Thus, the total exergy destruction is reduced because of the reduction of the temperature difference. Further, the unavoidable exergy destruction is reduced as most of the temperature difference can be avoided by reducing the pinch point temperature difference.

Another conclusion that should be drawn from Figs. 5.6 & 5.7 is that the combination of x_r and f that yields high exergy destruction rates for the operating conditions used in this study will not necessarily be the same for another operating condition. Hence, if the absorber temperature glide was increased to around 70 K the curvature of the absorption process seen in Fig. 5.6 would be more beneficial than that seen in Fig.

5.7. Therefore, it is important to find the correct combination of x_r and f related to the desired operating conditions.

5.3.2 Exergoeconomic analysis

Conventional exergoeconomic analysis of the HACHP system

As discussed in Chapter 4 the choice of ammonia mass fraction is expected to have an influence on the two-phase heat transfer coefficients of the absorber and desorber and thus on the investment of these components. Generally the absorber and desorber investment is expected to be lowest when x_r approaches 0 or 1. Further, as described in Chapter 2, reducing the ammonia mass fraction reduces the suction line pressure, which leads to an increased compressor displacement volume and thus increased compressor investment.

It is thus relevant to evaluate how the choice of ammonia mass fraction and circulation ratio influences the over all cost of the HACHP system. Fig. 5.8 shows the cost rate of system product, $\dot{C}_{P,\mathrm{sys}}$, system fuel, $\dot{C}_{F,\mathrm{sys}}$, the cost of system exergy destruction, $\dot{C}_{D,\mathrm{sys}}$ and the total non-exergetic cost rate, $\dot{Z}_{\mathrm{tot}}$. The hatched area indicates the regions in which the compressor discharge pressure and temperature are above the limits of commercially available components.

As seen in Fig. 5.8 the cost of operating the system (measured by $\dot{C}_{F,\mathrm{sys}}$ or $\dot{C}_{D,\mathrm{sys}}$) follows the same trend as the COP presented in Chapter 2 and 3, while, the total non-exergetic cost rate, $\dot{Z}_{\mathrm{tot}}$, increases with decreasing ammonia mass fraction. The total cost of the system is measured by $\dot{C}_{P,\mathrm{sys}}$ (sum of $\dot{C}_{F,\mathrm{sys}}$ and $\dot{Z}_{\mathrm{tot}}$) is seen in Fig. 5.8. From Fig. 5.8 it can be concluded that reducing ammonia mass fraction increases the total cost of the system mainly due to the increased investment.

To gain a deeper understanding of which components are responsible for the increased investment and to evaluate if these increases can be avoided by design improvements the advanced exergoeconomic analysis is applied to the three combinations of ammonia mass fraction and circulation ratio marked by the three dots in Fig. 5.8.

Figure 5.4: $\dot{E}^{\Sigma}_{D,k}$ for the compressor + pump, absorber, IHEX, throttling valve, desorber and the mexogenous exergy destruction $\dot{E}^{\mathrm{MX}}_{D,k}$

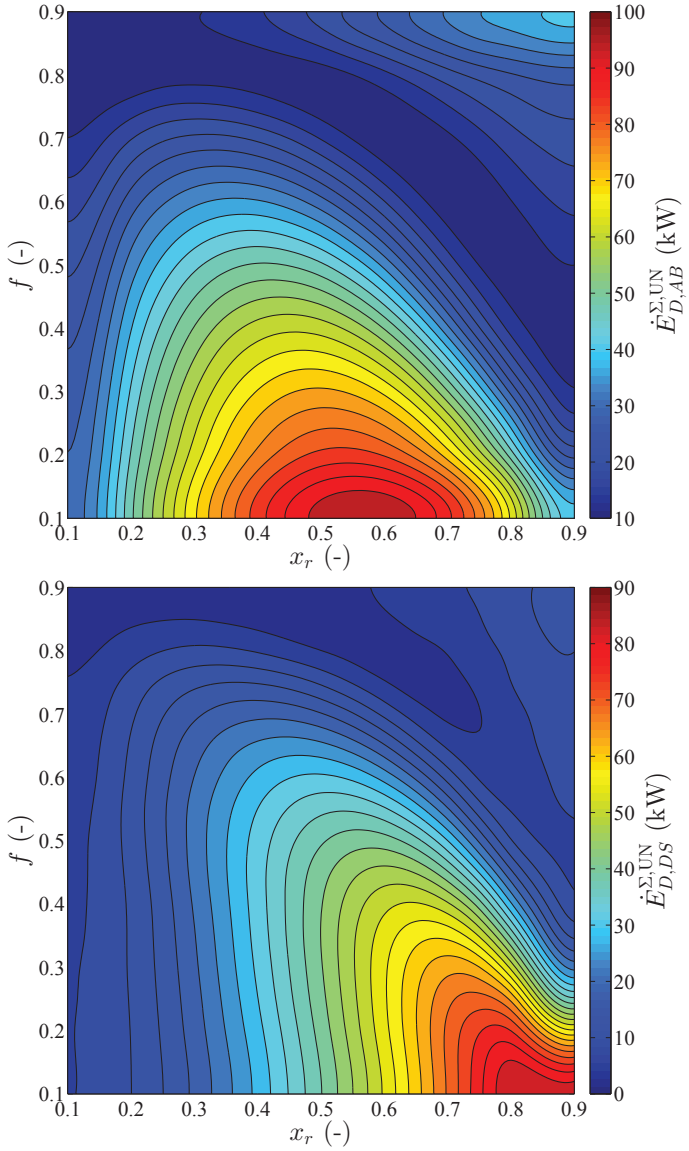

Figure 5.5: $\dot{E}_{D,k}^{\Sigma,\mathrm{UN}}$ for the absorber (a) and the desorber (b)

Advanced exergoeconomic analysis

Splitting the cost rate of exergy destruction Splitting the cost of exergy destruction for these three combinations of ammonia mass fraction

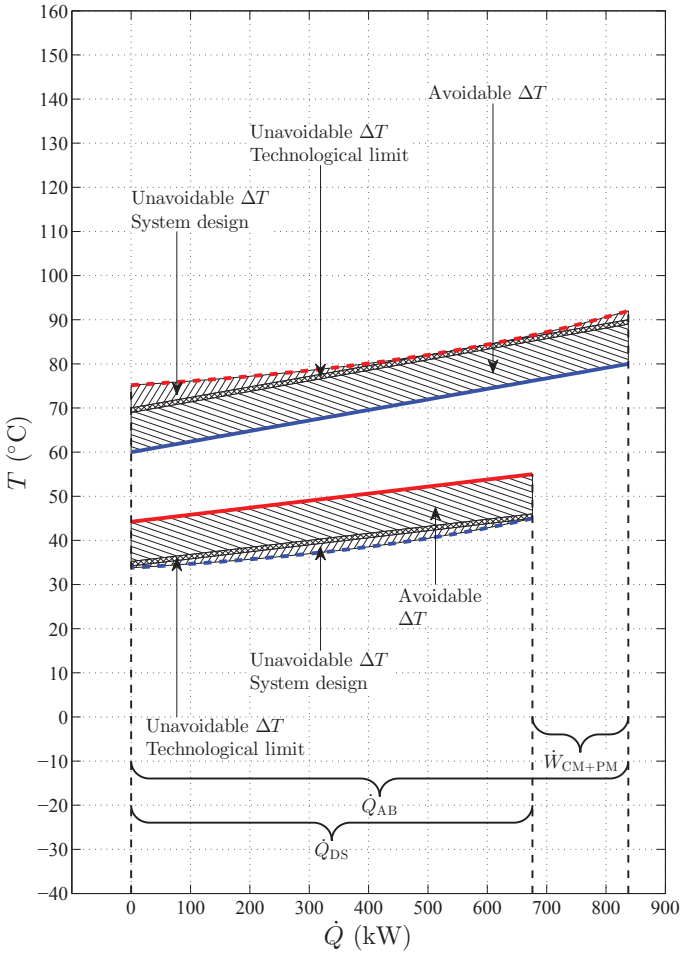

Figure 5.6: Temperature heat load diagram for the HACHP process with x_r = 0.5 and f = 0.8

and circulation ratio yields the results presented in Table 5.13.

By first examining the components real cost of exergy destruction, $\dot{C}_{D,k}^{\mathrm{real}}$, it may be seen that decreasing the ammonia mass fraction from x_r = 0.85 to x_r = 0.70 results in an increase in the exergy destruction cost of 55 ct/h, mainly due to the increased cost of the absorber and IHEX. A further decrease of the ammonia mass fraction to x_r = 0.55 causes a further increase of 94 ct/h, again caused by the increased destruction

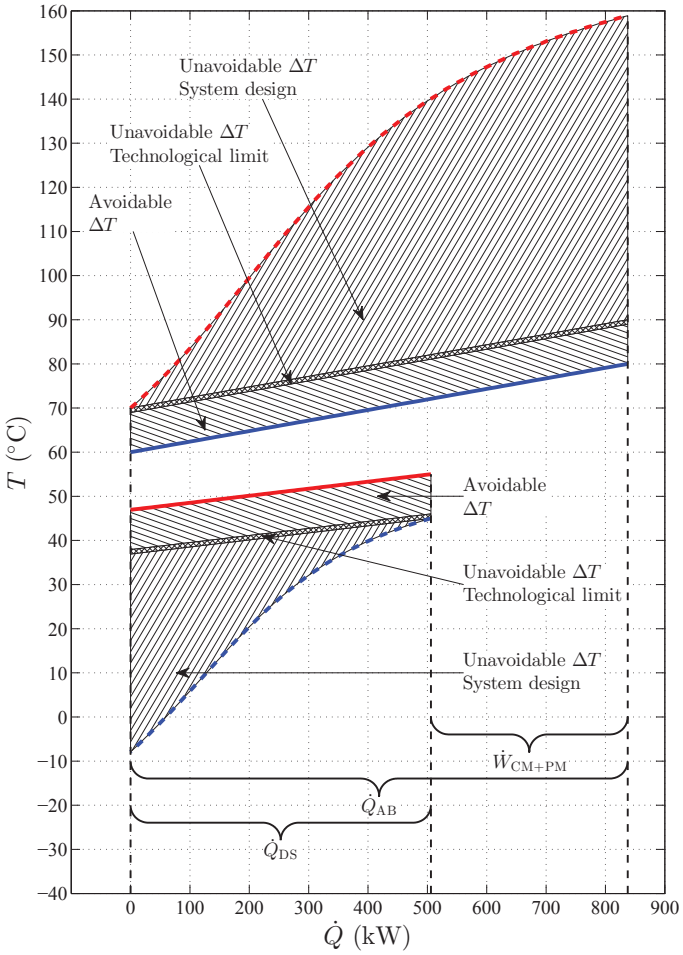

Figure 5.7: Temperature heat load diagram for the HACHP process with $x_r = 0.5$ and $f = 0.3$

cost in the absorber and IHEX. The increased cost of destruction in the IHEX is caused by the increased circulation ratio which results in more heat transfer between the lean and rich mixture. The increased destruction cost in the absorber is caused by an increased mismatch between the profiles of the sink and the absorption process, thus leading to increased thermal exergy destruction. This is evident as the increased destruction cost in the absorber is mainly unavoidable.

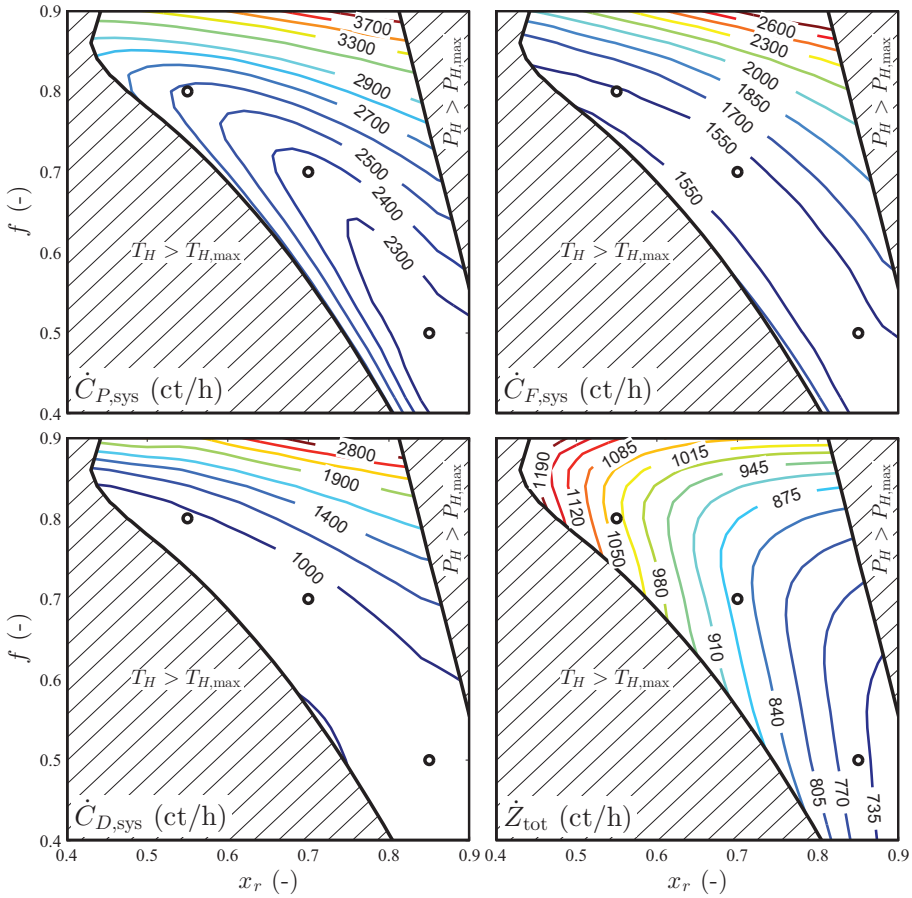

Figure 5.8: Variation of system product cost, fuel cost, exergy destruction cost and total non-exergetic cost with the ammonia mass fraction and circulation ratio

The main source of unavoidable exergy destruction, for all three ammonia mass fractions, is found in the absorber. The exergy destruction cost in the remaining components is mainly avoidable. Splitting the destruction cost into endogenous and exogenous reveals that the exergy destruction cost in the absorber is mainly endogenous while the destruction cost in the IHEX is mainly exogenous. The compressor cost is approximately 60 % endogenous.

Table 5.14 and 5.15 show a further split of the cost of avoidable ex-

ogenous exergy destruction cost into the contribution specific to the r^{th} component and a mexogeonous contribution. Here, it is seen that the main source of avoidable exogenous cost is induced by the desorber. This destruction cost is induced in the compressor and IHEX. The second highest contribution to the exogenous cost is induced in the absorber also causing destruction in the compressor and IHEX.

The total exergy destruction cost related to the component, $\dot{C}^{\Sigma}_{D,k}$, is listed in Table 5.13. Here, it is seen that accounting for interdependencies, allocates more destruction cost to the absorber, while less is associated with the compressor. The absorber and compressor still account for the most exergy destruction cost, 64 % and 37 %, respectively (for x_r = 0.85). For the conventional analysis this is 52 % and 40 %. Further, accounting for component interdependencies reveals that 10 % of the destruction cost is associated with the desorber.

The total avoidable exergy destruction cost related to the component, $\dot{C}^{\Sigma,\mathrm{AV}}_{D,k}$, is equally listed in Table 5.13. The cost associated with the absorber is still the highest, accounting for 57 %, followed by the compressor 24 % and 14 % stems from the desorber. As for the real destruction cost, decreasing the ammonia mass fraction increases the cost associated with the absorber and IHEX.

Splitting the non-exergetic cost rates Splitting the non-exergetic cost rates for the three ammonia mass fractions yields the results presented in Table 5.16.

Examining the real non-exergetic cost rate, $\dot{Z}^{\mathrm{real}}_{k}$, it is evident that the highest investment is located in the compressor. Dependent on the ammonia mass fraction the real non-exergetic cost rate of the compressor accounts for 72 % to 75 % of the total non-exergetic cost rate. For x_r = 0.85 the second highest cost rate is found in the absorber (12 %), followed by the desorber (8 %), IHEX (4 %) and finally the pump (1 %). Decreasing the ammonia mass fraction to x_r = 0.70 increases the cost rate in all components, however the order and distribution remains the same. Decreasing the ammonia mass fraction to x_r = 0.55, results in an increased cost rate in the compressor, IHEX and desorber, while resulting in a slight decrease in the absorber and pump. The increased cost in the IHEX causes the IHEX cost rate to exceed that of the desorber.

Table 5.13: Splitting cost of exergy destruction

k^{th}	$\dot{C}_{D,k}^{real}$ (¢/h)	$\dot{C}_{k}^{AV}$ (¢/h)	$\dot{C}_{k}^{UN}$ (¢/h)	$\dot{C}_{k}^{EN}$ (¢/h)	$\dot{C}_{k}^{EX}$ (¢/h)	$\dot{C}_{D,k}^{EN,AV}$ (¢/h)	$\dot{C}_{D,k}^{EN,UN}$ (¢/h)	$\dot{C}_{D,k}^{EX,AV}$ (¢/h)	$\dot{C}_{D,k}^{EX,UN}$ (¢/h)	$\dot{C}_{D,k}^{\Sigma}$ (¢/h)	$\dot{C}_{D,k}^{\Sigma,AV}$ (¢/h)
x_r=0.85 & f=0.50											
(1) CM	312.3	279.4	33.0	188.3	124.1	157.3	31.0	122.1	2.0	182.4	152.6
(2) PM	4.3	3.6	0.7	2.6	1.7	1.9	0.7	1.6	0.0	2.4	1.8
(4) AB	411.9	252.0	159.6	417.6	-6.1	256.7	161.0	-4.7	-1.4	496.2	330.2
(6) IH	53.8	47.3	6.6	7.4	46.5	2.9	4.5	44.4	2.0	14.6	6.6
(8) DS	0.0	0.0	0.0	0.0	0.0	0.0	0.0	0.0	0.0	82.3	80.4
Sys.	782.3	582.2	199.9	615.9	166.2	418.7	197.2	163.5	2.7	777.8	571.5
x_r=0.70 & f=0.70											
(1) CM	308.7	277.3	31.3	179.0	129.6	149.7	29.3	127.6	2.0	166.6	139.0
(2) PM	6.1	5.1	1.1	3.6	2.5	2.7	0.9	2.4	0.1	2.5	1.6
(4) AB	453.0	279.6	173.5	461.3	-8.2	286.1	175.2	-6.5	-1.7	541.3	358.9
(6) IH	70.1	63.9	6.1	8.3	61.8	4.5	3.8	59.5	2.3	24.9	13.3
(8) DS	0.0	0.0	0.0	0.0	0.0	0.0	0.0	0.0	0.0	81.8	80.3
Sys.	837.9	626.0	211.9	652.2	185.7	443.0	209.2	183.0	2.8	817.1	592.9
x_r=0.55 & f=0.80											
(1) CM	317.0	284.2	32.5	184.9	131.7	154.5	30.4	129.7	2.0	169.2	139.8
(2) PM	5.8	4.8	1.0	3.4	2.4	2.5	0.9	2.3	0.1	3.3	2.4
(4) AB	513.3	321.0	190.3	516.3	-5.0	324.4	191.8	-3.4	-1.5	603.8	402.7
(6) IH	96.2	88.4	7.5	11.4	84.5	6.4	5.1	82.0	2.5	34.2	19.8
(8) DS	0.0	0.0	0.0	0.0	0.0	0.0	0.0	0.0	0.0	87.9	86.3
Sys.	932.3	698.3	231.3	716.0	213.6	487.8	228.3	210.6	3.1	898.4	651.0

Table 5.14: Splitting the exergetic avoidable exogenous cost of the k^{th} component into the contribution specific to the r^{th} component and a mexogenous contribution

k^{th}	r^{th} $\dot{C}_{D,k}^{EX,AV,r}$	(1) CM $\dot{C}_{D,k}^{EX,AV,r}$ (¢/h)	(4) AB $\dot{C}_{D,k}^{EX,AV,r}$ (¢/h)	(5) IH $\dot{C}_{D,k}^{EX,AV,r}$ (¢/h)	(7) DS $\dot{C}_{D,k}^{MX,AV}$ (¢/h)	Mexo. (¢/h)
(1)	CM	0.0	52.0	3.7	62.7	3.8
(2)	PM	-0.1	1.2	0.0	0.6	-0.1
(4)	AB	-3.4	0.0	0.0	-3.2	2.1
(6)	IH	-1.1	20.3	0.0	20.3	5.0
(8)	DS	0.0	0.0	0.0	0.0	0.0
$\sum_{\substack{k=1 \\ k\neq r}}^{n-1}$		-4.7	73.5	3.7	80.4	-

Table 5.15: Splitting the non-exergetic avoidable exogenous cost of the k^{th} component into the contribution specific to the r^{th} component and a mexogenous contribution

k^{th}	r^{th}	(1) CM $\dot{Z}_k^{EX,AV,r}$ (¢/h)	(4) AB $\dot{Z}_k^{EX,AV,r}$ (¢/h)	(5) IH $\dot{Z}_k^{EX,AV,r}$ (¢/h)	(7) DS $\dot{Z}_k^{EX,AV,r}$ (¢/h)	Mexo. $\dot{Z}_k^{MX,AV}$ (¢/h)
(1)	CM	0.0	16.2	1.0	17.6	2.3
(2)	PM	0.0	0.4	0.0	0.1	0.0
(4)	AB	0.0	0.0	0.0	0.0	0.0
(6)	IH	-1.0	10.3	0.0	3.8	-1.8
(8)	DS	0.0	0.2	1.4	0.0	-2.1
$\sum_{\substack{k=1 \\ k\neq r}}^{n-1}$		-1.1	27.1	2.4	21.5	-

Thus, the order becomes: compressor (74 %), absorber (9 %), IHEX (8 %), desorber (7 %) and finally the pump (1 %).

Splitting the non-exergetic cost into avoidable and unavoidable reveals that the highest rate of unavoidable investment is located in the compressor. For x_r = 0.85 the compressor thus only accounts for 40

% of the total avoidable non-exergetic cost, followed by the absorber (27 %), desorber (20 %), IHEX (12 %) and finally the pump (0.5 %). Decreasing the ammonia mass fraction to x_r = 0.70 yields an increased avoidable cost rate in all components, the largest increase in the found in the IHEX, the distribution thus becomes, compressor (35 %), absorber (24 %), desorber (22 %), IHEX (20 %) and pump (1 %). A further reduction to x_r = 0.55 causes an increase in all components except for the pump. Again the increase is highest in the IHEX resulting in a change of both the order and the distribution of the unavoidable non-exergetic cost rates. The order becomes, compressor (36 %), IHEX (24 %), absorber (20 %), desorber (19 %) and pump (1 %). Accounting for the avoidability of investment, reveals that the attention should be focused on the heat transfer components rather than the compressor.

Splitting the non-exergetic cost into endogenous and exogenous reveals that the absorber investment is all endogenous. This, as the absorber product is kept constant. The desorber exhibits a negative exogenous cost rate, which implies that a decrease in the desorber investment results in an increased investment in the remaining components. The compressor and pump show a close to equal distribution between the endogenous and exogenous cost. The IHEX is found to have the second highest exogenous cost rate. The distribution for x_r = 0.85 is 60 % endogenous and 40 % exogenous. Decreasing the ammonia mass fraction to x_r = 0.70 changes the distribution to 42 % endogenous and 58 % exogenous. A further decrease to x_r = 0.55 results in only 38 % of the non-exergetic cost rate of the IHEX to be endogenous and thus 62 % to be exogenous. This change is a result of the increased circulation ratio, which results in a greater dependence on the IHEX.

Splitting the endogenous and exogenous non-exergetic cost rate into avoidable and unavoidable shows that the main source of avoidable non-exergetic cost, on a system level, is endogenous. However, a reduction of the ammonia mass fraction shifts the distribution towards the exogenous cost. For x_r = 0.85: 77 % of the system cost is endogenous, reducing the ammonia mass fraction to x_r = 0.70, reduces this to 73 % and a further reduction to x_r = 0.55 results in 60 % endogenous cost. The main source of exogenous avoidable cost is found the compressor and IHEX.

Between 23 % and 31 % of the avoidable non-exergetic cost is exogenous, it is therefore relevant to allocate this cost to the component that induces it. Table 5.14 and 5.15 show the contribution of the r^{th} component to the k^{th} component avoidable exogenous non-exergetic cost, $\dot{Z}_k^{\mathrm{EX,AV},r}$. The results in Table 5.14 and 5.15 are for an ammonia mass fraction of x_r = 0.85. As may be seen the main source of avoidable exogenous cost is associated with the absorber and desorber. Both induces exogenous avoidable cost in the compressor and IHEX.

The total avoidable non-exergetic cost rate, $\dot{Z}_k^{\Sigma,\mathrm{AV}}$, accounting for both avoidability and interdependencies is listed in Table 5.16. As may be seen this yields a significantly different results than that attained from the conventional analysis. Here, it is seen that for all ammonia mass fractions the highest cost rate is associated with the absorber (38 %-40 %), the second highest is the desorber (31 %-34 %) followed by the compressor (18 %-22 %) and finally the IHEX (8 %-10 %). The pump is shown to have no significant contribution to the total non-exergetic cost.

Comparison of the three ammonia mass fractions Table 5.17, compares the results of the three ammonia mass fractions for the conventional and advanced exergoeconomic analysis. The total component cost (sum of $\dot{C}_{D,k}^{\mathrm{real}}$ and $\dot{Z}_k^{\mathrm{real}}$) for the conventional exergoeconomic analysis is shown along with the conventional exergoeconomic factor, $f_{c,k}$ and the relative cost difference, r. This shows the highest total cost to be associated with the compressor. The compressor also has the highest relative cost difference and thus judging from the conventional analysis the compressor is the most important component for the improvement of the HACHP. The compressors conventional exergoeconomic factor is 64 %-70 % which indicates that the compressor investment should be reduced to attain cost savings.

The second highest real total cost is found in the absorber, however this component has the lowest relative cost difference. The absorber exergoeconomic factor is between 15 %-17 %, implying that exergy destruction should be decreased to reduce the total cost. The third highest total cost is found in the IHEX with an exergoeconomic factor of 34-46 % and the third highest relative cost difference. The desorber ex-

Table 5.16: Splitting the non-exergetic cost

k^{th}	comp.	$\dot{Z}_k^{real}$ (¢/h)	$\dot{Z}_k^{AV}$ (¢/h)	$\dot{Z}_k^{UN}$ (¢/h)	$\dot{Z}_k^{EN}$ (¢/h)	$\dot{Z}_k^{EX}$ (¢/h)	$\dot{Z}_k^{EN,AV}$ (¢/h)	$\dot{Z}_k^{EN,UN}$ (¢/h)	$\dot{Z}_k^{EX,AV}$ (¢/h)	$\dot{Z}_k^{EX,UN}$ (¢/h)	$\dot{Z}_k^{\Sigma}$ (¢/h)	$\dot{Z}_k^{\Sigma,AV}$ (¢/h)
x_r=0.85 & f=0.50												
(1)	CM	561.5	84.2	477.2	314.2	247.3	47.1	267.0	37.1	210.2	312.7	46.0
(2)	PM	8.7	1.3	7.4	5.6	3.1	0.8	4.7	0.5	2.6	5.4	0.8
(4)	AB	88.1	57.0	31.1	88.1	0.0	57.0	31.1	0.0	0.0	210.7	84.2
(6)	IH	28.7	25.4	3.2	16.1	12.6	14.3	1.8	11.2	1.4	24.8	16.7
(8)	DS	59.7	43.9	15.8	60.4	-0.7	44.4	16.0	-0.5	-0.2	182.9	65.9
Sys.		746.6	211.9	534.7	484.3	262.3	163.7	320.6	48.2	214.1	736.4	213.5
x_r=0.70 & f=0.70												
(1)	CM	621.7	93.3	528.4	331.0	290.6	49.7	281.4	43.6	247.1	328.7	47.8
(2)	PM	11.3	1.7	9.6	6.8	4.5	1.0	5.8	0.7	3.8	5.9	0.8
(4)	AB	94.2	63.9	30.3	94.2	0.0	63.9	30.3	0.0	0.0	240.6	105.5
(6)	IH	57.1	51.4	5.7	24.6	32.5	22.2	2.5	29.2	3.3	34.6	23.9
(8)	DS	76.6	58.4	18.2	79.3	-2.7	60.5	18.8	-2.1	-0.6	216.5	90.9
Sys.		860.8	268.6	592.2	535.9	324.9	197.2	338.7	71.4	253.5	826.3	269.0
x_r=0.55 & f=0.80												
(1)	CM	760.3	114.0	646.3	401.8	358.5	60.3	341.5	53.8	304.7	396.1	55.8
(2)	PM	10.9	1.6	9.3	6.5	4.4	1.0	5.5	0.7	3.8	6.3	0.9
(4)	AB	93.9	64.8	29.1	93.9	0.0	64.8	29.1	0.0	0.0	274.6	121.7
(6)	IH	84.8	76.7	8.1	32.7	52.1	29.6	3.1	47.1	5.0	50.9	32.8
(8)	DS	78.0	59.3	18.7	83.6	-5.6	63.5	20.1	-4.2	-1.3	253.5	105.2
Sys.		1028.0	316.5	711.5	618.5	409.5	219.2	399.4	97.3	312.1	981.5	316.3

ergoeconomic factor is 100 % and thus all cost is associated with the investment, this is because no cost is associated with the heat source ($c_{F,7} = 0$) wherefore the cost of exergy destruction is zero.

The total cost when accounting for component interdependencies (sum of $\dot{C}_{D,k}^{\Sigma}$ and $\dot{Z}_k^{\Sigma}$), shifts the order of importance between the components. The highest cost is here associated with the absorber (47 %-48 %) followed by the compressor (30 %-33 %), desorber (18 %) and IHEX (3 %-5 %). Accounting for interdependencies yields the advanced exergoeconomic factor $f_{c,k}^{\Sigma}$. From Table 5.17 it may be seen that this does not differ significantly for the compressor while there is a noticeable difference for the remaining components. For the absorber the exergoeconomic factor is increased from 15 %-17 % to approximately 30 %, implying a more even distribution of the investment and running costs. The desorber exergoeconomic factor is reduced from 100 % to 69 %-74 %. The IHEX exergoeconomic factor is increase from 34 % - 46 % to 58 % - 62 % and thus shifts from being dominated by exergy destruction cost to being dominated by investment.

The total cost when accounting for both avoidability and component interdependencies (sum of $\dot{C}_{D,k}^{\Sigma,\mathrm{AV}}$ and $\dot{Z}_k^{\Sigma,\mathrm{AV}}$), does not shift the order of the components but it changes the distribution. The absorber here accounts for 53 % - 54 %, while the compressor accounts for (20 % - 25 %), followed closely by the desorber (19 % - 20 %) and finally the IHEX (3 % - 5 %).

Accounting for both avoidability and interdependencies reveals the most important component for cost improvement to be the absorber. Judging from the absorbers avoidable advanced exergoeconomic factor, $f_{c,k}^{\Sigma,\mathrm{AV}}$, ranging from 20 % to 23 %, the absorber cost is dominated by the cost of exergy destruction. Therefore, the pinch point temperature difference should be reduced to increase the exergy efficiency at the expense of an increased investment. There is no significant difference between the advanced and conventional exergoeconomic factor for the absorber. The second most important component is the compressor. Here, the avoidable advanced exergoeconomic factor ranges from 23 % - 28 %. This is significantly different than the conventional exergoeconomic factor, which ranges from 64 % - 70 %. Based on the results of the advanced exergoeconomic analysis it is suggested that the compres-

sor efficiency is increased at the expense of an increased investment. The third most important component is the desorber. Here, the avoidable advanced exergoeconomic factor ranges from 45 % - 54 %, which differs significantly from the result of the conventional analysis. Judging from the absorber avoidable advanced exergoeconomic factor there should not be made any changes to this component.

The IHEX avoidable advanced exergoeconomic factor and relative cost difference decreases with ammonia mass fraction. For all three ammonia mass fractions the IHEX total cost is dominated by investment and thus the effectiveness should be reduced at the expense of an increased cost of exergy destruction. However, when decreasing ammonia mass fraction (and increasing circulation ratio) the chosen effectiveness approaches the optimal distribution of investment and exergy destruction costs.

Sensitivity analysis of the economic assumptions

Fig. 5.9 presents a sensitivity analysis of the assumed values of electricity cost, operating hours, technical life time, interest rate and inflation rate. The percentage change in the cost rate of system product (absorber heat) is evaluated for a percentage change in the stated input parameters. The results presented in Fig. 5.9 are for an ammonia mass fraction of x_r = 0.85 and circulation ratio of f = 0.5.

As may be seen the cost of electricity has the highest influence of the cost of the HACHP product. A $\pm$50 % change in electricity cost results in a $\pm$33 % change in the product cost. The second highest influence is from the number of operating hours, here it may be seen that a reduction of operating hours has a higher influence on the product cost than a reduction. A 50 % reduction of the operating hours results in a 34 % increase in cost, while a 50 % increase results in an 11 % reduction of cost. The trend of the technical life time is similar to the operating hours. A 50 % reduction of the lifetime results in a 24 % increase in cost, while a 50 % increase in lifetime results in a 7 % decrease in product cost.

The lowest influence on product cost is associated with the interest and inflation rate. A $\pm$50 % change in these result in $\pm$7 % and $\pm$2

Table 5.17: Comparison of the conventional and advanced exergoeconomic analysis and the results of the three ammonia mass fractions

k^{th}	$\dot{Z}_k^{\text{real}} + \dot{C}_{D,k}^{\text{real}}$ (¢/h)	$\dot{Z}_k^{\Sigma} + \dot{C}_{D,k}^{\Sigma}$ (¢/h)	$\dot{Z}_k^{\Sigma,\text{AV}} + \dot{C}_{D,k}^{\Sigma,\text{AV}}$ (¢/h)	$f_{c,k}$ (%)	$f_{c,k}^{\Sigma}$ (%)	$f_{c,k}^{\Sigma,\text{AV}}$ (%)	r_k (%)
x_r=0.85 & f=0.50							
(1) CM	873.7	495.0	198.6	64.3	63.2	23.2	78.1
(2) PM	12.9	7.9	2.5	67.0	69.1	29.9	70.5
(4) AB	500.1	706.8	414.4	17.6	29.8	20.3	29.4
(6) IH	82.5	39.4	23.2	34.7	62.9	71.8	58.1
(8) DS	59.7	265.1	146.3	100.0	69.0	45.0	-
Sys.	1528.9	1514.3	785.1	48.8	48.6	27.2	-
x_r=0.70 & f=0.70							
(1) CM	930.4	495.2	186.8	66.8	66.4	25.6	83.6
(2) PM	17.4	8.4	2.3	64.7	70.5	33.2	62.8
(4) AB	547.2	781.9	464.4	17.2	30.8	22.7	30.9
(6) IH	127.2	59.6	37.2	44.9	58.1	64.4	46.9
(8) DS	76.6	298.3	171.2	100.0	72.6	53.1	-
Sys.	1698.8	1643.5	861.9	50.7	50.3	31.2	-
x_r=0.55 & f=0.80							
(1) CM	1077.3	565.3	195.6	70.6	70.1	28.5	91.0
(2) PM	16.7	9.6	3.3	65.1	65.5	26.2	63.5
(4) AB	607.2	878.4	524.4	15.5	31.3	23.2	31.1
(6) IH	181.1	85.1	52.6	46.8	59.8	62.4	43.7
(8) DS	78.0	341.4	191.5	100.0	74.3	54.9	-
Sys.	1960.3	1879.8	967.3	52.4	52.2	32.7	-

% change in product cost for the interest rate and inflation rate, respectively.

5.3.3 Exergoenvironmental analysis

Conventional exergoenvironmental analysis of HACHP system

Influence of ammonia mass fraction and circulation ratio Fig. 5.10 shows the variation of $\dot{B}_{D,\text{sys}}$ and $\dot{Y}_{\text{sys}}$ with the choice of x_r and f. The real efficiencies from Table 5.6 were applied along with operating conditions from Table 5.1.

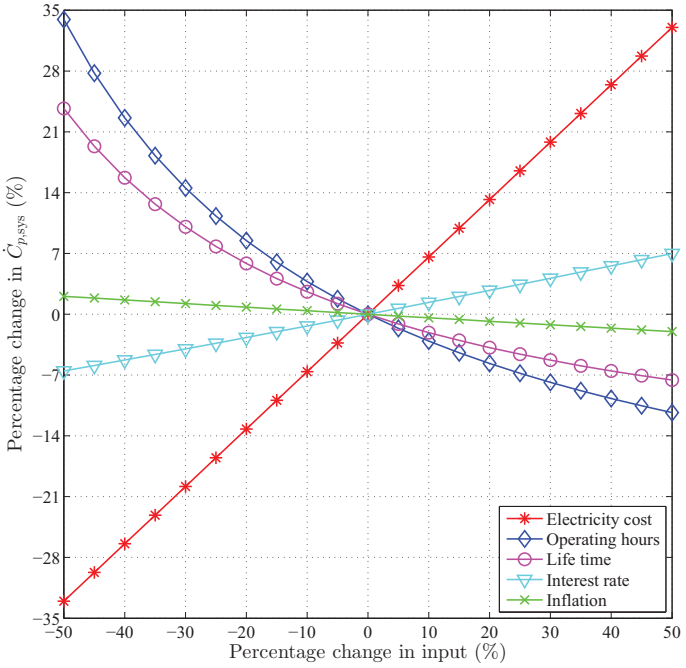

Figure 5.9: Sensitivity of the cost rate of system exergy product for the electricity price, operating hours, life time, interest and inflation rate.

As for the exergoeconomic analysis, for all values of x_r there exists one value of f that minimizes $\dot{B}_{D,\text{sys}}$. It is seen that the minimum value of $\dot{B}_{D,\text{sys}}$ increases slightly with a reduction of x_r. From Fig. 5.10 (b) it is seen that $\dot{Y}_{\text{sys}}$ is more influenced by the choice of x_r than that of f, showing a large increase of $\dot{Y}_{\text{sys}}$ with the reduction of x_r. This is caused mainly by the increased size of the compressor but also due to the increased size of the absorber, desorber and IHEX.

It should be noted that the value $\dot{Y}_{\text{sys}}$ is two orders of magnitude lower than $\dot{B}_{D,\text{sys}}$ and thus seems to be of minor importance for the total environmental impact of the system, at applied real component efficiencies. For the further analysis the value of x_r and f have been set to 0.85 and 0.5, respectively, as indicated by the dot on Fig. 5.10.

Influence of component efficiency and comparison with exergoeconomic analysis. As concluded in the advanced exergoeconimic analy-

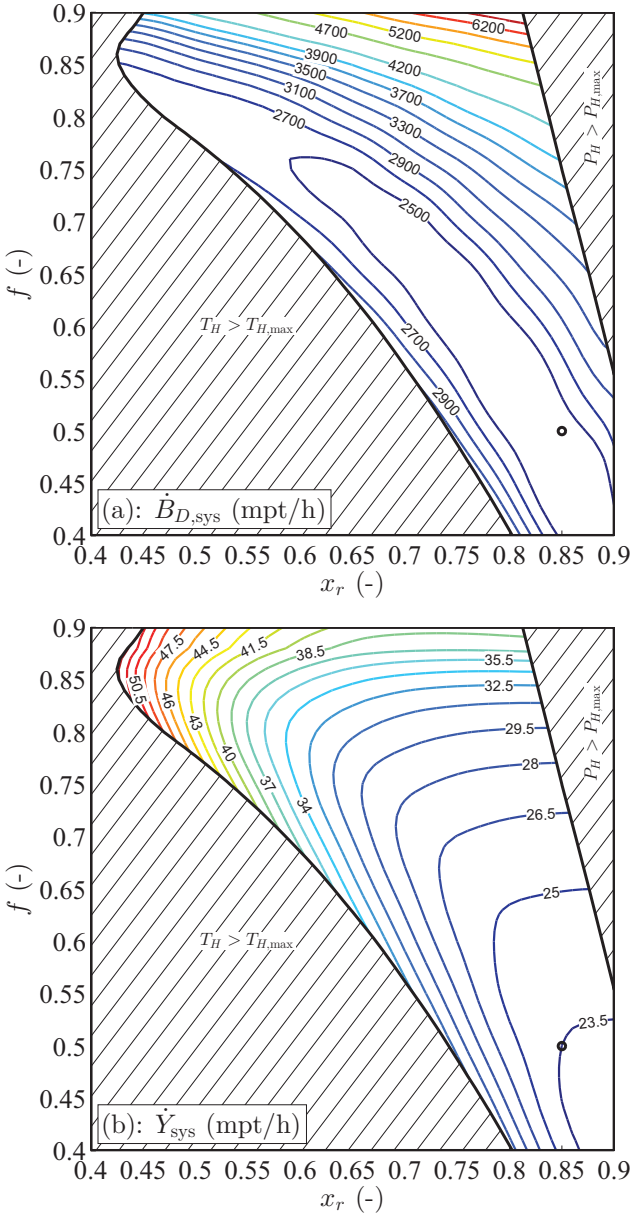

Figure 5.10: Variation of the system environmental impact rates: $\dot{B}_{D,\mathrm{sys}}$ (a) and $\dot{Y}_{\mathrm{sys}}$ (b) with x_r and f

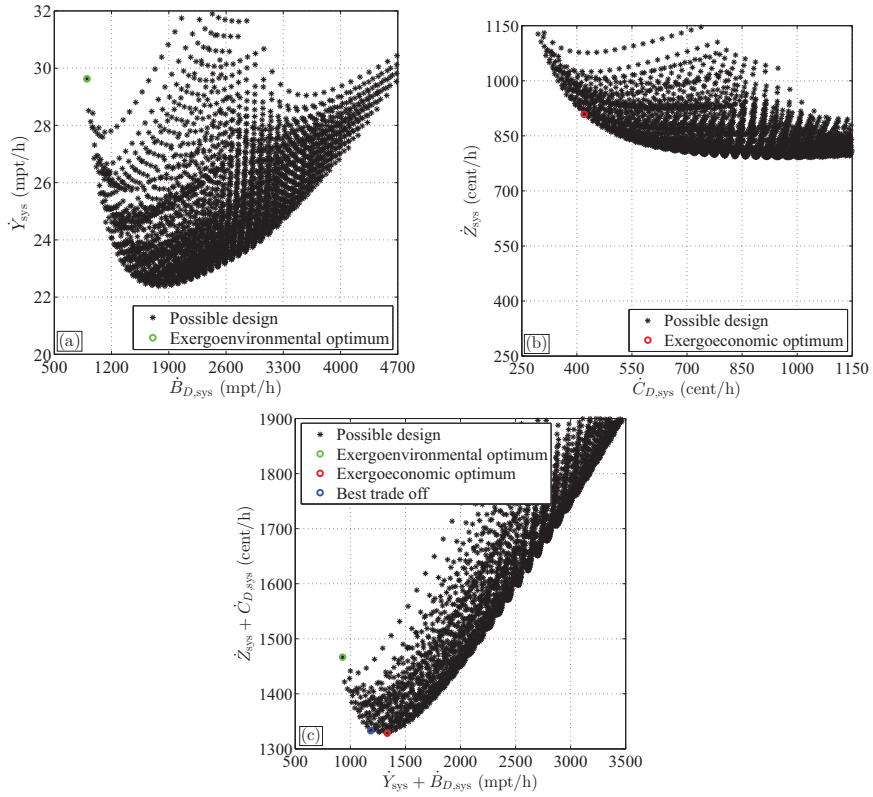

Figure 5.11: System environmental impact rates: $\dot{B}_{D,\mathrm{sys}}$ and $\dot{Y}_{\mathrm{sys}}$ and system cost rates: $\dot{C}_{D,\mathrm{sys}}$ and $\dot{Z}_{\mathrm{sys}}$ for a variation of $\Delta T_{\mathrm{pp},4}$, $\Delta T_{\mathrm{pp},8}$ and ϵ_6

sis the applied real efficiencies were not optimal for the given operating conditions and economic inputs. Before the advanced exergoenvironmental analysis is applied, more viable real efficiencies are identified.

Fig. 5.11 (a) shows the variations of $\dot{B}_{D,\mathrm{sys}}$ and $\dot{Y}_{\mathrm{sys}}$ with the choice of $\Delta T_{\mathrm{pp},4}$, $\Delta T_{\mathrm{pp},8}$ and ϵ_6. $\Delta T_{\mathrm{pp},4}$ and $\Delta T_{\mathrm{pp},8}$ have been varied from 1 K - 20 K and ϵ_6 from 0.3 to 0.98. Fig. 5.11 (b) shows the variations of $\dot{C}_{D,\mathrm{sys}}$ and $\dot{Z}_{\mathrm{sys}}$ for the same parameter variations and thus gives the exergoeconomic perspective. As seen from Fig. 5.11 (a) and (b) both the exergoenvironmental and exergoeconomic analyses result in a front of pareto optimal solutions. For the exergoenvironmental analysis it can again be noted that the values of $\dot{Y}_{\mathrm{sys}}$ is two orders of magnitude lower

than $\dot{B}_{D,\mathrm{sys}}$. This results in an exergoenvironmental optimum at the unavoidable conditions, see Table 5.8. Hence, the increased component size at these conditions is not enough to counteract the benefit of the reduced exergy destruction.

For the exergoeconomic analysis in Fig. 5.11 (b) it can be seen that the cost related to the total capital investment and maintenance, $\dot{Z}_{\mathrm{sys}}$, and the cost related to the operation of the system, $\dot{C}_{D,\mathrm{sys}}$, are of equal magnitude and thus that a trade off between the non-exergetic and exergetic cost exists. This is shown in Fig. 5.11 (b) by the red dot, indicating the exergoeconomic optimum.

Fig. 5.11 (c) shows the variation of the total environmental impact $\dot{B}_{D,\mathrm{sys}} + \dot{Y}_{\mathrm{sys}}$ and the total cost $\dot{C}_{D,\mathrm{sys}} + \dot{Z}_{\mathrm{sys}}$ for the same parameter variation. As seen this also results in a front of pareto optimal solutions. Both the exergoenvironmental and the exergoeconomic optimum are shown along with a suggested best trade off, indicated by the blue dot.

The values of decision variables at this point will be used as the real conditions for the further analysis. The values at this point are, $\Delta T_{\mathrm{pp},8}^{\mathrm{real}}$ = 2 K, $\Delta T_{\mathrm{pp},4}^{\mathrm{real}}$ = 4 K and $\epsilon_6^{\mathrm{real}}$ = 0.8 -. For the compressor, the real conditions were $\eta_{1,\mathrm{is}}^{\mathrm{real}}$ = 0.75 and $\eta_{1,\mathrm{el}}^{\mathrm{real}}$ = 0.95, for the pump $\eta_{2,\mathrm{is}}^{\mathrm{real}}$ = 0.85 and $\eta_{1,\mathrm{el}}^{\mathrm{real}}$ = 0.95.

Advanced exergoenvironmental analysis

Table 5.18 shows the results of the advanced exergoenvironmental analysis at the best trade off conditions described above. It can be seen that for the real cycle, and thus for the results of the conventional exergoenvironmental analysis the largest exergy-related environmental impact stems from the compressor followed by the absorber. For the non-exergetic environmental impact it is seen that the highest impact also stems from the compressor followed by the LVS, desorber and absorber.

Splitting the environmental impact into avoidable and unavoidable parts shows that the largest avoidable exergy related environmental impact also stems from the compressor where 85 % of $\dot{B}_{D,k}^{\mathrm{real}}$ is avoidable. For the absorber this is only 35 %. Conversely, the largest avoidable non-exergetic environmental impact is related to the desorber where 96 % of the environmental impact is avoidable. The second highest stems

Table 5.18: Results of the advanced exergoenvironmetal analysis.

k^{th}	$\dot{B}_{D,k}^{\text{real}}$ (mpt/h)	$\dot{B}_{k}^{\text{AV}}$ (mpt/h)	$\dot{B}_{k}^{\text{UN}}$ (mpt/h)	$\dot{B}_{k}^{\text{EN}}$ (mpt/h)	$\dot{B}_{k}^{\text{EX}}$ (mpt/h)	$\dot{B}_{D,k}^{\text{EN,AV}}$ (mpt/h)	$\dot{B}_{D,k}^{\text{EN,UN}}$ (mpt/h)	$\dot{B}_{D,k}^{\text{EX,AV}}$ (mpt/h)	$\dot{B}_{D,k}^{\text{EX,UN}}$ (mpt/h)	$\dot{B}_{D,k}^{\Sigma}$ (mpt/h)	$\dot{B}_{D,k}^{\Sigma,\text{AV}}$ (mpt/h)
(1)	712	609	103	588	124	491	97.0	118	6.20	576	481
(2)	9.59	7.33	2.26	8.12	1.47	5.98	2.14	1.35	0.122	7.87	5.80
(4)	409	145	263	416	−7.34	150	266	−5.02	−2.32	492	216
(5)	-	-	-	-	-	-	-	-	-	-	-
(6)	24.3	13.5	10.9	12.3	12.1	4.77	7.49	8.76	3.37	30.5	17.1
(8)	0.00	0.00	0.00	0.00	0.00	0.00	0.00	0.00	0.00	46.6	41.9
(9)	-	-	-	-	-	-	-	-	-	-	-
k^{th}	$\dot{Y}_{k}^{\text{real}}$ (mpt/h)	$\dot{Y}_{k}^{\text{AV}}$ (mpt/h)	$\dot{Y}_{k}^{\text{UN}}$ (mpt/h)	$\dot{Y}_{k}^{\text{EN}}$ (mpt/h)	$\dot{Y}_{k}^{\text{EX}}$ (mpt/h)	$\dot{Y}_{k}^{\text{EN,AV}}$ (mpt/h)	$\dot{Y}_{k}^{\text{EN,UN}}$ (mpt/h)	$\dot{Y}_{k}^{\text{EX,AV}}$ (mpt/h)	$\dot{Y}_{k}^{\text{EX,UN}}$ (mpt/h)	$\dot{Y}_{k}^{\Sigma}$ (mpt/h)	$\dot{Y}_{k}^{\Sigma,\text{AV}}$ (mpt/h)
(1)	13.3	1.99	11.3	10.7	2.604	1.61	9.10	0.390	2.21	10.6	1.55
(2)	0.423	0.0634	0.359	0.359	0.0633	0.0539	0.306	0.00	0.0537	0.356	0.0516
(4)	2.98	2.67	0.318	2.98	0.00	2.67	0.318	0.00	0.00	4.46	42.89
(5)	1.44	-	-	-	-	-	-	-	-	-	-
(6)	0.294	0.278	0.0154	0.24	0.0560	0.225	0.0124	0.0531	0.00	0.414	0.2034
(8)	3.80	3.66	0.136	3.93	−0.132	3.79	0.141	−0.127	0.00	4.78	3.93
(9)	5.59	-	-	-	-	-	-	-	-	-	-

from the absorber where 89 % can be avoided, while only 15 % can be avoided in the compressor.

Splitting the environmental impact into endogenous and exogenous parts shows that the compressor environmental impact is mainly endogenous with 82 % for $\dot{B}_{D,k}$ and 80 % for $\dot{Y}_k$. A similar distribution is found for the pump. For the absorber, the exogenous environmental impact was found to be negative which means that an improvement of the exergy efficiency of the remaining components results in an increased environmental impact in the absorber. For the absorber the non-exergetic environmental impact is all endogenous. For the IHEX $\dot{B}_{D,k}$ is evenly distributed between endogenous and exogenous, while $\dot{Y}_k$ is 90 % endogenous. For the desorber, the exogenous non-exergetic environmental impact is negative and thus increasing the efficiency of the remaining components results in the need for a larger desorber.

Combining the split of avoidable and unavoidable with exogenous and endogenous and further splitting the exogenous part into a contribution specific to the r^{th} component, results in the values of $\dot{B}_{D,k}^{\Sigma,\mathrm{AV}}$ and $\dot{Y}_k^{\Sigma,\mathrm{AV}}$ also stated in Table 5.18. These values represent the total avoidable environmental impact related to each component. As seen the highest value $\dot{B}_{D,k}^{\Sigma,\mathrm{AV}}$ stems from the compressor followed by the absorber and desorber. Conversely, the highest values of $\dot{Y}_k^{\Sigma,\mathrm{AV}}$ stem from the desorber followed by the absorber.

Fig. 5.12 summarizes the distribution of $\dot{B}_{D,k}^{\Sigma}$ and $\dot{Y}_k^{\Sigma}$ as well as $\dot{C}_{D,k}^{\Sigma}$ and $\dot{Z}_k^{\Sigma}$. As seen the component with the highest contributions are the compressor and absorber for both the exergoenvironmental and exergoeconomic analysis. Further, while the non-exergetic cost has a high impact on the cost of the system the non-exergetic environmental impact is negligible compared to the environmental impact related to the exergy destruction. Accounting for unavoidabilities and interdependencies further showed that far from all costs or environmental impact can be removed by design improvements.

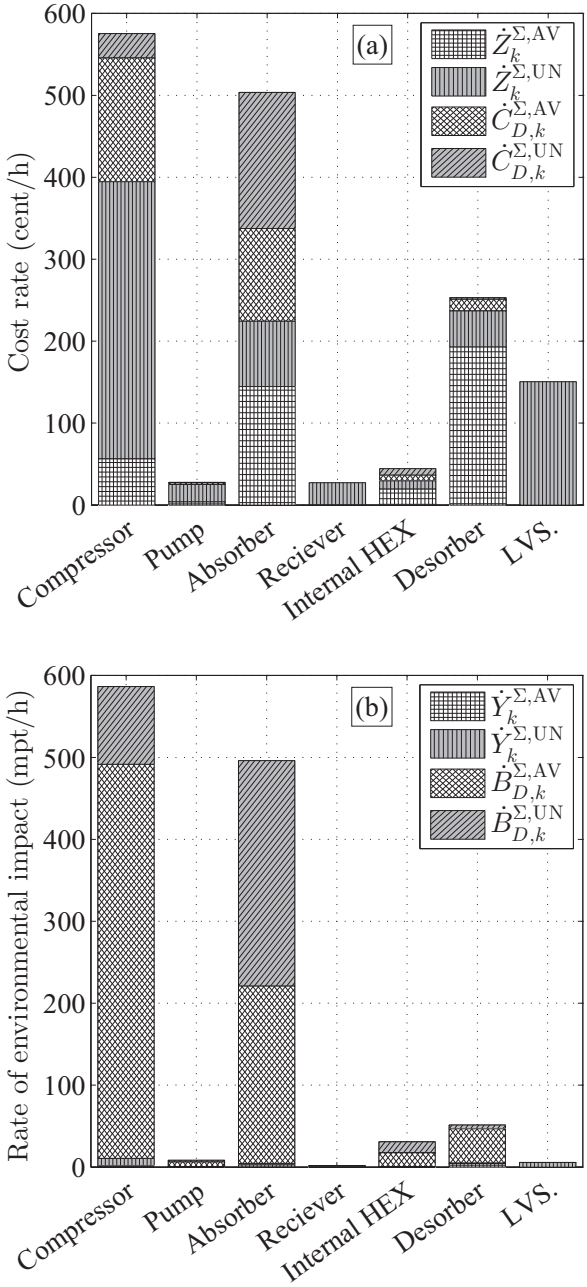

Figure 5.12: Distribution of $\dot{C}_{D,k}$, $\dot{Z}_k$, $\dot{B}_{D,k}$ and $\dot{Y}_k$

5.4 Discussion

As seen from the presented results there is a significant difference between the results attained by the conventional and advanced exergyanalysis. However, getting to this result is computationally demanding due the larger number of simulations needed to conduct the analysis. K simulations are needed to split the exergy destruction into endogenous and exogenous, to further split into avoidable and unavoidable requires an additional K+1. To allocate the exogenous destruction to the component that induces it required $\frac{1}{2}(K^2 - K)$ additional simulations and splitting this into avoidable and unavoidable requires an equal amount.

All in all the results presented for the advanced exergy analysis is based on 58 simulations, while those of the conventional analysis requires only one. It can be discussed whether the general conclusion attained from the advanced method could be achieved with less simulations by performing sensitivity analysis of the input parameters. However, what such an approach does not provide is the standardised procedure and presentation of results provided by the advanced method. This allows the conclusions and results to be compared to alternative systems analysed with the same method.

Further, the advanced exergy-based analysis serves directly as the basis for an advanced exergoeconomic or exergoenvironmental analysis. Applying the advanced methods in the procedure for exergoeconomic or exergoenvironmental optimisation reduces the number of iterations needed to attain the optimum values of the decision variables, this, as not accounting for interdependencies and technological limitations can lead to false conclusions from the conventional analysis.

The results of the advanced analysis depend highly on the choice of real and unavoidable efficiencies of the components. As the values of real and unavoidable efficiencies approach each other, the difference between the results of the conventional and advanced diminish. Equally when the real efficiencies approach the thermodynamic maximum efficiencies the result of the conventional and advanced analysis will converge.

5.5 Conclusion

A conventional and advanced exergy-based analysis is applied to the HACHP. Using the thermodynamic cycle approach the exergy destruction in each component was split into an endogenous/exogenous and avoidable/unavoidable part. These splits were then combined to find the endogenous/exogenous part of both the avoidable and unavoidable exergy destruction. Furthermore, the contribution from the r^{th} component to the exogenous exergy destruction of the k^{th} component was found. This was done for both the total and avoidable part. The advanced exergy analysis was combined with conventional exergoeconomic and exergoenvironmental to split the cost and environmental impact related to the exergy destruction. Further, the non-exergetic cost and environmental impact rates were split.

The results from the conventional exergy analysis showed that 72 % of the total exergy destruction was located in the compressor (27 %), absorber (24 %) and desorber (21 %). Thus, based on the conventional exergy analysis the first component to improve would be the compressor then the absorber followed by the desorber. Based on the conventional exergoeconomic analysis the most important component for system improvement is the compressor, as this has the highest total cost and the highest relative cost difference. Based on the conventional exergoeconomic factor of the compressor the total cost is dominated by investment.

Applying the advanced exergy analysis showed that 27 % of the total exergy destruction could not be avoided. Analysing the total avoidable exergy destruction associated to the component inefficiency, rearranged the order of importance. The three highest ranking components remain the same but the order is reversed: Desorber (38 %), absorber (35 %) and compressor (19 %). In total 92 % of the avoidable exergy destruction can be allocated to these three components.

The advanced exergoeconomic analysis shows that 53 % - 54 % of the avoidable total cost stems from the absorber. While the compressor total cost accounts for 20 % - 25 % and the desorber 19 % - 20 %. This differs significantly from the results of the conventional analysis. Also the exergoeconomic factors change when the advanced analysis is

applied. The conventional analysis shows that the compressor, pump and desorber total cost are dominated by investment, while the absorber and IHEX total cost are dominated by the cost of exergy destruction. Applying the advanced analysis shows that only the IHEX total cost is dominated by investment while the compressor and absorber total cost are dominated by the cost of exergy destruction. The desorber is found to have a close to equal distribution of the investment and exergy destruction cost.

It was found that the environmental impact of the HACHP system was mainly driven by the operation of the system and thus linked to the electricity consumption. The environmental impact related to the construction of the system was found to negligible and for all cases the environmental impact related to the increased size of the components could be justified by the decreased energy consumption over the life time of the system. Thus, the exeroenvironmental optimum was found at the unavoidable conditions.

However, these conditions were found not to be economically viable, wherefore a trade off was suggested, that reduced the environmental impact to a close to optimal solution, without any significant increase in cost.

At this condition the advanced exergoenvironmental analysis was applied. This showed that 62 % of the avoidable environmental impact was related to the compressor, followed by the absorber with 28 %. 7 % of the avoidable impact stems from the desorber while the last 3 % were accounted to the IHEX and pump.

The application of the advanced exergy-based analysis has provided a level of detail not supplied by the conventional approach. By accounting for component interdependencies and the unavoidable parts of investment and exergy destruction cost the system designer is supplied with costs and indicators that account for the technological and economic constraints of the specific component and thus a more useful result for the further improvement of the system. It is shown that the conventional analysis gives results that can be directly contradicted by the results of the advanced analysis and therefore the conclusion based on the two approaches differ significantly.

CHAPTER 6

TECHNICAL AND ECONOMIC WORKING DOMAINS OF HYBRID ABSORPTION COMPRESSION HEAT PUMPS AND COMPARISON WITH VAPOUR COMPRESSION

The work presented in this chapter concerns the technical and economic limitations of industrial heat pumps. The analysis was first presented as a two part paper at the 11th IIR - Gustav Lorentzen Conference on Natural Refrigerants. Here the analysis was applied to vapour compression heat pumps in [77] ([P14]) and to the HACHP in [47] ([P15]). Revisions of both papers were later published in the International Journal of Refrigeration [75] ([P4]), [46] ([P5]). The limitations of vapour compression heat pumps operated in series was later presented at the 24th IIR International Congress of Refrigeration [76] ([P17]).

To ensure easy interpretations of the results presented in this chapter, it is recommended that the reader has read [75] ([P4]) in which the analysis of the vapour compression heat pump is presented

6.1 Introduction

Industrial scale heat pumps may be applied to improve the energy efficiency of industrial processes [99] or for utility production in urban areas with district heating networks[79]. The temperature range where heat pumps for such purposes are applicable is bound by several technical constraints. The technical constraints are governed by the thermodynamic behaviour of the working fluid and the limits of commercially available components, such as compressor discharge temperature and

pressure. Further, for a heat pump to be a viable investment, the installation should be the more profitable alternative compared to a competitive technology such as a natural gas burner.

Brunin et al. [23] evaluates the working domain of the HACHP based on one technical constraint: maximum pressure and two physical parameters applied as economic indicators: minimum coefficient of performance (COP) and minimum volumetric heat capacity (ratio between heat output and compressor displacement volume). The working domain by [23] is evaluated at a fixed 10 K temperature difference, between inlet and outlet, for both the heat sink and heat source. Under these constraints, Brunin et al. [23] shows that the HACHP can attain allowable heat supply temperatures up to 140 °C with a maximum pressure of 20 bar.

Further, Brunin et al. [23] does not include the compressor discharge temperature as a constraint but, as discussed in Chapter 3 the compressor discharge temperature is a limiting factor for the development of a high temperature HACHP.

As discussed Ommen et al [75], the use of COP and VHC as indicators for the economic viability of a heat pump investment may not always lead to a precise conclusion. This is because components for different refrigerants may vary in cost due to e.g. different material requirements or different heat transfer coefficients and thus, the level of COP needed to attain a viable investment will differ based on the level of investment required for the specific refrigerant. Evaluating the working domain based on a complete economic evaluation of the heat pump installation, over the lifetime of the system may result in valuable information not provided by Brunin et al. [23].

The application of a complete economic analysis allows the different heat pump solutions to be compared based on an objective measure. Thus, evaluating the difference in the expected economic gain of the investment and thereby identifying the most relevant technologies.

Ommen et al. [78] compared the economy of the HACHP to the VCHP and showed that the HACHP is a competitive technology. However, the study did not consider the degradation of heat transfer coefficients caused by the application of a zeotropic mixture working fluid. Further, the reduced vapour pressure of the mixture increases the spe-

cific volume of the low pressure vapour and consequently entails the need for an increased compressor displacement volume. It is therefore relevant to evaluate, whether this increased investment in heat transfer area and compressor volume can be justified by the increased efficiency of the heat pump.

As seen in Chapter 2, the fixed concentration difference of 0.1, applied by Brunin et al. [23], does not necessary ensure the best COP. Further, as seen in Chapter 5 the investment is highly sensitive to the choice of ammonia mass fraction. As both Brunin et al. [23] and Ommen et al. [78] have restricted their HACHP analysis to a limited number of ammonia mass fractions and used a fixed value of concentration difference the HACHP is not necessarily analysed under the best possible design conditions, which may result in an unfair comparison.

Ommen et al. [75] shows that the heat sink and heat source temperature differences have a significant influence on both the economic and technical constraints of VCHPs. Ommen et al. [75] investigates four cases with different combinations of heat sink and heat source temperature differences. These are:

- ΔT_{sink} =10 K, ΔT_{source} =10 K (10K/10K)
- ΔT_{sink} =20 K, ΔT_{source} =20 K (20K/20K)
- ΔT_{sink} =20 K, ΔT_{source} =10 K (20K/10K)
- ΔT_{sink} =40 K, ΔT_{source} =10 K (40K/10K)

The same four cases will be applied in the present study of HACHP.

This study investigates the working domain of the HACHP for these four cases. For each case the operating conditions, defined by the heat supply temperature, $T_{\text{sink,out}}$, and the temperature lift, ΔT_{lift}, will be varied. The heat supply temperature from 40-140 °C and the temperature lift from 0-70 K. For each operating condition the ammonia mass fraction and circulation ratio are found by an optimisation of the net present value (NPV) under the technical constraints of the studied components.

The working domains are presented graphically for all four cases, showing which operating conditions are possible to supply with a HACHP while respecting both the technical and economic constraints. Fi-

Table 6.1: Fixed input variables applied in the thermodynamic model of the HACHP

Input variable			Components to which they are applied	
η_{is}	0.80	-	Compressor	Pump
η_{vol}	0.80	-	Compressor	
η_{el}	0.95	-	Compressor	Pump
ΔT_{pp}	5.00	K	Absorber	Desorber
ε	0.90	-	Internal HEX	
$\dot{Q}$	1000	kW	Absorber	

Table 6.2: Plate dimensions for V120 T and V10 T

	V120 T	V10 T	
L	456	243	(-)
L_{HT}	525	289	(-)
W	243	119	(mm)
β	30	30	($^\circ$)
Λ	8.0	8.0	(mm)
b	1.8	1.8	(mm)
t	0.5	0.5	(mm)
λ	16.0	16.0	($Wm^{-1}K^{-1}$)

nally, the present value (PV) of the HACHP will be compared to the PV of the best available VCHP technology presented by Ommen et al. [75].

6.2 Methodology

6.2.1 Dimensioning heat exchangers

All three heat exchangers were assumed to be of a plate type with a chevron corrugation which is assumed to be the preferred option [12]. The plate size correspond to either the "V120T" or the "V10T" [11], for which a complete list of the applied dimensions are given in Table

6.2. The small plate size (V10T) was applied when the pressure loss using the large plate (V120T) exceeds Δp = 0.5 bar. This tends to happen when there is a large difference in the mass flow rate between the exchanging fluids. This occurred in the absorber and desorber when ΔT_{sink} and ΔT_{source} were small and in the internal HEX when the circulation ratio, f, was large.

The procedure for plate heat exchanger dimensioning presented in Chapter 4 was applied.

6.2.2 Refrigerant charge estimation and dimensioning of high pressure receiver

Based on the calculated size of the three heat exchangers the working fluid charge, m, was estimated by evaluating the volume occupied by the working fluid and the mean specific volume, $\overline{v}$, of the HEX, see Eq. (6.1)

$$m_k = M_k \cdot W_k \cdot b_k \cdot \frac{1}{\overline{v}_k} \tag{6.1}$$

Here M is the number op channels occupied by the working fluid. The total m_{tot} was defined as the sum of the working fluid charge in the absorber, desorber and internal HEX.

The high pressure receiver was dimensioned such that it can contain the entire charge at the high pressure (state of stream 5). The receiver was over-sized by 25% as suggested by [91]. The receiver volume, V_4, was calculated as stated in Eq. (6.2).

$$V_4 = (m_3 + m_5 + m_6) \cdot v_5 \cdot 1.25 \tag{6.2}$$

The application of an oversized high pressure receiver ensures a saturated state at the outlet from the absorber [27].

6.2.3 Compressors and technological constraints

The maximum heat supply temperature achievable by a heat pump is restricted by the maximum pressure of the applied compressor technology. Further, the maximum achievable temperature lift is restricted

Table 6.3: Fixed parameters applied in the economic analysis

Interest rate	i	7 %
Inflation rate	i_L	2 %
Technical lifetime	LT	15 years
Operating time	H	3500 hours pr. year
Gas burner efficiency	η_{NG}	0.9 -
Gas burner investment cost	TCI_{NG}	0 €
Gas burner maintenance cost	OMC_{NG}	0 €

by the compressor discharge temperature and in some cases differential pressure. This is to ensure the thermal stability of the lubricating oil and to reduce wear by thermal stress. As discussed in [75], the compressor discharge temperature is of special concern for ammonia heat pumps.

In the present study two compressor technologies were investigated: low pressure ammonia ([75]: Type 3) and high pressure ammonia ([75]: Type 4). The low pressure ammonia compressor (LP R717) has a maximum pressure of 28 bar. The discharge temperature is limited to 180 °C. The high pressure ammonia compressor (HP R717) has a maximum pressure of 50 bar and can equally tolerate discharge temperatures up to 180 °C.

Generally the water content in the compressed vapour stream is negligible but as shown in Chapter 3: for low ammonia mass fractions the water content can be substantial for some operating conditions. These solutions should be avoided and therefore solutions with $x_v < 0.95$ were deemed infeasible.

6.2.4 Economic evaluation

The basis of the economic analysis was the replacement of an existing gas burner with a HACHP of the same heat load. Thus, it was necessary to evaluate the total capital investment (TCI) of the HACHP. To determine TCI_{HP}, first the purchased equipment cost (PEC) of all major components was found. The PEC cost functions presented in Chapter 5 were applied. As in Chapter 5 is assumed that the TCI is a factor 4.16

higher the PEC.

Annual costs for the fuel consumption of both the existing gas burner and the proposed HACHP was determined as seen in Eqs. (6.3) and (6.4) [19], respectively.

$$\mathrm{FC_{NG}} = \frac{\dot{Q}}{\eta_{\mathrm{NG}}} \cdot c_{\mathrm{NG}} \cdot H \tag{6.3}$$

$$\mathrm{FC_{HP}} = \frac{\dot{Q}}{\mathrm{COP}} \cdot c_w \cdot H \tag{6.4}$$

Here c_{NG} and c_w are the natural gas and electricity prices, H is the operating time per year and η_{NG} is the assumed gas burner efficiency. The applied values of H and η_{NG} are stated in Table 6.3, while c_{NG} and c_w corresponding to an industrial consumer in the Danish fiscal environment for year the 2012, prices from [1] were applied.

To account for the time value of money the CRF was applied to discount future expenditure to a PV.

CRF depends on the effective interest rate over the life time of the system, i^{eff}, and the technical life time LT. The effective interest rate was calculated from the interest rate, i, and inflation rate, i_L. The assumed value of LT ,i and i_L are stated in Table 6.3.

The PV of the two alternatives: keeping the natural gas burner or replacing it with a HACHP was found using Eq. (6.5).

$$\mathrm{PV}_i = \mathrm{TCI}_i + \frac{\mathrm{FC}_i}{\mathrm{CRF}} + \mathrm{OMC}_i \tag{6.5}$$

For the natural gas burner the capital investment was assumed as sunk costs ($\mathrm{TCI_{NG}}$=0 €) and further the operation and maintenance cost (OMC) were neglected ($\mathrm{OMC_{NG}}$=0 €). Thus, $\mathrm{PV_{NG}}$ is equivalent to the discounted FC over the technical life time of the project. For the HACHP the OMC were assumed to attain a PV equivalent to 20% of the TCI as suggested by [19].

The criteria for the economic viability of the HACHP installation was a positive NPV when replacing a natural gas boiler as the source of heat supply. The NPV was defined as the difference in PV of the two alternatives as seen in Eq. (6.6).

$$\mathrm{NPV} = \mathrm{PV_{NG}} - \mathrm{PV_{HP}} \tag{6.6}$$

Thus, if the NPV is positive the HACHP investment will be profitable while if the NPV is negative keeping the natural gas burner would be the more profitable solution.

Further, a simple pay back period (PBP) was determined as stated in Eq. (6.7). The PBP is calculated as the ratio of the TCI_{HP} and the yearly savings in running costs.

$$PBP = \frac{TCI_{HP}}{(FC_{NG} - FC_{HP}) + (OMC_{NG} - OMC_{HP}) \cdot CRF} \tag{6.7}$$

PBP is not a precise measure of the economic viability of an investment as it does not account for the time value of money and thus should be used with caution [19]. However, PBP is often used as a selection criterion in industry typically with a maximum allowable value [19]. The maximum PBP is not easily defined as this depends highly on the industry and the type of investment. For the present study PBPs of 4 and 8 years will be reported, however the overall criteria for the economic viability will be NPV > 0 €, regardless of the actually allowed PBP. NPV = 0 € indicates that the PBP equals the technical lifetime of the system, which was assumed to be 15 years.

6.3 Results

6.3.1 The influence of x_r and f on the HACHP working domain

Fig. 6.1 shows the HACHP working domain for two fixed combinations of x_r and f. Fig. 6.1a has a high ammonia mass fraction of x_r = 0.9 while 6.1b has a low ammonia mass fraction of x_r = 0.5. The circulation ratio, f, was chosen to give high values of COP and thus as suggested by [48] the circulation ratio is reduced with an increase in ammonia mass fraction. Fig. 6.1a has a circulation ratio of f = 0.35 while 6.1b has a circulation ratio of f = 0.85.

The working domains in Fig. 6.1 are presented with the heat supply temperature, $T_{sink,out}$, as the abscissa and the temperature lift, ΔT_{lift}, as the ordinate. Further, a fixed sink/source configuration of 10K/10K

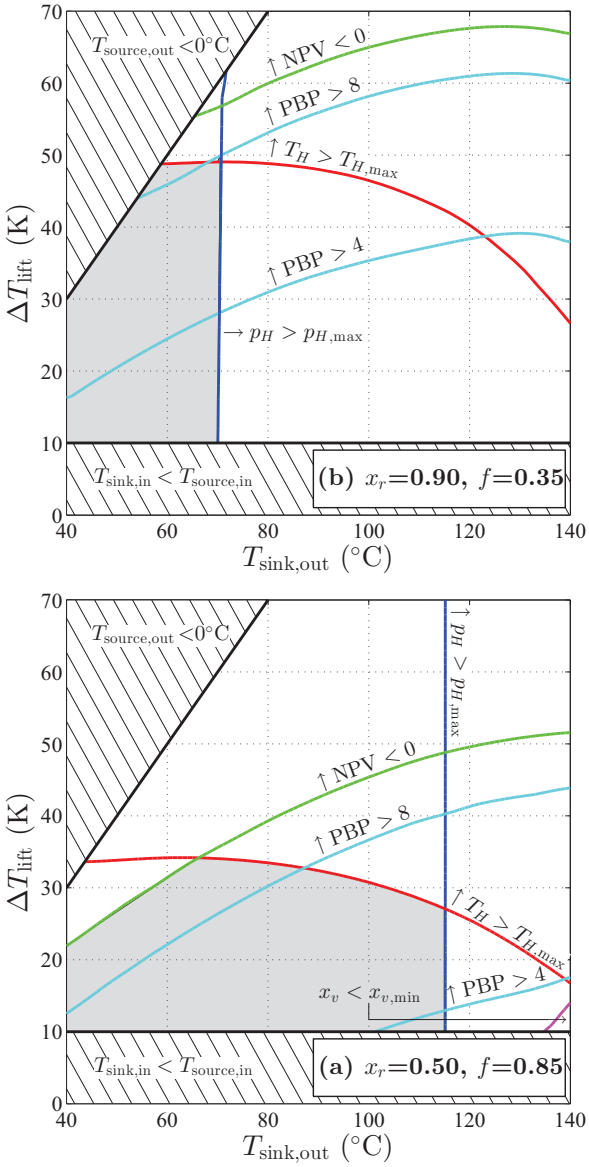

Figure 6.1: Working domain for a HACHP with fixed ammonia mass fraction and circulation ratio. (a) x_r = 0.90 and f = 0.35, (b) x_r = 0.50 and f = 0.85. Both for a sink/source configuration of 10K/10K. The technical and economic constraints correspond to the LP R717 components

is applied and thus ΔT_{sink} and ΔT_{source} are both fixed at a value of 10 K. Thus, for a given $T_{\text{sink,out}}$: $T_{\text{sink,in}}$ is determined from ΔT_{sink}. Likewise, from a given ΔT_{lift} and $T_{\text{sink,out}}$: $T_{\text{source,in}}$ is determined and finally $T_{\text{source,out}}$ is found from ΔT_{source}.

The hatched areas in Fig. 6.1 define operating conditions for which heat pump implementation is not applicable. The upper left corner indicates operating points that are infeasible as these require $T_{\text{source,out}} < 0$ °C, which implies a phase change for the chosen heat transfer fluid (water). This could be feasible if a brine was applied. However, it should be noted that this also implies cooling the heat source well below ambient temperature, which might not be reasonable unless a cooling demand is met.

The bottom rectangle indicates operating points at which $T_{\text{sink,in}} < T_{\text{source,in}}$. These operating points are neglected as for these conditions, direct heat transfer between the sink and source is possible for some range of the heat transfer process. Therefore, this should be applied first, as suggested by the principles of pinch analysis [53, 99].

The resulting working domains are indicated in Fig. 6.1 by the gray areas. These areas represent values of $T_{\text{sink,out}}$ and ΔT_{lift} where the HACHP simultaneously complies with all technical and economic constraints.

Further, all constraints are presented in Fig. 6.1. The dark blue line indicates the $T_{\text{sink,out}}$ and ΔT_{lift} at which the high pressure is equal to the maximum allowable pressure, $p_{H,\text{max}}$, for Figs. 6.1a and 6.1b 28 bar, corresponding to LP R717 components. Solutions to the left of the blue line thus have high pressures within the limit of the applied technology, while solutions to the right of the blue line have pressures above the allowable limit and are thus infeasible. As seen, the high pressure constraint only shows a weak dependence on ΔT_{lift}. Further, it is seen that the $T_{\text{sink,out}}$ at which $p_{H,\text{max}}$ is reached differs significantly for the two values of x_r presented. As seen in Fig. 6.1a with $x_r = 0.9$: heat supply temperature of only 70 °C can be reached while, as seen in Fig. 6.1b with $x_r = 0.5$: a heat supply temperature up to 115 °C can be attained.

The red line indicates the $T_{\text{sink,out}}$ and ΔT_{lift} at which the compressor discharge temperature is equal to the maximum allowable temperature,

$T_{H,\max}$. As seen $T_{H,\max}$ depends mainly of ΔT_{lift}. Hence, solutions with $T_{\text{sink,out}}$ and ΔT_{lift} below the red line have compressor discharge temperatures below $T_{H,\max}$ while solutions with $T_{\text{sink,out}}$ and ΔT_{lift} above the red line exceed the limitations of $T_{H,\max}$ and are thus infeasible. As seen the higher the $T_{\text{sink,out}}$ the lower the ΔT_{lift} is possible. When comparing the compressor discharge temperature constraint in Figs. 6.1a and 6.1b it is clear that the choice of ammonia mass fraction has an impact on attainable temperature lifts. As seen a reduction of the ammonia mass fraction entails a reduction of the attainable temperature lift.

The green line indicates the $T_{\text{sink,out}}$ and ΔT_{lift} at which the NPV of the investment is zero and thus where the installation of a HACHP is equivalent to keeping the existing natural gas burner. Solutions with $T_{\text{sink,out}}$ and ΔT_{lift} below the green line have positive NPV and are thus economically feasible while solutions above the green line have a negative NPV and are thus not economically viable.

As seen, NPV is dependent on both $T_{\text{sink,out}}$ and ΔT_{lift}, because an increase in ΔT_{lift} decreases the COP and consequently increases the annual fuel costs. Further, increasing ΔT_{lift} for a given $T_{\text{sink,out}}$ reduces the temperature level of the heat source, which results in a reduction of the low pressure and consequently an increased suction line volume flow and the need for a larger compressor investment. Likewise, increasing $T_{\text{sink,out}}$ for a given ΔT_{lift} increases the temperature of the heat source subsequently resulting in a reduced compressor investment.

When comparing the NPV constraint in Figs. 6.1a and 6.1b it is clear that the choice of ammonia mass fraction also influences NPV. As seen a reduction of the ammonia mass fraction reduces the number of economically viable solutions. This is due to the an increase in TCI_{HP} caused by the sum of three phenomena:

- The reduction of vapour pressure results in an increased suction line volume flow rate, and thus a large compressor investment.
- The reduction of the two-phase heat transfer coefficient, results in a larger absorber and desorber investment.
- The increase in circulation ratio increases the heat transfer in the internal HEX and thus the internal HEX investment

The light blue lines indicate the $T_{\text{sink,out}}$ and ΔT_{lift} at which the PBP is 4 and 8 years, respectively. As seen the PBP follows the same trend as the NPV.

Finally, the magenta line, seen only in the bottom right corner of Fig. 6.1b, indicates the $T_{\text{sink,out}}$ and ΔT_{lift} at which the ammonia mass fraction of the vapour stream supplied to the compressor is equal to the minimum allowable value. Solutions below this line are thus infeasible as these have too low a vapour ammonia mass fraction.

When comparing the two working domains presented in Figs. 6.1a and 6.1b it is clear that the choices of ammonia mass fraction and circulation ratio influence the amount of feasible HACHP solutions. As seen, when the ammonia mass fraction is high temperature lifts up to 49 K can be attained, while the HACHP under these conditions is only capable of reaching a heat supply temperature of 70 °C. Conversely, the low ammonia mass fraction solution is capable of reaching heat supply temperatures up to 115 °C but can only attain temperature lifts up to 35 K.

Consequently, defining the HACHP working domain based on fixed values of ammonia mass fraction and circulation ratio may not fairly represent the strengths and limitations of the HACHP technology as a whole.

6.3.2 Optimization of x_r and f to determine complete HACHP working domain

In order to assess the complete working domain of the HACHP technology, a selection criterion was defined to choose the economically optimal design at each operating condition (defined by $T_{\text{sink,out}}$ and ΔT_{lift}). Values of x_r and f have been set individually for each computed operating condition for all four cases, to maximize the NPV of the installation. The technical constraints of the high pressure, p_H, compressor discharge temperature, T_H, and vapour ammonia mass fraction, x_v, have been imposed on the optimization of NPV.

Figs. 6.2 (a) and 6.2 (b) show the optimum value of x_r and f, respectively, for a sink/source configuration of 10K/10K and with the application of the HP R717 components. The corresponding COP is presented

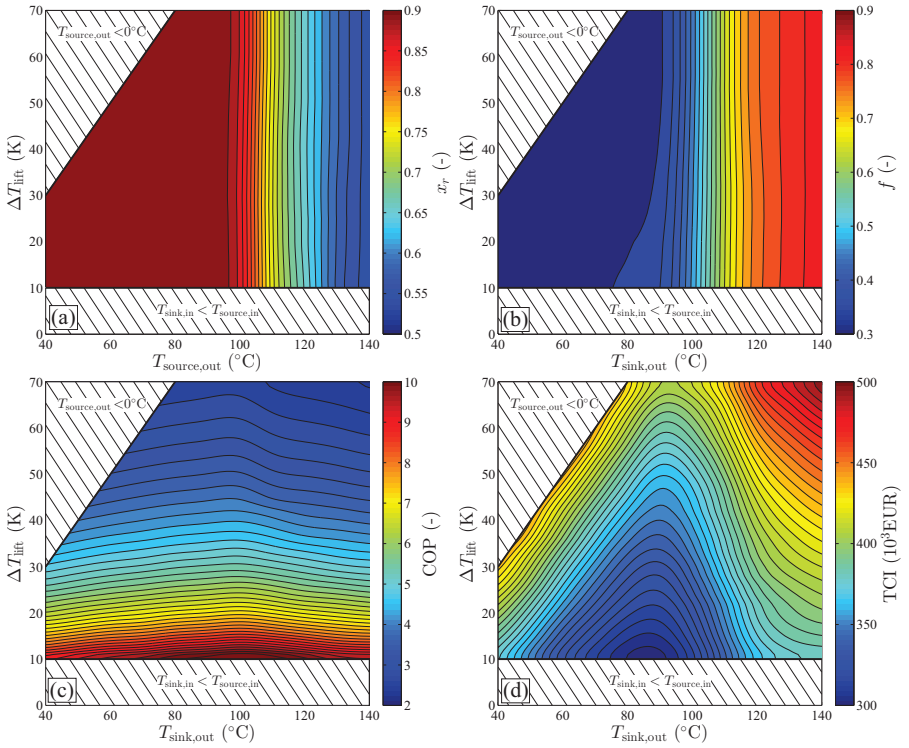

Figure 6.2: Optimal choice of x_r (a) and f (b) and the corresponding COP (c) and TCI (d) for a sink/source configuration of 10K/10K

in Fig. 6.2 (c), and TCI in Fig. 6.2 (d). As seen the optimum value of x_r is 0.9 up to a heat supply temperature of approximately, $T_{\text{sink,out}}$ = 100 °C. At this point the high pressure with x_r = 0.9 attains a value 50 bar, corresponding to the limits of the HP R717 compressor. When increasing the supply temperature beyond this point the ammonia mass fraction must consequently be reduced to comply with the high pressure constraint. All optimal solutions beyond this point have the maximum allowable pressure and thus the maximum allowable ammonia mass fraction. This is in alignment with what was shown in Fig. 6.1 and is also in alignment with the conclusions of studies such as [37, 38].

From Fig. 6.2 (b) it is be seen that optimal choice of f remains close to constant as long as x_r = 0.9, while it starts to increase when the ammonia mass fraction is reduced.

As seen from Fig. 6.2 (c) the COP increases slightly up to the point at which the ammonia mass fraction is reduced. Moving beyond this point COP decreases slightly. However, it is seen that the COP is more sensitive to the value of ΔT_{lift} than to $T_{\text{sink,out}}$.

Fig. 6.2 (d) shows that the TCI decreases up to the point at which the ammonia mass fraction is reduced. The reduction of TCI combined with the increased COP results in an improved NPV up to the point at which $p_{H,\max}$ is reached. Moving beyond this point, TCI increases while COP decreases, thus reducing NPV. However, it may be seen that the increase of the investment flattens out for $T_{\text{sink,out}} > 120$ °C. This occurs as the higher temperatures increase the specific volume in the suction line thus countering the increase due to the reduction of x_r. Further, going below an x_r of approximately 0.5 will cause the two-phase heat transfer coefficient to increase again as pure water is approached.

6.3.3 HACHP working domain

Figs. 6.3 and 6.4 show the derived working domains of the HACHP under the four investigated sink/source configuration cases and under the application of both the LP R717 and HP R717 components.

Fig. 6.3 shows the working domain for the sink/source configurations of 10K/ 10K (6.3a & 6.3b) and 20K/20K (6.3c & 6.3d). Figs. 6.3a and 6.3c correspond to the use of the LP R717 components while the HP R717 components have been applied in Figs. 6.3b and 6.3d.

Fig. 6.4 shows the working domain for the sink/source configuration of 20K/ 10K (6.4a & 6.4b) and 40K/10K (6.4c & 6.4d). Equally, Figs. 6.4a and 6.4c are for LP R717 components, while Figs. 6.4b and 6.4d are with the HP R717 components.

As in Fig. 6.1 the grey areas in Figs. 6.3 and 6.4 indicate the operating conditions that comply with all technical and economic constraints. Further, all constraints are presented as in Fig. 6.1. However, it should be noted that the dashed blue line presented in Figs. 6.3 and 6.4 indicate the point at which the optimal solution attains the maximum allowable pressure. Thus, all solutions to the left of the dashed blue line have pressures below $p_{H,\max}$ while all solutions to the right of the dashed blue line have $p_H = p_{H,\max}$. The solutions to the right of dashed blue

line are thus feasible solutions but they operate on the pressure boundary to attain the best economy.

As may be seen from Fig. 6.3a, the HACHP using the LP R717 components at a sink/source configuration of 10K/10K can deliver a maximum heat supply temperature of $T_{\text{sink,out}}$ = 125 °C and a maximum temperature lift of ΔT_{lift} = 48 K. It can be seen that the maximum heat supply temperature is limited by the vapour ammonia mass fraction, x_v, while the maximum temperature lift is limited by the compressor discharge temperature. Further, it may be seen that all technically feasible solutions attain a positive NPV and almost all attain a simple PBP lower than 8 years. To attain a PBP below 4 years a maximum temperature lift of 28 K can be attained at a heat supply temperature of 65 °C.

Applying the HP R717 compressors to the 10K/10K sink/source configuration, the maximum heat supply temperature is increased to above $T_{\text{sink,out}}$ = 140 °C, see Fig. 6.3b. Further, it can be seen that the maximum lift of 48 K can be retained at higher heat supply temperatures when applying the high pressure compressor. It can be seen that the maximum heat supply temperature and maximum temperature lift are both bound by the compressor discharge temperature. Again all technically feasible solutions attain a positive NPV.

For the sink/source configuration of 20K/20K, Figs. 6.3c and 6.3d, the maximum temperature lift is 42 K while the maximum heat supply temperature is 119 °C for LP R717 and 130 °C for HP R717. For 20K/10K, Figs. 6.4a and 6.4b, this is reduced to a maximum temperature lift of 54 K and a maximum heat supply temperature of 125 °C for LP R717 and 135 °C for HP R717. For sink/source configuration 40K/10K, Figs. 6.4c and 6.4d, the maximum temperature lift is 60 K while the maximum heat supply temperature is 100 °C and 125 °C for LP and HP R717 respectively.

It can be seen that mainly the working domain for the LP R717 compressor at a sink/source configuration of 10K/10K is bound by the x_v constraint. For 20K/10K a minor area is also limited by x_v. All other working domains are limited entirely by the compressor discharge temperature. Further, all technically feasible solutions have a positive NPV and almost all have a PBP below 8 years. In general, when increasing the sink glide the maximum heat supply temperature is reduced while

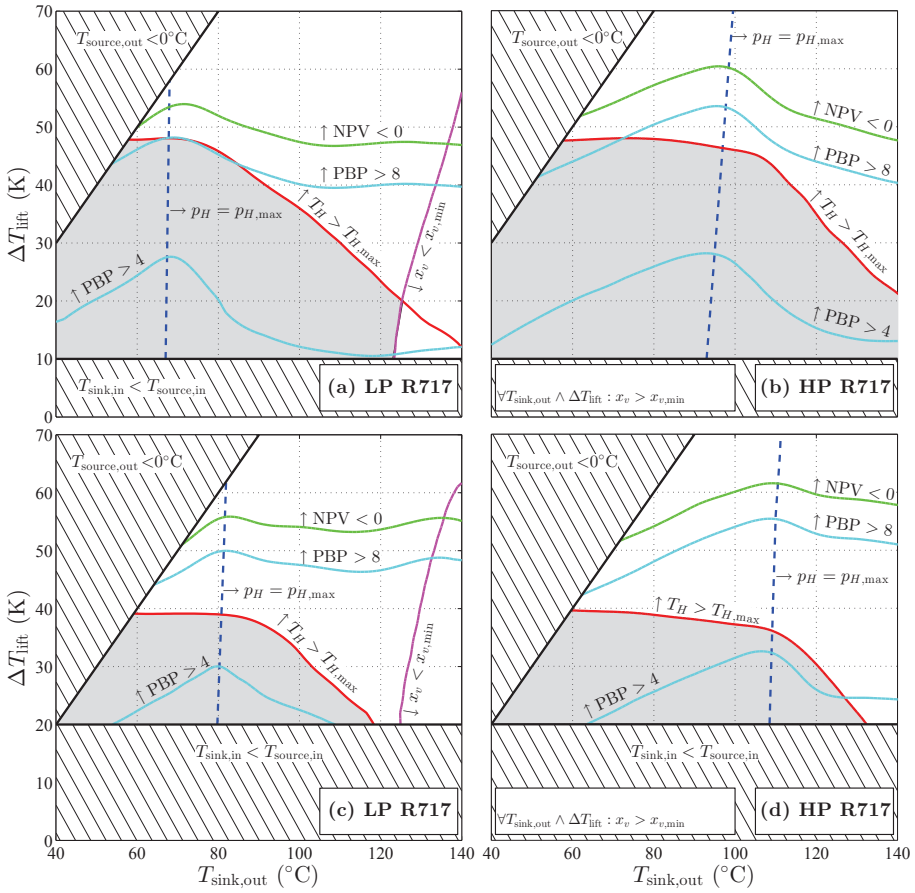

Figure 6.3: Feasible working domains indicated by grey background for HACHP using LP R717 and HP R717 compressors at ΔT_{sink}=10 K, ΔT_{source}=10 K (a) and (b) and ΔT_{sink}=20 K, ΔT_{source}=20 K (c) and (d). Hatched areas define technically infeasible domains. Curves indicate technical operating limits of components and economic limits

the maximum lift is increased.

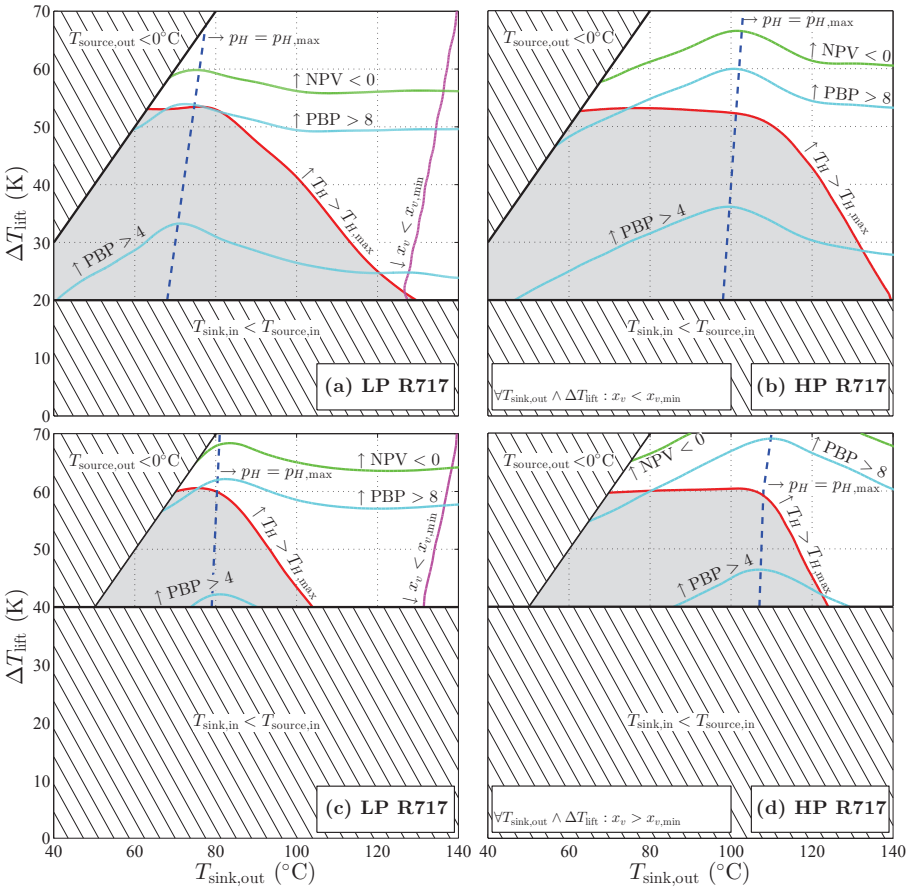

Figure 6.4: Working domains for HACHP using LP R717 and HP R717 compressors at at ΔT_{sink}=20 K, ΔT_{source}=10 K (a) and (b) and ΔT_{sink}=40 K, ΔT_{source}=10 K (c) and (d)

6.3.4 Best available HACHP and comparison with the VCHP

From Figs. 6.3 and 6.4 it can be seen that the working domains of the LP and HP R717 components overlap in the low temperature range. It is therefore relevant to evaluate when it is more profitable to chose a high pressure solution over the low pressure solution. Fig. 6.5 shows which component technology yields the highest possible NPV for all

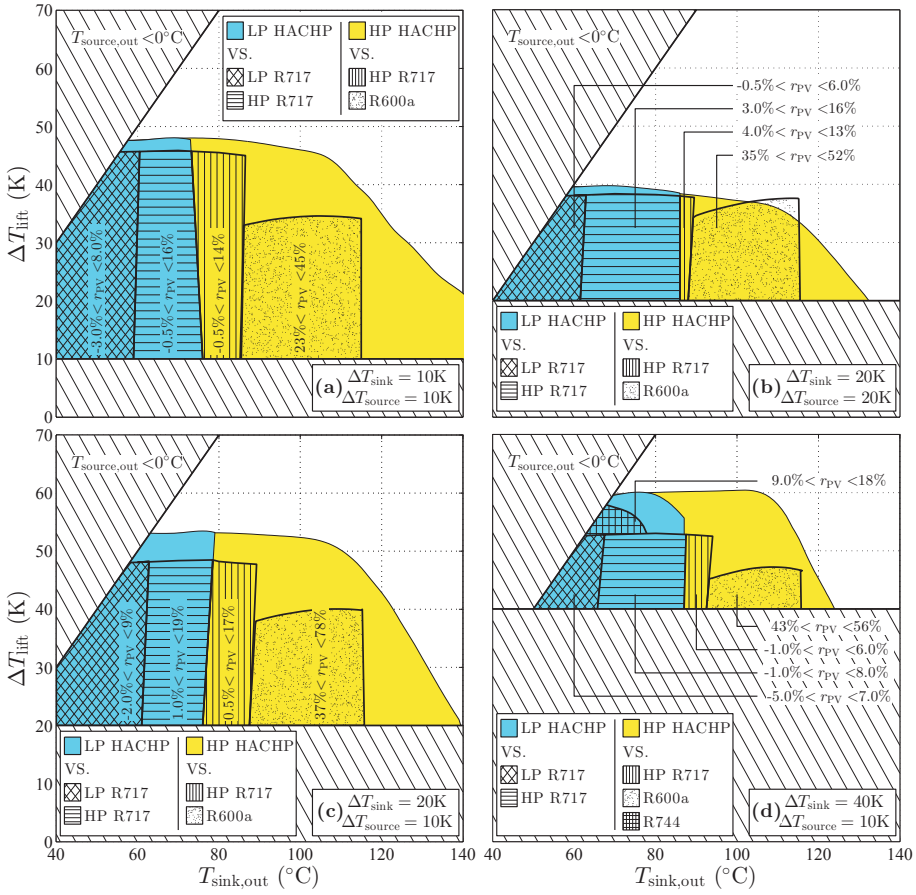

Figure 6.5: Most profitable HACHP and comparison with the best available VCHP. The blue area indicates the region in which the NPV of the LP R717 is higher than the NPV of the HP R717 solution. The hatched areas indicate which VCHP is the best competing technology.

four evaluated sink/source configurations. As seen, this results in two regions: a low temperature region (blue) in which the LP R717 components should be used and a high temperature region (yellow) in which the HP R717 components should be used. The supply temperature at which the high pressure option becomes favourable is approximately $T_{sink,out}$ = 75 °C for 10K/10K, $T_{sink,out}$ = 85 °C for 20K/20K, $T_{sink,out}$ = 78 °C for 20K/10K and $T_{sink,out}$ = 90 °C for 40K/10K. If this is com-

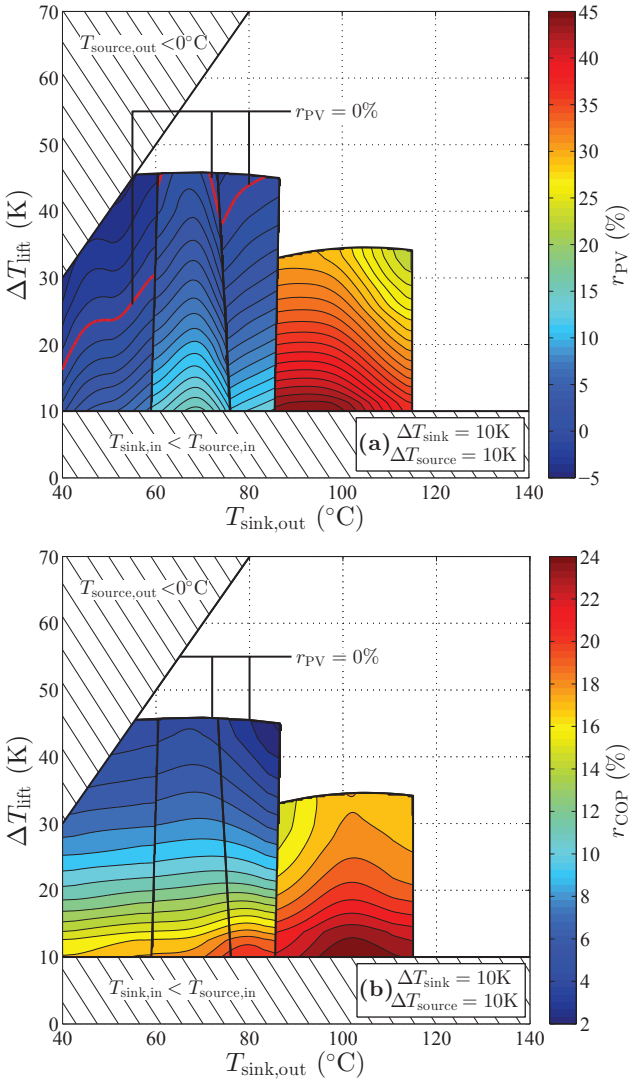

Figure 6.6: Contours of relative difference in PV, r_{PV}, (a) and the relative difference in COP, r_{COP}, between the best available HACHP and VCHP. Both for a sink/source configuration of 10K/10K

pared to the dashed blue lines in Figs. 6.3 and 6.4 it may be seen that the switch from LP to HP R717 happens approximately 5-8 °C above the point where the LP R717 reaches $p_{H,\max}$. This is due the retention of the high ammonia mass fraction for the HP R717 meaning that the compressor volume will be smaller and the heat transfer coefficient will be higher. Hence, the HP R717 investment becomes smaller than the LP R717 investment although the investment in the HP R717 components are higher per unit of displacement volume and heat transfer area.

Further, Fig. 6.5 shows the working domain of the best available VCHP, as concluded from [75]. As seen, the HACHP competes mainly with low and high pressure R717 and R600a but also with R744 for 40K/10K. Comparing the working domain of the HACHP to the working domain of the best possible VCHP solution it is clear that the HACHP expands the range of operating conditions for which heat pump application is technically feasible and economically viable. The HACHP allows both higher temperature lifts and higher heat supply temperatures, especially when ΔT_{sink} is large.

Fig. 6.5 also shows the difference in cost between the HACHP and the VCHP. This is represented by the relative difference in present value:

$$r_{\text{PV}} = \frac{\text{PV}_{\text{VCHP}} - \text{PV}_{\text{HACHP}}}{\text{PV}_{\text{VCHP}}} \cdot 100\%. \tag{6.8}$$

As seen, r_{PV} is between -5.0% and +9% for the range in which low pressure HACHP competes with low pressure R717. For low pressure HACHP against high pressure R717, r_{PV} is between -1.0% and +19% while high pressure HACHP versus high pressure R717 results in r_{PV} is between -1.0% and +17%.

For the range where the HACHP competes with R600a the r_{PV} is between 23% and 78%. This is due to the large investment and poor COP associated with R600a. Hence, for heat supply temperatures above $T_{\text{sink,out}}$ = 90 °C where R717 can no longer be applied, the HACHP seem to be the more profitable solution.

Also for the range where LP HACHP competes with the transcritical R744 heat pump, the HACHP seem to be the preferred option with r_{PV} between 9-18%.

Fig. 6.6 shows the trend of r_{PV} for the sink/source configuration of 10K/10K. As seen, the economic advantage of the HACHP is larger

at low temperature lifts. Further, it may be seen that the advantage increases with increasing heat supply temperature. Fig. 6.6 shows the relative difference in COP between the HACHP and VCHP:

$$r_{\mathrm{COP}} = \frac{\mathrm{COP}_{\mathrm{HACHP}} - \mathrm{COP}_{\mathrm{VCHP}}}{\mathrm{COP}_{\mathrm{VCHP}}} \cdot 100\% \tag{6.9}$$

As seen, the HACHP offers significantly increased COP at low lifts. However, when the temperature lift is increased the COP of the HACHP and the VCHP approach one another. This as the advantage of the HACHP is the reduction of irreversibilities related to the heat exchange processes. However, as the temperature lift is increased the irreversibilities related to the compression is more dominant and thus the efficiency of the two systems become similar. This results in the trend of r_{PV} seen in Fig. 6.6. As seen, for low temperature range (LP R717 versus LP HACHP), where compressor investment is high, this results in an area where the HACHP is not economically favourable compared to the VCHP. This is indicated by the red line in Fig. 6.6.

As seen from Fig. 6.5 the HACHP offers the best economic improvement for the sink/source configuration of 20K/10K. One could expect the improvement to be even higher for 40K/10K due to the large sink temperature difference, but this is not the case as a high sink temperature difference also entails a high temperature lift and thus the HACHP and VCHP are only compared at lifts where the COP is similar.

6.4 Discussion

Comparing R717 VCHP to the HACHP, the r_{PV} for most operating points is between 5-10%. However, the PEC cost of commercial components may vary with up to 40% from the indicated price. This might be an advantage for large manufactures where large quantities are purchased and PEC thereby can be reduced. This could cause the R717 VCHP to attain equal or higher NPV as VCHPs are a more mature technology with more competition between the suppliers. As shown in [75] one of the highest uncertainty on the NPV is related to the electricity price. An increased electricity cost would be an advantage for the HACHP over the VCHP due to the higher COP, while a reduction of

the electricity price would be an advantage for the VCHP as the NPV would be more influenced by investment.

Further, the performance of VCHP could be further optimized by the application of exergoeconomic optimization [19] to the temperature difference in the evaporator and condenser. This would allow the best trade-off between investment and running cost to be determined for each refrigerant and at each operating point. This, however could also be applied to HACHP. If exergoeconomic optimization was applied the technologies would be compared at the best possible design, which might change the conclusion from this study.

Further, the HACHP is just one method for vapour compression systems to approach the Lorenz cycle. Conventional vapour compression heat pumps set in series are an alternative measure of this. This could prove to be a more cost efficient solution and should be investigated.

It should be noted that the application of the high pressure compressor to the HACHP did not increase the range of feasible heat supply temperatures compared to those concluded from [23]. This is mainly due to the applied constraint on the compressor discharge temperature, which was neglected in [23]. The use of a cooled screw compressor or an oil free compressor could relax the constraints on the compressor discharge temperature and allow heat supply temperatures above 150 °C. Alternatively, the application of a gas cooler prior to the mixing of vapour and lean solution can reduce the compressor discharge temperature as shown in [48]. Further, a two-stage compression could be a measure of reducing the compressor discharge temperature and thus extending the working domain of the HACHP.

6.5 Conclusion

The feasible working domain of a HACHP has been evaluated based on a detailed economic analysis and a comprehensive investigation of the design variables: ammonia mass fraction and circulation ratio. The results show that the HACHP is capable of delivering both higher heat supply temperatures and higher temperature lifts than conventional VCHP.

Heat supply temperatures up to 150 °C and temperature lifts up to 60 K can be attained with commercially available components and with an economic benefit compared to gas combustion. It is found that the dominating constraint for the HACHP is the compressor discharge temperature. Further, it is found that reducing the sink/source temperature difference increases the maximum attainable heat supply temperature while reducing the maximum attainable lift.

When comparing the PV of the HACHP with the VCHP at the operating points where both are applicable: the cost of the HACHP is lower for almost all operating conditions with a heat supply temperature above 80 °C. For the range where the HACHP competes with R717 the difference in PV can be insignificant and both technologies should be considered. For the high temperature range where the only applicable VCHP technology is R600a the difference in PV is large and the HACHP should be applied.

CHAPTER 7

CASE STUDY: HYBRID ABSORPTION COMPRESSION HEAT PUMP IMPLEMENTATION FOR WASTE HEAT RECOVERY IN A SPRAY DRYING FACILITY

In this chapter a case study on the implications of applying a HACHP as a waste heat recovery measure in spray drying facility is investigated. The work was first presented at the 27th International Conference on Efficiency, Cost, Optimization, Simulation and environmental Impact of Energy Systems (ECOS 2014) [44] ([P13]). The work was later published in the International Journal of Energy and Environmental Engineering [42] ([P2]).

7.1 Introduction

Industrial spray drying facilities are among the most energy intensive industrial processes. They are applied in the production of dry solids from a liquid feedstock. This is typically needed in the chemical, pharmaceutical or food industry. Typical products of spray drying processes are powdered milk, detergents and dyes. A survey from 2005 [17] showed that the yearly energy consumption for drying operation in the United Kingdom was 348.6 PJ, corresponding to 17.7 % of industrial energy consumption. Spray drying processes are typically fuelled by fossil fuel combustion, most commonly natural gas [17]. Therefore, spray drying facilities are not only accountable for a large energy consumption but also for a large quantity of green house gas emissions. Improving the energy efficiency of spray drying facilities is thus important to reach the

goals for a sustainable development of the industrial sector.

Given the recent and projected increase in renewable electricity generation from sources such as wind and solar [1], moving energy consumption from gas combustion to an electrically driven heat pump could be an environmental benefit.

The implementation of heat pumps in spray drying facilities is typically restricted by the high temperature of the exhaust air (80-100 °C), which is out of the working domain for most industrial vapour compression heat pumps. However, as described in the previous chapters, The HACHP has several attributes making it applicable for high temperature operation.

Heat pump driven drying processes has been studied by Prasertsan et al. [86], Gungor et al. [33] and Chua et al. [25]. These investigations have been limited to low temperature drying processes due to the constrained heat supply temperature of conventional vapour compression heat pumps. The maximum supply temperature of vapour compression heat pumps is bound by the maximum allowable pressure of the compressor technology and the corresponding saturation temperature of the refrigerant [75].

This case study will investigate the economic and environmental implication of implementing a HACHP in a spray drying facility. Using the detailed heat transfer correlations, described in Chapter 4, the effect of changing ammonia mass fraction will be accounted for. The heat pump load, ammonia mass fraction and the circulation ratio in the HACHP will all be analysed and optimized within commercial component constraints. Combination of four ammonia concentrations and four heat pump loads will be investigated. This yields a total of 16 design conditions at which the HACHP design will be optimized.

To optimize the design an exergoeconomic optimization [19, 55] is applied in each of the 16 conditions. By optimizing the design of each of the these 16 conditions the best possible design can be found and the effect of changing heat pump load and ammonia mass fraction can be evaluated without bias.

The objective of the present work is thus to evaluate if implementing a HACHP in a spray drying facility is: technically feasible, using current commercial components and further, if such an installation will be

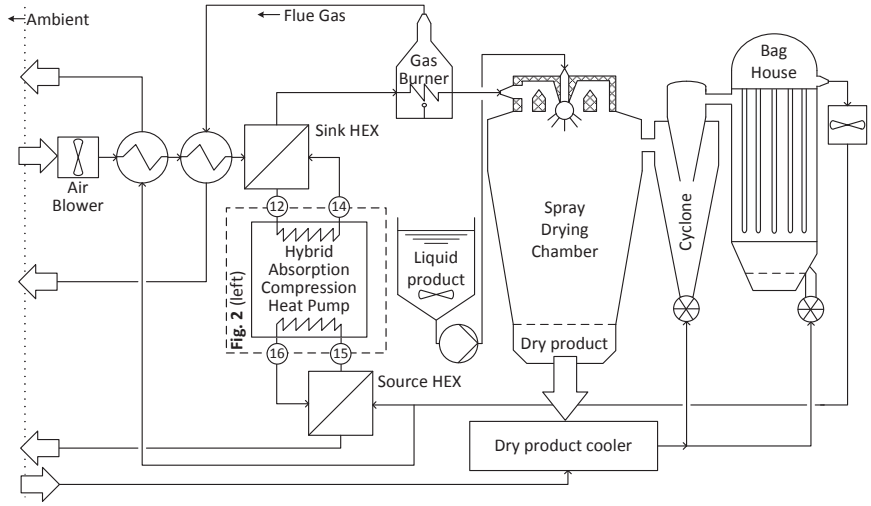

Figure 7.1: Principle sketch of the investigated spray drying facility

economically viable as well as environmentally beneficial.

7.2 Methodology

7.2.1 Spray drying facility and heat pump implementation

A generic spray drying facility, as seen in Fig. 7.1, was studied. The HACHP was implemented to heat the drying air prior to the gas burner. The ambient air is introduced to the system by an air blower at a rate of 100,000 m^3/h. The air stream is first heated by a fraction of the exhaust air. Hereafter, it is heated by a flue gas heat recovery heat exchanger. The ambient air has a temperature of 20 °C and a humidity ratio of 0.006 kg/kg. At the outlet of the flue gas heat recovery heat exchanger the drying air is 80 °C. From here the drying air is heated by the HACHP, utilizing exhaust air as the heat source. The drying air is then heated to 200 °C by a natural gas burner.

Heating the air from 20-200 °C results in a total heat load of 6.1 MW. The larger the HACHP load the more of the total heat load will

be moved from the gas burner to the HACHP. As the exhaust temperature is uninfluenced by this: the temperature lift supplied by the HACHP increases with increasing load, thus decreasing the coefficient of performance (COP). It is therefore necessary to find a suitable HACHP load to ensure the viability of the investment.

When the air has reached the target temperature of 200 °C it enters the spray drying chamber and is mixed with the atomized stream of the liquid product. This causes the liquid in the product to evaporate. The dry product can then be extracted from the bottom of the chamber. The now more humid air is passed first through a cyclone and then a bag house filter to remove left over product. Here, air heated by the dry product is introduced. The exhaust air exiting the bag house has a temperature of 80 °C, humidity ratio of 0.045 kg/kg and approximately twice the mass flow rate of the drying air. This means that the capacity rate of the exhaust is higher than that of the air being heated. Therefore, the exhaust stream can be split such that half can be used to heat the air directly and the rest can be used as the heat source in the HACHP. This, in combination with the use of a flue gas heat recovery heat exchanger ensures that there is an actual heat surplus at the exhaust air temperature. Consequently the HACHP as implemented here will transfer heat across the pinch temperature [19]. The analysis and results presented in this paper is only valid for such systems. This is not always the case [52] and as a consequence of pinch analysis [19], the exhaust air is best utilized by heating the incoming air directly.

To reduce the risk of contamination two secondary circuits are used to transfer the heat between the drying/exhaust air and the HACHP. The heat transfer fluid is water. On the sink side this is pressurized to prevent evaporation. The secondary circuits will increase the HACHP temperature lift, thus reducing the COP but is assumed to be a necessary safety measure.

The layout of the HACHP applied in this study is presented in Fig. 7.2. Here, the stream and component index applies is also presented.

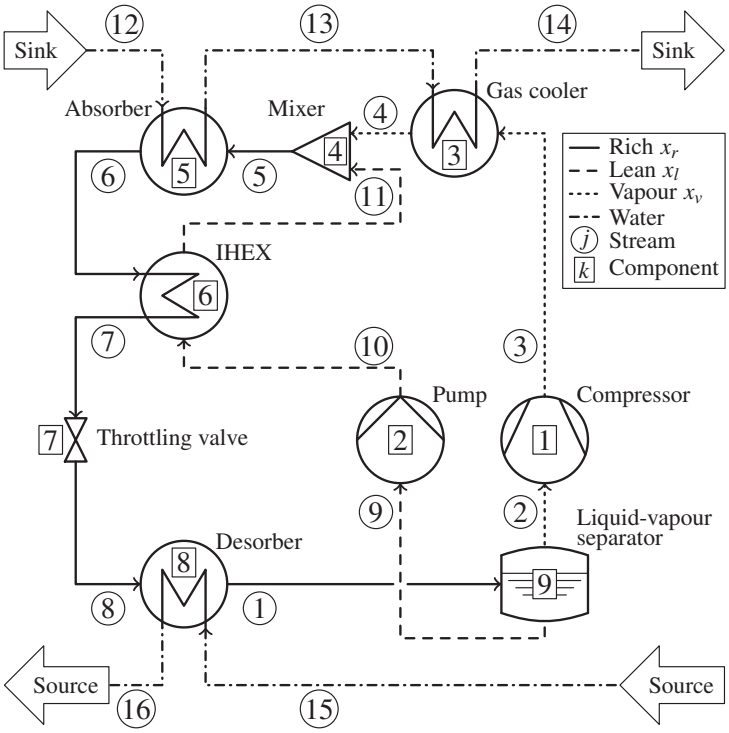

Figure 7.2: General layout of the investigated HACHP

7.2.2 Exergoeconomic optimization using partial derivatives

Exergoeconomic analysis and optimization is a method for estimating and minimizing the total cost of a single component or an energy conversion system as a whole, over the course of its lifetime [19]. The objective of an exergoeconomic optimization is the minimization of the component or system product cost rate, $\dot{C}_P$.

By the application of a cost balance [19] the product cost rate for a single component can be derived as:

$$\dot{C}_{P,k} = \dot{Z}_k + \dot{C}_{F,k} \tag{7.1}$$

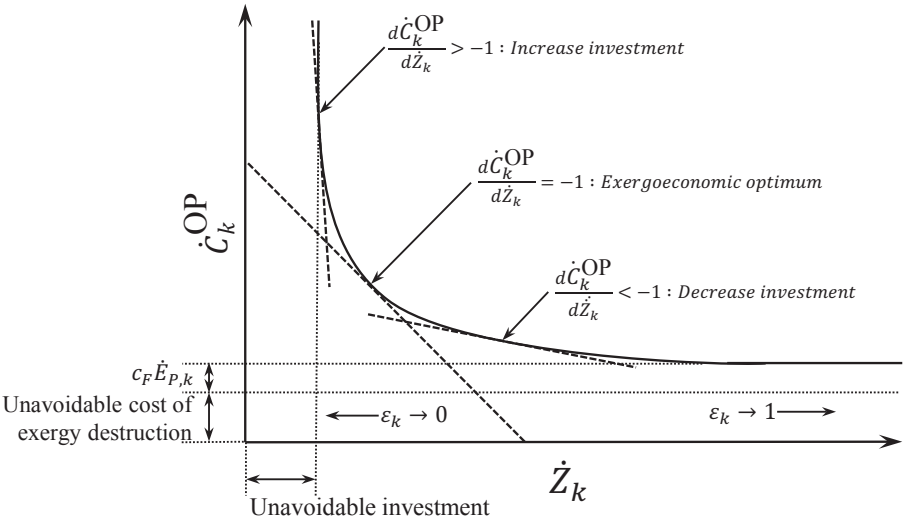

Figure 7.3: Graphical representation of the exergoeconomic optimum

Utilizing that: $\dot{E}_D = \dot{E}_F - \dot{E}_P$ and $\dot{C}_D = c_F\dot{E}_D$, this becomes:

$$\dot{C}_{P,k} = \underbrace{\dot{Z}_k}_{\text{Investment}} + \underbrace{\dot{C}_{D,k} + c_{F,k}\dot{E}_{P,k}}_{\text{Operation}} \tag{7.2}$$

Equally for the system as a whole:

$$\dot{C}_{P,\text{sys}} = \underbrace{\sum_{k=1}^{K} \dot{Z}_k}_{\text{Investment}} + \underbrace{\dot{C}_{D,\text{sys}} + c_{F,\text{sys}}\dot{E}_{P,\text{sys}}}_{\text{Operation}} \tag{7.3}$$

As seen in Eq. (7.2) or (7.3) the cost of the component or system product is comprised of three contributions, 1: the capital investment cost rate $\dot{Z}$, 2: the exergy destruction cost rate $\dot{C}_D$ and 3: the term $c_F\dot{E}_P$. As indicated in Eq. (7.2) and (7.3) the sum of $\dot{C}_D$ and $c_F\dot{E}_P$ can be viewed as the operational cost of the component or system and will in the following be referred to as:

$$\dot{C}^{\text{OP}} = \dot{C}_D + c_F\dot{E}_P \tag{7.4}$$

In the current study the objective is the minimization of the cost of heat supplied by the HACHP and is thus a minimization of $\dot{C}_{P,\text{sys}}$. The

objective for the HACHP system can be stated as:

$$\text{Objective function}: \quad \min\left(\sum_{k=1}^{K}\dot{Z}_k + \dot{C}_{\text{sys}}^{\text{OP}}\right) \tag{7.5}$$

The objective of the optimization is thus to balance the cost of capital investment with the cost of operation. From Eq. (7.4) it is clear that the cost of operation can be reduced by increasing exergy efficiency and consequently reducing the cost of exergy destruction, $\dot{C}_{D,\text{sys}}$. However, for most components this will require an increased investment. E.g. for a heat exchanger, the exergy efficiency is increased if the temperature difference is reduced, consequently the heat transfer area and subsequently the investment must increase to adapt to the reduced temperature difference.

This behaviour is depicted in Fig. 7.3. Here it may be seen that the relation of $\dot{C}_k^{\text{OP}}$ to $\dot{Z}_k$ has a horizontal and vertical asymptote. As the investment approaches infinity, some exergy destruction will prevail, due to technological limitations, this is known as the unavoidable exergy destruction [105]. Further, no matter how much the exergy efficiency is decreased, some investment will be needed, this is known as the unavoidable investment [105]. This behaviour is limiting for system improvement based on the conventional exergoeconomic analysis as this uses indicators based on absolute values of $\dot{C}_D$ and $\dot{Z}$ and thus does not account for the unavoidable parts.

In the present study cost functions for the component PEC were applied. Therefore, component investment costs were expressed mathematically, as a function of the HACHP design. This also allows the exergoeconomic optimum to be defined mathematically.

As seen in Fig. 7.3, the exergoeconomic optimum choice of exergy efficiency, ε_k, is defined where the marginal cost rate of the levelized investment and maintenance cost, $\dot{Z}_k$, is equal to the marginal cost rate of operation, $\dot{C}_k^{\text{OP}}$. Mathematically this statement can be justified by taking the derivative of Eq. (7.2) with respect to the exergy effeciency, ε_k:

$$\frac{d\dot{C}_{P,k}}{d\varepsilon_k} = \frac{d\dot{Z}_k}{d\varepsilon_k} + \frac{d\dot{C}_k^{\text{OP}}}{d\varepsilon_k} \tag{7.6}$$

Thus, if $\frac{d\dot{Z}_k}{d\varepsilon_k} = -\frac{d\dot{C}_k^{\mathrm{OP}}}{d\varepsilon_k}$ then $\frac{d\dot{C}_{P,k}}{d\varepsilon_k}$=0 and it can be confirmed that an optimum condition is attained. Further, if the component follows the behaviour seen in Fig. 7.3 this optimum will be the global minimum for $\dot{C}_{P,k}$ as: $\dot{C}_{P,k} \to \infty$ for both $\varepsilon_k \to = 0$ and $\varepsilon_k \to = 1$

Hence, for a component that follows the behaviour seen in Fig. 7.3 the cost of the component exergy product, Eq. (7.2), is minimized when:

$$\frac{d\dot{C}_k^{\mathrm{OP}}}{d\dot{Z}_k} = -1 \tag{7.7}$$

Subsequently, if:

$$\frac{d\dot{C}_k^{\mathrm{OP}}}{d\dot{Z}_k} > -1 \tag{7.8}$$

the total cost can be reduced by increasing the exergy efficiency, at the expense of an increased investment. Conversely if:

$$\frac{d\dot{C}_k^{\mathrm{OP}}}{d\dot{Z}_k} < -1 \tag{7.9}$$

the total cost is reduced by reducing the investment, at the expense of a reduced exergy efficiency.

The design of the HACHP was governed by four decision variables. These were, $\Delta T_{\mathrm{pp},k}$ for the absorber and desorber and ϵ_k for the IHEX and gas-cooler. A change in these variables will all exhibit the behaviour presented in Fig. 7.3. It was the objective of the exergoeconomic optimization, to determine the optimum values of these four variables. This was done by an iterative optimization procedure minimizing the objective function stated in Eq. (7.5).

Initial guess values for the four decision variables were made. Using the "Uncertainty Propagation" procedure in EES [54], the partial derivatives of both the investment cost rate, $\dot{Z}^{\Sigma}$ and the operational cost rate, $\dot{C}_{\mathrm{sys}}^{\mathrm{OP}}$, was found with respect to the four decision variables individually. The superscript Σ, here indicates the sum over all K components. Based on these partial derivatives, it was decided whether to increases

or decrease the values. E.g. if:

$$\left|\frac{\partial \dot{C}_{\text{sys}}^{\text{OP}}}{\partial \Delta T_{\text{pp},5}}\right| > \left|\frac{\partial \dot{Z}^{\Sigma}}{\partial \Delta T_{\text{pp},5}}\right| \tag{7.10}$$

the absorber pinch point temperature difference should be reduced.

This procedure was repeated until:

$$\left(\frac{\partial \dot{C}_{\text{sys}}^{\text{OP}}}{\partial \dot{Z}^{\Sigma}}\right)_k \in \{-0.9, -1.1\} \tag{7.11}$$

for all the four decision variables simultaneously, at which an optimum was said to be attained.

To justify this approach the results of the described procedure will, for one case, be compared to the result of a Genetic Optimization Algorithm maximizing the present value of the savings attained by the installation. The boundaries for the decision variables where set to: $\Delta T_{\text{pp}} \in \{1;20\}$ and $\epsilon \in \{0;1\}$. The Genetic Optimization Algorithm was performed with 32 individuals and 64 generations. The build in Genetic Optimization Algorithm in EES [54] was applied.

The yearly savings in operational costs attained by the installations was determined as:

$$\text{Savings}_{\text{yearly}} = \dot{Q}_{\text{HP}} h_{\text{op}} \left(c_{\text{gas}} - \frac{c_{\text{elec}}}{\text{COP}}\right) \tag{7.12}$$

Here c_{gas} and c_{elec} are the gas and electricity prices, respectively and h_{op} is the of operating time per year. The present value of the savings, including the initial capital investment and maintenance cost, over the technical life time was then calculated as:

$$\text{Savings} = \frac{\text{Savings}_{\text{yearly}}}{\text{CRF}} - 1.2 \cdot \text{Investment} \tag{7.13}$$

7.3 Results

7.3.1 Thermodynamic analysis

Fig. 7.4, shows the COP of the HACHP, as a function of the ammonia mass fraction and circulation ratio, with $\Delta T_{\text{pp},5} = \Delta T_{\text{pp},8}$ = 10 K and

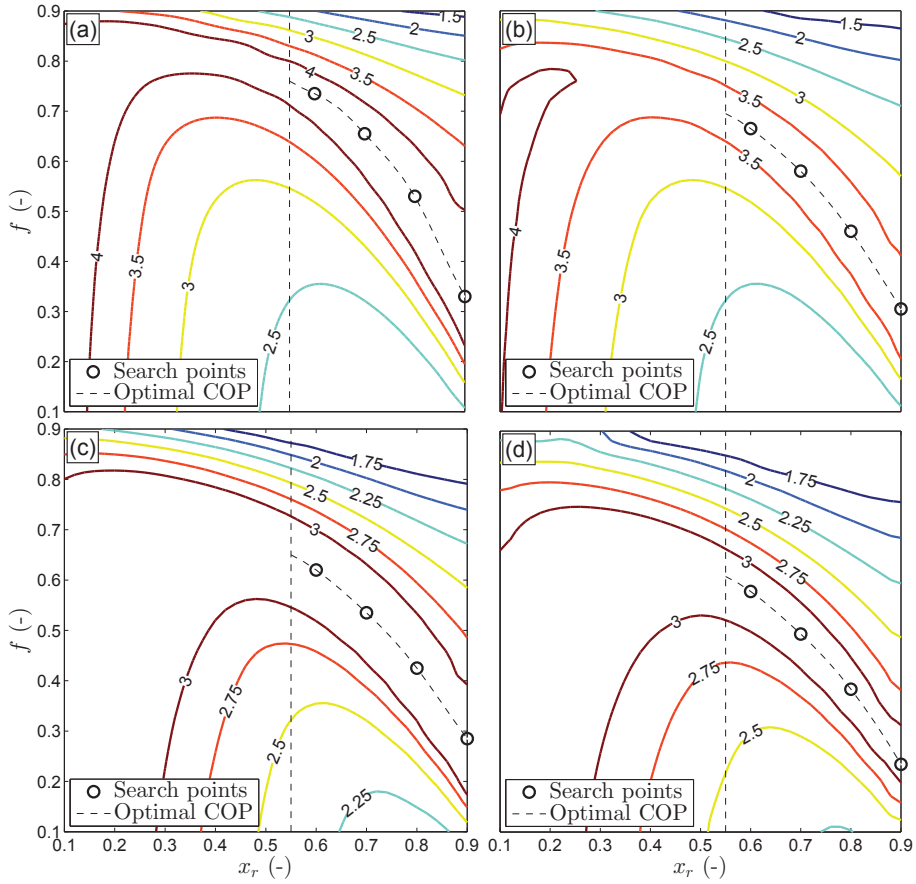

Figure 7.4: COP of the HACHP as function of x_r and f for a HACHP covering (a): 10 %, (b): 15 %, (c): 20 % and (d): 25 % of the total heat load

$\epsilon_3 = \epsilon_6 = 0.7$. Fig. 7.4 (a) is for a HACHP covering 10 % of the total heat load. Fig. 7.4 (b) is for 15%, 7.4 (c) for 20 % and 7.4 (d) is for 25 %. The solutions with $x_r < 0.55$ are discarded, as these tend to result in sub-atmospheric desorber pressures and large volumetric flow rates in the compressor suction line. It is seen, that for all four load shares, in the range of $x_r > 0.55$, one circulation ratio optimizes the COP for each value of x_r. The optimum COP line for all four loads are shown with the dashed line. It can be seen that this line shifts downwards as

the HACHP load is increased. Hence, the higher the load, the lower the circulation ratio. This is mainly due to the increased temperature glide in the heat sink.

Four points are chosen at each HACHP load, these are with x_r of: 0.6, 0.7, 0.8 and 0.9 and the corresponding optimum circulation ratios. These points are indicated with circles on Fig. 7.4.

7.3.2 Exergoeconomic optimization

The exergoeconomic analysis can then be applied to determine the exergoeconomic optimum design, at the 16 points derived from the thermodynamic analysis. Table 7.1 shows the result of the exergoeconomic analysis, at an initial set of guess values and at the exergoeconomic optimum. Both, have a HACHP load of 15 % and a rich ammonia mass fraction x_r = 0.8. The initial guess values are $\Delta T_{\mathrm{pp},5} = \Delta T_{\mathrm{pp},8}$ = 15 K and $\epsilon_3 = \epsilon_6$ = 0.9.

As may be seen in Table 7.1, for the initial guess values, the total cost rate for the gas-cooler is the third highest only surpassed by the compressor and absorber. The gas-cooler also has the second highest relative cost difference. Judging from the low exergoeconomic factor, conventional exergoeconomic optimization states, that the investment should be increased but judging from the partial derivative the investment should actually be decreased, to reduce the overall cost.

This difference arises, as the partial derivatives account for both the interdependencies between component exergy efficiencies and for the unavoidable part of exergy destruction and investment.

In the case of the absorber and IHEX, it may be seen that the conclusions of the conventional exergoeconomic analysis and the partial derivatives coincide.

The exergoeconomic factor for the desorber is $f_{ex,8}$ = 1. This is because no cost is associated with the waste heat and thus, $c_{F,k}$ = 0. Therefore, the relative cost difference cannot be calculated as, $c_{F,k}$ is the fraction denominator. This makes it hard to judge whether or not the choice of the design parameter for the desorber is appropriate. However, judging from the partial derivative it is clear that savings to the overall cost can be attained by increasing the desorber exergy efficiency.

Table 7.1: Non-exergetic and exergetic cost rates and exergoeconomic indicators for the initial guess and optimal solution for a HACHP with x_r = 0.8 covering 15 % of the total heat load

k^{th}	Decision var.		$\dot{Z}_k$+$\dot{C}_{D,k}$ (cent/h)	$f_{ex,k}$ (%)	r_k (%)	$\left(\frac{\partial \dot{C}^{\mathrm{OP}}}{\partial \dot{Z}^{\Sigma}}\right)_k$
Initial guess variables						
(1)			779	56	45	-
(2)			16.7	53	60	-
(3)	ϵ	= 0.9 -	351	8.3	62	-0.294
(4)	ΔT_{pp}	= 15 K	374	26	24	-2.02
(6)	ϵ	= 0.9 -	206	75	92	-0.263
(8)	ΔT_{pp}	= 15 K	74.8	100	-	-3.64
Objective function value, Eq. (7.5):						2896 cent/h
Present value of Savings, Eq. (7.13):						€81,138
Exergoeconomic optimum by partial derivatives						
(1)			728	57	48	-
(2)			15.7	54	61	-
(3)	ϵ	= 0.864 -	271	9.6	58	-0.933
(4)	ΔT_{pp}	= 11.3 K	387	44	26	-1.00
(6)	ϵ	= 0.719 -	76.6	53	54	-1.05
(8)	ΔT_{pp}	= 9.49 K	193	100	-	-1.02
Objective function value, Eq. (7.5)						2742 cent/h
Present value of Savings, Eq. (7.13):						€138,078
Genetic optimization algorithm maximizing Savings						
(1)			728	57	48	-
(2)			15.7	54	61	-
(3)	ϵ	= 0.864 -	271	9.6	58	-0.965
(4)	ΔT_{pp}	= 11.3 K	387	44	26	-1.04
(6)	ϵ	= 0.719 -	76.6	53	54	-1.01
(8)	ΔT_{pp}	= 9.49 K	193	100	-	-0.979
Objective function value, Eq. (7.5):						2742 cent/h
Present value of Savings, Eq. (7.13):						€138,117

The conclusion from the partial derivatives of the initial guess is that: The effectiveness of the IHEX and gas-cooler should be reduced to lower the investment, the IHEX effectiveness should be lowered more than for the gas-cooler. Further, the absorber and desorber pinch point temperature difference should both be reduced, more for the desorber than for the absorber.

Table 7.1 states the cost rates and exergoeconomic indicators at the optimum values of the decision variables, suggested by the partial derivatives. Here the absorber and desorber pinch point temperature differences are reduced to $\Delta T_{\mathrm{pp},5}$ = 11.3 K and $\Delta T_{\mathrm{pp},8}$ = 9.49 K, respectively. The IHEX effectiveness is reduced to ϵ_6 = 0.719 and the gas-cooler effectiveness to ϵ_3 = 0.864. Hence, the direction and the magnitude of the change in variables is consistent with the conclusion of the partial derivatives from the initial guess. Further, it can be seen that only the exergoeconomic factor and relative cost difference of the IHEX undergo substantial change between the initial guess and the optimum.

The present value of the savings attained by the HACHP is €81,138 with the initial guess values. This is increased by 70 %, at the exergoeconomic optimum, to a value of €138,078. The physical variables of the HACHP process, for the exergoeconomic optimum from Table 7.1, are listed in Table 7.2.

Further, the results of a Genetic Optimization Algorithm maximizing the PV of the savings is presented. The Genetic Optimization Algorithm was given the same initial guess as provided to the exergoeconomic optimization. As seen from Table 7.1 the Genetic Optimization Algorithm finds the same decision variables as found by the exergoeconomic optimization, which suggests that the applied optimization procedure is capable of determining the true optimum. It is seen that the Genetic Optimization Algorithm finds a savings that is 0.3% higher than what is attianed by the exergoeconomic optimization. However, the partial derivatives also suggest that the solution found by the Genetic Optimization Algorithm is closer to the exergoeconomic optimum. The exergoeconomic approach using partial derivatives found the four optimum decision variables after five iterations, each with a computation time of approximately 1 minute. While the computation time for the Genetic Optimization Algorithm was several hours.

Table 7.2: Thermodynamic state point variables for the exergoeconomic optimum seen in Table 7.1, x_r = 0.8 and 15 % of the total heat load covered by HACHP

j^{th}	$\dot{m}_j$	p_j	T_j	x_j	h_j	s_j	e^{PH}	e^{CH}
	(kg/s)	(bar)	(°C)	(-)	(kJ/kg)	(kJ/kgK)	(kJ/kg)	(kJ/kg)
1	1.39	13.3	64.3	0.800	776	2.80	221	15.9e3
2	0.749	13.3	64.3	0.995	1386	4.52	360	19.8e3
3	0.749	49.1	196	0.995	1665	4.64	603	19.8e3
4	0.749	49.1	125	0.995	1428	4.11	525	19.8e3
5	1.39	49.1	120	0.800	856	2.75	316	15.9e3
6	1.39	49.1	101	0.800	355	1.43	207	15.9e3
7	1.39	49.1	90.1	0.800	299	1.28	197	15.9e3
8	1.39	13.3	45.4	0.800	299	1.34	178	15.9e3
9	0.638	13.3	64.3	0.571	60.6	0.787	56.3	11.3e3
10	0.638	49.1	65.3	0.571	66.5	0.790	61.1	11.3e3
11	0.638	49.1	90.9	0.571	189	1.14	79.6	11.3e3
12	7.89	5.00	85.0	-	356	1.13	23.0	-
13	7.89	4.97	106	-	445	1.37	40.0	-
14	7.89	4.67	111	-	467	1.43	45.0	-
15	7.89	5.00	75.0	-	314	1.02	16.0	-
16	7.89	4.98	54.9	-	230	0.767	6.00	-

This optimization procedure has been conducted for all of the 16 design configurations. Fig. 7.5 (a) shows the non-exergetic cost rate, $\dot{Z}_k$, for the components at all 16 optimal designs. Fig. 7.5 (b) shows the exergy destruction cost, $\dot{C}_{D,k}$. It may be seen that the total non-exergetic cost rate, $\dot{Z}^{\Sigma}$, increases when decreasing the ammonia mass fraction. This is caused by an increase in the compressor, IHEX and desorber $\dot{Z}_k$. The remaining components are indifferent to the change in ammonia mass fraction. The compressor $\dot{Z}_k$ increases the most. This is caused by the reduced vapour pressure of the working fluid, resulting in an increased displacement volume. The IHEX $\dot{Z}_k$ is increased due to the increased circulation ratio for reduced ammonia mass fractions. Thereby, the capacity rates of the rich and lean mixtures approach each other, consequently reducing the LMTD and increasing the needed heat

load. Both resulting in the need for an increased area. Fig. 7.5 (a) also shows that the total non-exergetic cost rate, $\dot{Z}^{\Sigma}$ increases when the heat pump load is increased. The marginal $\dot{Z}^{\Sigma}$ is close to constant.

From Fig. 7.5 (b), it is seen that the total exergy destruction cost, $\dot{C}_D^{\Sigma}$, increases when decreasing the ammonia mass fraction. It is seen that the cost of operating the compressor is not significantly influenced by the ammonia mass fraction. Further, the gas-cooler $\dot{C}_{D,k}$, is indifferent to x_r for HACHP loads of 10% and 15%. For the absorber and IHEX, the $\dot{C}_{D,k}$ is increased, when decreasing the ammonia mass fraction. For the absorber, this is caused by the degradation of the two-phase heat transfer coefficient. The reduced heat transfer coefficient, shifts the optimal size of the absorber to a lower exergy efficiency. For the IHEX, the increased $\dot{C}_{D,k}$ is caused by the increased circulation ratio. For the desorber, $\dot{C}_{D,k}$ decreases when the ammonia mass fraction is reduced. This, in spite of the decreased heat transfer coefficient. This is caused by the interdependency between the low pressure and the compressor investment, as a larger desorber investment can reduce the compressor investment by increasing the suction line pressure. The total exergy destruction cost, $\dot{C}_D^{\Sigma}$, increases with the delivered heat load. The marginal $\dot{C}_D^{\Sigma}$ is also increased with the heat load.

7.3.3 HACHP implementation, economic and environmental savings

Several issues govern the implementation of the HACHP. As shown in Fig. 7.5, both the choice of ammonia mass fraction and heat pump load influence the investment and the operating costs of the HACHP.

To estimate yearly CO_2 emissions the fuel specific emission factors for electricity and natural gas in the Danish energy system is used [1].

Fig. 7.6 shows the economic and CO_2 savings as well as the compressor discharge temperature and pressure. All are shown as a function of the HACHP load $\dot{Q}_{\mathrm{HP}}$. The values are given for the exergoeconomic optimum designs. Fig. 7.6 (a) shows the present value of the economic savings in Euro. As can be seen: for each ammonia mass fraction, one heat pump load maximizes the savings. At this point the marginal total cost of the HACHP (sum of investment and operation) is equal to the

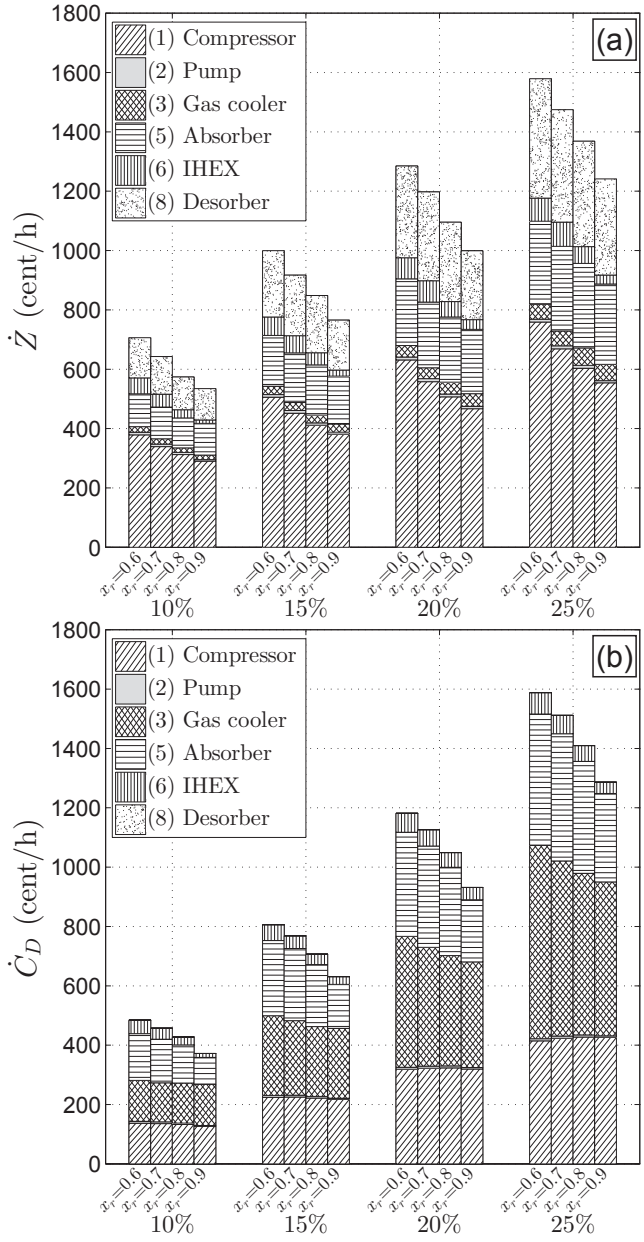

Figure 7.5: $\dot{Z}_k$ (a) and $\dot{C}_{D,k}$ (b) of the k^{th} component at HPLS of 10%, 15%, 20% and 25% and x_r of 0.6, 0.7, 0.8 and 0.9

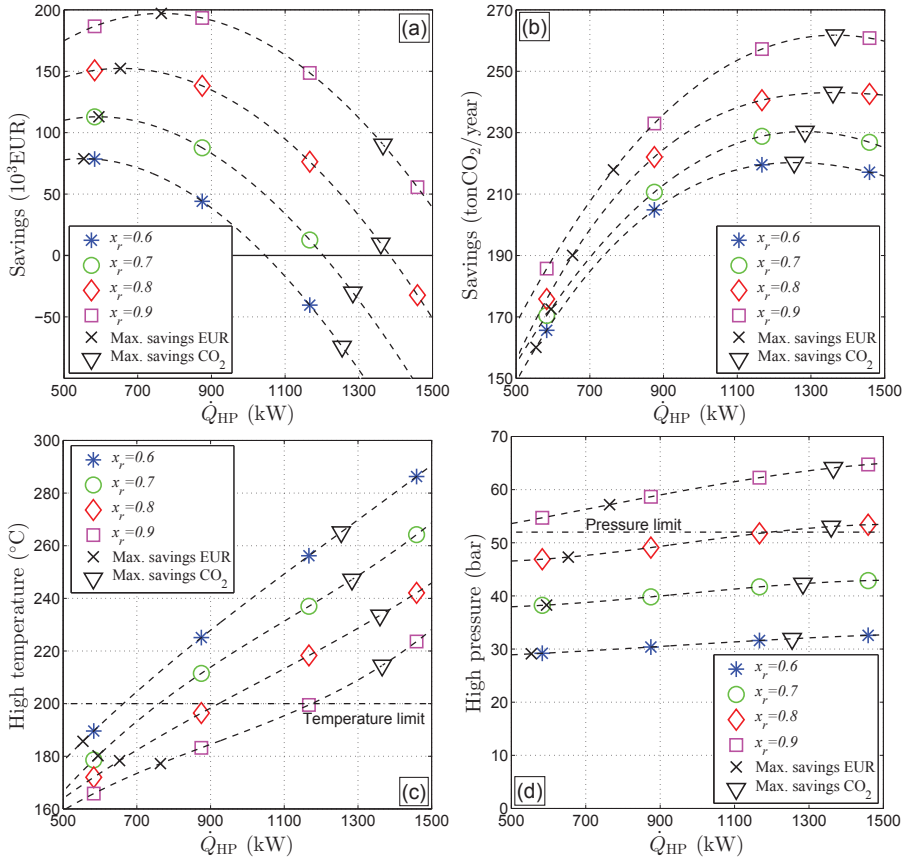

Figure 7.6: (a) Present value of the economic savings. (b) Yearly CO_2 emission savings. (c) Compressor discharge temperature. (d) Compressor discharge pressure. All shown a function of the design heat pump load and ammonia mass fraction

marginal cost of gas heating. As seen, the higher the ammonia mass fraction, the higher the savings and the higher the optimum HACHP load. Fig. 7.6 (b) shows the yearly CO_2 emissions savings. It can be seen that the maximum emission savings occur at a higher HACHP load than the maximum economic savings. Further, it is seen that, the higher the ammonia mass fraction, the higher the emissions savings.

Fig. 7.6 (c) shows the compressor discharge temperature and the temperature limit. It can be seen that none of the economic optimum loads

are restricted by the temperature limit, while all of the optimum emission loads exceed this constraint. Further, it can be seen that increasing the ammonia mass fraction decreases the compressor discharge temperature. Fig. 7.6 (d) shows the compressor discharge pressure. Here it can be seen that only the optimal savings for $x_r = 0.9$ is restricted by the pressure limit. Further, it can be seen that increasing the ammonia mass fraction increases the discharge pressure.

As the best possible implementation of the HACHP may be one with an ammonia mass fraction between the curves shown in Fig. 7.6, an interpolation between HACHP load and the ammonia mass fraction for the 16 exegoeconomic optimum points has been made.

Fig. 7.7 (a) shows the interpolation of economic savings with the pressure and temperature limits imposed. The area below the blue dashed line satisfies the pressure constraint, while the area to the left of the red dash-dot line satisfies the temperature constraint. A similar plot for the emission savings is shown in Fig. 7.7 (b). The chosen implementation is indicated by the $\times$. This is chosen to attain both high economic and emission savings. The chosen load is $\dot{Q}_{\mathrm{HP}} = 895$ kW with an ammonia mass fraction 0.82. The circulation ratio is then 0.43. The exergoeconomic optimum values of pinch point temperature difference and effectiveness are: $\Delta T_{\mathrm{pp},5} = 11.2$ K, $\Delta T_{\mathrm{pp},8} = 8.98$ K, $\epsilon_6 = 0.730$ and $\epsilon_3 = 0.864$. Here the present value of the saving is € 146,426 and the yearly CO_2 emissions is reduced by a total 227 ton.

Table 7.3 shows the results of the exergy and exergoeconomic analysis of the chosen implementation. As seen, the highest contribution to the exergy destruction in the system is caused by the compressor and the throttling valve, both accounting for 22 % of the total exergy destruction. The gas-cooler, absorber and desorber are the other main contributors, responsible for 17 %, 16 % and 15 % respectively. The component with the highest total cost rate is the compressor, while this component has the second lowest relative cost difference. The highest relative cost difference is found in the gas-cooler.

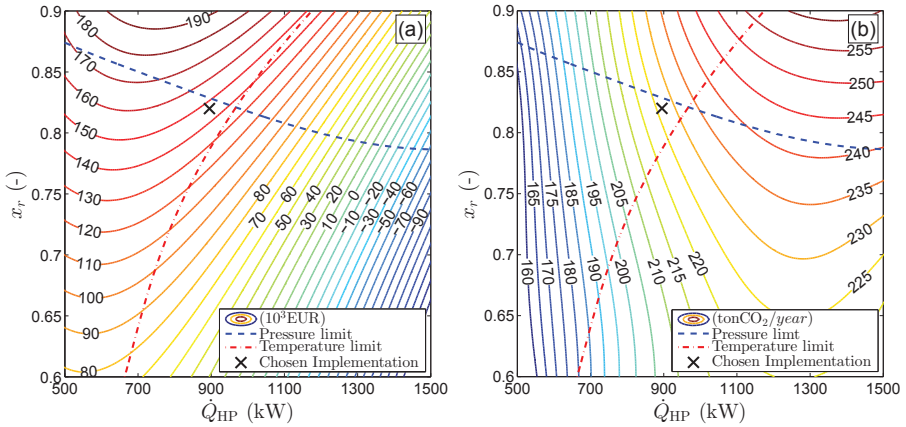

Figure 7.7: (a) Interpolation of the economic savings. (b) Interpolation of the emission savings. Both as a function of the design heat load and ammonia mass fraction and with compressor discharge pressure and temperature limit imposed

Table 7.3: Results of the exergy and exergoecnomic analysis of the chosen implementation

k^{th}	$\dot{E}_{P,k}$ (kW)	$\dot{E}_{F,k}$ (kW)	$\dot{E}_{D,k}$ (kW)	ε_k (%)	y_k (%)	y_k^* (%)	$\dot{Z}_k$ (¢/h)	$\dot{C}_{D,k}$ (¢/h)	$f_{ex,k}$ (%)	r_k (%)
(1)	187	226	38.7	83	13	29	415	322	56	47
(2)	2.99	3.82	0.830	78	0.27	0.63	8.35	6.92	55	61
(3)	40.3	61.3	21.0	66	6.8	16	27.6	253	10	58
(4)	-	-	4.95	-	1.6	3.7	27.2	-	-	0
(5)	136	154	18.0	88	5.8	14	172	214	45	26
(6)	11.4	14.3	2.95	79	0.95	2.2	38.8	35.5	52	54
(7)	-	-	26.7	-	8.6	20	0	-	-	-
(8)	59.8	79.4	19.6	75	6.3	15	190	0	100	-

7.4 Discussion

In the present study partial derivatives were applied as an aid to determine the exergoeconomic optimum of the HACHP, which proved to be a helpful tool. However, this approach was only applicable due to the ap-

plication of cost functions. Thereby, the investment cost of a component was linked mathematically to the choice of the design variables, which allows the numerical partial derivatives to be determined. In real life applications, this is hardly ever the case, wherefore the partial derivatives cannot be attained. In these cases, the advanced exergoeconomic analysis, as applied in [71], could be used. The advanced exergoeconomic method can explicitly determine the unavoidable costs of both investment and operation and component interdependencies and does not require the application of cost function. The advanced exergoeconomic method does not constitute a mathematical optimization procedure but defines the best possible design as one at which the advanced exergoeconomic factors for all components are 50 %. The advanced exergoeconomic factor subtracts the unavoidable parts of $\dot{Z}_k$ and $\dot{C}_{D,k}$ shown in Fig. 7.3. Thus, if the advanced exergoeconomic factor is close to 50 % it is likely that the design is close to the exergoeconomic optimum.

Further, the use of cost functions would allow the application of any mathematical optimization procedure to maximize the savings, without the use of exergy or exergoeconomics. This approach would however not yield the detailed information on the sources of investment and operational cost that is attained with the exergoeconomic analysis.

This information is gathered in Table 7.3 and from this, insight to how the HACHP can be further improved is attained. As can be seen in Table 7.3, the gas-cooler accounts for both a significant part of the exergy destruction cost rate and also has the highest relative cost difference. The high cost rate and relative cost difference is caused by the superheat of the gas exiting the compressor. This cannot be changed directly by changing the design of the gas-cooler, but could be reduced by the implementation of a two-stage compression. This could also reduce the exergy destruction cost of the compression. Therefore this could prove to be a good improvement of the system.

Ommen et al. [78] tested ammonia mass fractions of 0.7 and 0.9 and also found the total cost to increase with the reduction of ammonia mass fraction. The optimum pinch point temperatures found in [78] are significantly lower that those presented in the current study. This is assumed to be caused by the use of constant overall heat transfer coefficient applied in [78]. Hence, the degradation of two-phase heat

transfer due to mass diffusion resistance is not captured. This has been shown to have an influence on both the PEC and the exergoeconomic optimum design and should be accounted for.

7.5 Conclusion

The implementation of a HACHP in a spray drying facility was investigated and optimized. Heat transfer and pressure drop correlations from the open literature were gathered and implemented in the thermodynamic model of the HACHP. Cost functions based on Danish intermediate trade price were constructed to assess the heat pump investment. The exergoeconomic method has been used to minimize the total cost of the HACHP. The influence of ammonia mass fraction, circulation ratio and heat pump load was also investigated. Constraints based on commercially available technologies were imposed.

The best possible implementation was found to be a 895 kW HACHP with an ammonia mass fraction of 0.82 and circulation ratio of 0.43. This resulted in an economic saving with a present value of € 146.426 and a yearly reduction of the CO_2 emissions by 227 ton.

The use of numerical partial derivatives was applied to implicitly account for the unavoidable costs and component interdependencies. This gave a more precise indication of the exergoeconomic optimum compared to what is attained based only on the exergoeconomic indicators: exegoeconomic factor and relative cost difference. However, the exergoeconomic indicators still gave valuable insight of the sources of investment and the cost of irreversibilities. The indicators gave useful information to the further improvement of the system.

CHAPTER 8

CONCLUDING REMARKS

8.1 Summary of findings

The thesis statement was sought answered through four sub-statements. Each of the sub-statements were answered separately throughout the chapters of the thesis. The first sub-statement regarded the HACHP cycle configurations and the optimal choice of design parameters. This statement was answered in Chapter 2 - Modelling and process optimization. The second statement regarded the maximum supply temperature of the HACHP technology and was answered in Chapter 3 - Feasibility of high temperature HACHP development.

The source of irreversibilities and the formation of cost and environmental impact was the focus of the third sub-statement and was addressed in Chapter 5 - Advanced exergy based analysis.

The final sub-statement regard the viability of HACHP implementation and a comparison of the economics to a VCHP installation. These issues where addressed by Chapter 6 - Technical and economic working domains of HACHP and comparison with VCHP and Chapter 7 - Case study: hybrid absorption compression heat implementation for waste heat recovery in a spray drying facility.

In the following the conclusions of the mention chapters are summarized. Together the findings of these chapters seeking to answer the thesis statement.

Modelling and process optimization was applied to one one-stage HACHP and several two-stage HACHP. The performance of the identified system configurations were evaluated at several operating conditions. It was found that of the many suggestions given in literature to attain optimum COP none are valid at all operating conditions. Both sink and source glide matching as well as a con-

stant concentration different can be applied at low sink source glides and low lifts. If both the sink glide and source glides are large, sink and source glide matching can be used to optimize COP for high ammonia mass fractions while only sink matching can be used at low ammonia mass fractions. For sink and source glides larger than 10 K it is recommended to optimize COP rather than match the glides of sink or source, as this will ensure a better performance of the HACHP.

All the identified two-stage configuration were compared with the one-stage HACHP in terms of both COP, VHC and compressor discharge temperature. This clearly showed that the two-stage configuration with internal heat exchange, placement option 1, is always the preferable two-stage configuration. This is regardless of the ammonia mass fraction and operating conditions.

The feasibility of high temperature HACHP development was investigated by imposing technical constraints and economic indicator constraints to a parameter variation of the ammonia mass fraction and circulation ratio. The set of feasible combinations was subsequently identified for three types of components: standard pressure (28 bar) components, high pressure ammonia (50 bar) components and transcritical CO_2 (140 bar) components.

The maximum heat supply temperature was determined as the temperature at which no combination of ammonia mass fraction and circulation ratio result in a design that simultaneously satisfies all the imposed constraints. This showed that standard pressure components can be applied up to 111 °C in the one-stage HACHP and 126 °C in the two-stage. For the high pressure ammonia components the one-stage HACHP will allow a maximum temperature of 129 °C while the two-stage HACHP increases this to 146 °C. The transcritical CO_2 components can attain a heat supply up to 147 °C for the one-stage HACHP and 187 °C for the two-stage configuration.

The dominating constraints when evaluating the maximum heat supply temperature are the high pressure, the compressor discharge temperature and the vapour ammonia mass fraction. If

the attainable heat supply temperature of the HACHP is to be increased it is not sufficient to only increase allowable pressure, the allowable compressor discharge temperature and vapour ammonia mass fraction must also be increased. Removing the constraint on the vapour mass fraction and increasing the compressor discharge temperature to 250 °C increases the allowable temperature for the two-stage HACHP to 215 °C for standard components, 225 °C for high pressure ammonia components and 231 °C for transcritical CO_2 components.

Conventional and advanced exergy-based analysis was applied to the HACHP to identify the sources of thermodynamic irreversibilities as well as the sources of cost and environmental impact formation.

The conventional exergy analysis showed that 72% of the total exergy destruction was located in the compressor (27%), absorber (24%) and desorber (21%). Thus, based on the conventional exergy analysis the first component to improve would be the compressor then the absorber followed by the desorber. Based on the conventional exergoeconomic analysis the most important component for system improvement is the compressor, as this has the highest total cost and the highest relative cost difference. Based on the compressor's conventional exergoeconomic factor the total cost is dominated by investment.

Applying the advanced exergy analysis showed that 27% of the total exergy destruction could not be avoided. Analysing the total avoidable exergy destruction associated to the component inefficiency, rearranged the order of importance. The three highest ranking components remain the same but the order is reversed: Desorber (38%), absorber (35%) and compressor (19%). In total 92% of the avoidable exergy destruction is allocated to these three components.

The advanced exergoeconomic analysis shows that 53%-54% of the system's avoidable total cost stems from the absorber. While the compressor total cost accounts for 20%-25% and the desorber 19%-20%. Also the exergoeconomic factors change when the

advanced analysis is applied. The conventional analysis shows that the compressor, pump and desorber total cost are dominated by investment, while the absorber and IHEX total cost are dominated by the cost of exergy destruction. Applying the advanced analysis shows that only the IHEX total cost is dominated by investment while the compressor and absorber total cost are dominated by the cost of exergy destruction. The desorber is found to have a close to equal distribution of the investment and exergy destruction cost.

The environmental impact of the HACHP system was mainly driven by the operation of the system and thus linked to the electricity consumption. The environmental impact related to the construction of the system was found to be negligible and for all cases the environmental impact related to the increased size of the components could be justified by the decreased energy consumption over the life time of the system. Thus, the exergoenvironmental optimum was found at the unavoidable conditions. The unavoidable conditions were found not to be economically viable, wherefore a trade off was suggested, that reduced the environmental impact to a close to optimal solution, without any significant increase in cost. At this condition the advanced exergoenvironmental analysis was applied. This showed that 62% of the avoidable environmental impact was related to the compressor, followed by the absorber with 28%. 7% of the avoidable impact stems from the desorber while the last 3% were accounted to the internal HEX and pump.

The technical and economic working domain of HACHP was evaluated based on a detailed economic analysis and a comprehensive investigation of the design variables: ammonia mass fraction and circulation ratio. The results show that the HACHP is capable of delivering both higher heat supply temperatures and higher temperature lifts than conventional VCHP.

Heat supply temperatures up to 150 °C and temperature lifts up to 60 K can be attained with commercially available components and with an economic benefit compared to gas combustion. It is

found that the dominating constraint for the HACHP is the compressor discharge temperature. Further, it is found that reducing the sink/source temperature difference increases the maximum attainable heat supply temperature while reducing the maximum attainable lift.

When comparing the present value of the HACHP with the VCHP at the operating points where both are applicable: the cost of the HACHP is lower for almost all operating conditions with a heat supply temperature above 80 °C. For the range where the HACHP competes with R717 the difference in present value can be insignificant and both technologies should be considered. For the high temperature range where the only applicable VCHP technology is R600a the difference in present value is large and the HACHP should be applied.

Implementation of a HACHP in a spray drying facility was investigated and optimized. A exergoeconomic optimization method based on partial derivates of the exergetic and non-exergetic cost was proposed and applied to minimize the total cost of the HACHP. The influence of ammonia mass fraction, circulation ratio and heat pump load was also investigated. Constraints based on commercially available technologies were imposed.

The best possible implementation was found to be a 895 kW HACHP with an ammonia mass fraction of 0.82 and circulation ratio of 0.43. This resulted in an economic saving with a present value of € 146.426 and a yearly reduction of the CO_2 emissions by 227 ton.

The applied exergoeconomic optimization method implicitly accounted for the unavoidable costs and component interdependencies. This gave a more precise indication of the exergoeconomic optimum compared to what is attained based on the conventional exergoeconomic indicators: exegoeconomic factor and relative cost difference. However, the exergoeconomic indicators still gave valuable insight of the sources of investment and the cost of irreversibilities.

8.2 Recommendations for future work

Heat transfer characteristics of ammonia-water absorption and desorption is of prime importance for the development of cost efficient HACHP. As shown the highest potential for reducing cost in a HACHP is by improving the design of the absorber and desorber. Hence, understanding the heat transfer phenomena is crucial. The amount of experimental work on absorption and desorption in plate heat exchangers is limited, especially for high temperature applications. More studies should be provided to allow good correlations with a wide applicability range in terms of both ammonia mass fraction, temperature and pressure.

Liquid/vapour maldistribution in plate heat exchangers is an important phenomena for the design of HACHP plate heat exchangers. Liquid/vapour maldistribution can occur in both the absorber and desorber as the entering state in both will be a liquid/vapour mixture. Liquid/vapour maldistribution may cause severe reduction of the overall heat transfer coefficient in pure refrigerant evaporators. This may be even worse for zeotropic mixtures as an improper liquid/vapour distribution will cause a difference in the bulk ammonia mass fraction of each channel, subsequently changing the temperature gradient of the absorption desorption processes making the matching of the temperature profiles harder to attain in practice. It is suggested to further investigate the consequences of liquid/vapour maldistribution on the performance of plate absorbers and desorbers.

Two-stage HACHP working domains have yet to be fully established. As shown it is feasible to develop a two-stage HACHP that can deliver a significantly higher heat supply temperature, as the compressor discharge temperature is reduced. However, a full economic analysis of the two-stage HACHP has not yet been applied. By applying the full economic analysis the technical and economic working domain of the two-stage HACHP could be produced. Further, the present value of the two-stage HACHP could be compared to that of the one-stage to shown under which op-

erating conditions, if any, it is economically preferable to apply the two-stage HACHP. The application of HACHP connected in series should also be investigated.

Off design and part load operation of the HACHP has been claimed to be superior to the VCHP due to the two extra degrees of freedom. Few studies have shown that changing ammonia mass fraction is a feasible measure of capacity control but however this requires simultaneously controlling the circulation ratio to attain the optimum COP. Controlling ammonia mass fraction and circulation ratio may also be applied to ensure good off design operation when sink/source temperature glide change during operation. Thus, the ammonia mass fraction and circulation ratio could be varied to optimize the COP under the new conditions. To attain this it is suggested that off design models are constructed such the operation of the HACHP can be simulated. From these control strategies and algorithm can be suggested.

High temperature compressor development is shown to be a necessary step in the development of high temperature heat pumps. It is shown that the pressures levels available today can cover significantly higher temperature levels if higher compressor discharge temperatures can be sustained. Hence, it seems to be more important for compressor manufacturers to increase the temperature limits of their compressors rather than increasing the pressure level. However, currently the opposite is observed, as some manufacturers have launched 60 bar compressors which have a lower compressor discharge temperature tolerance than the low pressure compressors. Further, it seems that the need for restricting compressor discharge temperatures is not fully established. Some claim the restrictions to be due to the thermal stability of the lubricant while others claim that they are set to prevent the discharge valve from being subjected to corrosion. The lubrication issues may be solving by identifying thermally stable synthetic oils that meet the requirements of miscibility etc. Further, more frequent oil changes may reduce the consequences of oil degradation.

To some extent it seems that some of the restrictions imposed on

the discharge temperature of high pressure compressors is due to the fact that the compressor manufacturer do not test their compressors in these temperature ranges and will therefore not guarantee operation in this range under their warranty. Seeing as most heat pump compressor manufacturers emerged from the refrigeration industry this may be caused by manufacturers still having their mindset on the supply of cooling and are therefore not in line with requirements of industrial heat pumps.

It is suggested that high temperature compressors are investigated experimentally to determine whether or not compressor failure is caused by increased discharge temperature and if so where the failure occurs. Subsequently, measures can be identified to ensure safe high temperature operation.

Bibliography

[1] Energistatistik 2012. Technical report, Danish Energy Agency, ISBN: 978-87-93071-39-1 www.

[2] Annex–21 - Industrial Heat Pumps - Experiences, potential and Global Environmental Benefits. Technical report, IEA Heat Pump Centre, 1995.

[3] Thermophysical properties of NH3 + H2O solutions for the industrial design of absorption refrigeration equiptment. Technical report, M. Conde Engineering, 2004.

[4] International organization for standardization (iso), environmental management - life cycle assessment, european standard eniso14040 and 14044, 2006.

[5] Ahlsell Danmark ApS, Priskatalog 2013, [accessed 26.09.13], 2013.

[6] FK Teknik A/S, Priskatalog 2013, [accessed 26.09.13], 2013.

[7] H. Jessen Jürgensen A/S, Price catalog 2013, [accessed 26.09.13], 2013.

[8] Johnson Controls, personal communication with Sørensen, K. HPO R717 compressor cost, , 2013.

[9] Grundfos DK A/S, Indicative retail prices, 2014.

[10] SWEP international AB, private communication, SWEP - products & solutions (B400, B120T F-pressure, B17 product sheets) - non-disclosure agreement , 2014.

[11] SWEP international AB, Technical information v120t anf v10t. [accessed 01.06.14] , 2014.

[12] M. M. Abu-Khader. Plate heat exchangers: Recent advances. *Renewable and Sustainable Energy Reviews*, 16(4):1883 – 1891, 2012.

[13] E. Açıkkalp, H. Aras, and A. Hepbasli. Advanced exergoeconomic analysis of a trigeneration system using a diesel-gas engine. *Applied Thermal Engineering*, 67(1–2):388 – 395, 2014.

[14] E. Açıkkalp, H. Aras, and A. Hepbasli. Advanced exergoeconomic analysis of an electricity-generating facility that operates with natural gas. *Energy Conversion and Management*, 78(0):452 – 460, 2014.

[15] E. Altenkirch. Kompressionskältemachine mit lösungskreislauf. *Kältetechnik*, 2(10,11,12):251–259, 310–315, 279–284, 1950.

[16] Hybrid Energy AS. http://www.hybridenergy.no/en/clients/, [accessed 28.01.15], 2015.

[17] C. G. J. Baker and K. A. McKenzie. Energy Consumption of Industrial Spray Dryers. *Drying Technology: An International Journal*, 23(1-2):365–386, February 2005.

[18] A. Bejan. *Advanced engineering thermodynamics*. Wiley, New York, 3 edition, 2006.

[19] A. Bejan, G. Tsatsaronis, and M. J. Moran. *Thermal Design and Optimization*. Wiley-Interscience publication. Wiley, 1996.

[20] K. J. Bell and M. A. Ghaly. An approximate generalized design method for multicomponent/partial condensers. In *13th National Heat Transfer Conference*, Denver, Colorado, USA, 1972. AIChE-ASME.

[21] F. Bühler, F. M. Holm, B. Huang, J. G. Andreasen, and B. Elmegaard. Mapping of low temperature heat sources in denmark. In *Proceedings of ECOS 2015 - The 28th International Conference on Efficiency, Cost, Optimization, Simulation and environmental Impact of Energy Systems*, Pau, France, June 29 - July 13, 2015.

[22] A. Boyano, A. M. Blanco-Marigorta, T. Morosuk, and G. Tsatsaronis. Exergoenvironmental analysis of a steam methane reforming process for hydrogen production. *Energy*, 36(4):2202 – 2214, 2011.

[23] O. Brunin, M. Fiedt, and B. Hivet. Comparison of the working domains of some compression heat pumps and a compression-absorption heat pump. *International Journal of Refrigeration*, 20(5):308–318, 1997.

[24] D. Chisholm. A theoretical basis for lockhartemartinelli correlation for 2-phase flow. *Int. J. Heat Mass Transf.*, 10(12):1767 – 1778, 1967.

[25] J. Chua, K, K. Chou, S, C. Ho, J, and A. Hawlader, M, N. Heat Pump Drying : Recent Developments and Future Trends. *Drying Technology: An International Journal*, 20(8):1579–1610, 2002.

[26] J.G. Collier and J.R. Thome. *Convective Boiling and Condensation*. Clarendon Press, 1994.

[27] J. M. Corberan. 2nd IIR workshop on refrigerant charge reduction in refrigerating systems. *Int. J. Refrigeration*, 34:600, 2011.

[28] F. Cziesla, G. Tsatsaronis, and Z. Gao. Avoidable thermodynamic inefficiencies and costs in an externally fired combined cycle power plant. *Energy*, 31(10-11):1472–1489, August 2006.

[29] Y. M. El-Sayed. in proceedings of asme winter annual meeting. volume I-11, pages 19–24. ASME, Chicago, 1988, 1985.

[30] Energistyrelsen. Virksomhedsrentabel udnyttelse af overskudsvarme, samt afdækning af evt . potentiale. Technical report.

[31] NIST National Institute for Standards and Technology. Refprop 9.1, matlab interface, in: Matlabapplications, 2013.

[32] Goedkoop, M. and Spriensma, R. Eco-indicator 99 manual for designers: A damage oriented method for life cycle impact assessment, 2000.

[33] A. Gungor, Z. Erbay, and A. Hepbasli. Exergoeconomic analyses of a gas engine driven heat pump drier and food drying process. *Applied Energy*, 88(8):2677–2684, 2011.

[34] L. Åhlby, D. Hodgett, and T. Berntsson. Optimization study of the compression/absorption cycle. *International Journal of Refrigeration*, 14(April 1990):16–23, 1991.

[35] L. Åhlby, D. Hodgett, and R. Radermacher. NH3/H2O-LiBr as working fluid for the compression/absorption cycle. *International Journal of Refrigeration*, 16(4):265–273, 1993.

[36] Y. Y. Hsieh and T. F. Lin. Saturated flow boiling heat transfer and pressure drop of refrigerant r-410a in a vertical plate heat exchanger. *International Journal of Heat and Mass Transfer*, 45(5):1033 – 1044, 2002.

[37] M. Hultén and T. Berntsson. The compression/absorption cycle – influence of some major parameters on COP and a comparison with the compression cycle. *International Journal of Refrigeration*, 22:91–106, 1999.

[38] M. Hultén and T. Berntsson. The compression/absorption heat pump cycle — conceptual design improvements and comparisons with the compression cycle. *International Journal of Refrigeration*, 25:487–497, 2002.

[39] O. M. Ibrahim and S. A Klein. Thermodynamic Properties of Ammonia-Water Mixtures. In *ASHRAE Trans.: Symposia*, pages 21, 2 1495–1502, 1993.

[40] L. C. M. Itard and C. H. M. Machielsen. Considerations when modelling compression/resorption heat pumps. *International Journal of Refrigeration*, 17(7):453–460, 1994.

[41] J. K. Jensen, M. R. Kærn, T. Ommen, W. B. Markussen, L. Reinholdt, and B. Elmegaard. Effect of liquid/vapour maldistribution on performance of plate heat exchanger evaporators. In *Proceedings of ICR 2015 - 24th IIR International Congress of Refrigeration*, Yokohama, Japan, August 16 - 22, 2015.

[42] J. K. Jensen, W. B. Markussen, L. Reinholdt, and B. Elmegaard. Exergoeconomic optimization of an ammonia–water hybrid absorption–compression heat pump for heat supply in a spray-drying facility. *International Journal of Energy and Environmental Engineering*, 6(2):195–211, 2015.

[43] J. K. Jensen, W. B. Markussen, L. Reinholdt, and B. Elmegaard. On the development of high temperature ammonia-water hybrid absorption-compression heat pumps. *International Journal of Refrigeration*, -(-):–, 2015. In Press, Accepted Manuscript.

[44] J. K. Jensen, W. B. Markussen, L. Reinholdt, and B. Elmegaard. Exergoeconomic optimization of an ammonia-water hybrid heat pump for heat supply in a spray drying facility. In *Proceedings of ECOS 2014 - The 27th International Conference on Efficiency, Cost, Optimization, Simulation and environmental Impact of Energy Systems*, Åbo, Finland, June 15 - 19, 2014.

[45] J. K. Jensen, W. B. Markussen, L. Reinholdt, and B. Elmegaard. Conventional and advanced exergoenvironmental analysis of an ammonia-water hybrid absorption-compression heat pump. In *Proceedings of ECOS 2015 - The 28th International Conference on Efficiency, Cost, Optimization, Simulation and environmental Impact of Energy Systems*, Pau, France, June 29 - July 13, 2015.

[46] J. K. Jensen, T. Ommen, W. B. Markussen, L. Reinholdt, and B. Elmegaard. Technical and economic working domains of industrial heat pumps: Part 2 - ammonia-water hybrid absorption-compression heat pumps. *International Journal of Refrigeration*, 55:183 – 200, 2015.

[47] J. K. Jensen, T. Ommen, W. B. Markussen, L. Reinholdt, and B. Elmegaard. Technical and economic working domains of industrial heat pumps: Part 2 - ammonia–water hybrid absorption–compression heat pumps. In *Proceedings of GL 2014 - 11*$^{\text{th}}$ *IIR - Gustav Lorentzen Conference on Natural Refrigerants*, Hangzhou, China, August 31 - September 2, 2014.

[48] J. K. Jensen, L. Reinholdt, W. B. Markussen, and B. Elmegaard. Investigation of ammonia/water hybrid absorption/compression heat pumps for heat supply temperatures above 100°c. In *Proceedings of ISHPC 2014 - International Sorption Heat Pump Conference, University of Maryland*, Washington D.C, USA, March 31 - April 2, 2014.

[49] A. Keçebaş and A. Hepbasli. Conventional and advanced exergoeconomic analyses of geothermal district heating systems. *Energy and Buildings*, 69(0):434 – 441, 2014.

[50] S. Kelly. *Energy Systems Improvement based on Endogenous and Exogenous Exergy Destruction*. Phd thesis, Technischen Universität Berlin, 2008.

[51] S. Kelly, G. Tsatsaronis, and T. Morosuk. Advanced exergetic analysis: Approaches for splitting the exergy destruction into endogenous and exogenous parts. *Energy*, 34(3):384–391, March 2009.

[52] I. C. Kemp. Reducing Dryer Energy Use by Process Integration and Pinch Analysis. *Drying Technology: An International Journal*, 23(9-11):2089–2104, September 2005.

[53] I. C. Kemp. *Pinch Analysis and Process Integration: A User Guide on Process Integration for the Efficient Use of Energy*. Elsevier Science, 2011.

[54] S. A. Klein. Engineering Equation Solver Academic Professional V9.459-3D, 2013.

[55] T. J. Kotas. *The exergy method of thermal plant analysis*. Butterworths, 1985.

[56] M. R. Kærn, A. Modi, J. K. Jensen, J. G Andreasen, and F. Haglind. An assessment of in-tube flow boiling correlations for ammonia-water mixtures and their influence on heat exchanger size. *Applied Thermal Engineering*, 2015. Under review.

[57] M. R. Kærn, A. Modi, J. K. Jensen, and F. Haglind. An assessment of transport property estimation methods for ammonia–water mixtures and their influence on heat exchanger size. *International Journal of Thermophysics*, 36:1468 – 1497, 2015.

[58] A. Lazzaretto and G. Tsatsaronis. SPECO: A systematic and general methodology for calculating efficiencies and costs in thermal systems. *Energy*, 31:1257–1289, 2006.

[59] E. W. Lemmon, M. L. Huber, and M. O. McLinden. Refprop, reference fluid thermodynamic and transport properties, 2013.

[60] H. Lorenz. Beiträge zur beurteilung von kühlmaschinen. *Z VDI*, 38:62–68, 98–103, 124–130, 1894.

[61] M. H. Khoshgoftar Manesh, P. Navid, A. M. Blanco-Marigorta, M. Amidpour, and M. H. Hamedi. New procedure for optimal design and evaluation of cogeneration system based on advanced exergoeconomic and exergoenvironmental analyses. *Energy*, 59(0):314 – 333, 2013.

[62] L. Margat, B. Thonon, and L. Tadrist. *Heat transfer and two phase flow characteristics during convective boiling in a corrugated channel. In:Compact Heat Exchangers For The Process Industry*. Begell House, 1997.

[63] H. Martin. A theoretical approach to predict the performance of chevron-type plate heat exchangers. *Chemical Engineering and Processing: Process Intensification*, 35(4):301 – 310, 1996.

[64] MathWorks. Matlab 2015a, 2015.

[65] L. Meyer, G. Tsatsaronis, J. Buchgeister, and L. Schebek. Exergoenvironmental analysis for evaluation of the environmental impact of energy conversion systems. *Energy*, 34(1):75 – 89, 2009.

[66] A. Modi and F. Haglind. Thermodynamic optimisation and analysis of four kalina cycle layouts for high temperature applications. *Appl. Therm. Eng*, 76:196–205, 2015.

[67] T. Morosuk and G. Tsatsaronis. A new approach to the exergy analysis of absorption refrigeration machines. *Energy*, 33(6):890–907, June 2008.

[68] T. Morosuk and G. Tsatsaronis. Advanced exergetic evaluation of refrigeration machines using different working fluids. *Energy*, 34(12):2248–2258, December 2009.

[69] T. Morosuk and G. Tsatsaronis. Advanced exergoeconomic analysis of a refrigeration machine: Part 1—methodology and first evaluation. In *ASME 2011 International Mechanical Engineering Congress and Exposition*, pages 47–56. American Society of Mechanical Engineers, 2011.

[70] T. Morosuk and G. Tsatsaronis. Advanced exergoeconomic analysis of a refrigeration machine: Part 2—improvement. In *ASME 2011 International Mechanical Engineering Congress and Exposition*, pages 57–65. American Society of Mechanical Engineers, 2011.

[71] T. Morosuk, G. Tsatsaronis, A. Boyano, and C. Gantiva. Advanced exergy-based analyses applied to a system including LNG regasification and electricity generation. *International Journal of Energy and Environmental Engineering*, 3(1), 2012.

[72] T. Morosuk, G. Tsatsaronis, and C. Zhang. Conventional thermodynamic and advanced exergetic analysis of a refrigeration machine using a Voorhees' compression process. *Energy Conversion and Management*, 60:143–151, August 2012.

[73] P. Neksa, H. Rekstad, G. R. Zakeri, and P. A. Schiefloe. CO2-heat pump water heater: characteristics , system design and experimental results. *International Journal of refrigeration*, 21(3):172–179, 1998.

[74] S. R. Nordtvedt. *Experimental and theoretical study of a compression/absorption heat pump with ammonia/water as working fluid*. Ph.d. thesis, Norwegian University of Science and Technology, 2005.

[75] T. Ommen, J. K. Jensen, W. B. Markussen, L. Reinholdt, and B. Elmegaard. Technical and economic working domains of industrial heat pumps: Part 1 - single stage vapour compression heat pumps. *International Journal of Refrigeration*, (0):–, 2015.

[76] T. Ommen, J. K. Jensen, W. B. Markussen, L. Reinholdt, and B. Elmegaard. Enhanced technical and economic working domains of heat pumps operated in series. In *Proceedings of ICR 2015 - 24th IIR International Congress of Refrigeration*, Yokohama, Japan, August 16 - 22, 2015.

[77] T. Ommen, J. K. Jensen, W. B. Markussen, L. Reinholdt, and B. Elmegaard. Technical and economic working domains of industrial heat pumps: Part 1 - vapour compression heat pumps. In *Proceedings of GL 2014 - 11*th *IIR - Gustav Lorentzen Conference on Natural Refrigerants*, Hangzhou, China, August 31 - September 2, 2014.

[78] T. Ommen, C. Markussen, L. Reinholdt, and B. Elmegaard. Thermoeconomic comparison of industrial heat pumps. In *ICR 2011, August 21 - 26 - Prague, Czech Republic*, 2011.

[79] T. Ommen, W. B. Markussen, and B. Elmegaard. Heat pumps in combined heat and power systems. *Energy*, 76:989–1000, 2014.

[80] A. Osenbrück. Verfaren kalteerzeugung bei absorptions- maschinen, 1895.

[81] B. Palm and J. Claesson. Plate heat exchangers: Calculation methods for single and two-phase flow. *Heat Transfer Engineering*, 27:88 – 98, 2006.

[82] F. Petrakopoulou, G. Tsatsaronis, and T. Morosuk. Cost reduction strategies for an oxy-fuel power plant with co2 capture: application of an advanced exergoeconomic analysis to an advanced zero emission plant. In *ASME 2011 International Mechanical Engineering Congress and Exposition*, pages 1063–1073. American Society of Mechanical Engineers, 2011.

[83] F. Petrakopoulou, G. Tsatsaronis, and T. Morosuk. Evaluation of a power plant with chemical looping combustion using an advanced exergoeconomic analysis. *Sustainable Energy Technologies and Assessments*, 3:9–16, September 2013.

[84] F. Petrakopoulou, G. Tsatsaronis, T. Morosuk, and A. Carassai. Conventional and advanced exergetic analyses applied to a combined cycle power plant. *Energy*, 41(1):146–152, May 2012.

[85] R. Plank. *Handbuch der Kältetechnik*. Springer-Verlag, 1988.

[86] S. Prasertsan and P. Saen-saby. Heat Pump Dryers: Research and Development Needs and Opportunities. *Drying Technology: An International Journal*, 16(1-2):251–270, January 1998.

[87] R. Radermacher and Y. Hwang. *Vapor Compression Heat Pumps with Refrigerant Mixtures*. Mechanical Engineering. Taylor & Francis, 2005.

[88] R.C. Reid, J.M. Prausnitz, and T.K. Sherwood. *The properties of gases and liquids*. McGraw-Hill chemical engineering series. McGraw-Hill, 1977.

[89] P. K. Satapathy. Exergy analysis of a compression–absorption system for heating and cooling applications. *International Journal of Energy Research*, (February):1266–1278, 2008.

[90] L. Silver. Gas cooling with aqueous condensation: A new procedure for calculating heat transfer coefficients. *The Industial Chemist*, pages 380–386, June 1947.

[91] W. Stoecker. *Industrial Refrigeration Handbook*. McGraw-Hill Education, 1998.

[92] M. Stokar. Compression heat pump with solution circuit Part 2: sensitivity analysis of construction and control parameters. *International Journal of Refrigeration*, 10(May):134–142, May 1987.

[93] M. Stokar and C. H. Trepp. Compression heat pump with solution circuit Part 1 : design and experimental results. *International Journal of Refrigeration*, 10(March):87–96, 1987.

[94] F. Táboas, M. Vallès, M. Bourouis, and A. Coronas. Pool boiling of ammonia/water and its pure components: comparison of experimental data in the literature with the predictions of standard correlations. *International Journal of Refrigeration*, 30(5):778–788, 2007.

[95] F. Táboas, M. Vallès, M. Bourouis, and A. Coronas. Flow boiling heat transfer of ammonia/water mixture in a plate heat exchanger. *International Journal of Refrigeration*, 33(4):695–705, June 2010.

[96] F. Táboas, M. Vallès, M. Bourouis, and A. Coronas. Assessment of boiling heat transfer and pressure drop correlations of ammonia/water mixture in a plate heat exchanger. *International Journal of Refrigeration*, 35(3):633–644, May 2012.

[97] E. Thorin. Thermophysical Properties of Ammonia Water Mixtures for Prediction of Heat Transfer Areas in Power Cycles 1. 22(1), 2001.

[98] R. Tillner-Roth and D. G. Friend. A helmholtz free energy formulation of the thermodynamic properties of the mixture {Water + Ammonia}. *J. Phys. Chem. Ref. Data*, 27:63–94, 1998.

[99] D. Townsend and B. Linnhoff. Heat and power networks in process design. part i: Criteria for placement of heat engines and heat pumps in process networks. *AIChE Journal*, 35:742–748, 1983.

[100] G. Tsatsaronis. Definitions and nomenclature in exergy analysis and exergoeconomics. *Energy*, 32(4):249–253, April 2007.

[101] G. Tsatsaronis. Recent developments in exergy analysis and exergoeconomics. *International Journal of Exergy*, 5(5):489–499, 2008.

[102] G. Tsatsaronis, S. Kelly, and T. Morosuk. Endogenous and exogenous exergy destruction in thermal systems. In *Proceedings of IMECE 2006*, pages 311–317, 2006.

[103] G. Tsatsaronis and T. Morosuk. Advanced exergoeconomic evaluation and its application to compression refrigeration machines. In *ASME 2007 International Mechanical Engineering Congress and Exposition*, pages 859–868. American Society of Mechanical Engineers, 2007.

[104] G. Tsatsaronis and T. Morosuk. Understanding and improving energy conversion systems with the aid of exergy-based methods. *International Jouranl of Exergy*, 11(4):518–542, 2012.

[105] G. Tsatsaronis and M. H. Park. On avoidable and unavoidable exergy destructions and investment costs in thermal systems. *Energy Conversion and Management*, 43(9-12):1259–1270, June 2002.

[106] Y. Yan, C. Lio, and F. Lin. Condensation heat transfer and pressure drop of refrigerant R-134a in a plate heat exchanger. *International Journal of Heat and Mass Transfer*, 42:993–1006, 1998.

[107] N. Zheng, W. Song, and L. Zhao. Theoretical and experimental investigations on the changing regularity of the extreme point of the temperature difference between zeotropic mixtures and heat transfer fluid. *Energy*, 55:541–552, June 2013.

APPENDIX A

AMMONIA-WATER TRANSPORT PROPERTY ESTIMATION METHODS

A.1 Viscosity

A.1.1 Vapour viscosity

Reichenberg

The Reichenberg method requires that the following pure component properties are known: viscosities, critical temperatures, dipole momentum and molecular weight. From these the mixture properties is calculated using an interpolative approach based on the molar composition of the mixture.

First the reduced temperature, T_r of the pure components and the mixture is calculated. This is done using Eq. (A.1)

$$T_{r,1} = \frac{T}{T_{c,1}}, \quad T_{r,2} = \frac{T}{T_{c,2}}, \quad T_{r,12} = \frac{T}{\sqrt{T_{c,1}T_{c,2}}} \tag{A.1}$$

Following the reduced dipole momentum, μ_r of the pure components and the mixture is calculated using Eq. (A.2). Here the temperature should be in degrees K and the pressure in Pa.

$$\mu_{r,1} = 52.46\frac{\mu_1^2 p_{c,1}}{T_{c,1}^2}, \quad \mu_{r,2} = 52.46\frac{\mu_2^2 p_{c,2}}{T_{c,2}^2}, \quad \mu_{r,12} = \sqrt{\mu_{r,1}\mu_{r,2}} \tag{A.2}$$

From this the polar correction factors $F_{r,1}$ and $F_{r,2}$ can be calculated using Eq. (A.3).

$$F_{r,1} = \frac{T_{r,1}^{3.5} + (10\mu_{r,1})^7}{T_{r,1}^{3.5}, (1 + (10\mu_{r,1})^7)} \quad F_{r,2} = \frac{T_{r,2}^{3.5} + (10\mu_{r,2})^7}{T_{r,2}^{3.5}(1 + (10\mu_{r,2})^7)} \tag{A.3}$$

Further the factors U_1, U_2, C_1 and C_2 is calculated using Eqs. (A.4), (A.5) and (A.6)

$$U_1 = \frac{(1+0.36T_{r,1}(T_{r,1}-1))^{1/6}}{\sqrt{T_{r,1}}}F_{r,1} \tag{A.4}$$

$$U_2 = \frac{(1+0.36T_{r,2}(T_{r,2}-1))^{1/6}}{\sqrt{T_{r,2}}}F_{r,1} \tag{A.5}$$

$$C_1 = \frac{M_{w,1}^{1/4}}{\sqrt{\eta_1 U_1}}, \quad C_2 = \frac{M_{w,2}^{1/4}}{\sqrt{\eta_2 U_2}} \tag{A.6}$$

Finally the factors H_{12}, K_1 and K_2 can be calculated using Eqs. (A.7) and (A.8), leading to the evaluation of the mixture viscosity using Eq. (A.9)

$$H_{12} = \frac{\sqrt{\frac{M_{w,1}M_{w,2}}{32}}}{(M_{w,1}+M_{w,2})^{3/2}} \frac{(1+0.36T_{r,12}(T_{r,12}-1))^{1/6}}{\sqrt{T_{r,12}}} (C_1+C_2)^2 \frac{T_{r,12}^{3.5}+(10\mu_{r,12})^7}{T_{r,12}^{3.5}(1+(10\mu_{r,12})^7)} \tag{A.7}$$

$$K_1 = \frac{y_1\eta_1}{y_1+\eta_1 y_2 H_{12}\left(3+2\frac{M_{w,2}}{M_{w,1}}\right)}, \qquad K_1 = \frac{y_2\eta_2}{y_2+\eta_2 y_1 H_{12}\left(3+2\frac{M_{w,1}}{M_{w,2}}\right)} \tag{A.8}$$

$$\eta_m = K_1\left(1+H_{12}^2K_2^2\right)+K_2\left(1+2H_{12}K_1+H_{12}^2K_1^2\right) \tag{A.9}$$

Wilke

The method provided by Wilke is a further simplification of the kinetic theory. In this method second order effects and the polar correction

is neglected[88]. To apply the Wilke equations the pure component viscosities and molecular weights are needed. The mixture viscosity is then calculated using on an interpolative approach based on molar composition.

The factors F_{12} and F_{21} are first calculated using Eqs. (A.10) and (A.11). Using these two values the mixture viscosity is calculated using Eq. (A.12).

$$F_{12} = \frac{\left[1+\left(\frac{\eta_1}{\eta_2}\right)^{0.5}\left(\frac{M_{w,2}}{M_{w,1}}\right)^{0.25}\right]^2}{\left[8\left(1+\frac{M_{w,1}}{M_{w,2}}\right)\right]^{0.5}} \tag{A.10}$$

$$F_{21} = F_{12}\left(\frac{\eta_2}{\eta_1}\right)\frac{M_{w,1}}{M_{w,2}} \tag{A.11}$$

$$\eta_m = \frac{\eta_1 y_1}{y_1 + F_{12} y_2} + \frac{\eta_2 y_2}{y_2 + F_{21} y_1} \tag{A.12}$$

El-Sayed

El-Sayed[29] suggested the application of the Wilke correlation but with the alteration that the pure component viscosities be evaluated with the pure components corresponding temperature. The definition of corresponding temperature can be seen in Eq. (A.13), here the mixture critical temperature, $T_{c,m}$, is calculated according to Eq. (4.2).

$$T_{corr,1} = T\frac{T_{c,1}}{T_{c,m}}, \quad T_{corr,2} = T\frac{T_{c,2}}{T_{c,m}} \tag{A.13}$$

Lucas

The method presented by Lucas combines the application of kinetic theory with corresponding states theory[88], thereby the need for pure component viscosities is avoided. The following pure component properties are need to apply the Lucas equations: dipole momentum μ, critical temperature T_c, critical pressure p_c, critical compressibility factor Z_c and the critical volume V_c.

First the reduced dipole momentum, μ_r of the pure components are calculated using Eq. (A.14)

$$\mu_{r,1} = 52.46\frac{\mu_1^2 p_{c,1}}{T_{c,1}^2}, \quad \mu_{r,2} = 52.46\frac{\mu_2^2 p_{c,2}}{T_{c,2}^2} \tag{A.14}$$

Based on the reduced dipole momentum the pure component low pressure polar correction factor $F_{P,i}^0$ is determined using either Eq. (A.15), (A.16) or (A.17) dependent on the magnitude of $\mu_{r,i}$.

$$\text{IF} \quad (0.000 <= \mu_{r,i} < 0.022): \qquad F_{P,i}^0 = 1 \tag{A.15}$$

$$\text{IF} \quad (0.022 <= \mu_{r,i} < 0.075): \qquad F_{P,i}^0 = 1 + (30.55(0.292 - Z_{c,i}^{1.72} \tag{A.16}$$

$$\text{IF} \quad (\mu_{r,i} > 0.075): \qquad F_{P,i}^0 = 1 + (30.55(0.292 - Z_{c,i})^{1.72}|0.96 + 0.1(T_{r,i} - 0,7)| \tag{A.17}$$

Further the following mixture properties should be calculated: critical temperature $T_{c,m}$, critical pressure $p_{c,m}$, molecular weight $M_{w,m}$ and low pressure polar correction factor $F_{p,m}^0$. These are calculated using the mixing rules presented in Eqs. (A.18), (A.19), (A.20) and (A.21)

$$T_{c,m} = y_1 T_{c,1} + y_2 T_{c,2} \tag{A.18}$$

$$p_{c,m} = 8.314 T_{c,m} \frac{y_1 Z_{c,1} + y_2 Z_{c,2}}{y_1 V_{c,1} + y_2 V_{c,2}} \tag{A.19}$$

$$M_{w,m} = y_1 M_{w,1} + y_2 M_{w,2} \tag{A.20}$$

$$F_{P,m}^0 = y_1 F_{P,1}^0 + y_2 F_{P,2}^0 \tag{A.21}$$

Following the mixture reduced temperature and pressure is calculated using Eq. (A.22)

$$T_{r,m} = \frac{T}{T_{c,m}}, \quad p_{r,m} = \frac{p}{p_{c,m}} \tag{A.22}$$

Based on the reduced values of temperature and pressure the factor Z_1 is calculated using Eq. (A.23). Here $F^0_{Q,m}$ is the low pressure mixture quantum correction factor which is set to $F^0_{Q,m} = 1$ unless one of the components is a quantum gas i.e Hydrogen, Deuterium or Helium.

$$\begin{aligned} Z_1 = (0.807 T_{r,m}^{0.618} - 0.357 \exp(-0.449 T_{r,m}) + \\ 0.340 \exp(-4.058 T_{r,m}) + 0.018) F^0_{P,m} F^0_{Q,m} \end{aligned} \tag{A.23}$$

Further the factor Z_2 must be calculated. Dependent on the magnitude of the reduced mixture temperature and pressure either Eq. (A.24) or (A.25) is used.

$$\begin{aligned} &\text{IF} \quad T_{r,m} \leq 1 \quad \text{and} \quad p_{r,m} \leq \frac{p_{vp}}{p_{c,m}} : \\ &\alpha = 3.262 + 14.98 p_{r,m}^{5.508}, \quad \beta = 1.390 + 5.746 p_{r,m} \\ &Z_2 = 0.6 + 0.76 p_{r,m}^{\alpha} + (6.99 p_{r,m}^{\beta} - 0.6)(1 - T_{r,m}) \end{aligned} \tag{A.24}$$

$$\begin{aligned} &\text{IF} \quad 1 < T_{r,m} < 40 \quad \text{and} \quad \frac{p_{vp}}{p_{c,m}} < p_{r,m} \leq 100 : \\ &a = \frac{1.245e-3}{T_{r,m}} \exp\left(5.1726 T_{r,m}^{-0.3286}\right) \\ &b = a(1.6553 T_{r,m} - 1.2723) \\ &c = \frac{0.4489}{T_{r,m}} \exp\left(3.0578 T_{r,m}^{-37.7332}\right) \\ &d = \frac{1.7368}{T_{r,m}} \exp\left(2.2310 T_{r,m}^{-7.6351}\right) \\ &e = 1.3088 \\ &f = 0.9425 \exp\left(-0.1853 T_{r,m}^{0.4489}\right) \\ &Z_2 = Z_1 \left(\frac{1 + a p_{r,m}^{e}}{b p_{r,m}^{f} + (1 + c p_{r,m}^{d}} \right)^{-1} \end{aligned} \tag{A.25}$$

When the factors Z_1 and Z_2 are calculated the factor Y is calculated as the ratio between these, see Eq. (A.26).

$$Y = \frac{Z_2}{Z_1} \tag{A.26}$$

Based on Y the pressure dependent polar and quantum correction factors F_P and F_Q are calculated using Eqs. (A.27) and (A.28). It can noted that if the low pressure quantum correction factor is $F^0_{Q,m} = 1$ then the pressure dependent quantum correction factor will also be $F_{Q,m} = 1$.

$$F_{P,m} = \frac{(1 + (F^0_{p,m} - 1)Y^{-3})}{F^0_{p,m}} \tag{A.27}$$

$$F_{Q,m} = (1 + (F^0_{Q,m} - 1)(Y^{-1} - 0.007\ln(Y)^4))/F^0_{Q,m} \tag{A.28}$$

Finally the factor ξ is calculated, see Eq. (A.29), and used to determine the mixture viscosity using Eq. (A.30).

$$\xi = 0.176 \left(\frac{T_{c,m}}{M^3_{w,m} p^4_{c,m}} \right)^{1/6} \tag{A.29}$$

$$\eta_m = \frac{Z_2 F_P F_Q}{\xi} \tag{A.30}$$

A.1.2 Liquid viscosity

El-Sayed

To apply the El-Sayed method the pure component viscosities must be evaluated at the saturation point of the corresponding temperature. The definition of corresponding temperature can be seen in Eq. (A.13), here the mixture critical temperature is calculated according to Eq. (4.2).

Following the factors F_x and F_t are calculated according to Eqs. (A.31) and (A.33). Here η_1 and η_2 are the pure component viscosities at the saturation point of the corresponding temperature and T^R is the bulk mixture temperature in degrees Rankine.

$$F_x = \left(y_1 y_2 - 0.125 y_1^2 y_2\right) \ln\left(\eta_1 \eta_2\right)^{0.5} \tag{A.31}$$

$$F_t = 4.219 - 3.7996\frac{T^R}{492} + 0.842\left(\frac{T^R}{492}\right)^2 \tag{A.32}$$

Further the factor F_{12} is calculated as the product of F_t and F_x. Using F_{12} the mixture viscosity can be determined as seen in Eq. (A.34)

$$F_{12} = F_t F_x \tag{A.33}$$

$$\eta_m = \exp\left(y_1 \ln(\eta_1) + y_2 \ln(\eta_2) + F_{12}\right) \tag{A.34}$$

M. Conde

M. Conde[3] prosed an updated version of El-Sayed's method which should increase the accuracy. Again the pure component viscosities are calculated based on the saturated conditions at the corresponding temperatures, see Eq. (A.35).

$$T_{corr,1} = T\frac{T_{c,1}}{T_{cm}}, \quad T_{corr,2} = T\frac{T_{c,2}}{T_{c,m}} \tag{A.35}$$

Based on this the factor F_x is calculated as in Eq. (A.36).

$$F_x = 6.38\left(y_2^{1.125y_1}\right)\left(1 - \exp(-0.585 y_1 y_2^{0.18})\right)\ln\left(\eta_1^{0.5}\eta_2^{0.5}\right) \tag{A.36}$$

From the reduced temperature of the water and the factor F_x the term $\Delta\eta$ can be calculated using Eq. (A.37), which finally is used to determine the mixture viscosity, see Eq. (A.38)

$$\Delta\eta = \left(0.534 - 0.815\frac{T}{T_{c,2}}\right)F_x \tag{A.37}$$

$$\eta_m = \exp\left(y_1 \ln(\eta_1) + y_2 \ln(\eta_2) + \Delta\eta\right) \tag{A.38}$$

Handbuch der Kältetechnik

Handbuch der Kältetechnik[85] presents a liquid viscosity correlation developed explicitly for ammonia-water. The correlation is based on a curve fit of experimental data as has the form seen in Eq. (A.39). Here T is the temperature in degrees Celsius and x is the ammonia mass fraction.

$$\log\log(\eta_m+1) = \frac{2000}{500+T} - 4.41 + 0.925x - 1.743x^2 + 0.021x^3 - 1 \tag{A.39}$$

A.2 Conductivity

A.2.1 Vapour conductivity

El-Sayed

El-Sayed proposed to calculate the vapour mixture conductivity using the mixing rules from Wilke's viscosity correlation and thereby relies on a viscosity conductivity analogy. The factors F_{12} and F_{21} is calculated using Eqs. (A.10) and (A.11) from section A.1.1 and hence both the pure component viscosity and the pure component conductivity must be known in order to apply the El-Sayed vapour conductivity correlation. The mixture conductivity is calculated using Eq. (A.40).

$$\lambda_m = \frac{\lambda_1 y_1}{y_1 + F_{12} y_2} + \frac{\lambda_2 y_2}{y_2 + F_{21} y_1} \tag{A.40}$$

A.2.2 Liquid conductivity

El-Sayed

El-Sayed proposes a linear interpolation of the pure component viscosities weighted on mole fraction. This is seen in Eq. (A.41)

$$\lambda_m = y_1\lambda_1 + y_2\lambda_2 \tag{A.41}$$

M. Conde

M. Conde suggested a quasi-ideal approach based on the corresponding values of the pure component conductivities. The pure water conductivity is evaluated at the saturation point of the corresponding temperature as described in section A.1.2. The pure ammonia conductivity is calculated using a correlation based on the corresponding density, ρ^* . ρ^* is the density of the ammonia at the saturation point of the corresponding temperature. Using this the density ρ_1^+ can be calculated using Eq. (A.42). The corresponding value of of the pure ammonia conductivity is then evaluated at the saturation point of density ρ_1^+.

$$\rho_1^+ = \rho^* y_1^{0.425} \tag{A.42}$$

The mixture conductivity is then calculated using Eq. (A.43)

$$\lambda_m = y_1 \lambda_1^+ + y_2 \lambda_2^* \tag{A.43}$$

Jamieson

Jamieson has proposed an estimation correlation for the thermal conductivity of binary mixtures. This is based on fitting of experimental data. The correlation can be seen in Eq. (A.44). Here the parameter α is a mixture specific variable, if this is unknown for the evaluated mixture it should be set to one. Further the equation is made such that $\lambda_2 \geq \lambda_1$

$$\lambda_m = x_2 \lambda_2 + x_1 \lambda_1 - \alpha(\lambda_1 - \lambda_2)(1 - \sqrt{x_1})x_1 \tag{A.44}$$

Fillipov

In a similar approach as Jamieson, Fillipov suggested Eq. (A.45) for the estimation of binary mixture conductivity. Here the value of 0.72 may be exchanged with a mixture specific value if known. Again the equation is made such that $\lambda_2 \geq \lambda_1$.

$$\lambda_m = x_1 \lambda_1 + x_2 \lambda_2 - 0.72 \lambda_1 x_2 (\lambda_2 - \lambda_1) \tag{A.45}$$

APPENDIX B

AMMONIA-WATER HEAT TRANSFER AND PRESSURE DROP CORRELATIONS

B.1 Single phase heat transfer - Martin

Martin's correlation [63] is a semi-empirical correlation based on a heat transfer to friction analogy. The Moody friction factor is calculated using Eq. (B.1), this friction factor also accounts for the pressure drop in the port holes.

$$\frac{1}{\xi} = \frac{\cos\varphi}{\sqrt{0.18\tan\varphi + 0.36\sin\varphi + \xi_0/\cos\varphi}} + \frac{1-\cos\varphi}{\sqrt{3.8\xi_{1.0}}} \tag{B.1}$$

In Eq. (B.1) φ is the corrugation inclination angle ($\varphi = 90° - \beta$). Further, ξ_0 is the friction factor for straight longitudinal flow ($\varphi = 0°$) and $\xi_{1.0}$ is the friction factor for wavy longitudinal flow ($\varphi = 90°$).

If the flow is laminar ($Re/\phi < 2000$): ξ_0 and $\xi_{1.0}$ can found by Eq. (B.2).

$$\xi_0 = \frac{64\phi}{\mathrm{Re}}, \quad \xi_{1.0} = \frac{597\phi}{\mathrm{Re}} + 3.85 \tag{B.2}$$

If the flow is turbulent ($Re/\phi \geq 2000$): ξ_0 and $\xi_{1.0}$ can found by Eq. (B.3)

$$\xi_0 = \left(1.8\log_{10}\frac{\mathrm{Re}}{\phi} - 1.5\right)^{-2}, \quad \xi_{1.0} = \frac{39}{(\mathrm{Re}/\phi)^{0.289}} \tag{B.3}$$

The Nusselt number is then determined by Eq. (B.4). Here η is the dynamic viscosity of the bulk flow while η_w is evaluated at the wall temperature. Further, Pr is the Prandtl number calculated from the specific

heat c_p, the viscosity η and the thermal conductivity λ.

$$\mathrm{Nu} = \phi \cdot 0.122 \cdot \mathrm{Pr}^{1/3} \frac{\eta}{\eta_w}^{1/6} \left(\xi \left(\frac{\mathrm{Re}}{\phi} \right)^2 \sin(2\varphi) \right)^{0.374} \tag{B.4}$$

The Reynolds number is estimated based on the mass flux, G and the hydraulic diameter assumed to be two times the press depth of the plate: $D_h = 2b$. The cross sectional area used to estimate the mass flux is $A_{\mathrm{cross,h}} = N_{\mathrm{ch,h}} \cdot W \cdot b$ and $A_{\mathrm{cross,c}} = N_{\mathrm{ch,c}} \cdot W \cdot b$ for the hot and cold part respectively.

The pressure drop, Δp, and convective heat transfer coefficient, α, for t single-phase flows can the be found using Eq. (B.5) and Eq. (B.6), respectively.

$$\alpha = \frac{\mathrm{Nu}\lambda}{D_h} \tag{B.5}$$

$$\Delta p = \frac{2\xi G^2 L_p}{D_h \rho} \tag{B.6}$$

B.2 Desorption - Taboas et al.

Taboas et al.[96, 95, 94] have investigated the two-phase flow of ammonia-water mixtures in plate heat exchanger during desorption. This work resulted in a correlation, which is applied. This correlation uses a transition criterion to asses whether the desorption is dominated by apparent nucleate or convective flow boiling. The transition is based on the estimates of vapour and liquid velocities, these calculated as seen in Eq. (B.7). Here q is the vapour mass fraction and ρ is the density for vapour (subscript v) and liquid (subscript l) respectively.

$$u_{\mathrm{SL}} = \frac{G(1-q)}{\rho_{\mathrm{l}}} \quad u_{\mathrm{SV}} = \frac{Gq}{\rho_{\mathrm{v}}} \tag{B.7}$$

If the inequality in Eq. (B.8) is satisfied: the desorption is dominated by apparent nucleate boiling and is mainly influenced by heat flux, q''.

The two-phase heat transfer coefficient can be found by Eq. (B.9). Here α_{lo} is the liquid only heat transfer coefficient calculated using Martin's correlation. Bo is the boiling number, Eq. (B.10) calculated based heat and mass flux and h_{lv}: the latent heat of evaporation calculated as the difference between the dew point and bubble point enthalpy at the local liquid ammonia mass fraction and the bulk temperature.

$$u_{SV} < 111.88u_{SL} + 11.848[m/s] \tag{B.8}$$

$$\alpha_{TP,DS} = 5\text{Bo}^{0.15}\alpha_{lo} \tag{B.9}$$

$$\text{Bo} = \frac{q''}{Gh_{lv}} \tag{B.10}$$

If the inequality in Eq. (B.11) is satisfied: the two-phase heat transfer coefficient is calculated by using Eq. (B.12). Here it is assumed that nucleate boiling is suppressed and the influence of heat flux on the heat transfer coefficient diminishes. Chisholm's two-phase enhancement factor F, see Eq. (B.13), is used to estimate the two-phase heat transfer coefficient. Here X_{tt} is the Lockhartt-Martinelli factor calculated as seen in Eq. (B.14).

$$u_{SV} > 111.88u_{SL} + 11.848[m/s] \tag{B.11}$$

$$\alpha_{TP,DS} = \max\{ \quad F\alpha_{lo} \quad , \quad 5\text{Bo}^{0.15}\alpha_{lo} \quad \} \tag{B.12}$$

$$F = \left(1 + \frac{3}{X_{tt}} + \frac{1}{X_{tt}^2}\right)^{0.2} \tag{B.13}$$

$$X_{tt} = \left(\frac{\eta_l}{\eta_v}\right)^{0.1}\left(\frac{1-q}{q}\right)^{0.9}\left(\frac{\rho_v}{\rho_l}\right)^{0.5} \tag{B.14}$$

The liquid only friction factor is correlated to the liquid only Reynold's number, see Eq. (B.15). The liquid only pressure drop is calculated as shown in Eq. (B.15). The two-phase pressure drop is found by multiplying this with the two-phase enhancement factor F Eq. (B.13).

$$\xi_{lo} = 4.779\text{Re}_{lo}^{-0.118} \tag{B.15}$$

B.3 Absorption - Silver/Bell-Ghaly

Nordtvedt[74] suggested the use of the Silver/Bell-Ghaly method[90, 20]. This states that the effective two-phase heat transfer coefficient can be calculated as seen in Eq. (B.16). Here α_{vo} is the vapour only heat transfer coefficient calculated by Martin's correlation. α_{lo} is the heat transfer coefficient of the condensate layer corrected for two-phase flow effects. This is estimated using Yan and Lin[106]. Here the Nusselt's number is correlated as seen in Eq. (B.17).

$$\alpha_{\text{TP,AB}} = \left(\frac{1}{\alpha_{\text{lo}}} + \frac{Z}{\alpha_{\text{vo}}} \right)^{-1} \tag{B.16}$$

$$\text{Nu}_{\text{lo}} = 4.188 \text{Re}_{\text{lo}}^{0.4} \text{Pr}_{\text{l}}^{1/3} \tag{B.17}$$

The factor Z in Eq. (B.16) is defined as seen in Eq. (B.18). Here, q is the vapour mass fraction, $c_{p,\text{v}}$ is the specific heat of the vapour phase and dT/dh is the gradient of the equilibrium absorption curve.

$$Z = q c_{p,\text{v}} \frac{dT}{dh} \tag{B.18}$$

The two-phase friction factor correlation by Yan and Lin[106] is applied to estimate the pressure drop

DTU Mechanical Engineering
Section of Thermal Energy
Technical University of Denmark

Nils Koppels Alle, Bld. 403
DK-2800 Kgs. Lyngby
Denmark
Phone (+45) 45 25 41 31
Fax (+45) 45 88 43 25

www.mek.dtu.dk

DTU Mechanical Engineering
Section of Thermal Energy
Technical University of Denmark

Nils Koppels Allé, Bld. 403
DK-2800 Kgs. Lyngby
Denmark
Phone (+45) 4525 4131
Fax (+45) 4588 4325
www.mek.dtu.dk
ISBN: 978-87-7475-459-6

DCAMM
Danish Center for Applied Mathematics and Mechanics

Nils Koppels Allé, Bld. 404
DK-2800 Kgs. Lyngby
Denmark
Phone (+45) 4525 4250
Fax (+45) 4593 1475
www.dcamm.dk
ISSN: 0903-1685